DECONSTRUCTING THE WISE NEARBY GALAXY POPULATION

Tamlyn August

Supervisors:
Prof. T. Jarrett (UCT)
& Dr. M. Cluver (UWC)

Astronomy Department
University of Cape Town (UCT)

A research project submitted in partial fulfilment of the requirements for the National Astrophysics and Space Science Programme (NASSP) M.Sc. degree.

July 2017

This work is funded fully by the South African National Research Foundation (SA NRF) and the National Astrophysics and Space Science Program (NASSP) through their postgraduate student scholarship. Opinions expressed and conclusions made, are those of the author and not necessarily those of the SA NRF, NASSP and/or UCT.

Abstract

This thesis aims to test the reliability of the Wide-Field Infrared Space Explorer (*WISE*) star formation indicators centred at 12 and 22 μm. To accomplish this, the total infrared (TIR) luminosity was used as a calibrator to understand the behaviour of the two indicators.

Our sample consists of *Spitzer* galaxies from the SINGS and KINGFISH surveys, with a select few excluded. The TIR calibration also necessitates that most of our galaxies have FIR data from *Herschel*.

The photometric analysis done on the raw *WISE* and *Spitzer* images of our galaxies is explained, including how the isophotes and background sky level were determined for each band/image.

Once the reliability of the *WISE* indicators was established, new star formation rate relations were formulated. The new relations are comparable to previous relations in the literature, but improve on them in stellar mass-, metallicity-, and luminosity range. We also find that metallicity of the galaxies has minimal effect on our relations.

In our comparison of emission from PAH molecules, the two bands in question, IRAC4 and W 3 are strongly correlated. This may suggest that the W_3 band is dominated by emission from the 11.3 μm PAH molecule, or it might be an effect of the band overlap between IRAC4 and W_3.

Acknowledgements

This work is funded fully by the South African National Research Foundation (SA NRF) and the National Astrophysics and Space Science Programme (NASSP) through their postgraduate student scholarship.

The help and guidance of my supervisors, Prof. Tom Jarrett and Dr. Michelle Cluver, was pivotal throughout my research.

Data Sources

Galaxies are drawn from the SINGS and KINGFISH databases. Morphologies and activity types were sourced from NED.

Plagiarism Declaration

I, Tamlyn August, know the meaning of plagiarism and hereby declare that all of the work in this document, save for that which is properly acknowledged, is my own.

Signature: Signed by candidate

____

Date:

____

Contents

List of Figures

List of Tables

Chapter 1

Introduction

Studies have shown that the universe reached its star formation peak at a redshift of ~ 2 and has been declining ever since (Madau & Dickinson 2014). But the actual mechanism of star formation itself is still relatively poorly understood. In order to determine how typical galaxies in the local universe form stars and build their stellar mass, we need to be able to accurately measure the current star formation and stellar mass of statistically significant samples.

Therefore, it is essential that we use reliable measures of star formation in our galaxy evolution studies. Thus, in this thesis, we will investigate the reliability of the star formation measures in the *WISE* survey (see section 1.3), using data from nearby galaxies. SINGS, with its photometry from both *WISE* and *Spitzer*, affords us the opportunity to study star formation at the hand of galaxies with a wide range of stellar masses and morphological types. We will compare the *Spitzer* and *WISE* star formation tracers, and will investigate their trend with the total infrared luminosity (L_{TIR}). This luminosity gives us a long-term, averaged view of the star formation in the galaxy (see section 1.6.1).

1.1 Multi-wavelength star formation indicators

There is a range of star formation indicators currently in use in the literature, depending on which wavelength regime is appropriate and which data are available.
The near-UV wavelength range directly traces the photospheric emission of young stars, making it one of the more direct methods of tracing recent star formation. The main weakness in using the UV as a tracer is its sensitivity to dust attenuation. Many calibrations for this dust attenuation have been published, but they depend heavily on factors such as the shape of the dust extinction curve, geometry and scattering effects (Kennicutt & Evans 2012).
Most other techniques rely on reprocessed emission from interstellar dust or gas. The most common of these techniques involve optical or near-infrared emission lines from ionized clouds that surround young stars. For nearby and very distant galaxies, the favoured emission line is that of Hα. For mid-redshift galaxies the bluer lines such as the forbidden [OII] line have been used. Other lines investigated include the fine structure cooling lines associated with HII regions (eg. Ho & Keto 2007, Boselli et al. 2002).

Infrared measures of the SFR are essential for a complete characterisation of the star formation in any particular galaxy. Interstellar dust absorbs roughly half the starlight in the universe and re-emits it in the infrared wavelength range. Since these are the indicators investigated in this thesis, more details follow in the subsequent sections.

Other indicators currently in use are from the radio continuum as well as X-ray emission.
The radio continuum indicator consists of two components: a free-free component, and a synchotron component. A calibration for SFR from the radio continuum has not been found from first principles, thus the current calibrations have been inferred from the tight radio-infrared correlation. The synchotron contribution makes these calibrations highly wavelength-dependent, and most have been referenced to 1.4GHz (Kennicutt & Evans 2012).
X-ray emission in galaxies is made up of contributions from AGN accretion disks, X-ray binaries, supernovae, supernova remnants, and massive stars. All these apart from the AGN accretion disks are associated with young stellar populations and recent star formation, and thus can be used as an indicator for SFR. The calibrations are usually inferred from the radio or infrared (Kennicutt & Evans 2012).

1.2 *Spitzer*

The *Spitzer* Space Telescope, NASA's Great Observatory for infrared astronomy, was launched on 25 August 2003. Its cryostat was expected to last at least five years, which was accomplished when the cryogenic phase ended in May 2009 (www.spitzer.caltech.edu). The telescope has an Earth-trailing solar orbit. It houses three scientific instruments:

the Infrared Array Camera (IRAC), the Infrared Spectrograph (IRS), and the Multiband Imaging Photometer for *Spitzer* (MIPS). IRAC is a four-channel Infrared Imager, with photometric bands centred at 3.6, 4.5, 5.8 and 8.0 μm, known as IRAC 1, 2, 3, and 4 respectively. The IRS is a low- to moderate-resolution spectrometer, while MIPS is a far-infrared (FIR) imager and spectral energy distribution (SED) photometer with bands centred at 24, 70 and 160 μm, known as MIPS 24, 70 and 160 respectively. All three instruments have a common focal plane (Werner et al. 2004).

Spitzer traces similar physics to *WISE* with its bands centred at 3.6, 4.5, 5.8, 8.0, and 24 μm. The IRAC 1 and 2 bands are chiefly made up of starlight from evolved stars, while the IRAC 3 and 4 bands consist largely of PAH emission at 5.8 and 8.0 μm. These PAHs are highly energized, and thus trace star formation (Calzetti et al. 2007). It has both cryo-phase and warm-phase missions. Point source sensitivity is 3.4, 4.3, 27 and 110 μJy at 3.6, 4.5, 8.0 and 24 μm respectively, with confusion. Spatial resolution for the IRAC bands is 1.2 arcsec, with 2.55 arcsec for MIPS24 (Van Dyk et al., *Spitzer* Space Telescope Handbook).

1.3 *WISE*

The Wide-field Infrared Space Explorer (*WISE*) conducted an all-sky mid-infrared (MIR) survey during the period December 2009 - August 2010; with photometric bands centred at 3.4, 4.6, 12 and 22 μm, known as W_1, W_2, W_3 and W_4 respectively (see figure 1.1 below). W_1 and W_2 characterize the evolved stellar population of the galaxy, the stellar “backbone,” with W_2 being additionally sensitive to hot dust in the galaxy (Cluver et al. 2014).

W_3 traces several different features, amongst them the forbidden neon lines [Ne II] at 12.8 μm and [Ne III] at 15.5 μm (Hemachandra et al. 2015), silicate absorption at 10 μm, and the 11.3 μm PAH (see section 1.5) molecule. PAH molecules absorb UV and optical radiation from starlight and ionised gas; and re-emit in the mid-infrared (MIR) band. The average ionization potential of PAHs is 6 eV. This ensures the rarity of PAH emission in intense starburst galaxies, but makes their emission common, and thus a good star formation tracer, in normal dust-rich galaxies. The 11.3 μm PAH, in particular, can be excited by radiation from both young stars and evolved stars, making it an ambiguous indicator of star formation in some cases.
The two ionized neon lines are emitted when neon atoms are irradiated by energetic photons from young stars, and thus trace star formation. The sum of their luminosities increases with the total infrared (TIR) luminosity, a known star formation indicator (Ho & Keto 2007).

W_4, on the other hand, traces the warm dust continuum of the galaxy, and thus traces star formation reliably. It is, however, much less sensitive than W_3.

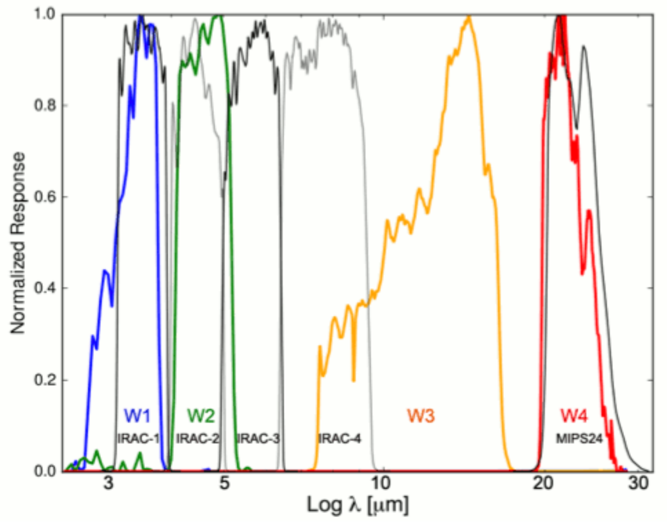

Figure 1.1: WISE *transmission curves,* W_1*,* W_2*,* W_3 *and* W_4 *from left to right, with the* Spitzer *transmission curves also shown. Source: http://wise2.ipac.caltech.edu/.*

WISE achieves 5σ point source sensitivities better than 0.08, 0.11, 1, and 6 mJy in unconfused regions on the ecliptic; with angular resolution at 6.1, 6.4, 6.5, and 12.0 arcseconds in W_1, W_2, W_3 and W_4 respectively (Wright et al. 2010).

We will compare the *WISE* and *Spitzer* (see section 1.2) data. *Spitzer* has slightly different bands to *WISE* with better resolution and sensitivity.

In order to compare the *WISE* and *Spitzer* data, we require a sample that has been imaged with both the *WISE* and *Spitzer* telescopes, with the added advantage of far-infrared data which makes our TIR calibration possible. The next section details the surveys from which our sample is drawn, since they satisfy all these criteria.

1.4 SINGS and KINGFISH

The *Spitzer* Infrared Nearby Galaxy Survey (SINGS), consisting of 75 galaxies, was part of *Spitzer*'s cryogenic phase. Containing multi-wavelength data ranging from the radio regime to X-ray wavelengths, it aims to characterize the link between star formation and the interstellar medium (ISM) in the galaxy (Kennicutt et al. 2003), and has produced complete *Spitzer* imaging and spectroscopic mapping and a comprehensive set of multi-wavelength ancillary observations for the sample.

The Key Insights on Nearby Galaxies: a Far-Infrared Survey with *Herschel* (KINGFISH; Kennicutt et al. 2011) project is a direct descendant of SINGS. It consists of 61 nearby ($d < 30$ Mpc) galaxies, on which both imaging and spectroscopy have been conducted. The *Herschel* imaging consists of complete maps for the galaxies at 70, 100, 160, 250, 350, and 500 μm. Its broad science goals include characterizing the ISM of present-day galaxies; the heating and cooling of their gaseous and dust components; and better understanding the physical processes linking star formation and the ISM.

The SINGS and KINGFISH multi-wavelength datasets combined provide panchromatic mapping of the galaxies sufficient to resolve individual star-forming regions, and tracing the important heating and cooling channels of the ISM, across a wide range of local extragalactic ISM environments (Kennicutt et al. 2011). The wide wavelength range of the data also reliably determines the TIR luminosity, which is essential to our calibration. In order to take advantage of this wealth of data to understand star formation, however, understanding PAH molecules and the conditions in which they trace star formation is essential.

Our sample thus consists of 76 galaxies in total, 74 of which are either in the SINGS or KINGFISH surveys. The additional ones are M87 and M82/NGC3034.

1.5 Infrared emission from PAH molecules

Polycyclic aromatic hydrocarbons (hereafter referred to as PAHs) are organic molecules found in the interstellar medium (ISM) of most galaxies, usually in those regions in which newly-formed stars are present (Cox et al. 2007; Rhee et al. 2007; Witt et al. 2008; Cordiner et al. 2008). They are thus potentially good tracers of star formation. PAH emission is largely due to the vibration of the molecules, and thus the emitted wavelength is associated with the size of the molecule (Draine & Li 2007).

The main features in the MIR band, as seen in Figure 1.2, peak at 3.3, 6.2, 7.7, 8.6, 11.3 and 12.7 μm (Sellgren 1984; Allamandola, Tielens & Barker 1989). There are several noteworthy trends observed about the different PAH features according to Smith et al. (2007). For example, the 11.3 μm feature (which lies within the W_3 band) has the highest luminosity-to-wavelength ratio, so it doesn't suffer from continuum dilution as much as the smaller PAHs. As a consequence, this feature can dominate the PAH spectrum. Secondly, PAH emission (and dust/grain mass) is suppressed in sources with metallicity[1] below 8.1. Thirdly, the IRAC4 8μm broadband flux correlates well with PAH strength, but can be overwhelmed by other MIR features or the continuum.
In most galaxies, the PAH contributions are dominated by the flux at 7.7 μm (IRAC4 band at low redshift) and 8.6 μm (MIPS24 band at redshift 2). We assume that these two bands are a direct proxy for PAH emission, and thus the TIR power, and potentially the star formation rate (SFR). This assumption is not always valid, even when the PAH-to-TIR ratio is high (Smith et al. 2007).

The PAH emission also depends on the type of activity in the galaxy: at the lowest 7.7-to-11.3 luminosity ratios, all sources show LINER or Seyfert activity. Short-wavelength PAH emission is suppressed in these systems by up to a factor of 10, when compared to star-forming galaxies (Smith et al. 2007).

The molecules' charge also plays a role in which wavelength is emitted: the 11.3 μm emission is most likely produced by neutral PAHs, and the 7.7 μm by cations. The 11.3 μm emission feature can be produced by single-photon heating of PAH molecules that are larger than those that produce the 7.7 μm emission more easily. The reddening (emission of longer wavelengths) might then be due to the destruction of the smaller PAH molecules (Smith et al. 2007).

---

[1] $12 + log(O/H) < 8.1$

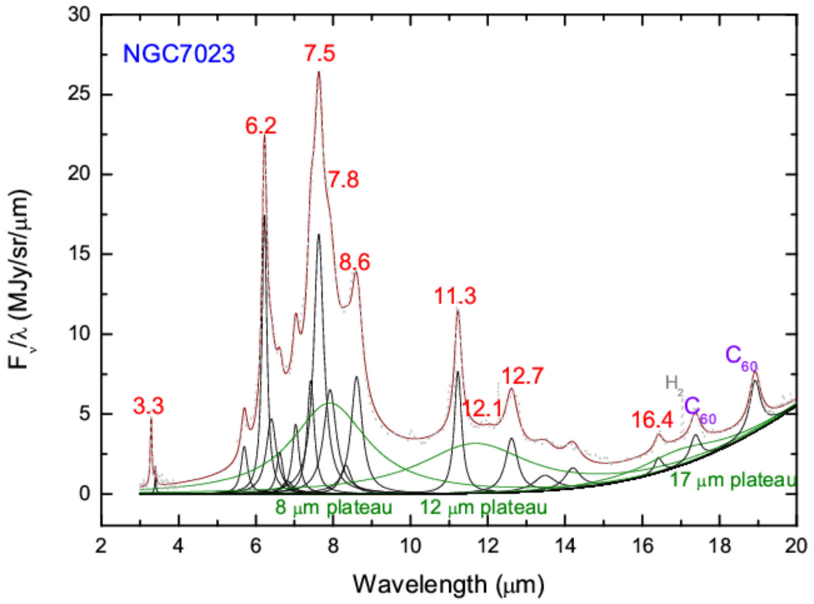

Figure 1.2: *SED of reflection nebula NGC7023 (Kwok & Zhang 2013).*

PAH luminosities are just one way of determining star formation rates. The next section details some of the common infrared measurements used to calculate this important quantity.

1.6 Infrared luminosities as a star formation indicator

In order to formulate new SFR relations, we need star formation data. We chose the total infrared (TIR) luminosity as our star formation indicator (see 1.6.1 below). There are several ways of determining the TIR flux. We chose the integrated flux under SED fits from Draine & Li (2007) as our TIR metric.

Theoretical expressions for SFR are heavily dependent on assumptions, such as the relevant timescales and the stellar population distribution. There are two classes of SFR: 1) global, for the whole galaxy - it is luminosity-weighted, averaged across local variations in star formation history and physical conditions in the galaxy, thus good for distant galaxies; 2) local SFR: for regions within the galaxy, measured on a sub-galactic or sub-kpc scale, it is good for investigating star formation mechanisms. The regions considered should be a few hundred parsecs or larger to include more than one star forming region so that star formation can be considered constant over the relevant timescale (Calzetti 2012).

Below is an SED of the late-type spiral galaxy NGC0337. It illustrates the different types of indicators discussed next, that is, monochromatic indicators (a single broadband data-point) and the TIR luminosity (integrated under the fitted curve over the whole wavelength range).

1.6.1 Total infrared luminosity

To first order, the infrared SED of a galaxy depends on its starlight SED. The emissivity of dust grains is higher in the infrared; whereas their cross-section, and thus absorption, is higher in the UV wavelength range than in the optical. Therefore, the SED of dust grains radiated by UV light from young stars will be more luminous and peaked at shorter wavelengths than dust irradiated by UV-faint, evolved stars. Thus the motivation to use the total infrared luminosity as a star formation indicator. This star formation rate applies to long timescales of ~ 100 Myr (Calzetti 2012). Thus it gives us a long-term, averaged view of the star formation in the galaxy. It is not sensitive to starbursts and local variations in the star formation.

$$SFR(TIR) = 2.8 \times 10^{-44} L_{TIR} \tag{1.1}$$

where SFR(TIR) is in $M_{\odot}\ yr^{-1}$ and L_{TIR} is in $erg\ s^{-1}$, and a Kroupa (2001) IMF was used. It is assumed that the Starburst99, solar-metallicity stellar bolometric emission is completely absorbed and re-emitted by the dust in the

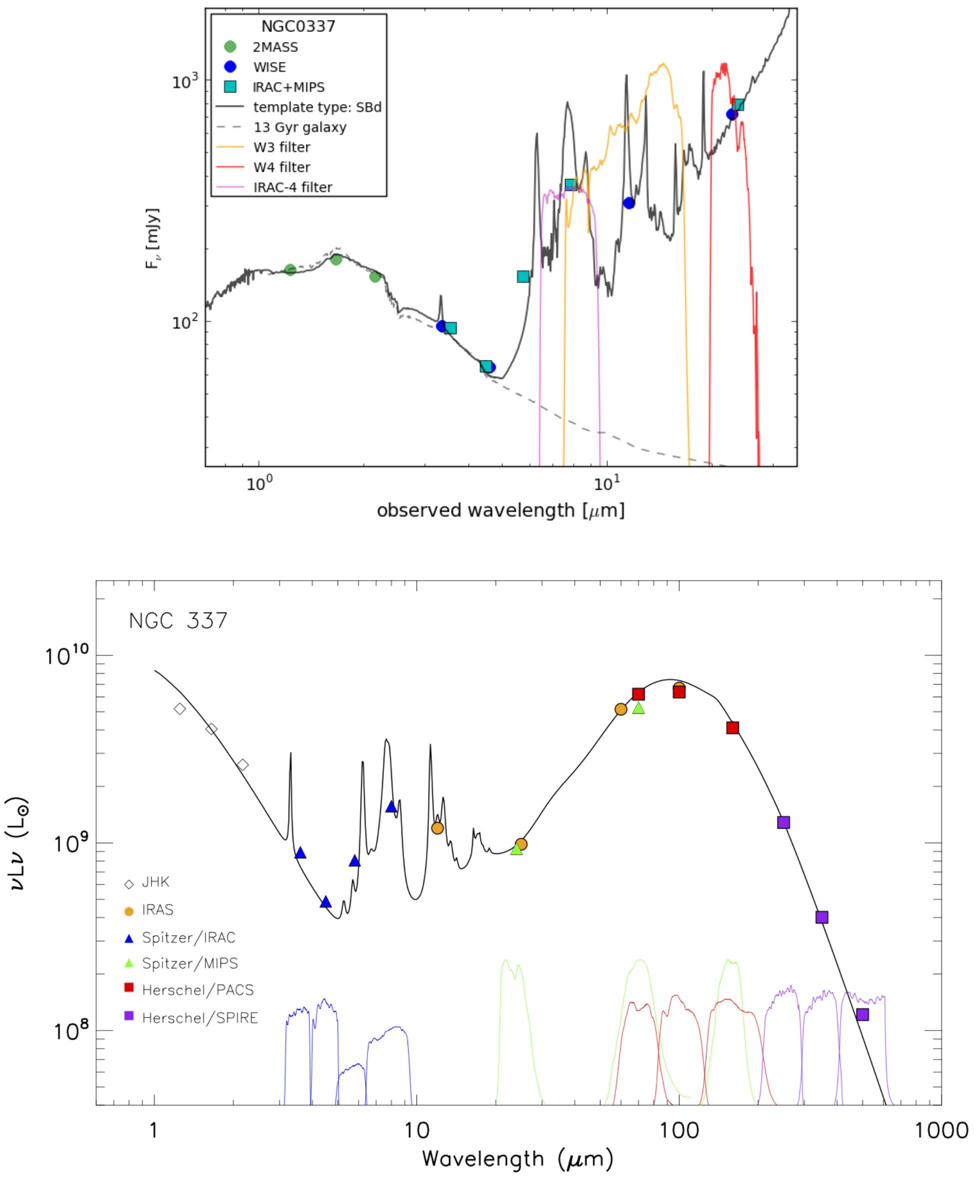

Figure 1.3: *SED of late-type spiral galaxy NGC0337. Top: with data-points from 2MASS,* WISE*, and* Spitzer*. Bottom: with data points from* IRAS*,* Spitzer *and* Herschel *(Kennicutt et al. 2011).*

galaxy (Calzetti 2012).

The TIR luminosity used in this thesis was obtained by integrating under SED curves from Draine & Li (2007) in the wavelength range $\sim 3 - 1000$ μm. A good approximation of the TIR luminosity is given by this equation in Dale et al. 2014 (see Figures B.4 and B.5):

$$f_{TIR} = \varepsilon_0 \nu f_\nu(8\mu m) + \varepsilon_1 \nu f_\nu(24\mu m) + \varepsilon_2 \nu f_\nu(70\mu m) + \varepsilon_3 \nu f_\nu(160\mu m) \tag{1.2}$$

The photometric measurements used were from *Spitzer* (IRAC) and *Herschel* (PACS and SPIRE), and the coefficients depend on the AGN contribution to the mid-infrared luminosity in the galaxy (Dale et al. 2014).

Equation (1.1) assumes that *all* the stellar light is absorbed and re-emitted by dust. This is not typically the case. Only about half the stellar light is absorbed (Dole et al. 2006). This fraction is also dependent on the dust distribution in the galaxy and the geometry compared to the line of sight.

To use the SFR calculated from the integrated TIR measurement to form our relations, it is essential that we know exactly what our measurements are tracing, otherwise our SFR will not be representative of the physical conditions in the galaxy. In the MIR wavelength range there are several features *not* due to star formation indicators, which can confuse our results and thus we must take care when dealing with them. The next section details these objects and the types of emission they produce.

1.7 SED contaminates

There are many astronomical objects that emit/absorb in the MIR range, among them silicate dust, post-AGB stars and planetary nebulae. This emission/absorption can confuse our results, and thus we must remain aware of this when doing the analysis.

1.7.1 Silicate absorption

Silicate absorption, which occurs at 9.7 and 18 μm, is due to the presence of silicate molecules such as Al_2SiO_3 and Mg_2SiO_4 (Li & Draine 2001). These absorption features affect the PAH spectrum, which confuses the link between PAH grains and star formation in the galaxy.
In star-forming galaxies, increasing silicate absorption changes the shape of the 15-20 μm continuum. Most normal galaxies do not show significant silicate absorption in their central regions (a few kpc) (Smith et al. 2007).
For shallower silicate absorption and stronger (relative to continuum) PAH emission, features at 7.7 (IRAC4 band at low redshift) or 8.6 (MIPS24 band at redshift 2) and 11.3 μm can mimic or mask the silicate absorption. This is because they flank the $\lambda_{Si} = 9.7\mu m$ wavelength (which lies within the W_3 bandpass). This makes it difficult to distinguish between moderate PAH on top of silicate-absorbed continuum; and a strong PAH component with relatively weak continuum.

1.7.2 Post-AGB stars

Stars in the post-AGB stage of evolution have intermediate masses (0.8 - 8 $M_{\odot}$), and are good laboratories for studying stellar nucleosynthesis. Classical post-AGBs are optically bright. Many post-AGBs are obscured by dust, and are thus infrared-bright (Carroll & Ostlie 2006).

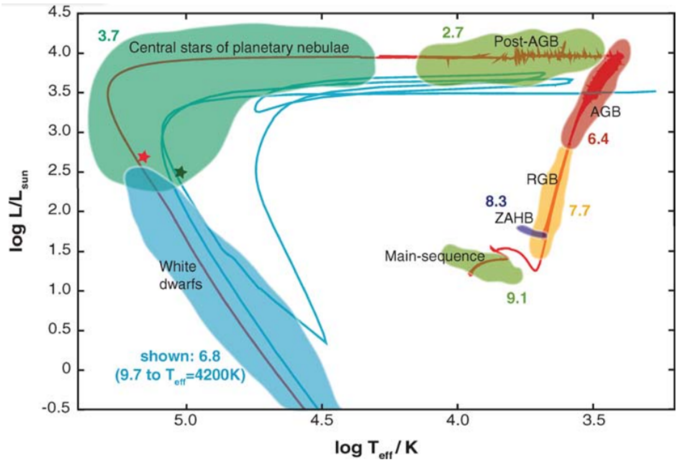

Figure 1.4: *Hertzsprung-Russel depicting the evolution of massive stars, including the post-AGB and planetary nebula stage. Source: Herwig (2005).*

The cloud around the star expands, and when it becomes optically thin the central star is exposed. The star's evolution track moves blueward in a near-horizontal line across the HR diagram (see Fig. 1.4), luminosity almost constant. When the final stage of mass loss occurs the remainder of the envelope is expelled, both the hydrogen- and helium-burning shells are extinguished, and the star's luminosity decreases swiftly. The hot central object, which is basically the degenerate C-O (or ONeMg in more massive stars) core of the old red giant star, cools down to a white dwarf (Carroll & Ostlie 2006).

They have spectroscopic features at 10 and 20 μm, as well as an unidentified infrared (UIR) emission feature at 21 μm, for cool post-AGBs (Justtanont et al. 1996).

1.7.3 Planetary Nebulae

Planetary nebulae (PNe) owe their appearance to the ultraviolet light being radiated from the central star. The UV photons are absorbed by the gas in the nebula, which excites or ionizes the gas atoms. When the electrons cascade back down, visible light is emitted.
The morphologies of PNe are more complex than expected for a spherically-symmetric thermally-pulsing AGB (TP-AGB) parent star. The Helix nebula, for example, has a ring structure. Here the gas is preferentially ejected along

the equator to ensure conservation of angular momentum. Possible reasons for the variety of PNe structures include our viewing angles, multiple material ejections, the presence of companion stars, and magnetic fields.

The lifetime of a PNe is minuscule compared to a star's lifetime - after only approximately 50 kyr, the PNe dissipates into the ISM. The number of PNe in the Milky Way is estimated to be close to 15,000. If each of these PNe contains $0.5 M_{\odot}$ of material, the ISM gains 1 $M_{\odot}$ yr^{-1} (Carroll & Ostlie 2006).

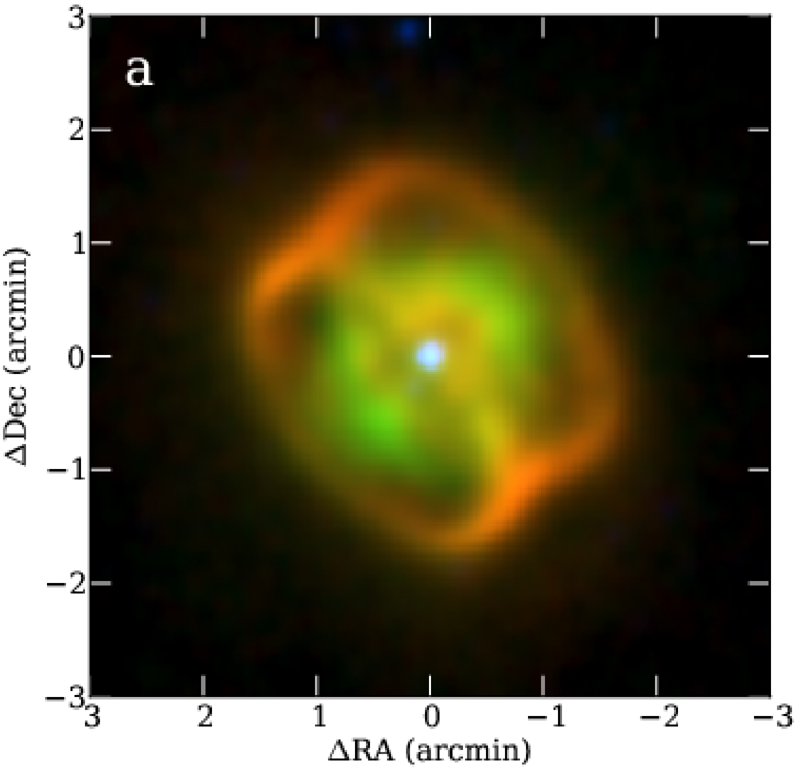

Figure 1.5: *Planetary nebula NGC1514, detected in* WISE. *(Ressler et al. 2010).*

The MIR emission from PNe can be attributed to six different components, among them PAH and very small grain (VSG) populations in the galaxy. Other components are associated with the destruction of aliphatic (non-aromatic) hydrocarbons in the circumstellar environment of post-AGB stars; as well as with the population of large, ionized PAHs that is caused by the extreme conditions in PNe.
This species of PAH, called $\mathrm{PAH}^{\mathrm{x}}$, are thought to be the carriers of the band at 7.90 μm, which can be used as a diagnostic for PNe in nearby galaxies. This band is also observed in compact HII regions. These results support the formation of aromatic VSG *in* the envelope of evolved stars and their survival in the ISM.

Planetary nebulae (such as NGC7023, see figure 1.2) are known PAH-rich sources (Kwok & Zhang 2013). A possible explanation of the 7.7 μm PAH feature is: In cool and less-evolved stars, such as in the post-AGB stage, emission from aliphatic-rich material dominates; while in hotter star environments the aliphatic material has been processed and thus aromatic material dominates the emission. In PAH processing, however, there is an extra step that results in the $\mathrm{PAH}^{\mathrm{x}}$ selective emission. These large, ionized PAHs are only found in extreme radiative conditions (Joblin et al. 2008), making them good probes of extreme physics.

PAH emission, where the wavelength emitted is associated with the size of the molecule, can have several different sources: star formation in galaxies; planetary nebulae, including a particular species of large ionized PAHs which result from extreme conditions in PNe.
We will be investigating the potential diluting effects of these sources on the two *WISE* star formation indicators.

1.8 Outline of thesis

This thesis aims to establish the reliability of the *WISE* star formation indicators, using multi-wavelength data from nearby galaxies. The two indicators are calibrated with total infrared flux (TIR) measurements. Once it has been determined when (or if) they are reliable, two new star formation relations will be formulated, one for each *WISE* indicator.

Chapter 2 details the galaxies in our compiled sample, while chapter 3 explains the photometric analysis conducted on the images of the galaxies, as well as containing the raw photometric measurements resulting from the analysis. Chapter 4 contains the derived values from the raw photometric data, as well as plots of the different derived values, some of them with best-fit relations. Commentary on the plots is included in chapter 4. Thereafter, in chapter 5, conclusions about the star formation in terms of other parameters of the galaxies are presented.

This thesis includes two appendices: one consisting of the raw photometric images and SEDs of all 76 galaxies in our sample (A), and another with additional plots from the derived values (B).

Chapter 2

Sample

As introduced in section 1.4, our sample is comprised of the SINGS (Kennicutt et al. 2003) and KINGFISH (Kennicutt et al. 2011) galaxies, excluding the four galaxies: M81dwA, HoI, HoII and HoIX. The images of these four low surface brightness galaxies did not allow the photometric analysis conducted to be of a sufficient standard.

The SINGS team selected a sample with the most diverse 'typical' nearby galaxies that still satisfied their technical requirements, the foremost of the requirements being the angular resolution. This varies from 2" for the IRAC bands to 40" for MIPS160. To maximise the linear resolution of the images, nearby objects were selected, most with distances less than 30 Mpc. The sample median distance is 9.5 Mpc. The other limiting factor was the apparent size of the galaxy. Since most of the IRAC and MIPS channels image an area of 5' square, most of the galaxies selected are in the 5' to 15' range, with a few smaller ones to cover the full range of physical conditions. The sample size was influenced by the need for a representative sample within the observing time constraints. Diversity in nuclear activity and environment were also sought. This led to a sample of 75 galaxies (see figure 2.1) which were observed with *Spitzer* for 512 hours in total (Kennicutt et al. 2003).

The KINGFISH sample is drawn from the SINGS sample. Ten of the SINGS galaxies were excluded due to their similarity to the rest of the sample, and four more galaxies were added from other *Spitzer* surveys due to their suitability for furthering the KINGFISH science goals. These four were: M101/NGC 5457, IC0342, NGC3077, and NGC2146.

Our sample thus consists of 76 galaxies in total, 74 of which are either in the SINGS or KINGFISH surveys. The additional ones are M87 and M82/NGC3034.

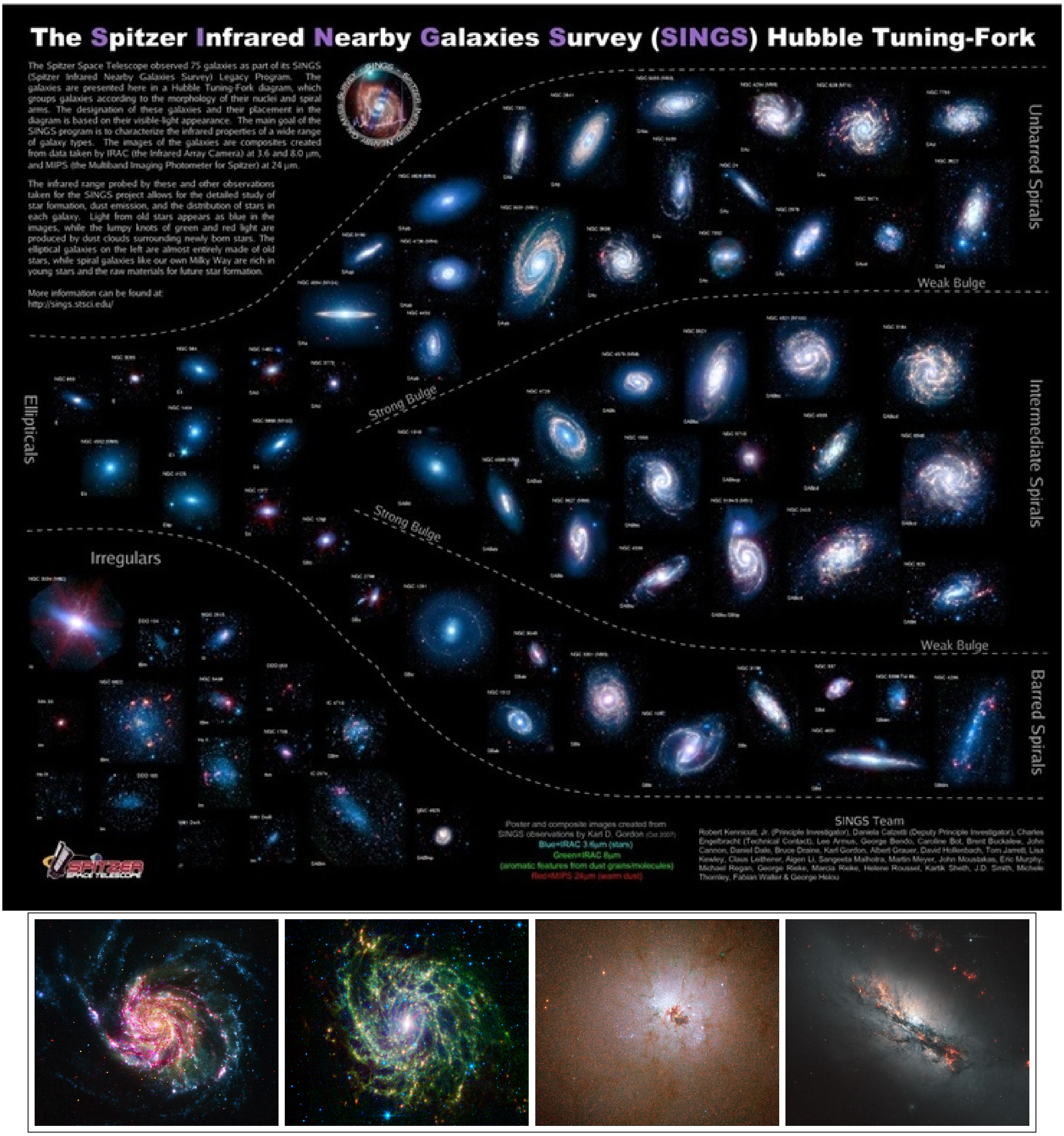

The Spitzer Space Telescope observed 75 galaxies as part of its SINGS (Spitzer Infrared Nearby Galaxies Survey) Legacy Program. The galaxies are presented here in a Hubble Tuning-Fork diagram, which groups galaxies according to the morphology of their nuclei and spiral arms. The designation of these galaxies and their placement in the diagram is based on their visible-light appearance. The main goal of the SINGS program is to characterize the infrared properties of a wide range of galaxy types. The images of the galaxies are composites created from data taken by IRAC (the Infrared Array Camera) at 3.6 and 8.0 µm, and MIPS (the Multiband Imaging Photometer for Spitzer) at 24 µm.

The infrared range probed by these and other observations taken for the SINGS project allows for the detailed study of star formation, dust emission, and the distribution of stars in each galaxy. Light from old stars appears as blue in the images, while the lumpy knots of green and red light are produced by dust clouds surrounding newly born stars. The elliptical galaxies on the left are almost entirely made of old stars, while spiral galaxies like our own Milky Way are rich in young stars and the raw materials for future star formation.

More information can be found at:
http://sings.stsci.edu/

Poster and composite images created from SINGS observations by Karl D. Gordon (Oct 2007)
Blue=IRAC 3.6µm (stars)
Green=IRAC 8µm
(aromatic features from dust grains/molecules)
Red=MIPS 24µm (warm dust)

Robert Kennicutt, Jr. (Principle Investigator), Daniela Calzetti (Deputy Principle Investigator), Charles Engelbracht (Technical Contact), Lee Armus, George Bendo, Caroline Bot, Brent Buckalew, John Cannon, Daniel Dale, Bruce Draine, Karl Gordon, Albert Grauer, David Hollenbach, Tom Jarrett, Lisa Kewley, Claus Leitherer, Aigen Li, Sangeeta Malhotra, Martin Meyer, John Moustakas, Eric Murphy, Michael Regan, George Rieke, Marcia Rieke, Helene Roussel, Kartik Sheth, J.D. Smith, Michele Thornley, Fabian Walter & George Helou

Figure 2.1: *Top: All 75 SINGS galaxies (*Spitzer*). Bottom, left to right: M101/NGC5457 (*Chandra, GALEX, Hubble, Spitzer*); IC0342 (*Spitzer*); NGC3077 (*ESA/Hubble*); NGC2146 (*ESA/Hubble*).*

Table 2.1 displays the basic data of the 76 galaxies in our compiled sample. It is apparent that a wide range of morphologies and activity types are included. The distances reflected are not the SINGS distances, but redshift-independent distances and redshifts from a variety of sources including: the S^{4}G database, NED (the NASA Extragalactic Database), the 2MASS Galaxy Redshift Catalogue (XSCz). Distance is derived using $H_0 = 70\ kms^{-1}Mpc^{-1}$ and Wickramashinge & Ukwatta (2010). Morphology and activity are sourced from NED.

Table 2.1: Basic data of sample

Name	R.A. (deg)	Dec (deg)	Redshift	D_L (Mpc)	Morphology[1]	Activity[1]
DDO053	128.53001	66.18223	8.4E-4	3.61	Im	None
DDO154	193.52061	27.14964	9.6E-4	4.12	IB(s)m	None
DDO165	196.60281	67.70802	0.00107	4.6	Im	None
IC0342[2]	56.70144	68.09635	7.3E-4	3.14	SAB(rs)cd	HII/Sbst[4]
IC2574	157.09784	68.41188	9.4E-4	4.04	SAB(s)m	HII
IC4710[3]	277.15536	-66.98228	0.00194	8.34	SB(s)m	HII
M101[2]	210.80225	54.34893	0.00168	7.22	SAB(rs)cd	HII
M81DwB	151.37836	70.36418	0.00165	7.09	Im	None
M87	187.70593	12.39113	0.00367	15.8	E0p, NLRG[4]	Sy
Mark33	158.13293	54.40088	0.00577	24.89	Imp	HII/WR[4]
NGC0024[3]	2.48408	-24.96425	0.0016	6.88	SA(s)c	HII
NGC0337	14.95818	-7.57715	0.00585	25.23	SB(s)d	HII
NGC0584	22.83642	-6.86802	0.00472	20.34	E4	None
NGC0628	24.17394	15.78366	0.00169	7.27	SA(s)c	HII
NGC0855	33.51487	27.87732	0.00226	9.72	SA(s)c	HII
NGC0925	36.81964	33.57917	0.00212	9.12	SAB(s)d	HII
NGC1097	41.57904	-30.27462	0.00407	17.53	SBb	Sy1
NGC1266	49.00312	-2.42736	0.00724	31.26	SB(rs)0p	LINER[4]
NGC1291	49.32742	-41.10804	0.002	8.6	SBa	HII
NGC1316	50.6738	-37.20796	0.00439	18.92	SAB(s)0	LINER[4]
NGC1377	54.1628	-20.90195	0.00572	24.67	S0	HII
NGC1404	54.71632	-35.59413	0.00446	19.22	E1	NELG[4]
NGC1482	58.66246	-20.50216	0.00455	19.61	SA0p	HII
NGC1512	60.97577	-43.34883	0.00279	12.01	SB(r)ab	AGN
NGC1566[3]	65.00169	-54.93805	0.0048	20.69	SAB(rs)bc	Sy1
NGC1705	73.55806	-53.36087	0.00119	5.11	SA0p	HII
NGC2403[1,3]	114.214167	65.602556	0.000445	3.401	SAB(s)cd	HII/LINER
NGC2146[2]	94.6578	78.35663	0.00477	20.56	SB(s)abp	HII, LIRG
NGC2798	139.34532	42.0	0.00595	25.67	SB(s)ap	HII
NGC2841	140.51106	50.97655	0.00304	13.08	SA(r)b	LINER[4]/Sy1
NGC2915	141.55038	-76.62688	8.8E-4	3.78	I0	HII
NGC2976	146.81364	67.91666	8.3E-4	3.57	SAcp	HII
NGC3031	148.88837	69.06528	8.3E-4	3.57	SA(s)ab	LINER[4]/Sy
NGC3034	148.96646	69.67978	8.6E-4	3.7	I0	HII/Sbst[4]
NGC3049	148.70677	9.27138	0.00713	30.78	SB(rs)ab	HII/Sbst[4]
NGC3077[2]	150.82985	68.73387	9.2E-4	3.95	I0p	HII
NGC3184	154.57062	41.42432	0.00263	11.32	SAB(rs)cd	HII
NGC3190	154.5237	21.83227	0.00548	23.63	SA(s)ap	LINER[4]
NGC3198	154.97932	45.54988	0.00337	14.51	SB(rs)c	HII
NGC3265	157.77821	28.79668	0.00417	17.96	E	HII/WR
NGC3351	160.99068	11.70356	0.00228	9.81	SB(r)b	HII/Sbst[4]
NGC3521	166.45242	-0.03587	0.002	8.6	SAB(rs)bc	HII/LINER[4]
NGC3621	169.56879	-32.81405	0.00157	6.75	SA(s)d	HII
NGC3627	170.06262	12.99155	0.00239	10.28	SAB(s)b	LINER[4]/Sy2
NGC3773	174.55397	12.11211	0.00395	17.01	SA0	HII
NGC3938	178.20604	44.12073	0.00405	17.45	SA(s)c	HII
NGC4125	182.02449	65.17439	0.0051	21.99	E6p	LINER[4]
NGC4236	184.17484	69.46288	0.00104	4.47	SB(s)dm	None
NGC4254	184.7067	14.41651	0.00358	15.42	SA(s)c	HII/LINER[4]
NGC4321	185.729	15.82236	0.00369	15.89	SAB(s)bc	LINER/HII
NGC4450[3]	187.12343	17.08496	0.00453	19.52	SA(s)ab	LINER[4]/Sy3

Continued on next page

Table 2.1 – continued from previous page

Name	R.A. (deg)	Dec (deg)	Redshift	D$_L$ (Mpc)	Morphology[1]	Activity[1]
NGC4536	188.61296	2.18817	0.00348	14.98	SAB(rs)bc	HII/Sbst
NGC4552	188.91588	12.55634	0.00358	15.42	E	HII/LINER[4]/Sy2
NGC4559	188.9902	27.96	0.00302	13.0	SAB(rs)cd	HII
NGC4569	189.20752	13.16296	0.00287	12.35	SAB(rs)ab	LINER[4]/Sy
NGC4579	189.43155	11.8182	0.00494	21.29	SAB(rs)b	LINER[4]/Sy
NGC4594	189.99765	-11.62305	0.00218	9.38	SA(s)a	LINER[4]/Sy
NGC4625	190.46968	41.27396	0.00237	10.2	SAB(rs)mp	None
NGC4631	190.53241	32.54292	0.00141	6.06	SB(s)d	HII
NGC4725	192.61075	25.50079	0.0029	12.48	SAB(r)abp	Sy2
NGC4736	192.7211	41.1202	0.00121	5.2	SA(r)ab	LINER[4]/Sy2
NGC4826	194.18185	21.683	0.00124	5.33	SA(rs)ab	HII/Sy2
NGC5033	198.36472	36.59392	0.00409	17.62	SA(s)c	HII/Sy1
NGC5055	198.95549	42.02931	0.00235	10.11	SA(rs)bc	HII/LINER[4]
NGC5194	202.46959	47.19518	0.00184	7.91	SA(s)bcp	HII/Sy
NGC5195	202.49785	47.26624	0.00187	8.04	SB0p	LINER[4]
NGC5398	210.34093	-33.0625	0.00341	14.68	SB(rs)dm	None
NGC5408	210.83711	-41.37661	0.00112	4.81	IB(s)m	HII
NGC5474	211.25624	53.66222	0.00167	7.18	SA(s)cdp	HII
NGC5713	220.04764	-0.28895	0.00552	23.8	SAB(rs)bcp	HII
NGC5866	226.62292	55.76322	0.00325	13.99	S0	HII/LINER[4]
NGC6822	296.24115	-14.80224	1.1E-4	0.47	IB(s)m	None
NGC6946	308.71796	60.15392	0.00143	6.15	SAB(rs)cd	HII/Sy2
NGC7331	339.26675	34.4158	0.00345	14.85	SA(s)b	HII/LINER[4]
NGC7552	349.04477	-42.58478	0.00398	17.14	SB(s)ab	HII/LINER[4]
NGC7793	359.45728	-32.59102	9.1E-4	3.91	SA(s)d	HII

---

[1] Source: NED.

[2] KINGFISH only, not SINGS.

[3] SINGS only, not KINGFISH.

[4] Sbst = Starburst; NLRG = Narrow emission-Line Radio Galaxy; WR = Wolf-Rayet; LINER = Low-Ionization Nuclear Emission-line Region; NELG = Narrow Emission-Line Galaxy

Chapter 3

Results: Photometry

Previous chapters have outlined the background information on the concepts involved in our hypothesis, as well as detailing the galaxies in our sample. This chapter describes the photometric analysis done on our galaxies - the apertures within which our fluxes were determined, the background sky annuli, and the manner in which colours were computed. This information is important when comparing our results with other work.

We will be using isophotal photometry that captures at least 90% of the total light. We have matched the apertures between the *WISE* and *Spitzer* images, which enables us to make a direct comparison between the matched bands (see section 3.2). These matched apertures also ensure the resulting colours will have satisfactory accuracy.

3.1 *WISE* photometry

Since we have chosen the *WISE* apertures as our 'fiducial' apertures, shown below (figure 3.1) is an example of the *WISE* drizzle images (top row) as well as the processed photometric images (bottom row). The drizzle images were constructed from *WISE* frames which are sized at 2.5 arcsec. The beam size in the four *WISE* bands are 8.1, 8.8, 11.0, and 17.5 arcseconds respectively. To better adhere to the resolution of the original mosaics, we use the "drizzle" resampling technique. Also known as Variable-Pixel Linear Reconstruction, drizzling is a co-adding algorithm that makes use of a point response function, in our case a tophat function, to improve the spatial resolution when compared to the mosaics (Jarrett et al. 2012). The software ICORE (Masci 2013) was used to create the drizzle images. They have an improved resolution of 5.9, 6.5, 7.0, and 12.4 arcseconds in W_1, W_2, W_3, and W_4 respectively (Cluver et al. 2014). This is roughly the same as the native *WISE* frame resolution.

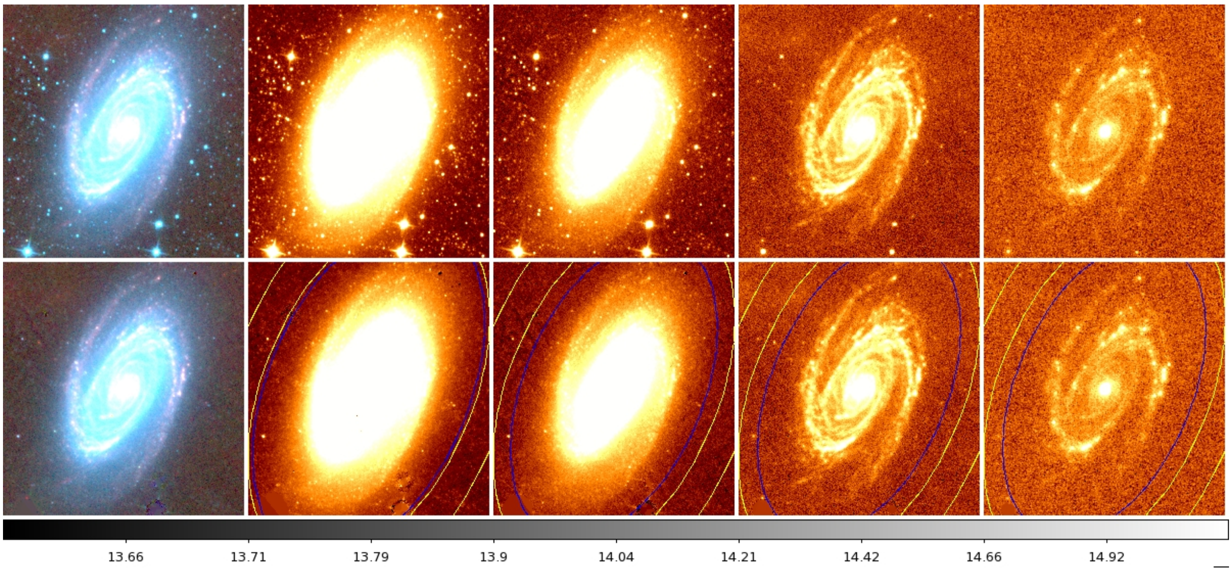

Figure 3.1: WISE *broadband images of NGC3031/M81 with* 1σ *(blue) isophotal ellipse, and sky annulus. Left to right: Three-colour (W1+2+3);* W_1*;* W_2*;* W_3*;* W_4*.*

The semi-interactive pipeline, coded by Prof. Jarrett, that conducts the photometric analysis has several functions: display the images including a three-colour image with W_1, W_2 and W_3; identify the foreground stars to be removed by using colours and proximity to the spiral arms; locate the centre of the galaxy, its size and shape; and determine the location of the sky annulus. These are used as initial inputs to the pipeline.

For each band, the background level is determined by the pixel value distribution found in an elliptical annulus centred on the galaxy (yellow annulus in figure 3.1). The histogram mode, the most frequent flux value after the pixel values have been binned, is a robust statistic for the background 'sky' level. However, to avoid the limitations of binning, the average value of the histogram about this mode was chosen as the metric for the background or 'sky' level (*WISE* Explanatory Supplement). The width of the region in which this average value is taken is dictated by the standard deviation of the pixel distribution to the left side of the histogram mode.
This background level is then removed from the mosaics, and also provides a noise estimate for the image. Stars are removed using the *WISE* point-spread function (PSF) for the applicable band. If the subtraction is not effective, they are masked to exclude them from the fit, and then recovered using local background and isophotal substitution drawn from the galaxy ellipsoid model (Jarrett et al. 2013).

The next step, since the stars have been removed, is to identify the galaxy's size and shape. These are best given by the elliptical approximation of the galaxy's W_1 3σ isophote. Due to the high signal-to-noise ratio (SNR) in our sample, this elliptical isophote is the same across all the *WISE* bands for the majority of our galaxies.
All the previous steps are then repeated using the updated galaxy size and shape until the changes become negligible (Jarrett et al. 2013). We assume that the isophotal shape does not change with radius. This is a simplification that is clearly incorrect for asymmetric galaxies, but since our sample consists of mainly 'normal' galaxies, this should not be a significant problem in our case.

The next task in the pipeline is to determine the surface brightness profile. The 1σ elliptical isophote (blue ellipse in figure 3.1) for each band corresponds to the rms value in the background annulus (Jarrett et al. 2013). This is then the aperture used for the isophotal fluxes in the four bands. Where possible, we match the apertures for W_2, W_3 and W_4 to the W_1 aperture (see R1_{iso} in table 3.1), since it is the chosen fiducial aperture for SINGS galaxies. For the majority of the galaxies, all four bands have the same aperture - i.e., they are fully matched. This is because they are all large galaxies with high signal-to-noise images.
The cases where the W_1 aperture is not used, usually early-type galaxies, is due to a lack of sensitivity in the longer-wavelength bands. In all cases, though, the total flux from W_1, W_3 and W_4 is used to address this deficiency.

This process was undertaken and completed by Prof. Jarrett, using the pipeline for both the *WISE* and *Spitzer* images. All our original photometric data was thus provided by him.

Tables 3.1 and 3.2 below display the isophotal photometry done on our galaxies, as well as some of the *WISE* colours. When computing colours, we match apertures between the two magnitudes, always the smaller of the two for both images. For example, when computing $W_1 - W_2$, we use the W_2 aperture for both flux measurements. The exception is when the two magnitudes trace different emission mechanisms, for example W_2 (evolved population) and W_3 (star formation). In these cases we simply subtract the isophotal fluxes.
The columns in tables 3.1 and 3.2 are outlined below:

- Ri_{iso} - radius in arcseconds of 1σ isophote for the W_i band.
- b/a - ratio of semi-major axis to semi-minor axis of the W_1 3σ isophote.
- P.A. - position angle in degrees of the W_1 3σ isophote.
- mag$_{Wi}$ - isophotal flux in the W_i band, converted[1] to a Vega[2] magnitude.
- err(W_i) - error in isophotal magnitude calculation in the W_i band.
- $W_i - W_j$ - *WISE* colour, determined in the manner outlined in the paragraph above.
- err($W_i - W_j$) - error in the *WISE* colour calculation.

---

[1] the Vega magnitude-to-flux conversion factors are 309.68, 170.66, 29.05, and 7.871 Jy, respectively, for W_1, W_2, W_3, and W_4 (Jarrett et al. 2017).

[2] the conversion from Vega system to the monochromatic AB system conversions are 2.67, 3.32, 5.24, and 6.66 mag (Jarrett et al. 2017).

Table 3.1: Isophotal *WISE* photometry of sample

Name	$R1_{iso}$ (”)	$R2_{ap}$ (”)	$R3_{ap}$ (”)	$R4_{ap}$ (”)	b/a	P.A. (deg)	mag_{W1} (mag)	err(W_1) (mag)	mag_{W2} (mag)	err(W_2) (mag)
DDO053	15.61	15.61	15.61	15.61	1	29.6	14.674	0.053	13.599	0.053
DDO154	46.88	46.88	*null*	*null*	0.65	38.2	12.77	0.028	13.013	0.097
DDO165	101.3	101.3	101.3	101.3	0.619	88.9	11.333	0.016	11.293	0.032
IC0342[1]	795.72	795.72	795.72	795.72	0.944	51.7	3.968	0.012	3.876	0.012
IC2574	317.18	317.18	317.18	317.18	0.49	39.6	8.729	0.012	8.589	0.014
IC4710	133.26	133.26	133.26	133.26	0.75	115.1	9.434	0.012	9.396	0.015
M101[1]	870.2	870.2	870.2	870.2	0.924	33.3	5.214	0.011	5.098	0.011
M81DwB	54	36.23	36.23	36.23	0.711	142	12.083	0.017	12.226	0.027
M87	628.68	424	111.6	111.6	0.79	152.9	5.313	0.011	5.453	0.011
Mark33	57.14	57.14	57.14	57.14	0.786	125	10.228	0.012	10.004	0.013
NGC0024[2]	186.86	142.03	142.03	142.03	0.298	45.1	8.663	0.011	8.749	0.012
NGC0337	101.19	101.19	101.19	101.19	0.622	131.6	8.779	0.011	8.561	0.012
NGC0584	184.91	124.04	53.83	28.9	0.784	75.4	7.2	0.011	7.307	0.011
NGC0628	318.53	318.53	318.53	318.53	0.843	78.7	6.444	0.011	6.336	0.011
NGC0855	106.47	70.5	38.43	38.43	0.446	65	9.665	0.012	9.694	0.013
NGC0925	310.95	310.95	310.95	310.95	0.501	110.1	7.574	0.011	7.532	0.012
NGC1097	323.63	323.63	323.63	323.63	0.795	113.6	5.981	0.011	5.885	0.011
NGC1266	65.79	65.79	65.79	65.79	0.738	115.1	9.385	0.012	9.092	0.012
NGC1291	435.59	376.09	376.09	376.09	0.983	49.3	5.345	0.011	5.403	0.011
NGC1316	769.41	599.1	190.12	190.12	0.645	34.7	5.079	0.011	5.144	0.011
NGC1317	135.6	118.72	82.05	82.05	0.87	156.6	7.634	0.011	7.617	0.011
NGC1377	72.84	72.84	72.84	72.84	0.633	92	9.506	0.012	8.153	0.012
NGC1404	218.31	169.14	86.45	50.01	0.88	160	6.606	0.014	6.691	0.011
NGC1482	119.94	119.94	119.94	119.94	0.68	105.2	7.961	0.011	7.642	0.012
NGC1512	290.96	211.89	164.78	164.78	0.644	45.3	7.245	0.011	7.3	0.011
NGC1566[2]	333.13	333.13	333.13	333.13	0.735	27.1	6.568	0.011	6.464	0.011
NGC1705	95.14	71.59	39.75	39.75	0.595	44.2	10.089	0.012	10.065	0.012
NGC2146[1]	252.95	252.95	252.95	252.95	0.545	126.2	6.383	0.011	6.041	0.011
NGC2798	94.27	94.27	94.27	94.27	0.522	158.4	8.658	0.011	8.385	0.012
NGC2841	384.35	295.51	195.86	195.86	0.47	151.4	5.889	0.011	5.915	0.011
NGC2915	123.75	97.35	49.81	49.81	0.497	129.8	9.42	0.012	9.425	0.012
NGC2976	237.09	190.19	148.65	148.65	0.589	144.3	7.155	0.011	7.083	0.011
NGC3031	868.41	868.41	868.41	868.41	0.557	155.9	3.606	0.011	3.609	0.011
NGC3034	404.2	374.98	500.33	530.74	0.65	57.8	4.065	0.012	3.611	0.012
NGC3049	78.4	78.4	78.4	78.4	0.623	25.7	9.774	0.012	9.726	0.015
NGC3077[1]	351.94	271.01	158.75	158.75	0.734	38.5	6.796	0.011	6.755	0.011
NGC3190	178.48	148.4	148.4	148.4	0.45	121.1	7.298	0.011	7.274	0.011
NGC3184	227.06	196.78	196.78	196.78	0.934	106.7	6.987	0.011	6.943	0.012

Continued on next page

Table 3.1 – continued from previous page

Name	R1$_{iso}$ (")	R2$_{ap}$ (")	R3$_{ap}$ (")	R4$_{ap}$ (")	b/a	P.A. (deg)	mag$_{W1}$ (mag)	err(W_1) (mag)	mag$_{W2}$ (mag)	err(W_2) (mag)
NGC3198	272.91	272.91	272.91	272.91	0.354	35.8	7.614	0.011	7.528	0.012
NGC3265	41.17	41.17	41.17	41.17	0.731	68.1	10.216	0.012	10.121	0.013
NGC3351	245.14	193.17	193.17	193.17	0.78	17.2	6.464	0.011	6.497	0.011
NGC3521	427.58	296.09	296.09	296.09	0.621	165.4	5.439	0.011	5.384	0.011
NGC3621	349.92	260.04	260.04	260.04	0.478	162.4	6.38	0.02	6.276	0.02
NGC3627	398.84	312.04	280.4	280.4	0.522	177.5	5.554	0.011	5.471	0.011
NGC3773	54.92	54.92	54.92	54.92	0.868	168.1	10.46	0.012	10.347	0.016
NGC3938	182.74	182.74	182.74	182.74	0.823	49.5	7.496	0.011	7.37	0.012
NGC4125	336.66	241.88	86.56	86.56	0.71	83.9	6.501	0.011	6.589	0.011
NGC4236	485.55	324.09	324.09	324.09	0.344	158.3	7.913	0.011	8.202	0.012
NGC4254	179.79	179.79	179.79	179.79	0.799	48.3	6.657	0.011	6.47	0.011
NGC4450[2]	217.15	181.51	181.51	181.51	0.671	172	6.883	0.011	6.919	0.011
NGC4536	268.35	268.35	268.35	268.35	0.376	122.8	7.182	0.011	7.021	0.011
NGC4552	321.51	173.91	75.87	34.37	0.882	134.4	6.359	0.011	6.574	0.011
NGC4559	293.56	293.56	293.56	293.56	0.392	149.1	7.387	0.011	7.226	0.012
NGC4569	323.57	265	159.74	159.74	0.404	25.3	6.491	0.011	6.452	0.011
NGC4579	250.03	176.04	176.04	176.04	0.78	92.4	6.32	0.011	6.333	0.011
NGC4594	660.83	556.14	556.14	556.14	0.455	90.7	4.617	0.011	4.662	0.011
NGC4625	64.48	64.48	64.48	64.48	0.9	177.5	9.592	0.012	9.517	0.013
NGC4631	485.08	485.08	485.08	485.08	0.275	87.2	6.006	0.011	5.798	0.011
NGC4725	391.03	308.54	200.32	200.32	0.62	39.2	6.086	0.011	6.15	0.011
NGC4736	578.63	431.1	431.1	431.1	0.89	105.6	4.765	0.011	4.78	0.011
NGC4826	364.28	288.19	288.19	288.19	0.535	114.7	5.186	0.011	5.197	0.011
NGC5033	284.95	284.95	284.95	284.95	0.569	176	6.72	0.011	6.62	0.011
NGC5055	523.49	410.6	410.6	410.6	0.601	103.4	5.257	0.011	5.222	0.011
NGC5194	462.82	462.82	462.82	462.82	0.666	17.6	5.088	0.011	4.969	0.011
NGC5195	174.12	174.12	174.12	174.12	0.776	106.9	6.451	0.011	6.432	0.011
NGC5398	101.89	83.83	83.83	83.83	0.642	178.4	9.772	0.012	9.786	0.013
NGC5408	83.87	83.87	83.87	83.87	0.601	60.5	10.006	0.012	9.915	0.014
NGC5474	155.32	155.32	155.32	155.32	0.85	1.1	8.645	0.011	8.606	0.012
NGC5713	113.3	113.3	113.3	113.3	0.865	5.7	7.966	0.011	7.751	0.012
NGC5866	288.69	226.62	112.56	112.56	0.551	122.4	6.617	0.011	6.621	0.011
NGC6822	535.22	535.22	535.22	535.22	0.757	28.3	5.921	0.011	5.908	0.012
NGC6946	478.14	478.14	478.14	478.14	0.847	99.9	5.015	0.011	4.843	0.011
NGC7331	371.2	371.2	371.2	371.2	0.426	172	5.703	0.011	5.611	0.011
NGC7552	178.38	178.38	178.38	178.38	0.61	99.6	7.137	0.011	6.744	0.011
NGC7793	335.46	335.46	335.46	335.46	0.612	98.8	6.522	0.011	6.433	0.011

---

[1] KINGFISH only, not SINGS.

[2] SINGS only, not KINGFISH.

Table 3.2: Isophotal *WISE* photometry of sample (cont.) with colours

Name	mag_{W3} (mag)	err(W_3) (mag)	mag_{W4} (mag)	err(W_4) (mag)	$W_1 - W_2$ (mag)	err($W_1 - W_2$) (mag)	$W_2 - W_3$ (mag)	err($W_2 - W_3$) (mag)
DDO053	10.375	0.08	7.297	0.09	1.075	0.075	3.224	0.096
DDO154	*null*	*null*	*null*	*null*	−0.243	0.101	*null*	*null*
DDO165	16.012	33.114	9.042	2.094	0.04	0.036	*null*	*null*
IC0342[1]	0.163	0.012	−1.853	0.011	0.092	0.016	3.713	0.017
IC2574	7.045	0.053	3.954	0.06	0.14	0.018	1.545	0.055
IC4710	7.083	0.033	4.835	0.076	0.037	0.019	2.313	0.036
M101[1]	1.612	0.012	−0.305	0.013	0.115	0.016	3.486	0.016
M81DwB	*null*	*null*	8.137	0.324	0.106	0.031	*null*	*null*
M87	5.136	0.012	3.836	0.022	−0.069	0.016	0.317	0.017
Mark33	5.761	0.012	2.5	0.012	0.224	0.018	4.243	0.018
NGC0024[2]	6.31	0.015	4.656	0.043	−0.024	0.017	2.439	0.019
NGC0337	4.967	0.012	2.618	0.014	0.219	0.017	3.594	0.017
NGC0584	6.951	0.015	6.372	0.055	−0.06	0.016	0.356	0.019
NGC0628	2.753	0.011	0.964	0.012	0.107	0.016	3.583	0.016
NGC0855	7.469	0.015	5.276	0.027	0.073	0.017	2.225	0.02
NGC0925	4.397	0.013	2.462	0.022	0.042	0.017	3.135	0.018
NGC1097	2.503	0.011	0.163	0.012	0.097	0.016	3.382	0.016
NGC1266	6.241	0.015	2.591	0.013	0.293	0.017	2.851	0.019
NGC1291	4.266	0.012	3.115	0.032	−0.04	0.016	1.137	0.017
NGC1316	4.519	0.012	3.259	0.016	−0.023	0.016	0.626	0.016
NGC1317	5.286	0.012	3.795	0.015	0.026	0.016	2.331	0.016
NGC1377	4.71	0.012	1.732	0.012	1.353	0.016	3.442	0.016
NGC1404	6.199	0.012	5.501	0.027	−0.051	0.017	0.491	0.017
NGC1482	3.492	0.011	0.89	0.012	0.319	0.016	4.151	0.016
NGC1512	4.819	0.012	3.167	0.014	−0.003	0.016	2.481	0.016
NGC1566[2]	2.981	0.011	1.082	0.012	0.103	0.016	3.483	0.016
NGC1705	8.203	0.015	5.768	0.025	0.088	0.017	1.862	0.02
NGC2146[1]	1.819	0.012	−0.758	0.011	0.343	0.016	4.221	0.016
NGC2798	4.307	0.012	1.324	0.012	0.274	0.016	4.077	0.016
NGC2841	3.825	0.011	2.315	0.013	−0.002	0.016	2.089	0.016
NGC2915	8.016	0.016	5.637	0.026	0.047	0.017	1.409	0.02
NGC2976	3.905	0.011	1.907	0.012	0.1	0.016	3.178	0.016
NGC3031	1.853	0.011	0.514	0.014	−0.002	0.016	1.755	0.016
NGC3034	−0.957	0.011	−4.131	0.011	0.454	0.017	4.569	0.016
NGC3049	6.087	0.015	3.28	0.017	0.048	0.019	3.638	0.021
NGC3077[1]	4.118	0.012	1.636	0.012	0.091	0.016	2.637	0.016
NGC3190	5.11	0.012	3.706	0.025	0.04	0.016	2.164	0.017
NGC3184	3.563	0.012	1.845	0.014	0.076	0.016	3.38	0.016

Continued on next page

Table 3.2 – continued from previous page

Name	mag$_{W3}$ (mag)	err(W_3) (mag)	mag$_{W4}$ (mag)	err(W_4) (mag)	$W_1 - W_2$ (mag)	err($W_1 - W_2$) (mag)	$W_2 - W_3$ (mag)	err($W_2 - W_3$) (mag)
NGC3198	4.249	0.012	2.224	0.015	0.086	0.016	3.279	0.017
NGC3265	6.445	0.013	3.731	0.015	0.095	0.018	3.676	0.019
NGC3351	3.566	0.012	1.273	0.012	0.005	0.016	2.931	0.016
NGC3521	1.98	0.011	0.331	0.012	0.097	0.016	3.404	0.016
NGC3621	2.621	0.011	0.896	0.012	0.141	0.029	3.655	0.023
NGC3627	2.038	0.011	0.028	0.011	0.108	0.016	3.433	0.016
NGC3773	7.21	0.022	4.488	0.03	0.113	0.02	3.136	0.027
NGC3938	3.868	0.012	2.126	0.014	0.125	0.016	3.502	0.016
NGC4125	6.269	0.013	5.198	0.042	−0.034	0.016	0.32	0.017
NGC4236	6.075	0.017	3.26	0.022	−0.065	0.016	2.127	0.021
NGC4254	2.417	0.011	0.649	0.012	0.187	0.016	4.053	0.016
NGC4450[2]	5.303	0.014	3.863	0.042	−0.009	0.016	1.616	0.018
NGC4536	3.385	0.011	0.91	0.012	0.161	0.016	3.636	0.016
NGC4552	6.084	0.013	5.6	0.036	−0.066	0.016	0.491	0.017
NGC4559	4.105	0.012	2.162	0.015	0.161	0.016	3.121	0.017
NGC4569	3.826	0.011	1.891	0.012	0.066	0.016	2.626	0.016
NGC4579	4.171	0.012	2.594	0.019	0.04	0.016	2.161	0.017
NGC4594	3.539	0.013	2.363	0.035	−0.022	0.016	1.124	0.017
NGC4625	6.217	0.014	4.518	0.032	0.075	0.017	3.3	0.019
NGC4631	1.989	0.011	−0.064	0.012	0.208	0.016	3.809	0.016
NGC4725	4.079	0.012	2.631	0.016	−0.021	0.016	2.07	0.016
NGC4736	2.032	0.011	0.319	0.012	0.027	0.016	2.748	0.016
NGC4826	2.965	0.011	1.2	0.012	0.005	0.016	2.232	0.016
NGC5033	3.139	0.011	1.461	0.013	0.101	0.016	3.48	0.016
NGC5055	1.891	0.011	0.259	0.012	0.068	0.016	3.331	0.016
NGC5194	1.193	0.011	−0.61	0.012	0.119	0.016	3.776	0.016
NGC5195	4.244	0.012	2.017	0.013	0.019	0.016	2.188	0.016
NGC5398	6.714	0.016	3.762	0.017	0.043	0.017	3.072	0.02
NGC5408	6.715	0.015	3.286	0.014	0.091	0.018	3.201	0.02
NGC5474	6.26	0.018	4.441	0.052	0.039	0.017	2.346	0.022
NGC5713	3.702	0.011	1.326	0.012	0.216	0.016	4.048	0.016
NGC5866	5.283	0.012	3.936	0.017	0.018	0.016	1.338	0.016
NGC6822	3.625	0.014	1.231	0.019	0.013	0.016	2.283	0.018
NGC6946	0.935	0.011	−1.047	0.011	0.172	0.016	3.908	0.016
NGC7331	2.359	0.011	0.669	0.012	0.092	0.016	3.252	0.016
NGC7552	2.634	0.011	−0.344	0.011	0.394	0.016	4.11	0.016
NGC7793	3.231	0.012	1.582	0.014	0.089	0.016	3.202	0.016

---

[1] KINGFISH only, not SINGS.

[2] SINGS only, not KINGFISH.

3.1.1 Distribution of *WISE* photometry

Figure 3.2 below displays the distribution in our sample of the *WISE* isophotal magnitudes and colours. It is noteworthy that the majority of our sample is bright in the W_3, seen both in the left plot in the second row, and supported by the last plot of the $W_2 - W_3$ colour.

Another noteworthy observation is that the W_3 magnitude has a greater range than the other bands, possibly because of its width. The range of W_4, on the other hand, is the only one with negative values. This suggests that warm dust is the brightest component in our galaxies.

The brightest galaxy in both the W_1 and W_2 is the radio-bright galaxy M81, while the faintest galaxy in W_1 and W_2 is the dwarf irregular DDO053. In both W_3 and W_4, the brightest source is NGC6946, while the dwarf irregular DDO165 is the faintest in this case.

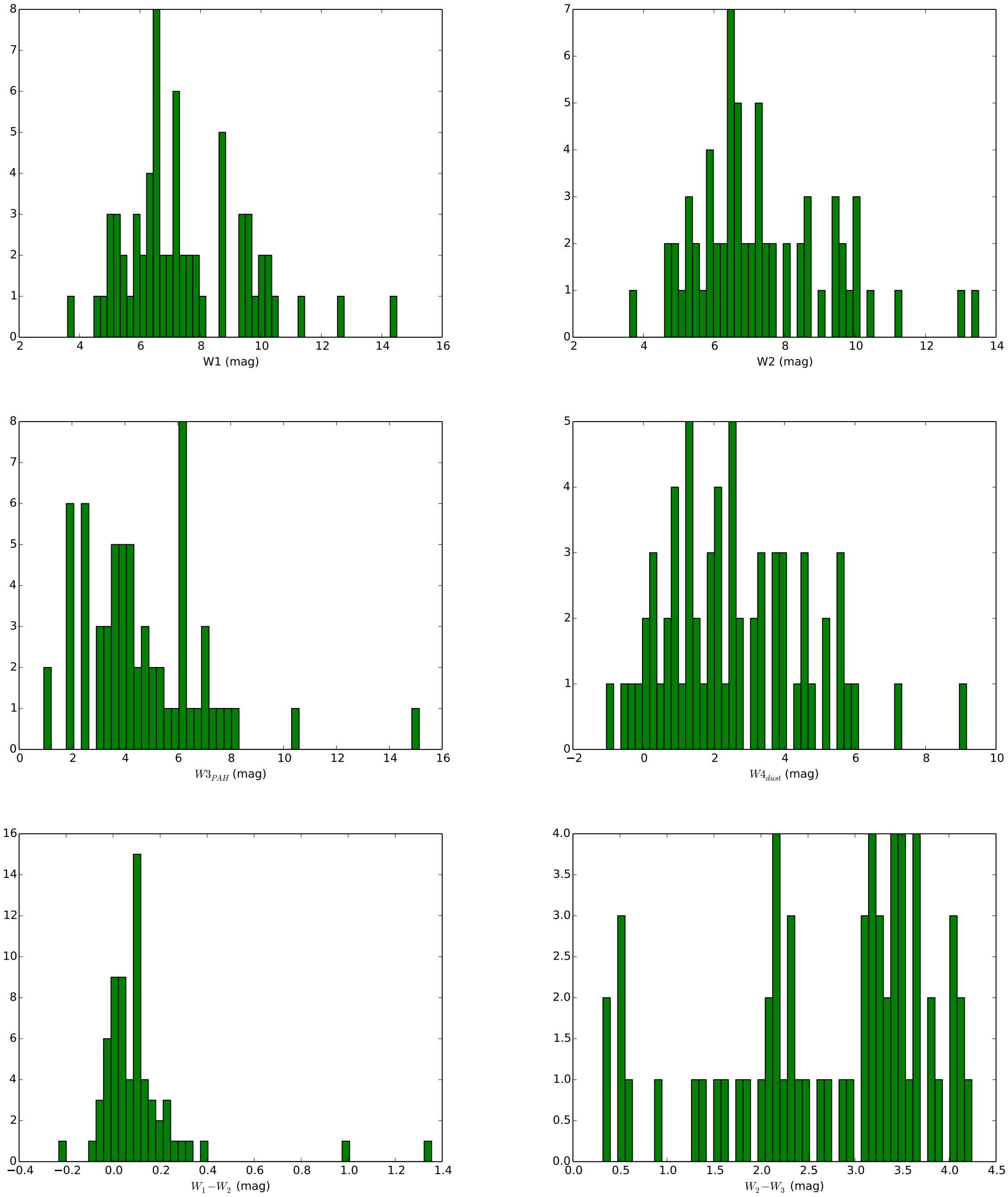

Figure 3.2: *Distribution of* WISE *isophotal photometric data, individual magnitudes and two colours.*

3.2 *Spitzer* photometry

To determine the *Spitzer* photometry, using the same pipeline as for the *WISE* images, we matched the *WISE* apertures to the *Spitzer* images: IRAC1 and 2 were matched to the W_1 and W_2 apertures respectively, IRAC3 and IRAC4 were both matched to the W_3 aperture, and the MIPS24 image was matched to the W_4 aperture. Since the IRAC instrument and *WISE* have similar sensitivity (Jarrett et al. 2013), matching apertures in this manner is a viable option. The exception here is that MIPS24 is significantly more sensitive than W_4; hence W_4 does not always capture the light that MIPS24 can detect, most notably for low surface-brightness galaxies.

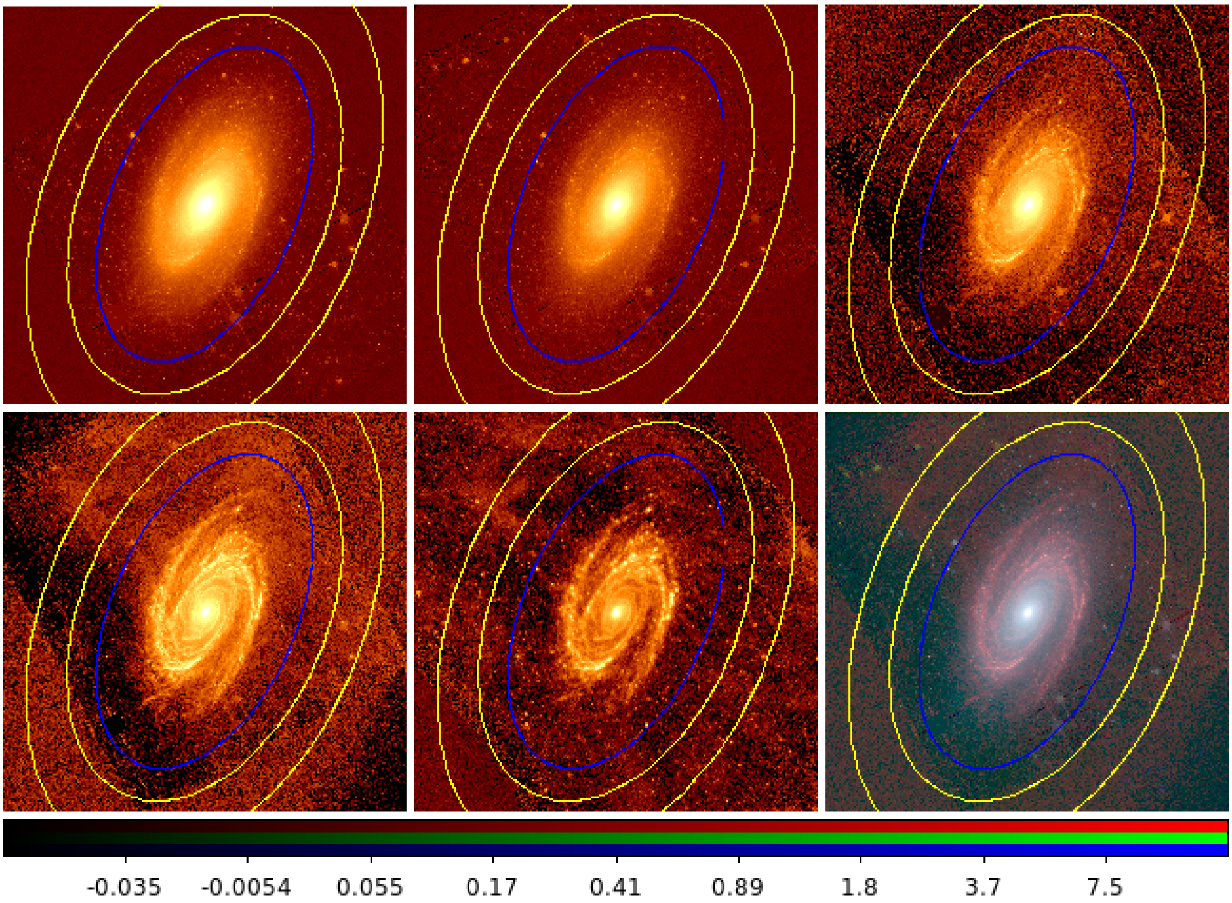

Figure 3.3: Spitzer *broadband images of NGC3031/M81 with* WISE *apertures and sky annulus. Top left to bottom right: IRAC1, IRAC2, IRAC3, IRAC4, MIPS24, three-colour (IRAC1+2+4).*

Similar to tables 3.1 and 3.2 above, the *Spitzer* photometry is displayed below. Since the apertures in this case were matched from the *WISE* , there are no details of their radii and sizes in the tables below (3.3 and 3.4). Furthermore, there are no colours computed. The columns are briefly outlined below:

- $\mathrm{mag}_{IRACi}/\mathrm{mag}_{MIPS24}$ - isophotal flux in the applicable *Spitzer* band, converted to a magnitude.
- $\mathrm{err}_{IRACi}/\mathrm{err}_{MIPS24}$ - error in isophotal magnitude calculation in the applicable *Spitzer* band.

Table 3.3: Isophotal *Spitzer* photometry of sample

Name	mag$_{IRAC1}$ (mag)	err$_{IRAC1}$ (mag)	mag$_{IRAC2}$ (mag)	err$_{IRAC2}$ (mag)	mag$_{IRAC3}$ (mag)	err$_{IRAC3}$ (mag)
DDO053	13.841	0.037	13.275	0.043	12.591	0.139
DDO154	12.583	0.027	12.66	0.045	12.28	0.208
DDO165	10.918	0.022	10.793	0.025	10.212	0.072
IC2574	8.393	0.02	8.397	0.021	7.703	0.026
IC4710	9.18	0.02	9.082	0.021	8.251	0.03
Mark33	10.028	0.02	9.884	0.021	8.2	0.022
NGC0024[2]	8.528	0.02	8.499	0.02	7.71	0.022
NGC0337	8.6	0.02	8.542	0.02	6.924	0.021
NGC0584	7.171	0.02	7.319	0.022	7.2	0.021
NGC0855	9.543	0.02	9.547	0.021	8.998	0.023
NGC0925	7.416	0.02	7.357	0.02	6.174	0.021
NGC1097	5.828	0.02	5.803	0.02	4.477	0.02
NGC1266	9.242	0.02	9.05	0.02	8.124	0.023
NGC1291	5.231	0.02	5.272	0.02	5.294	0.02
NGC1316	4.883	0.02	4.847	0.02	5.019	0.02
NGC1377	9.187	0.02	8.252	0.02	6.318	0.02
NGC1404	6.459	0.02	6.528	0.02	6.439	0.02
NGC1482	7.969	0.021	7.754	0.02	5.513	0.02
NGC1512	7.083	0.02	7.131	0.02	6.475	0.02
NGC1566[2]	6.393	0.02	6.343	0.02	5.27	0.021
NGC1705	9.981	0.02	9.877	0.021	9.73	0.026
NGC2798	8.547	0.02	8.392	0.02	6.592	0.02
NGC2841	5.815	0.02	6.138	0.02	5.23	0.02
NGC2915	9.256	0.02	9.247	0.021	9.197	0.024
NGC2976	7.013	0.02	6.966	0.02	5.704	0.02
NGC3031	3.477	0.02	3.525	0.02	2.853	0.02
NGC3049	9.594	0.02	9.606	0.021	8.12	0.023
NGC3184	6.818	0.02	6.833	0.02	5.385	0.02
NGC3190	7.173	0.02	7.227	0.02	6.665	0.021
NGC3198	7.463	0.02	7.446	0.02	6.376	0.022
NGC3265	10.055	0.02	10.022	0.021	8.528	0.023
NGC3351	6.328	0.02	6.334	0.02	5.312	0.02
NGC3521	5.277	0.02	5.256	0.02	3.859	0.02
NGC3621	6.143	0.02	6.125	0.02	4.455	0.02
NGC3627	5.398	0.02	5.382	0.02	3.982	0.02
NGC3773	10.232	0.021	10.183	0.021	9.097	0.029
NGC3938	7.326	0.02	7.301	0.02	5.791	0.02
NGC4125	6.368	0.02	6.323	0.02	6.549	0.02

Continued on next page

Table 3.3 – continued from previous page

Name	mag$_{IRAC1}$ (mag)	err$_{IRAC1}$ (mag)	mag$_{IRAC2}$ (mag)	err$_{IRAC2}$ (mag)	mag$_{IRAC3}$ (mag)	err$_{IRAC3}$ (mag)
NGC4236	7.596	0.02	7.589	0.02	7.707	0.039
NGC4254	6.463	0.02	6.404	0.02	4.475	0.02
NGC4321	6.075	0.02	6.05	0.02	4.544	0.02
NGC4450[2]	6.934	0.02	6.952	0.02	7.043	0.026
NGC4536	6.997	0.02	6.951	0.02	5.34	0.02
NGC4552	6.241	0.02	6.316	0.02	6.451	0.02
NGC4559	7.212	0.02	7.172	0.02	5.832	0.02
NGC4569	6.359	0.02	6.367	0.02	5.599	0.02
NGC4579	6.206	0.02	6.247	0.02	5.52	0.02
NGC4594	4.517	0.02	4.554	0.02	4.435	0.02
NGC4625	9.454	0.02	9.483	0.021	8.124	0.023
NGC4631	5.819	0.02	5.763	0.02	3.803	0.02
NGC4725	5.958	0.02	5.986	0.02	5.203	0.021
NGC4736	4.632	0.02	4.594	0.02	3.639	0.02
NGC4826	5.074	0.02	5.107	0.02	4.442	0.02
NGC5033	6.537	0.02	6.515	0.02	5.056	0.02
NGC5055	5.091	0.02	5.088	0.02	3.757	0.02
NGC5194	4.977	0.02	4.963	0.02	3.262	0.02
NGC5195	5.896	0.02	5.938	0.02	5.240	0.02
NGC5408	9.811	0.021	9.713	0.021	9.497	0.042
NGC5474	8.477	0.02	8.397	0.022	7.564	0.044
NGC5713	7.787	0.02	7.706	0.02	5.845	0.02
NGC5866	6.477	0.02	6.496	0.02	6.265	0.02
NGC6822	5.566	0.02	5.527	0.02	4.855	0.021
NGC6946	4.911	0.02	5.079	0.02	2.883	0.02
NGC7331	5.545	0.02	5.545	0.02	4.301	0.02
NGC7552	6.932	0.02	6.708	0.02	4.924	0.02
NGC7793	6.366	0.02	6.341	0.02	4.871	0.02

---

[2] SINGS only, not KINGFISH.

Table 3.4: Isophotal *Spitzer* photometry of sample (cont.)

Name	mag$_{IRAC4}$ (mag)	err$_{IRAC4}$ (mag)	mag$_{MIPS24}$ (mag)	err$_{MIPS24}$ (mag)
DDO053	11.333	0.1	6.692	0.026
DDO154	*null*	*null*	*null*	*null*
DDO165	11.283	0.388	7.394	0.092
IC2574	8.031	0.059	3.872	0.023
IC4710	7.47	0.031	4.576	0.023
Mark33	6.463	0.02	2.361	0.02
NGC0024[2]	6.529	0.021	4.522	0.022
NGC0337	5.304	0.02	2.481	0.02
NGC0584	7.113	0.023	5.93	0.026
NGC0855	7.786	0.021	5.074	0.021
NGC0925	4.743	0.02	2.334	0.02
NGC1097	2.981	0.02	0.106	0.02
NGC1266	6.873	0.021	2.349	0.02
NGC1291	5.132	0.02	3.82	0.021
NGC1316	4.864	0.02	3.274	0.02
NGC1377	5.15	0.02	1.576	0.02
NGC1404	6.34	0.02	5.589	0.023
NGC1482	3.746	0.02	0.781	0.02
NGC1512	5.203	0.02	3.101	0.02
NGC1566[2]	3.468	0.02	1.034	0.02
NGC1705	8.778	0.023	5.566	0.022
NGC2798	4.833	0.02	1.171	0.02
NGC2841	4.202	0.02	2.284	0.02
NGC2915	8.316	0.022	5.489	0.022
NGC2976	4.232	0.02	1.812	0.02
NGC3031	2.127	0.02	0.321	0.02
NGC3049	6.501	0.021	3.096	0.02
NGC3184	3.866	0.02	1.749	0.02
NGC3190	5.522	0.02	3.616	0.021
NGC3198	4.614	0.02	2.098	0.02
NGC3265	6.81	0.021	3.582	0.02
NGC3351	3.925	0.02	1.143	0.02
NGC3521	2.307	0.02	0.272	0.02
NGC3621	2.932	0.02	0.829	0.02
NGC3627	2.384	0.02	−0.042	0.02
NGC3773	7.567	0.023	4.312	0.021
NGC3938	4.23	0.02	2.047	0.02
NGC4125	6.437	0.02	5.163	0.022
NGC4236	6.177	0.025	2.877	0.02
NGC4254	2.735	0.02	0.59	0.02
NGC4321	2.968	0.02	0.793	0.02
NGC4450[2]	6.525	0.032	3.832	0.022
NGC4536	3.703	0.02	0.792	0.02
NGC4552	6.258	0.02	5.766	0.023
NGC4559	4.43	0.02	2.09	0.02
NGC4569	4.231	0.02	1.798	0.02
NGC4579	4.542	0.02	2.412	0.02
NGC4594	4.05	0.02	2.615	0.02
NGC4625	6.475	0.021	4.426	0.021
NGC4631	2.272	0.02	−0.125	0.02
NGC4725	3.922	0.02	2.242	0.02
NGC4736	2.406	0.02	0.289	0.02
NGC4826	3.373	0.02	1.161	0.02
NGC5033	3.499	0.02	1.416	0.02
NGC5055	2.287	0.02	0.221	0.02
NGC5194	1.599	0.02	−0.577	0.02
NGC5195	4.228	0.02	1.796	0.02
NGC5408	8.186	0.027	3.152	0.02

Continued on next page

Table 3.4 – continued from previous page

Name	mag_{IRAC4} (mag)	err_{IRAC4} (mag)	mag_{MIPS24} (mag)	err_{MIPS24} (mag)
NGC5474	6.502	0.034	4.126	0.022
NGC5713	4.047	0.02	1.214	0.02
NGC5866	5.589	0.02	3.834	0.02
NGC6822	4.462	0.025	1.281	0.02
NGC6946	1.443	0.02	-1.12	0.02
NGC7331	2.707	0.02	0.611	0.02
NGC7552	3.212	0.02	-0.4	0.02
NGC7793	3.5	0.02	1.318	0.02

The data in Tables 3.1 to 3.4 are the isophotal data, determined from our photometric images. There were some galaxies for which the Spitzer photometric data were not available, either because the galaxies were too faint in some of the bands or, as was the case with NGC3034/M82, the telescope was completely saturated in the *Spitzer* bands. These galaxies were: DDO154 (IRAC4, MIPS24 missing); IC342; M87; M101; NGC2146; NGC3034/M82; NGC3077; NGC5398 (see Appendix A). The null values signify that those galaxies were not detected in the relevant bands.

---

[2] SINGS only, not KINGFISH.

3.2.1 Distribution of *Spitzer* photometry

Below, figure 3.4 displays the distribution of the *Spitzer* magnitudes. There are no real trends in the IRAC bands, but the range of the $24\mu m$ MIPS24 band suggests that the warm dust component is the brightest in our galaxies. This was also suggested in the plot of the W_4 magnitude distribution in figure 3.2.

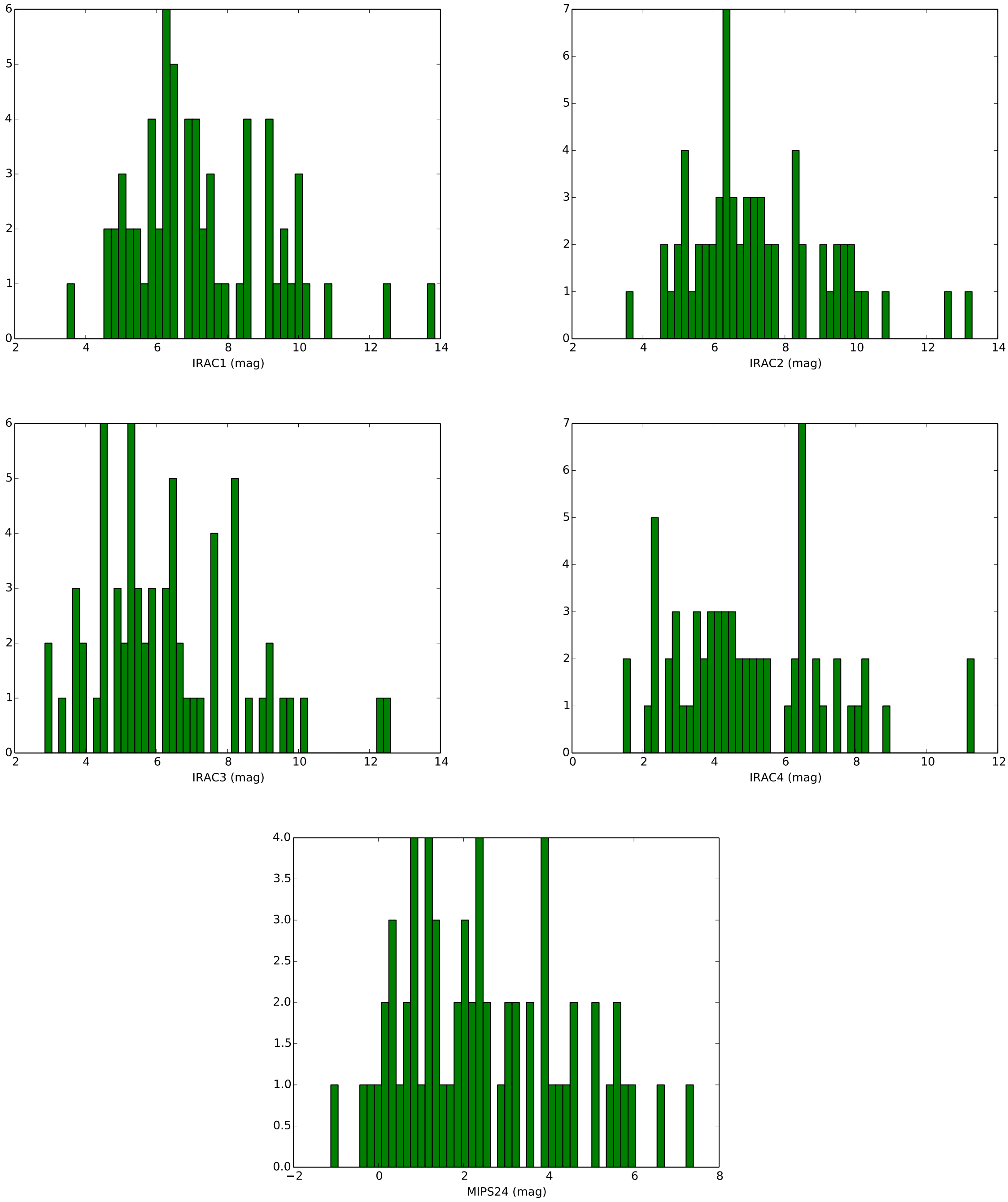

Figure 3.4: *Distribution of* Spitzer *isophotal photometric data in terms of individual magnitudes.*

The data depicted in figures 3.2 to 3.4 are the isophotal data, determined from our photometric images. In order to use this data to understand the conditions and processes in the galaxies, this photometry has to undergo some corrections, most notably correcting for redshift. The next section details the corrected and manipulated data which were used to do our analysis.

Chapter 4

Results: Global derived values

The previous chapters detailed all the necessary background information and presented the isophotal data used in our analysis. Thus, all that remains is to utilise this wealth of data at our disposal to better understand the processes at work in our galaxies. We will then draw conclusions as to what our results suggest about star formation in general.

The main parameters we look at are the star formation, the different star formation indicators; as well as the stellar mass, morphology, and metallicity of the galaxies. Our goal is to investigate relations with the various star formation indicators in our multi-wavelength data, and ultimately to formulate star formation relations for the two *WISE* indicators. We are interested in the stellar mass of our galaxies, since together with the star formation in the galaxy, this will give us a complete picture of how the galaxy uses its fuel to build its stellar mass.

Firstly, we present our redshift-corrected (k-corrected) photometry and derived luminosities. For the k-correction, templates from Brown et al. 2014 and Spitzer-SWIRE/GRASIL (Polletta et al. 2006, 2007) were used. To measure the flux ratios between rest and redshifted $(1 + z)\lambda$ spectra, the templates were redshifted, and synthetic photometry of the WISE filter response function in the W_1 band was determined. The standard k-correction magnitude is then $-2.5log[fluxratio * (1 + z)]$ (Jarrett et al. 2017).

As a precursor to any analysis, we compare our *WISE* and *Spitzer* photometry to ensure it is reliable and self-consistent. Once we are sure of the reliability and self-consistency of our photometry, we investigate the *WISE* and *Spitzer* bands that contain PAH contributions. We then calibrate the two *WISE* star formation indicators with respect to the TIR luminosity. This luminosity applies to long timescales of $\sim$ 100 Myr (Calzetti 2012). Thus it gives us a long-term, averaged view of the star formation in the galaxy. It is not sensitive to starbursts and local variations in the star formation. We also investigate relations between the *Spitzer* bands and the SFR.
We then formulate our SFR relations in terms of the *WISE* indicators at 12 and 22 μm. Finally, we compare our new relations with different measures of star formation to test the validity of our new relations.

Table 4.1 displays the *WISE* and *Spitzer* fluxes, corrected for redshift. Since all our galaxies are nearby, the shifting of the bands is minimal, and thus the changes in the fluxes are minimal. Nonetheless we corrected for redshift in order to be as accurate as possible.

Table 4.1: *Spitzer* and *WISE* k-corrected photometry of sample

Name	IRAC1 (mJy)	IRAC2 (mJy)	IRAC3 (mJy)	IRAC4 (mJy)	MIPS24 (mJy)	W1 (mJy)	W2 (mJy)	W3 (mJy)	W4 (mJy)
DDO053	0.786	0.879	0.967	1.607	16.332	0.250	0.491	2.379	16.294
DDO154	2.414	1.487	1.408	null	null	2.415	1.064	null	null
DDO165	10.740	7.960	7.252	null	8.350	8.836	5.047	null	null
IC0342	null	null	null	null	null	8011.489	4805.424	23 780.633	42 941.332
IC2574	112.367	73.972	69.622	29.241	219.294	99.842	62.594	28.397	200.567
IC4710	53.130	38.375	42.923	48.247	112.027	50.749	28.936	33.530	86.444
M101	null	null	null	null	null	2474.149	1517.368	6013.197	10 038.168
M81DwB	4.688	3.384	2.287	1.245	3.989	4.424	2.688	null	3.389
M87	null	null	null	null	null	2272.458	1171.606	12.500	250.148
Mark33	24.518	18.461	49.179	126.157	888.970	24.374	16.493	136.887	795.787
NGC0024	96.216	65.867	68.843	111.458	121.584	103.341	55.647	70.709	103.117
NGC0337	90.543	63.094	153.048	359.002	779.370	92.107	62.488	284.893	708.251
NGC0584	356.214	256.095	116.706	73.131	22.091	399.665	207.982	3.407	14.965
NGC0628	766.765	547.860	1018.108	2142.342	3290.611	797.760	484.668	2144.607	3140.649
NGC0855	38.157	25.274	24.609	39.192	70.814	41.065	24.179	30.504	69.300
NGC0925	265.649	191.949	232.514	589.759	882.422	282.045	161.230	458.079	819.587
NGC1097	1166.516	787.951	1330.444	2997.699	6967.876	1228.276	740.897	2688.246	6701.842
NGC1266	50.104	39.548	51.922	86.069	888.150	52.710	38.125	83.288	719.868
NGC1291	2031.342	1278.137	1098.877	752.911	533.619	2192.936	1165.979	219.110	350.830
NGC1316	2784.455	1900.132	826.438	530.593	373.541	2816.126	1517.841	70.248	249.703
NGC1317	268.685	120.731	139.042	258.300	251.360	265.239	149.557	189.067	222.747
NGC1377	53.941	83.890	270.644	421.110	1800.945	47.883	92.497	378.637	1591.370
NGC1404	652.581	403.200	234.370	138.747	44.203	690.710	361.690	47.157	29.791
NGC1482	163.252	131.328	559.012	1511.007	3749.198	198.490	148.091	1145.743	3485.659
NGC1512	367.235	232.046	219.938	390.514	438.511	383.047	210.294	317.859	444.042
NGC1566	695.176	480.461	646.024	1920.359	2966.883	713.851	432.983	1732.291	2842.602
NGC1705	24.926	18.554	12.168	15.741	44.681	27.760	16.590	14.053	51.368
NGC2146	null	null	null	null	null	849.928	648.287	5212.065	16 059.621
NGC2798	95.253	72.733	212.450	558.018	2609.895	103.178	73.712	537.553	2342.606
NGC2841	1182.959	580.107	688.040	980.531	931.584	1332.794	733.131	664.976	1023.475
NGC2915	50.968	34.042	20.347	24.011	49.457	52.834	30.404	14.369	49.319
NGC2976	400.686	276.616	459.165	977.759	1462.267	425.513	257.118	795.641	1382.335
NGC3031	10 394.411	6571.729	5754.864	6693.628	5773.335	11 181.837	6150.802	3504.914	4256.476
NGC3034	null	null	null	null	null	7326.779	6133.829	69 367.860	353 752.440
NGC3049	36.364	23.711	52.695	120.710	442.328	36.914	21.306	99.984	377.965
NGC3077	null	null	null	null	null	592.261	354.921	642.878	1811.899
NGC3184	468.795	305.259	580.211	1337.044	1523.282	485.794	286.831	1036.955	1410.882
NGC3190	338.712	212.499	189.164	293.699	273.996	365.171	208.366	202.953	233.999

Continued on next page

Table 4.1 – continued from previous page

Name	IRAC1 (mJy)	IRAC2 (mJy)	IRAC3 (mJy)	IRAC4 (mJy)	MIPS24 (mJy)	W1 (mJy)	W2 (mJy)	W3 (mJy)	W4 (mJy)
NGC3198	259.252	173.631	237.754	668.690	1107.908	272.401	162.823	543.717	998.461
NGC3265	24.301	16.548	37.595	94.276	283.285	24.823	14.976	74.200	261.821
NGC3351	733.184	481.987	624.976	1255.254	2645.583	783.199	433.156	1000.732	2361.059
NGC3521	1929.404	1298.833	2340.921	5551.340	5894.901	2013.131	1213.083	4421.126	5719.436
NGC3621	868.356	584.228	1377.021	3130.553	3532.818	845.329	530.995	2553.669	3533.397
NGC3627	1727.878	1156.568	2112.627	5178.434	7879.911	1808.947	1102.277	4202.727	7654.394
NGC3773	20.460	14.129	21.637	46.032	144.765	19.827	12.137	34.926	124.267
NGC3938	294.100	198.631	412.297	956.006	1161.191	304.296	188.154	784.398	1088.536
NGC4125	708.612	487.220	213.649	127.137	65.642	760.067	404.703	5.100	21.369
NGC4236	227.338	152.085	75.866	121.583	437.443	205.980	106.917	92.122	457.227
NGC4254	651.897	454.749	1388.415	3786.363	4452.293	659.016	432.316	3122.677	4330.167
NGC4450	421.040	273.744	128.616	115.316	223.883	534.628	292.193	132.949	188.944
NGC4536	399.016	274.473	616.792	1548.749	3688.958	406.346	259.726	1229.781	3439.459
NGC4552	795.932	499.368	323.406	249.709	118.210	867.153	448.772	126.405	52.308
NGC4559	326.237	223.636	389.590	792.431	1113.838	336.087	214.598	605.661	1196.427
NGC4569	716.267	469.013	502.637	962.983	1456.063	767.100	449.232	753.726	1325.438
NGC4579	823.719	522.868	524.577	717.216	830.508	897.949	511.843	472.027	658.737
NGC4594	3877.338	2473.868	1685.676	1342.562	910.398	4292.122	2315.499	437.950	617.397
NGC4625	41.462	26.698	51.098	123.576	128.492	43.921	25.909	89.634	130.676
NGC4631	1167.828	815.006	2457.407	5729.195	8505.920	1195.412	797.059	4459.543	8230.357
NGC4725	1028.078	665.076	568.501	931.916	751.986	1113.915	601.487	563.219	616.569
NGC4736	3497.929	2391.445	2780.155	5051.978	5809.267	3745.176	2113.706	3794.630	5543.042
NGC4826	2328.860	1491.617	1375.367	2081.689	2602.084	2541.395	1405.544	1523.789	2417.641
NGC5033	609.155	409.473	795.539	1864.638	2080.577	622.500	376.110	1544.398	2042.716
NGC5055	2287.412	1515.827	2532.273	5642.715	6178.408	2380.522	1395.226	4655.466	5995.470
NGC5194	2540.708	1702.426	3960.434	10 625.985	12 897.969	2778.601	1710.372	9078.091	13 297.138
NGC5195	1092.390	693.615	673.334	950.152	1449.844	791.819	444.063	443.157	1153.126
NGC5398	null	null	null	null	null	37.326	21.423	58.374	259.535
NGC5408	29.847	21.581	14.279	25.513	416.261	29.997	17.957	54.377	446.943
NGC5474	101.516	72.122	79.561	117.261	169.559	105.068	59.958	77.959	126.090
NGC5713	191.185	136.081	408.921	1132.698	2503.479	195.764	132.036	931.255	2315.186
NGC5866	642.457	416.047	275.284	276.802	223.244	683.049	382.319	137.057	182.001
NGC6822	1546.026	1097.719	931.292	773.923	2384.661	1325.907	739.489	1026.301	2955.872
NGC6946	2692.372	1536.929	5548.444	12 273.355	21 248.158	2974.898	1920.838	11 522.338	20 125.810
NGC7331	1513.991	999.349	1568.913	3859.058	4349.325	1585.083	950.759	3032.995	4127.574
NGC7552	423.451	344.208	930.071	2448.633	11 114.769	423.541	336.888	2518.313	10 902.077
NGC7793	726.683	491.349	936.000	1895.788	2304.766	762.278	455.965	1365.312	1798.470

4.1 Derived quantities

The stellar 'backbone' is made up of evolved stars that emit in a blackbody distribution. Thus, even though the peak of the radiation is in the NIR region, some emission in the form of the Rayleigh-Jeans tail lies in the MIR region as well. To eliminate this component in our MIR bands, namely W_3 and W_4, we utilised the spectrum (Figure 13 in Silva et al. 1998) of an elliptical galaxy, and determined the percentage of the flux at 3.4 μm that was present at 12 and 22 μm, respectively. Ellipticals were chosen since there should be very little PAH and warm dust ($T > 100K$) contribution in these galaxies, and are thus dominated by the evolved stellar population. The percentages found were 15.8% at 12μm and 5.9% at 22μm.
These continuum-subtracted flux densities were used in our luminosity calculations:

$$W3_{PAH} = W_3 - 0.158W_1 \tag{4.1}$$

$$W4_{dust} = W_4 - 0.059W_1 \tag{4.2}$$

We determined a similar statistic for our *Spitzer* data - the percentage of the flux at 3.6μm present at 8μm was found to be 28%:

$$IRAC4_{PAH} = IRAC_4 - 0.28IRAC_1 \tag{4.3}$$

This percentage is slightly higher than the value given for NGC300 by Helou et al. (2004) of $\sim 25\%$.
Table 4.1 above displays the *isophotal* photometric data, but since these data are distance-dependent, we need to convert them into information that is distance-independent, and thus intrinsic to the galaxy, in order to understand the processes occurring within our galaxies. To do this, we converted our fluxes into luminosities.

The tables below display this distance-independent information, divided up according to the type of parameters: Table 4.2 displays the *WISE* luminosities; table 4.3 has information related to the stellar mass of our galaxies; table 4.4 contains the star formation data; while table 4.5 showcases the MIPS24-derived parameters as well as metallicity data; finally, table 4.6 has data from the two more important TIR measurements.

These, apart from our first plot, are the parameters plotted in this chapter. Columns:

- $log(L_{Wi})$ - Log of WISE luminosities (νL_ν), integrated in the appropriate band, normalized by the bolometric solar luminosity.
- err(L_{Wi}) - Error in the log of the appropriate *WISE* luminosity.
- $W_i - W_j$ - Rest-frame *WISE* colours in units of magnitude.
- $log(L_{W1/Sun})$ - Log of the W_1 in-band luminosity (normalized by the equivalent solar value), used for the mass-to-light ratio.
- $err(L_{W1/Sun})$ - Error in the log of the W_1 in-band luminosity.
- $log(M/L)$ - derived from the $W_1 - W_2$ colour, then used in conjunction with W_1 to derive the stellar mass
- $log(M_{stellar})$ - Log of the stellar mass (normalized by the solar value); derived from M/L from Cluver et al. 2014 (see comparison figure 4.1 with KINGFISH masses from multicolor method below).
- $err(M_{stellar})$ - Error in the log of the stellar mass.
- $SFR_{12,22}$ - 12 and 22μm star formation rates, using νL_ν luminosities and the calibration from Cluver et al. 2014.
- $err(SFR_{12,22})$ - Error in the 12 and 22μm star formation rates.
- $log(sSFR_{12,22})$ - 12 and 22μm specific star formation rates.
- SFR_{24}, $logL_{24}$ - MIPS24 derived parameters; SFR using Rujopakarn et al. 2011.
- KK_{Char}, err(KK_{Char}) - Globally-averaged metallicity ($12 + logO/H$) for the galaxy (and the error in the measurement). Oxygen abundances from Kobulnicky & Kewley 2004.
- PT_{Char}, err(PT_{Char}) - Globally-averaged metallicity ($12 + logO/H$) for the galaxy (and the error in the measurement). Oxygen abundances from Pilyugin & Thuan 2005.

- log $L(TIR_{Int})$, log $SFR(TIR_{Int})$ - TIR determined by integrating under SED fits from Draine & Li 2007, provided by D.A. Dale (private communication). SFR obtained through Calzetti's relation (1.1).
- log $L(TIR_{D14})$, log $SFR(TIR_{D14})$ - TIR determined by using Equation 5 from , which uses photometry at 8, 24, 70 and 160 μm, provided by D.A. Dale (private communication). SFR obtained through Calzetti's relation (1.1) (see TIR comparison figure 4.2 below).

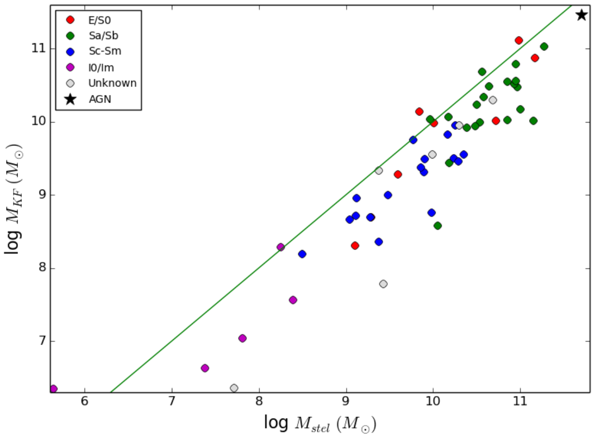

Figure 4.1: *Comparison of the stellar mass computed by the KINGFISH team (Kennicutt et al. 2011) and the derived stellar mass derived in this thesis from* WISE *colours. Colour-coded by morphology. The green line is the 1:1 line.*

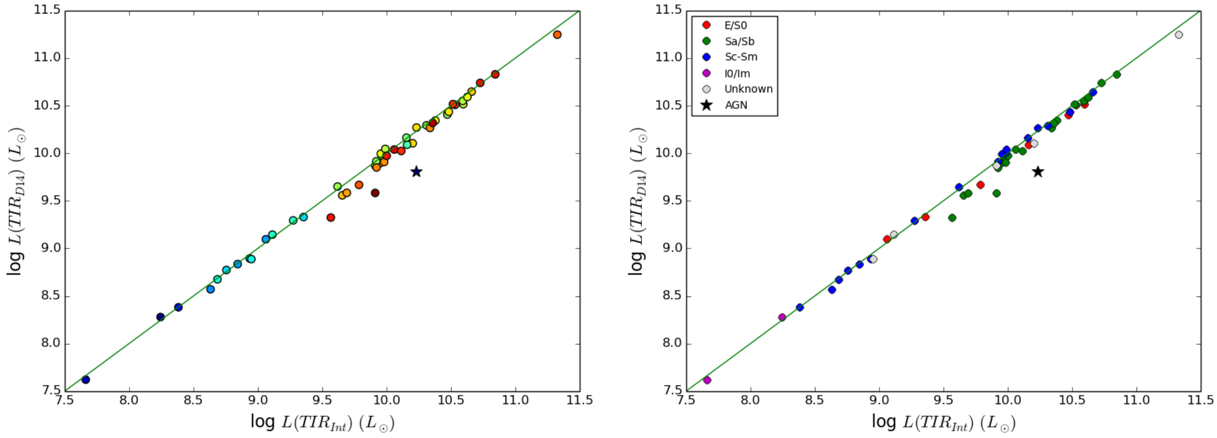

Figure 4.2: *Comparison of the integrated Draine & Li (2007) TIR luminosity and the datapoint-driven Dale et al. 2014 TIR luminosity. The green line is the 1:1 line.*

Table 4.2: Derived *WISE* luminosities

Name	$log(L_{W1})$ ($L_\odot$)	err(L_{W1}) ($L_\odot$)	$log(L_{W2})$ ($L_\odot$)	err(L_{W2}) ($L_\odot$)	$log(L_{W3})$ ($L_\odot$)	err(L_{W3}) ($L_\odot$)	$log(L_{W4})$ ($L_\odot$)	err(L_{W4}) ($L_\odot$)
DDO053	4.9587	0.043	5.1138	0.039	5.3991	0.0495	5.9398	0.065
DDO154	6.0592	0.028	5.5655	0.105	*null*	*null*	*null*	*null*
DDO165	6.7173	0.016	6.3363	0.039	*null*	*null*	*null*	*null*
IC0342	9.3427	0.012	8.983	0.02	9.2773	0.0201	9.239	0.011
IC2574	7.6576	0.012	7.3171	0.022	6.5736	0.056	7.1276	0.098
IC4710	7.9938	0.012	7.6121	0.022	7.2759	0.037	7.3922	0.091
M101	9.5566	0.011	9.2065	0.019	9.4043	0.0131	9.3319	0.016
M81DwB	6.7934	0.017	6.4393	0.035	*null*	*null*	5.8447	0.184
M87	10.1998	0.011	9.7743	0.019	7.4023	0.036	8.4086	0.061
Mark33	8.6247	0.012	8.3173	0.022	8.8362	0.0121	9.3057	0.012
NGC0024	8.135	0.011	7.7284	0.02	7.4323	0.0211	7.3012	0.05
NGC0337	9.214	0.011	8.9078	0.02	9.1665	0.0151	9.267	0.016
NGC0584	9.6642	0.011	9.2429	0.019	7.057	0.039	7.4047	0.064
NGC0628	9.0702	0.011	8.7161	0.019	8.9618	0.0121	8.8325	0.015
NGC0855	8.0346	0.012	7.6668	0.021	7.3676	0.0261	7.429	0.031
NGC0925	8.8157	0.011	8.4351	0.02	8.4884	0.0201	8.446	0.035
NGC1097	10.0227	0.011	9.6655	0.019	9.825	0.0111	9.9267	0.012
NGC1266	9.1577	0.012	8.8793	0.021	8.8185	0.0191	9.4602	0.014
NGC1291	9.6558	0.011	9.2438	0.019	8.1175	0.036	8.027	0.074
NGC1316	10.4491	0.011	10.0429	0.019	8.3081	0.0181	8.564	0.028
NGC1317	9.7026	0.011	9.3161	0.019	9.0177	0.0131	8.7939	0.019
NGC1377	8.9103	0.012	9.0586	0.02	9.2705	0.0131	9.599	0.012
NGC1404	9.8524	0.014	9.4337	0.022	8.1487	0.0441	7.6543	0.053
NGC1482	9.3283	0.011	9.0634	0.019	9.5517	0.0111	9.74	0.012
NGC1512	9.1878	0.011	8.7896	0.019	8.5688	0.0151	8.419	0.02
NGC1566	9.9308	0.011	9.576	0.019	9.7779	0.0111	9.698	0.013
NGC1705	7.3067	0.012	6.9454	0.021	6.4732	0.0291	6.7411	0.049
NGC2146	10.001	0.011	9.7457	0.019	10.2507	0.0121	10.4445	0.011
NGC2798	9.2781	0.011	8.9943	0.019	9.457	0.0121	9.8013	0.012
NGC2841	9.804	0.011	9.4067	0.019	8.9642	0.0121	8.8565	0.016
NGC2915	7.3236	0.012	6.9459	0.021	6.2202	0.0351	6.4608	0.037
NGC2976	8.1796	0.011	7.8231	0.019	7.9135	0.0131	7.8584	0.013
NGC3031	9.5992	0.011	9.2019	0.019	8.5574	0.0111	8.3468	0.016
NGC3034	9.4462	0.012	9.2313	0.021	9.8845	0.0112	10.2971	0.011
NGC3049	8.9896	0.012	8.6132	0.022	8.8844	0.0181	9.167	0.019
NGC3077	8.4122	0.011	8.0521	0.019	7.9099	0.0161	8.0649	0.014
NGC3184	9.2396	0.011	8.8731	0.019	9.031	0.0131	8.8698	0.016
NGC3190	9.7552	0.011	9.3739	0.019	8.9622	0.0151	8.7291	0.026

Continued on next page

Table 4.2 – continued from previous page

Name	$log(L_{W1})$ ($L_\odot$)	err(L_{W1}) ($L_\odot$)	$log(L_{W2})$ ($L_\odot$)	err(L_{W2}) ($L_\odot$)	$log(L_{W3})$ ($L_\odot$)	err(L_{W3}) ($L_\odot$)	$log(L_{W4})$ ($L_\odot$)	err(L_{W4}) ($L_\odot$)
NGC3198	9.2042	0.011	8.843	0.019	8.9665	0.0141	8.9354	0.018
NGC3265	8.3494	0.012	7.9923	0.022	8.2871	0.0141	8.5397	0.018
NGC3351	9.3227	0.011	8.9278	0.019	8.8913	0.0141	8.9691	0.014
NGC3521	9.6187	0.011	9.261	0.019	9.4224	0.0121	9.2393	0.013
NGC3621	9.0314	0.02	8.6918	0.035	8.9736	0.0124	8.8197	0.016
NGC3627	9.7274	0.011	9.3745	0.019	9.5556	0.0111	9.521	0.012
NGC3773	8.2045	0.012	7.8537	0.023	7.9125	0.0291	8.1688	0.031
NGC3938	9.4124	0.011	9.0659	0.019	9.2858	0.0131	9.1331	0.016
NGC4125	10.0109	0.011	9.5995	0.019	7.2997	0.0301	7.6269	0.056
NGC4236	8.0603	0.011	7.6378	0.019	7.1729	0.046	7.5737	0.037
NGC4254	9.6406	0.011	9.3198	0.019	9.7783	0.0111	9.6253	0.013
NGC4450	9.7547	0.011	9.3546	0.019	8.6125	0.0211	8.4701	0.052
NGC4536	9.4058	0.011	9.0737	0.019	9.3489	0.0121	9.5005	0.013
NGC4552	9.7598	0.011	9.336	0.019	8.3855	0.065	7.7073	0.074
NGC4559	9.2001	0.011	8.8675	0.019	8.9179	0.0141	8.9186	0.029
NGC4569	9.5141	0.011	9.144	0.019	8.9685	0.0111	8.9187	0.012
NGC4579	10.0555	0.011	9.6737	0.019	9.2383	0.0141	9.0881	0.02
NGC4594	10.0225	0.011	9.6168	0.019	8.4934	0.0221	8.3475	0.035
NGC4625	8.1053	0.012	7.7383	0.021	7.8771	0.0191	7.7459	0.049
NGC4631	9.0881	0.011	8.7744	0.019	9.122	0.0111	9.0932	0.012
NGC4725	9.685	0.011	9.2797	0.019	8.851	0.0151	8.5953	0.019
NGC4736	9.4514	0.011	9.0652	0.019	8.9192	0.0121	8.7888	0.015
NGC4826	9.3041	0.011	8.9092	0.019	8.544	0.0121	8.4495	0.014
NGC5033	9.7318	0.011	9.3752	0.019	9.5885	0.0121	9.4149	0.017
NGC5055	9.8319	0.011	9.4622	0.019	9.5853	0.0111	9.4002	0.013
NGC5194	9.6862	0.011	9.3378	0.019	9.6625	0.0111	9.5333	0.025
NGC5195	9.1551	0.011	8.7662	0.019	8.3651	0.0121	8.4855	0.013
NGC5398	8.3511	0.012	7.9723	0.021	8.0074	0.0201	8.3604	0.024
NGC5408	7.2875	0.012	6.927	0.022	7.008	0.0201	7.6278	0.021
NGC5474	8.1796	0.011	7.7983	0.02	7.5121	0.036	7.426	0.063
NGC5713	9.4908	0.011	9.1821	0.019	9.6302	0.0111	9.7308	0.012
NGC5866	9.5719	0.011	9.1822	0.019	8.3364	0.0151	8.1646	0.024
NGC6822	6.9163	0.011	6.525	0.019	6.2672	0.05	6.4316	0.064
NGC6946	9.4965	0.011	9.1688	0.019	9.5466	0.0111	9.4939	0.011
NGC7331	9.9895	0.011	9.6298	0.019	9.7334	0.0111	9.5723	0.013
NGC7552	9.5407	0.011	9.3036	0.019	9.777	0.0111	10.1185	0.011
NGC7793	8.5124	0.011	8.1515	0.019	8.2276	0.0131	8.0523	0.015

Table 4.3: Derived colours and masses from *WISE*

Name	$W_1 - W_2$ (mag)	$W_2 - W_3$ (mag)	$log(L_{W1/Sun})$	$err(L_{W1/Sun})$	$log(M/L)$	$log(M_{stellar})$ ($M_{\odot}$)	$err(M_{stellar})$ ($M_{\odot}$)
DDO053	1.379	3.654	6.3181	0.0474	−0.814	5.504	0.288
DDO154	−0.243	*null*	7.4185	0.0344	0.068	7.487	0.533
DDO165	0.039	*null*	8.0766	0.0256	−0.106	7.97	0.207
IC0342	0.092	3.715	10.702	0.0233	−0.21	10.492	0.115
IC2574	0.14	1.544	9.0169	0.0233	−0.304	8.713	0.123
IC4710	0.037	2.315	9.3531	0.0233	−0.103	9.251	0.123
M101	0.116	3.486	10.9159	0.0228	−0.258	10.658	0.108
M81DwB	0.106	*null*	8.1527	0.0262	−0.238	7.915	0.191
M87	−0.072	0.676	11.5591	0.0228	0.068	11.627	0.108
Mark33	0.223	4.25	9.984	0.0233	−0.467	9.517	0.123
NGC0024	−0.025	2.408	9.4943	0.0228	0.019	9.514	0.112
NGC0337	0.226	3.624	10.5734	0.0228	−0.472	10.101	0.112
NGC0584	−0.062	0.685	11.0236	0.0228	0.068	11.092	0.108
NGC0628	0.106	3.599	10.4295	0.0228	−0.238	10.192	0.108
NGC0855	0.072	2.384	9.3939	0.0233	−0.171	9.223	0.119
NGC0925	0.04	3.157	10.175	0.0228	−0.108	10.067	0.112
NGC1097	0.098	3.397	11.382	0.0228	−0.222	11.16	0.108
NGC1266	0.295	2.874	10.517	0.0233	−0.609	9.908	0.119
NGC1291	−0.039	1.137	11.0151	0.0228	0.046	11.061	0.108
NGC1316	−0.024	0.749	11.8084	0.0228	0.017	11.826	0.108
NGC1317	0.025	2.394	11.062	0.0228	−0.079	10.983	0.108
NGC1377	1.362	3.474	10.2697	0.0233	−0.814	9.456	0.115
NGC1404	−0.055	1.011	11.2117	0.0244	0.068	11.28	0.129
NGC1482	0.329	4.173	10.6876	0.0228	−0.675	10.013	0.108
NGC1512	−0.004	2.56	10.5471	0.0228	−0.022	10.525	0.108
NGC1566	0.104	3.496	11.2901	0.0228	−0.234	11.056	0.108
NGC1705	0.088	2.037	8.666	0.0233	−0.202	8.464	0.119
NGC2146	0.353	4.213	11.3603	0.0228	−0.722	10.639	0.108
NGC2798	0.282	4.112	10.6374	0.0228	−0.582	10.055	0.108
NGC2841	−0.002	2.115	11.1633	0.0228	−0.026	11.137	0.108
NGC2915	0.047	1.606	8.6829	0.0233	−0.122	8.561	0.119
NGC2976	0.1	3.237	9.5389	0.0228	−0.226	9.313	0.108
NGC3031	−0.002	1.755	10.9585	0.0228	−0.026	10.932	0.108
NGC3034	0.454	4.574	10.8055	0.0233	−0.814	9.991	0.119
NGC3049	0.05	3.663	10.3489	0.0233	−0.128	10.22	0.123
NGC3077	0.091	2.715	9.7715	0.0228	−0.208	9.563	0.108
NGC3184	0.075	3.395	10.5989	0.0228	−0.177	10.422	0.108
NGC3190	0.038	2.166	11.1146	0.0228	−0.104	11.011	0.108

Continued on next page

Table 4.3 – continued from previous page

Name	$W_1 - W_2$ (mag)	$W_2 - W_3$ (mag)	$log(L_{W1/Sun})$	$err(L_{W1/Sun})$	$log(M/L)$	$log(M_{stellar})$ ($M_\odot$)	$err(M_{stellar})$ ($M_\odot$)
NGC3198	0.088	3.314	10.5635	0.0228	−0.203	10.361	0.108
NGC3265	0.098	3.716	9.7087	0.0233	−0.223	9.486	0.123
NGC3351	0.004	2.958	10.682	0.0228	−0.038	10.644	0.108
NGC3521	0.097	3.402	10.978	0.0228	−0.22	10.758	0.108
NGC3621	0.142	3.683	10.3907	0.0283	−0.309	10.082	0.199
NGC3627	0.109	3.447	11.0867	0.0228	−0.244	10.843	0.108
NGC3773	0.114	3.163	9.5639	0.0233	−0.254	9.31	0.128
NGC3938	0.125	3.537	10.7717	0.0228	−0.275	10.497	0.108
NGC4125	−0.037	0.649	11.3702	0.0228	0.043	11.413	0.108
NGC4236	−0.065	2.089	9.4196	0.0228	0.068	9.488	0.108
NGC4254	0.189	4.105	10.9999	0.0228	−0.401	10.599	0.108
NGC4450	−0.009	1.602	11.114	0.0228	−0.012	11.102	0.108
NGC4536	0.161	3.666	10.7652	0.0228	−0.346	10.42	0.108
NGC4552	−0.068	1.344	11.1191	0.0228	0.068	11.187	0.108
NGC4559	0.16	3.14	10.5594	0.0228	−0.343	10.216	0.108
NGC4569	0.066	2.646	10.8734	0.0228	−0.159	10.714	0.108
NGC4579	0.037	2.12	11.4148	0.0228	−0.102	11.313	0.108
NGC4594	−0.023	1.13	11.3818	0.0228	0.015	11.397	0.108
NGC4625	0.074	3.351	9.4646	0.0233	−0.175	9.29	0.119
NGC4631	0.207	3.837	10.4475	0.0228	−0.435	10.012	0.108
NGC4725	−0.022	2.146	11.0444	0.0228	0.013	11.058	0.108
NGC4736	0.026	2.715	10.8107	0.0228	−0.081	10.73	0.108
NGC4826	0.004	2.264	10.6634	0.0228	−0.038	10.626	0.108
NGC5033	0.1	3.523	11.0911	0.0228	−0.226	10.865	0.108
NGC5055	0.067	3.315	11.1912	0.0228	−0.161	11.03	0.108
NGC5194	0.12	3.786	11.0455	0.0228	−0.265	10.78	0.108
NGC5195	0.019	2.19	10.5144	0.0228	−0.067	10.447	0.108
NGC5398	0.044	3.115	9.7104	0.0233	−0.116	9.594	0.119
NGC5408	0.09	3.216	8.6469	0.0233	−0.206	8.441	0.123
NGC5474	0.038	2.417	9.539	0.0228	−0.104	9.435	0.112
NGC5713	0.219	4.079	10.8501	0.0228	−0.46	10.39	0.108
NGC5866	0.017	1.439	10.9312	0.0228	−0.063	10.868	0.108
NGC6822	0.013	2.48	8.2756	0.0228	−0.055	8.22	0.108
NGC6946	0.172	3.911	10.8558	0.0228	−0.367	10.489	0.108
NGC7331	0.092	3.268	11.3488	0.0228	−0.21	11.138	0.108
NGC7552	0.398	4.135	10.9001	0.0228	−0.811	10.089	0.108
NGC7793	0.089	3.205	9.8717	0.0228	−0.204	9.667	0.108

Table 4.4: Star formation derived from *WISE*

Name	SFR_{12} ($M_\odot$ yr^{-1})	$err(SFR_{12})$ ($M_\odot$ yr^{-1})	SFR_{22} ($M_\odot$ yr^{-1})	$err(SFR_{22})$ ($M_\odot$ yr^{-1})	$log(sSFR_{12})$ (yr^{-1})	$log(sSFR_{22})$ (yr^{-1})
DDO053	null	null	null	null	−9.47	−8.07
DDO154	null	0.05	null	0.04	0.00	0.00
DDO165	null	0.02	null	0.02	0.00	0.00
IC0342	2.29	0.12	1.89	0.10	−9.94	−10.02
IC2574	null	null	0.04	null	−11.05	−9.95
IC4710	0.02	null	0.06	null	−10.89	−10.33
M81DwB	null	0.05	null	null	0.00	−10.22
M87	0.02	null	0.39	0.03	−13.18	−11.92
M101	3.14	0.16	2.25	0.12	−9.95	−10.10
Mark33	0.76	0.04	2.14	0.11	−9.42	−8.98
NGC0024	0.02	null	0.05	null	−11.02	−10.70
NGC0337	1.74	0.09	1.99	0.10	−9.66	−9.60
NGC0584	0.01	null	0.06	null	−13.02	−12.21
NGC0628	1.04	0.05	0.88	0.05	−9.97	−10.05
NGC0855	0.02	null	0.06	null	−10.74	−10.25
NGC0925	0.32	0.02	0.42	0.02	−10.40	−10.28
NGC1097	8.93	0.46	6.92	0.35	−10.01	−10.12
NGC1266	0.73	0.04	2.87	0.15	−9.98	−9.38
NGC1291	0.13	0.01	0.19	0.01	−11.84	−11.66
NGC1316	0.20	0.01	0.53	0.03	−12.39	−11.98
NGC1317	1.20	0.06	0.81	0.04	−10.75	−10.92
NGC1377	2.25	0.12	3.73	0.19	−9.24	−9.02
NGC1404	0.14	0.01	0.09	0.01	−12.03	−12.19
NGC1482	4.53	0.23	4.86	0.25	−9.35	−9.32
NGC1512	0.39	0.02	0.40	0.02	−10.79	−10.78
NGC1566	7.95	0.41	4.49	0.23	−9.96	−10.20
NGC1705	null	null	0.02	null	−10.94	−10.05
NGC2146	25.75	1.32	18.39	0.93	−9.27	−9.42
NGC2798	3.58	0.18	5.46	0.28	−9.41	−9.22
NGC2841	1.05	0.05	0.92	0.05	−10.98	−11.04
NGC2915	null	null	0.01	null	−11.34	−10.40
NGC2976	0.08	null	0.14	0.01	−10.23	−9.97
NGC3031	0.38	0.02	0.35	0.02	−11.21	−11.25
NGC3034	10.36	0.53	13.92	0.70	−9.11	−8.98
NGC3049	0.86	0.05	1.65	0.09	−10.12	−9.83
NGC3077	0.08	null	0.21	0.01	−10.49	−10.06
NGC3184	1.24	0.06	0.94	0.05	−10.15	−10.27
NGC3190	1.04	0.05	0.72	0.04	−10.83	−10.99

Continued on next page

Table 4.4 – continued from previous page

Name	SFR_{12} ($M_\odot$ yr^{-1})	$err(SFR_{12})$ ($M_\odot$ yr^{-1})	SFR_{22} ($M_\odot$ yr^{-1})	$err(SFR_{22})$ ($M_\odot$ yr^{-1})	$log(sSFR_{12})$ (yr^{-1})	$log(sSFR_{22})$ (yr^{-1})
NGC3198	1.06	0.05	1.06	0.05	−10.15	−10.14
NGC3265	0.19	0.01	0.50	0.03	−10.00	−9.59
NGC3351	0.88	0.05	1.13	0.06	−10.56	−10.45
NGC3521	3.28	0.17	1.89	0.10	−10.05	−10.29
NGC3621	1.08	0.05	0.86	0.04	−9.83	−9.93
NGC3627	4.57	0.23	3.21	0.16	−9.98	−10.13
NGC3773	0.08	null	0.25	0.01	−10.22	−9.71
NGC3938	2.34	0.12	1.55	0.08	−9.92	−10.10
NGC4125	0.02	null	0.09	0.01	−13.07	−12.34
NGC4236	0.01	null	0.08	null	−11.29	−10.47
NGC4254	7.95	0.41	3.91	0.20	−9.45	−9.76
NGC4450	0.44	0.02	0.44	0.03	−11.33	−11.32
NGC4536	2.73	0.14	3.09	0.16	−9.75	−9.70
NGC4552	0.25	0.02	0.10	0.01	−11.68	−12.06
NGC4559	0.94	0.05	1.03	0.06	−10.01	−9.97
NGC4569	1.06	0.05	1.03	0.05	−10.51	−10.52
NGC4579	2.08	0.11	1.42	0.07	−10.83	−11.00
NGC4594	0.33	0.02	0.35	0.02	−11.76	−11.73
NGC4625	0.07	null	0.11	0.01	−10.26	−10.06
NGC4631	1.55	0.08	1.43	0.07	−9.58	−9.61
NGC4725	0.79	0.04	0.56	0.03	−11.03	−11.18
NGC4736	0.94	0.05	0.81	0.04	−10.60	−10.67
NGC4826	0.37	0.02	0.43	0.02	−10.92	−10.86
NGC5033	4.96	0.25	2.63	0.14	−9.97	−10.25
NGC5055	4.92	0.25	2.56	0.13	−10.16	−10.44
NGC5194	5.96	0.31	3.29	0.18	−9.80	−10.05
NGC5195	0.24	0.01	0.46	0.02	−10.92	−10.64
NGC5398	0.10	null	0.36	0.02	−10.44	−9.87
NGC5408	0.01	null	0.09	null	−10.34	−9.29
NGC5474	0.03	null	0.06	null	−10.82	−10.48
NGC5713	5.50	0.28	4.78	0.24	−9.43	−9.49
NGC5866	0.22	0.01	0.25	0.01	−11.38	−11.32
NGC6822	null	null	0.01	null	−10.96	−10.10
NGC6946	4.47	0.23	3.06	0.16	−9.60	−9.76
NGC7331	7.11	0.36	3.54	0.18	−10.09	−10.40
NGC7552	7.93	0.41	9.93	0.50	−9.32	−9.23
NGC7793	0.17	0.01	0.20	0.01	−10.25	−10.17

Table 4.5: Derived quantities from *Spitzer* and galaxy metallicities

Name	SFR_{24} ($M_{\odot}$ yr^{-1})	$logL_{24}$ ($L_{\odot}$)	KK_{Char}	$err(KK_{Char})$	PT_{Char}	$err(PT_{Char})$
DDO053	0.00	5.924	8.0	0.09	7.6	0.11
DDO154	*null*	*null*	8.02	0.05	7.54	0.09
DDO165	0.00	5.843	8.04	0.07	7.63	0.08
IC0342	*null*	*null*	*null*	*null*	*null*	*null*
IC2574	0.01	7.15	8.24	0.11	7.85	0.14
IC4710	0.02	7.488	*null*	*null*	*null*	*null*
M81DwB	0.00	5.899	8.19	0.09	7.84	0.13
M87	*null*	*null*	*null*	*null*	*null*	*null*
M101	*null*	*null*	*null*	*null*	*null*	*null*
Mark33	1.70	9.337	*null*	*null*	*null*	*null*
NGC0024	0.02	7.356	*null*	*null*	*null*	*null*
NGC0337	1.53	9.292	8.84	0.05	8.18	0.07
NGC0584	0.03	7.558	*null*	*null*	*null*	*null*
NGC0628	0.54	8.836	9.02	0.01	8.35	0.01
NGC0855	0.02	7.422	8.8	0.09	8.29	0.1
NGC0925	0.23	8.462	8.79	0.01	8.25	0.01
NGC1097	6.60	9.927	9.09	0.01	8.47	0.02
NGC1266	2.67	9.535	*null*	*null*	*null*	*null*
NGC1291	0.12	8.193	*null*	*null*	*null*	*null*
NGC1316	0.41	8.723	*null*	*null*	*null*	*null*
NGC1317	0.53	8.83	*null*	*null*	*null*	*null*
NGC1377	3.38	9.636	*null*	*null*	*null*	*null*
NGC1404	0.05	7.809	*null*	*null*	*null*	*null*
NGC1482	4.44	9.755	8.95	0.08	8.11	0.13
NGC1512	0.19	8.397	9.11	0.04	8.56	0.12
NGC1566	3.91	9.7	*null*	*null*	*null*	*null*
NGC1705	0.00	6.664	*null*	*null*	*null*	*null*
NGC2146	*null*	*null*	*null*	*null*	*null*	*null*
NGC2798	5.30	9.832	9.04	0.03	8.34	0.08
NGC2841	0.49	8.799	9.21	0.02	8.54	0.03
NGC2915	0.00	6.446	8.28	0.08	7.94	0.13
NGC2976	0.06	7.866	8.98	0.03	8.36	0.06
NGC3031	0.23	8.463	*null*	*null*	*null*	*null*
NGC3034	*null*	*null*	*null*	*null*	*null*	*null*
NGC3049	1.29	9.219	9.1	0.01	8.53	0.01
NGC3077	*null*	*null*	*null*	*null*	*null*	*null*
NGC3184	0.60	8.887	9.15	0.01	8.51	0.01
NGC3190	0.47	8.781	*null*	*null*	*null*	*null*

Continued on next page

Table 4.5 – continued from previous page

Name	SFR_{24} ($M_\odot$ yr^{-1})	$logL_{24}$ ($L_\odot$)	KK_{Char}	$err(KK_{Char})$	PT_{Char}	$err(PT_{Char})$
NGC3198	0.72	8.964	8.9	0.02	8.34	0.02
NGC3265	0.28	8.558	8.99	0.06	8.27	0.14
NGC3351	0.78	9.002	9.19	0.01	8.6	0.01
NGC3521	1.34	9.236	9.01	0.02	8.39	0.02
NGC3621	0.50	8.803	8.8	0.01	8.27	0.02
NGC3627	2.57	9.517	8.99	0.1	8.34	0.24
NGC3773	0.13	8.219	8.92	0.03	8.43	0.03
NGC3938	1.09	9.145	*null*	*null*	*null*	*null*
NGC4125	0.10	8.098	*null*	*null*	*null*	*null*
NGC4236	0.03	7.538	*null*	*null*	*null*	*null*
NGC4254	3.26	9.621	9.13	0.01	8.45	0.01
NGC4450	0.26	8.527	*null*	*null*	*null*	*null*
NGC4536	2.55	9.515	9.0	0.04	8.21	0.08
NGC4552	0.09	8.045	*null*	*null*	*null*	*null*
NGC4559	0.58	8.871	8.81	0.01	8.29	0.01
NGC4569	0.68	8.943	*null*	*null*	*null*	*null*
NGC4579	1.16	9.172	*null*	*null*	*null*	*null*
NGC4594	0.25	8.5	*null*	*null*	*null*	*null*
NGC4625	0.04	7.722	9.05	0.07	8.35	0.17
NGC4631	0.96	9.091	8.75	0.09	8.12	0.11
NGC4725	0.36	8.665	9.1	0.08	8.35	0.13
NGC4736	0.48	8.793	9.01	0.03	8.31	0.03
NGC4826	0.23	8.465	9.2	0.04	8.54	0.1
NGC5033	1.99	9.407	*null*	*null*	*null*	*null*
NGC5055	1.95	9.397	9.14	0.02	8.4	0.03
NGC5194	2.49	9.504	*null*	*null*	*null*	*null*
NGC5195	0.29	8.569	*null*	*null*	*null*	*null*
NGC5398	*null*	*null*	8.69	0.06	8.35	0.05
NGC5408	0.03	7.581	8.23	0.06	7.81	0.09
NGC5474	0.03	7.538	8.83	0.14	8.31	0.22
NGC5713	4.37	9.748	9.03	0.03	8.24	0.06
NGC5866	0.14	8.237	*null*	*null*	*null*	*null*
NGC6822	0.00	6.322	*null*	*null*	*null*	*null*
NGC6946	2.47	9.501	9.05	0.02	8.4	0.03
NGC7331	2.96	9.579	9.02	0.02	8.34	0.02
NGC7552	10.06	10.11	*null*	*null*	*null*	*null*
NGC7793	0.11	8.144	8.88	0.01	8.31	0.02

Table 4.6: TIR-derived quantities

Name	log $L(TIR_{Int})$ ($L_\odot$)	log $L(TIR_{D14})$ ($L_\odot$)	log $SFR(TIR_{Int})$ ($M_\odot$ yr^{-1})	log $SFR(TIR_{D14})$ ($M_\odot$ yr^{-1})
IC0342	10.20	10.10	0.24	0.14
IC2574	8.38	8.38	−1.58	−1.58
NGC0337	10.31	10.29	0.35	0.33
NGC0628	9.91	9.87	0.05	0.09
NGC0855	8.63	8.57	−1.33	−1.39
NGC0925	9.62	9.65	0.34	0.31
NGC1097	10.84	10.83	0.88	0.87
NGC1266	10.47	10.41	0.51	0.44
NGC1291	9.57	9.32	0.39	0.64
NGC1316	10.23	9.81	0.27	0.16
NGC1377	10.16	10.09	0.20	0.13
NGC1482	10.60	10.52	0.63	0.55
NGC1512	9.66	9.56	0.31	0.40
NGC2146	11.33	11.25	1.36	1.28
NGC2798	10.59	10.55	0.63	0.59
NGC2841	10.06	10.04	0.10	0.08
NGC2915	7.66	7.62	−2.30	−2.34
NGC2976	8.94	8.89	−1.02	−1.07
NGC3049	9.98	9.94	0.02	0.02
NGC3077	8.95	8.89	−1.01	−1.07
NGC3184	9.98	10.01	0.02	0.04
NGC3190	10.11	10.02	0.15	0.06
NGC3198	9.96	9.99	0.01	0.03
NGC3265	9.36	9.33	0.61	0.63
NGC3351	9.95	9.89	0.01	0.07
NGC3521	10.34	10.27	0.38	0.30
NGC3621	9.92	9.92	0.04	0.05
NGC3627	10.53	10.51	0.57	0.55
NGC3773	9.06	9.10	0.90	0.87
NGC3938	10.23	10.27	0.27	0.31
NGC4236	8.69	8.68	−1.27	−1.29
NGC4254	10.66	10.65	0.70	0.69
NGC4536	10.38	10.34	0.42	0.38
NGC4559	9.99	10.05	0.03	0.08
NGC4569	9.98	9.91	0.02	0.05
NGC4579	10.36	10.32	0.40	0.36
NGC4594	9.91	9.58	0.05	0.38
NGC4625	8.84	8.84	−1.12	−1.13

Continued on next page

Table 4.6 – continued from previous page

Name	log $L(TIR_{Int})$ $(L_\odot)$	log $L(TIR_{D14})$ $(L_\odot)$	log $SFR(TIR_{Int})$ $(M_\odot\ yr^{-1})$	log $SFR(TIR_{D14})$ $(M_\odot\ yr^{-1})$
NGC4631	10.15	10.16	0.19	0.20
NGC4725	10.00	9.97	0.04	0.01
NGC4736	9.92	9.85	0.04	0.11
NGC4826	9.69	9.58	0.27	0.38
NGC5055	10.52	10.52	0.55	0.55
NGC5398	9.11	9.14	0.85	0.82
NGC5408	8.25	8.28	−1.72	−1.68
NGC5474	8.76	8.77	−1.20	−1.19
NGC5713	10.63	10.59	0.67	0.63
NGC5866	9.79	9.67	0.18	0.29
NGC6946	10.48	10.44	0.52	0.47
NGC7331	10.73	10.74	0.77	0.78
NGC7793	9.28	9.29	0.69	0.67

4.2 *WISE-Spitzer* photometry comparison

In the plots that follow, there are a number of sources that are highlighted for their interesting properties in our analysis. These sources, and some basic information about them, are listed in table 4.7 below.

Table 4.7: Highlighted sources

Name	Alt name	$log(M_*)$ $(M_\odot)$	Morphology	Activity
DDO053	None	5.64	Im	None
DDO165	None	7.808	Im	None
NGC1266	None	9.839	SB(rs)0p	LINER
NGC1316	Fornax A	11.7	SAB(s)0	AGN
NGC1377	None	9.592	S0	HII
NGC2146	None	10.682	None	None
NGC4552	None	11.076	E	HII/LINER/Sy2
NGC5408	None	8.249	IB(s)m	HII
NGC6822	None	8.073	IB(s)m	None
NGC1291	None	10.944	SBa	HII
NGC4594	M104	11.271	SA(s)a	LINER/Sy

Figure 4.3 is a comparison between the warm ($T > 100K$) dust fluxes from *WISE* and *Spitzer*. Since they both measure emission from warm dust, we expect them to be consistent, and since the mean difference (in the log) between the points and the 1:1 relation is within 2%, in the mass range 10^6 - 10^{11} $M_\odot$ this is indeed the case. This is our 'sanity check' plot, since we need to be able to trust that our photometry is reliable in order to go forward with any analysis.

The exceptions are two irregular dwarf galaxies and the AGN host NGC4552. They have been examined and as far as can be determined, there is no error in our photometry. The discrepancy may lie in the sensitivity of the *WISE* measurement - W_4 is less sensitive than MIPS24, and thus the *WISE* measurement may be in error.

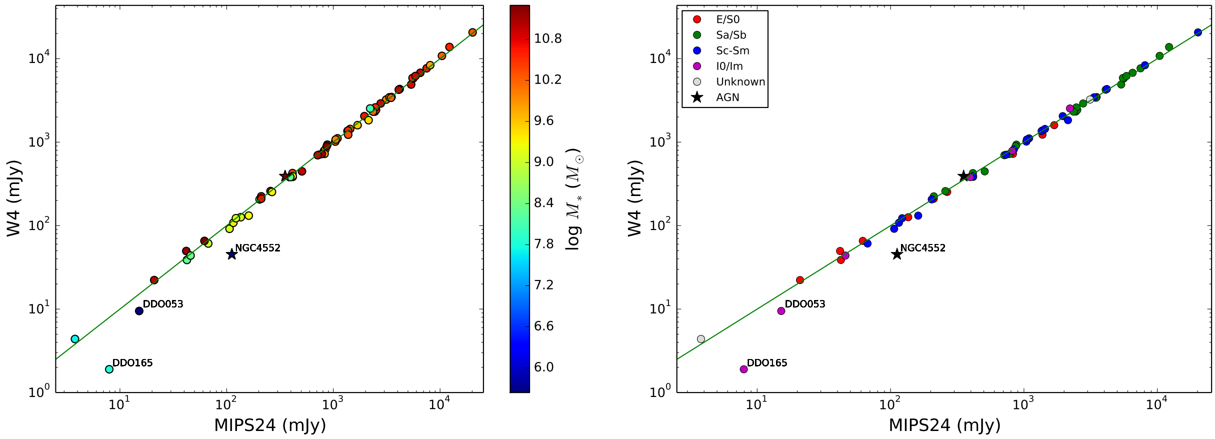

Figure 4.3: *Variation of the isophotal* WISE *22 μm flux in relation to* Spitzer *24 μm flux; colour-coded by stellar mass (left) and morphology (right). The green line is the 1:1 line. Highlighted sources: Table 4.7.*

4.3 W_3 vs IRAC4 comparison

One of the main questions that this thesis addresses is the difference between IRAC4 and W_3, and if the PAH differences can be discerned. This could teach us about PAH molecules as a star formation tracer.
Figure 4.4 compares the luminosities from the *WISE* 12μm band and *Spitzer* 8μm band, with the stellar continuum contribution subtracted. W_3 traces several different features, amongst them the forbidden neon lines [Ne II] at 12.8 μm and [Ne III] at 15.5 μm (Hemachandra et al. 2015), silicate absorption at 10 μm, and the 11.3 μm PAH (see section 1.5) molecule. The IRAC4 band, on the other hand, consists largely of PAH emission at 7.7μm. This PAH is highly energized, and thus traces star formation (Calzetti et al. 2007). The molecules' charge also plays a role in which wavelength is emitted: the 11.3 μm emission is most likely produced by neutral PAHs, and the 7.7 μm by cations. Since they measure emission from two different PAH molecules (among other sources in the W_3 case), we do not necessarily expect them to follow a 1:1 relation. However, the PAH molecules are possibly a by-product of the same process, namely star formation. Therefore we do expect some kind of relation between the two luminosities, at least in the case of 'normal' galaxies, which make up most of our sample. The latter expectation is confirmed in Fig. 4.4, as quantified by this relation:

$$log\nu L_{W3} = 0.93(\pm 0.01) log\nu L_{IRAC4} + 0.48(\pm 0.10) \tag{4.4}$$

This suggests that the luminosities of the starlight continuum-subtracted W_3 and IRAC4 correspond to within 10%. This may be purely due to the overlap of the two bands, and not directly related to the two PAH molecules.

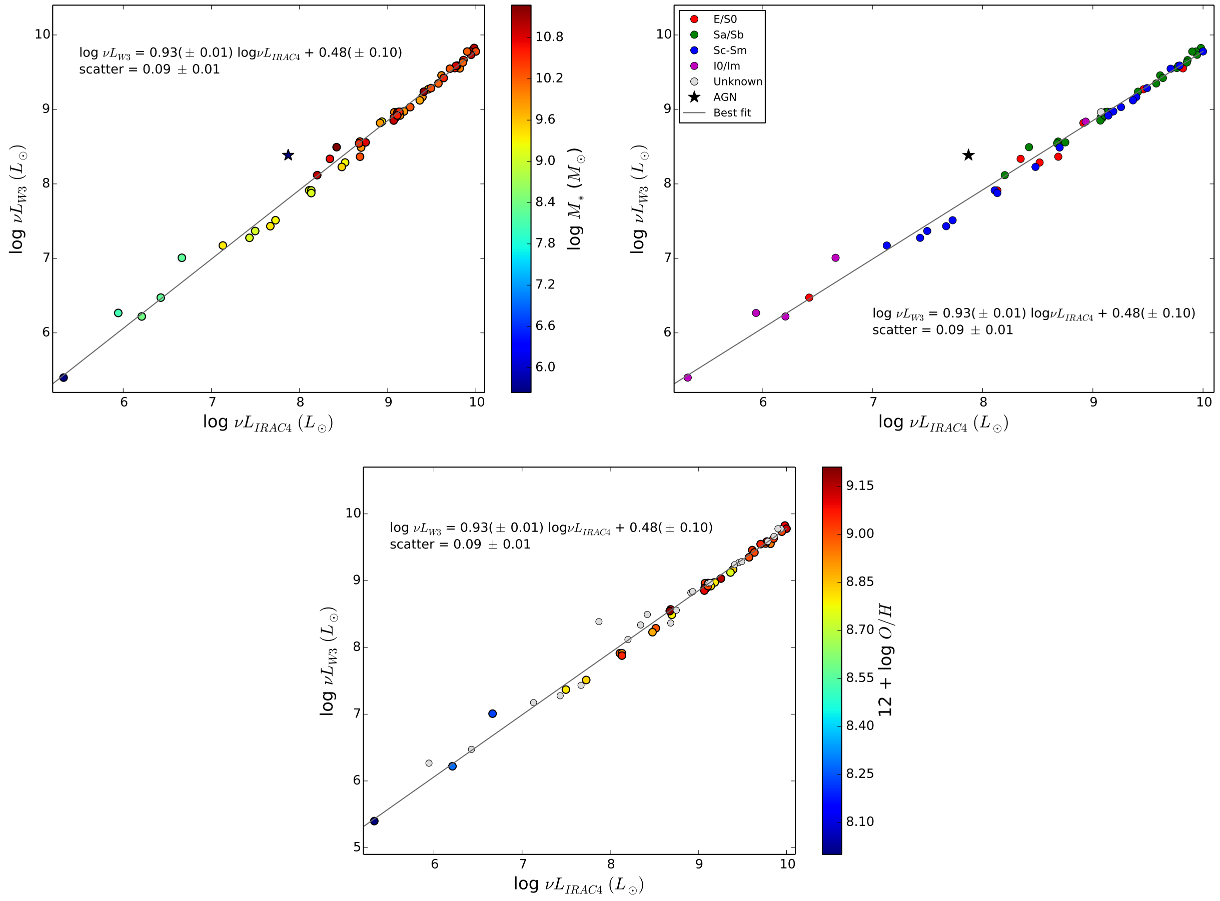

Figure 4.4: *Luminosity comparison between the stellar continuum-subtracted W_3 and IRAC4. Error bars are generally smaller than points. Top left: Colour-coded by stellar mass. Top right: Colour-coded by morphology. Bottom left: Colour-coded by metallicity (oxygen abundances from Kobulnicky & Kewley 2004). Grey points are those sources for which we did not have oxygen abundance data.*

It is apparent from the morphology (top right) plot that galaxies with the highest luminosity values in these two bands tend to be both early- and late-type spirals. There are also early type (elliptical/lenticular) galaxies in this region. There is no discernible trend with the morphologies, but the stellar mass (top left) plot makes it plain that the higher-mass galaxies have the higher luminosities. The same trend is observed with the metallicity - the higher luminosities belong to the higher-metallicity galaxies.

The fit is reasonable within our entire mass range which runs from 10^6 - 10^{11} $M_\odot$, as well as in the global galaxy metallicity range[15] $8.0 - 9.2$. It is surprising that the fit applies to 'normal' galaxies as well as the low surface brightness, low metallicity dwarfs. This is a remarkable result, since dwarf galaxies usually do not follow the same trends as normal galaxies in terms of luminosities and star formation (eg. Narayanan 2016).

Thus far we have ascertained that the *WISE* and *Spitzer* measurements are consistent. This is expected due to the band overlap of both the W_4 with MIPS24; and the W_3 with IRAC4 seen in figure 1.1. This may suggest, in the case of the PAH bands W_3 and IRAC4, that the correlation between them is purely an effect of the bandpasses, and has no physical significance to our galaxies.
Nonetheless, the *WISE* bands may still be good star formation indicators. The next section investigates this.

4.4 *Spitzer* star formation relations

As another means of comparing the *WISE* and *Spitzer* photometry, we formulate star formation relations in terms of the IRAC4 and MIPS24 luminosities to see how it compares to our *WISE* relations (see section 4.6).

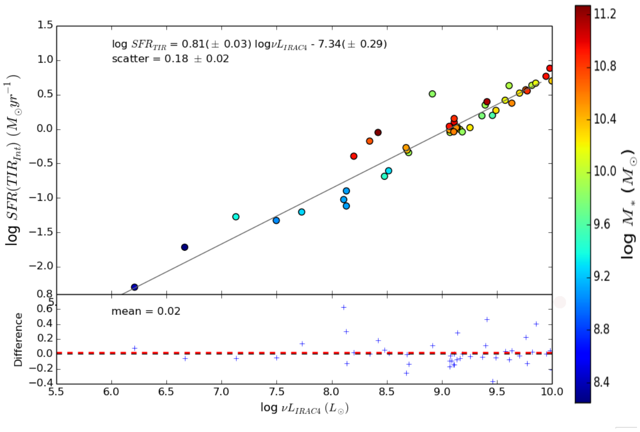

Figure 4.5: *SFR* (1.1) *comparison with stellar continuum-subtracted IRAC4 luminosity, with residual plots below. TIR is determined from integrating under the SED fits in Draine & Li* (2007). *Colour-coded by stellar mass (left) and morphology (right). Residuals: Excluding the AGN, differences are the y-value of the fitted line subtracted from the y-value of the point. The red dashed line indicates the mean difference.*

Figure 4.5 depicts the relationship between the SFR (TIR from Draine & Li 2007) and the broadband, stellar continuum-subtracted IRAC4 luminosity at $8\mu m$. As expected, there is a definite correlation, with small differences. The relation in this case is:

$$logSFR_{TIR} = 0.81(\pm 0.03)log\nu L_{IRAC4} - 7.34(\pm 0.29) \tag{4.5}$$

There are only a few AGN hosts in our sample, but the absence of these sources in these plots is notable. Since the $7.7\mu m$ PAH contributes to the IRAC4 flux, a possible reason for this is that AGN destroy PAHs in the galaxies in which they reside (Smith et al. 2007). The vertical scatter for this relation is 18%, and the error in the intercept is 29%, which are both larger than in the W_3 relation (15%, 22% respectively). This suggests that W_3 is measuring the star formation more robustly than IRAC4.

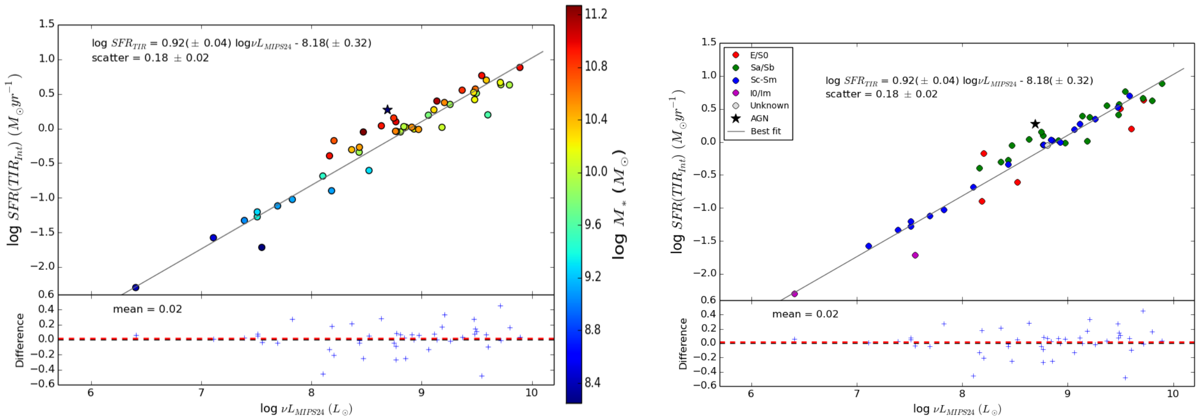

Figure 4.6: *SFR* (1.1) *comparison with MIPS24 luminosity, with residual plots below. TIR is determined from integrating under the SED fits in Draine & Li* (2007). *Colour-coded by stellar mass (left) and morphology (right). Residuals: Excluding the AGN, differences are the y-value of the fitted line subtracted from the y-value of the point. The red dashed line indicates the mean difference.*

Similar to figure 4.5 above, figure 4.6 depicts the relationship between the SFR from the TIR (Draine & Li 2007) measurements and the broadband MIPS24 luminosity at $24\mu m$. Since warm dust emitting at $24\mu m$ is a good tracer of star formation, we expect a clear correlation with small-magnitude residuals, and this is indeed the case. Also noteworthy is the fact that there is an AGN (NGC1316/Fornax A) in the plots that was not present in figure 4.5. The relation in this case is:

$$logSFR_{TIR} = 0.92(\pm 0.04)log\nu L_{MIPS24} - 8.18(\pm 0.32) \tag{4.6}$$

The vertical scatter for this relation is 18%, and the error in the intercept is 32%. The scatter is marginally better than the W_4 case (see figure 4.8), but the error in the intercept is the same. This suggests that W_4 is as good an indicator as MIPS24.

4.5 *WISE*-TIR luminosity calibration

As explained in section 1.6.1, our chosen star formation metric is the total infrared luminosity L_{TIR}. It probes the average, long-term dust-obscured star formation of the galaxy. We calibrated the two *WISE* star formation indicators in terms of the L_{TIR} to test their suitability as star formation indicators. If it was found that they each behaved similarly to the L_{TIR}, in other words, increasing when L_{TIR} increases and vice versa, then they would be suitable star formation indicators and can be used in our relations.

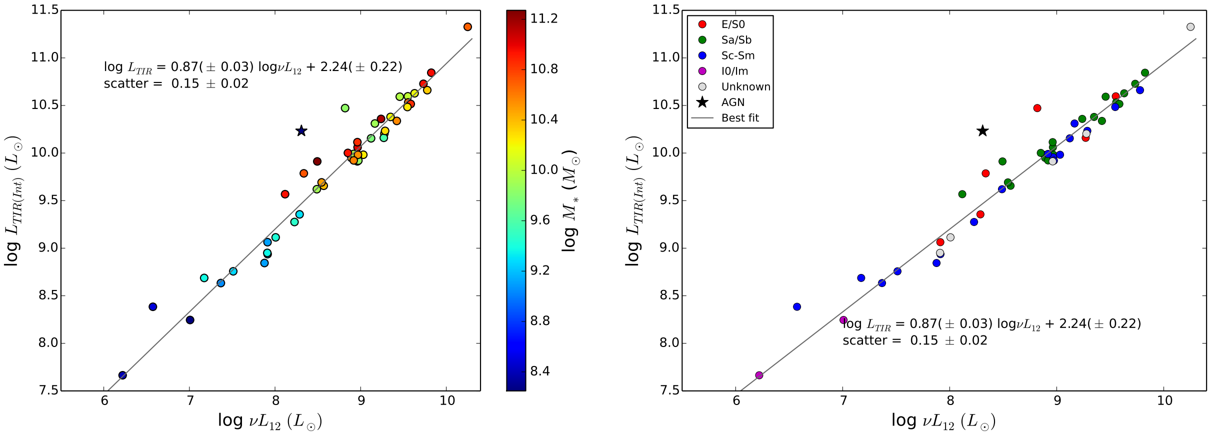

Figure 4.7: *Variation of the stellar continuum-subtracted* W_3 *and TIR luminosities. TIR is determined from integrating under the SED fits in Draine & Li (2007), colour-coded by stellar mass (left) and morphology (right). Best-fit line and scatter statistics obtained from HyperFit (Robotham & Obreschkow 2015). Error bars are generally smaller than points.*

These plots answer the question whether the $12\mu m$ luminosity behaves similarly to the TIR luminosity, and thus is a good indicator of the star formation. There is a definite correlation between the $12\mu m$ and the TIR luminosities, which is quantified by the relation:

$$logL_{TIR} = 0.87(\pm 0.03)log\nu L_{12} + 2.24(\pm 0.22) \tag{4.7}$$

The vertical scatter in the data is 15%, while the error in the intercept of the best-fit line is 22%, which is considerable. The magnitude of the error might in part be due to the limited quantity of points; but is also likely due to the nature of the relation linking the MIR to the far-infrared (FIR).

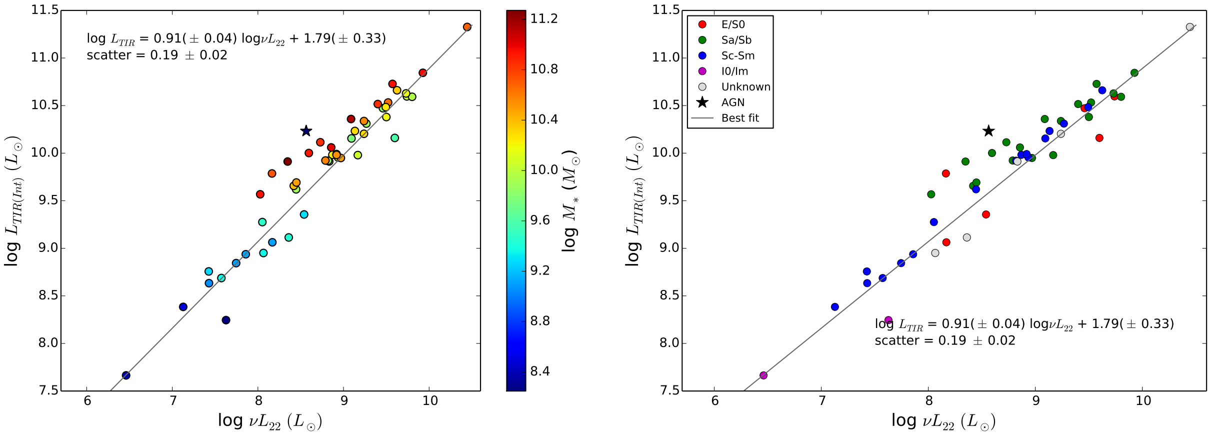

Figure 4.8: *Variation of the 22 μm dust and TIR luminosities. TIR is determined from integrating under the SED fits in Draine & Li (2007), colour-coded by stellar mass (left) and morphology (right). Error bars are generally smaller than points.*

Figure 4.8, similar to figure 4.7 above, illustrates that the $22\mu m$ luminosity behaves similarly to the TIR luminosity of the galaxy.

$$logL_{TIR} = 0.91(\pm 0.04)log\nu L_{22} + 1.79(\pm 0.33) \tag{4.8}$$

The correlation is clear, but the scatter is larger (19%) than the TIR-12μm (15%) relation. This is surprising - we expect greater scatter in the W_3 due to the width of the band. This large scatter in the W_4 may be due to the band's poorer sensitivity. The error in the intercept of the best-fit line (HyperFit; Robotham & Obreschkow 2015) is 33%, which is considerable.

The biggest contributor to the TIR flux is the FIR 'bump' (see figure 1.3) which characterizes the cold dust in the galaxy. The 22μm measurement, once the stellar component has been subtracted, characterizes the emission from warm dust in the galaxy. Thus, figure 4.8 suggests that the more warm dust present in the galaxy, the more cold dust is present in the long term as well. This makes intuitive sense - the dust present in the galaxy is heated by radiation from stars, emits in the 22μm band, then steadily cools down via blackbody radiation to emit in the FIR.

4.6 Comparison of star formation relations

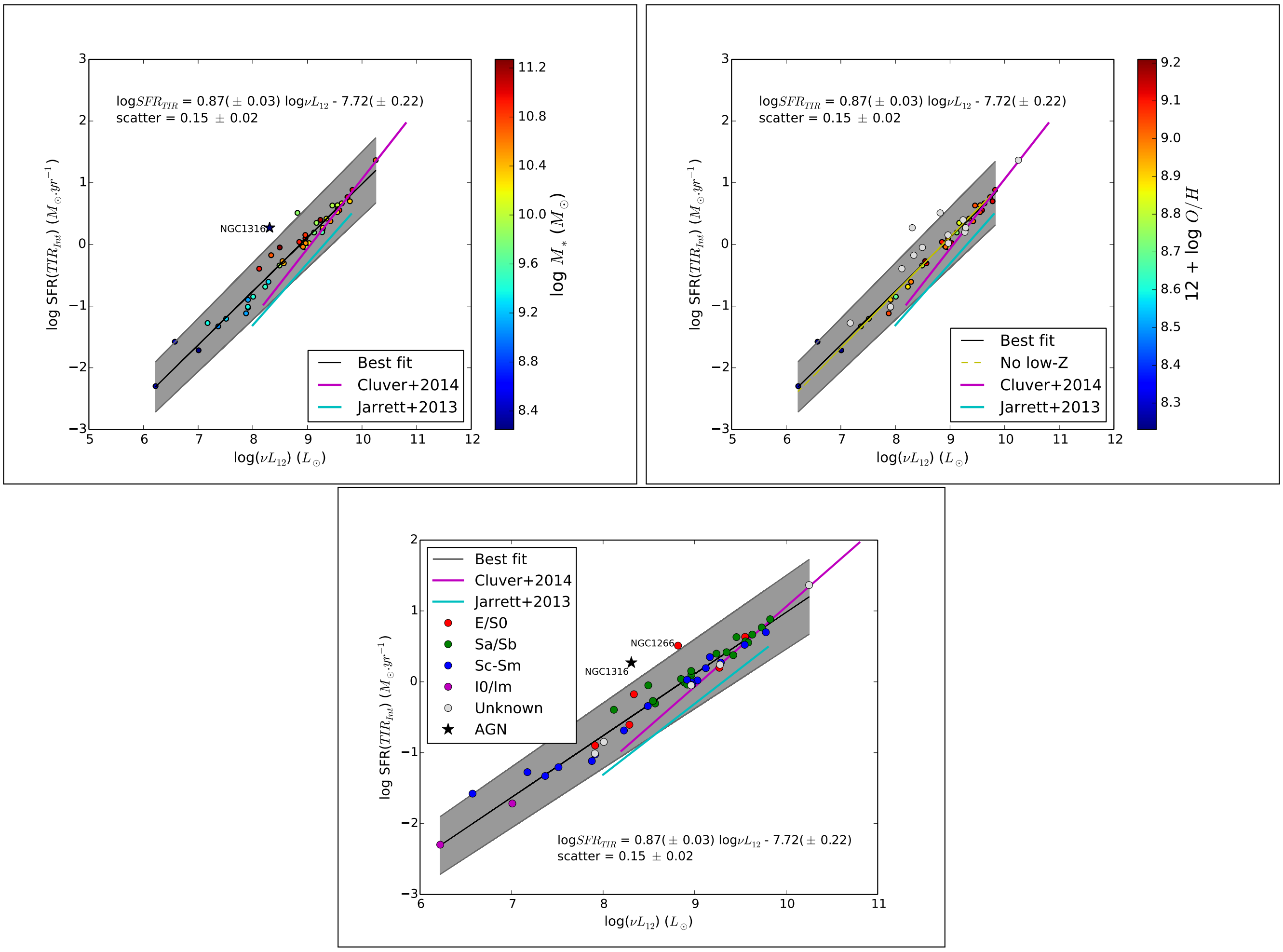

Figure 4.9: *SFR (1.1) comparison with W_3 luminosity. Plotted as well are SFR relations from Cluver et al. 2014 (B.3) and Jarrett et al. 2013 (B.5). Error bars are generally smaller than points. The shaded region lies between the minimum and maximum lines of best-fit (HyperFit; Robotham & Obreschkow 2015), i.e. the fit when the errors in the slope and intercept are incorporated. Thus, if a point lies in the shaded region, it lies within the parameters of our fit. Top left: Colour-coded by stellar mass. Top right: Colour-coded by metallicity (oxygen abundances from Kobulnicky & Kewley 2004). Grey points are those sources for which we did not have oxygen abundance data. The dashed yellow line is the best-fit relation for all the points excluding the three lowest-metallicity galaxies (IC2574, NGC2915, NGC5408). Bottom: Colour-coded by morphology.*

The best-fit (HyperFit; Robotham & Obreschkow 2015) line fits well for our entire stellar mass range, and thus all the different morphologies; as well as our entire metallicity range[15]. It is also apparent that our relation is comparable to the Jarrett and Cluver relations, but improves upon them in mass- (10^6 - 10^{11} $M_\odot$), metallicity- ($8.0 - 9.2$), and W_3 luminosity (10^6 - 10^{11} $L_\odot$) range.

Since the fitting was done without the AGN data points, it is no surprise that one of the outliers is NGC1316, also known as Fornax A. The other outlier is NGC1266; this suggests it might host an AGN.
Another notable feature is the yellow dashed line in the top-right hand plot. This is the best-fit line if the three galaxies with lowest metallicity are excluded. It appears that the low-metallicity dwarfs have a negligible effect on our relation.

---

[15] $12 + log(O/H)$

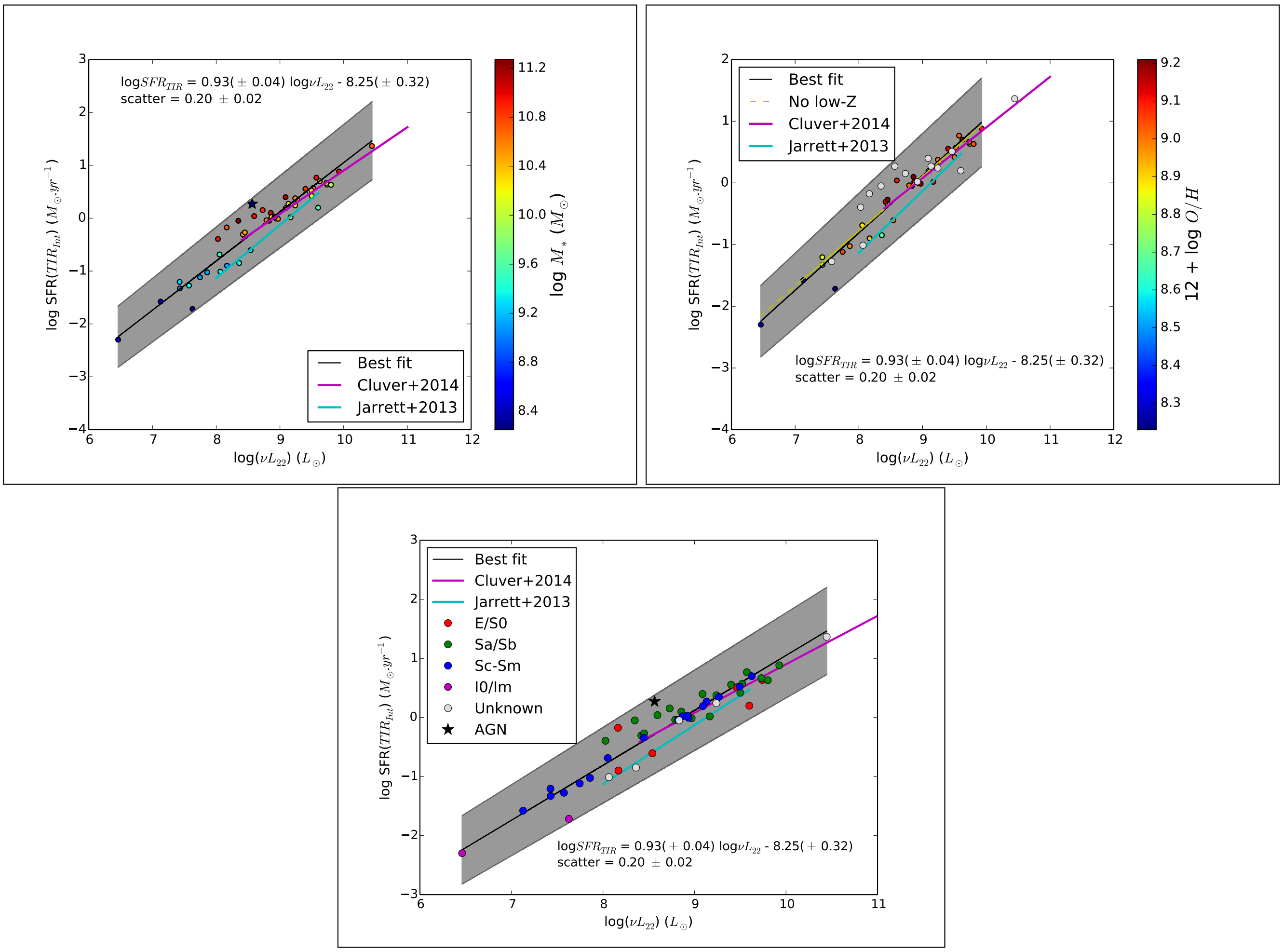

Figure 4.10: *SFR* (1.1) *comparison with* W_4 *luminosity. Plotted as well are SFR relations from Cluver et al. 2014* (B.4) *and Jarrett et al. 2013* (B.6)*. Error bars are generally smaller than points. The shaded region lies between the minimum and maximum lines of best-fit, i.e. the fit when the errors in the slope and intercept are incorporated. Thus, if a point lies in the shaded region, it lies within the parameters of our fit (HyperFit; Robotham & Obreshkow 2015). Top left: Colour-coded by stellar mass. Top right: Colour-coded by metallicity (oxygen abundances from Kobulnicky & Kewley 2004). Grey points are those sources for which we did not have oxygen abundance data. The dashed yellow line is the best-fit relation for all the points excluding the three lowest-metallicity galaxies (IC2574, NGC2915, NGC5408). Bottom: Colour-coded by morphology.*

The best-fit (HyperFit; Robotham & Obreschkow 2015) line fits well for our entire stellar mass range (10^6 - 10^{11} $M_\odot$), and thus all the different morphologies; as well as our entire metallicity[15] range[15] ($8.0 - 9.2$).
It is also apparent that our relation is comparable to the Jarrett and Cluver relations, but improves upon them in mass- (10^6 - 10^{11} $M_\odot$), metallicity- ($8.0 - 9.2$), and W_4 luminosity ($\sim 10^6$ - 10^{11} $L_\odot$) range.
Another notable feature of this set of plots is the vertical scatter - it is greater (20%) than in the W_3 case (15 %; see figure 4.9). This is surprising, W_4 is expected to have less scatter than W_3, since W_3 is such a broad band. This large scatter is most likely due to the poor sensitivity of the W_4 band.

4.6.1 This work's *WISE* star formation relations

In this work, we have described the data predominantly drawn from the SINGS and KINGFISH surveys; verified that the TIR flux is indeed a good indicator of star formation, and hence arrived at the following relationships between the *WISE* 12 and 22μm flux and SFR (see figures 4.9 and 4.10 respectively):

$$log_{10}SFR_{TIR}(M_{\odot}\,yr^{-1}) = 0.87(\pm 0.03)log_{10}\nu L_{12}(L_{\odot}) - 7.72(\pm 0.22) \tag{4.9}$$

$$log_{10}SFR_{TIR}(M_{\odot}\,yr^{-1}) = 0.39(\pm 0.04)log_{10}\nu L_{22}(L_{\odot}) - 8.25(\pm 0.32) \tag{4.10}$$

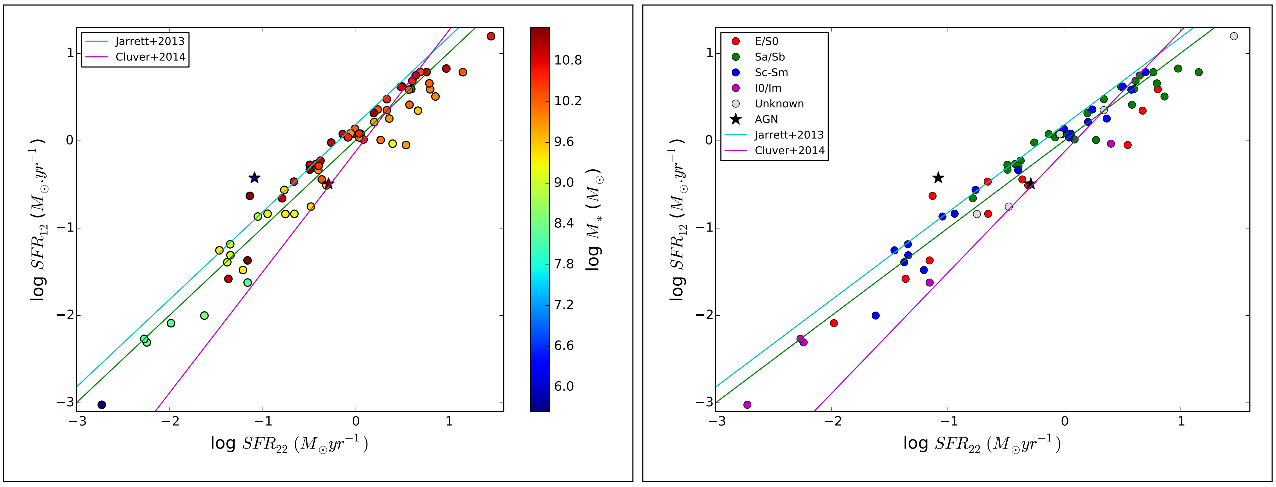

Figure 4.11: *Comparison of our star formation rates, from the 11.3 µm PAH (among possible other sources*[16]*) flux* (4.9) *and warm dust* (4.10) *fluxes, colour-coded by stellar mass (left) and morphology (right). Green line is 1:1 line. Error bars are generally smaller than points.*

Figure 4.11 is a comparison of our two relations. Since the fitted lines are the best-fit for the entire sample, we expect them to be in good but not perfect agreement, which is indeed the case. Since our relation is flatter than the Cluver relation, we will get systematically larger SFRs for dwarfs. This was expected since the sample used to formulate the Cluver relation excluded dwarf galaxies.

It is interesting that the relations seem to converge most closely at higher SFRs, around $10^{0.5} \simeq 3\ M_{\odot}yr^{-1}$. The points in this region are among the furthest from the green 1:1 line, but since their masses and morphologies are diverse, there is no discernible pattern or reason for the disparity.

---

[16] see section 1.5

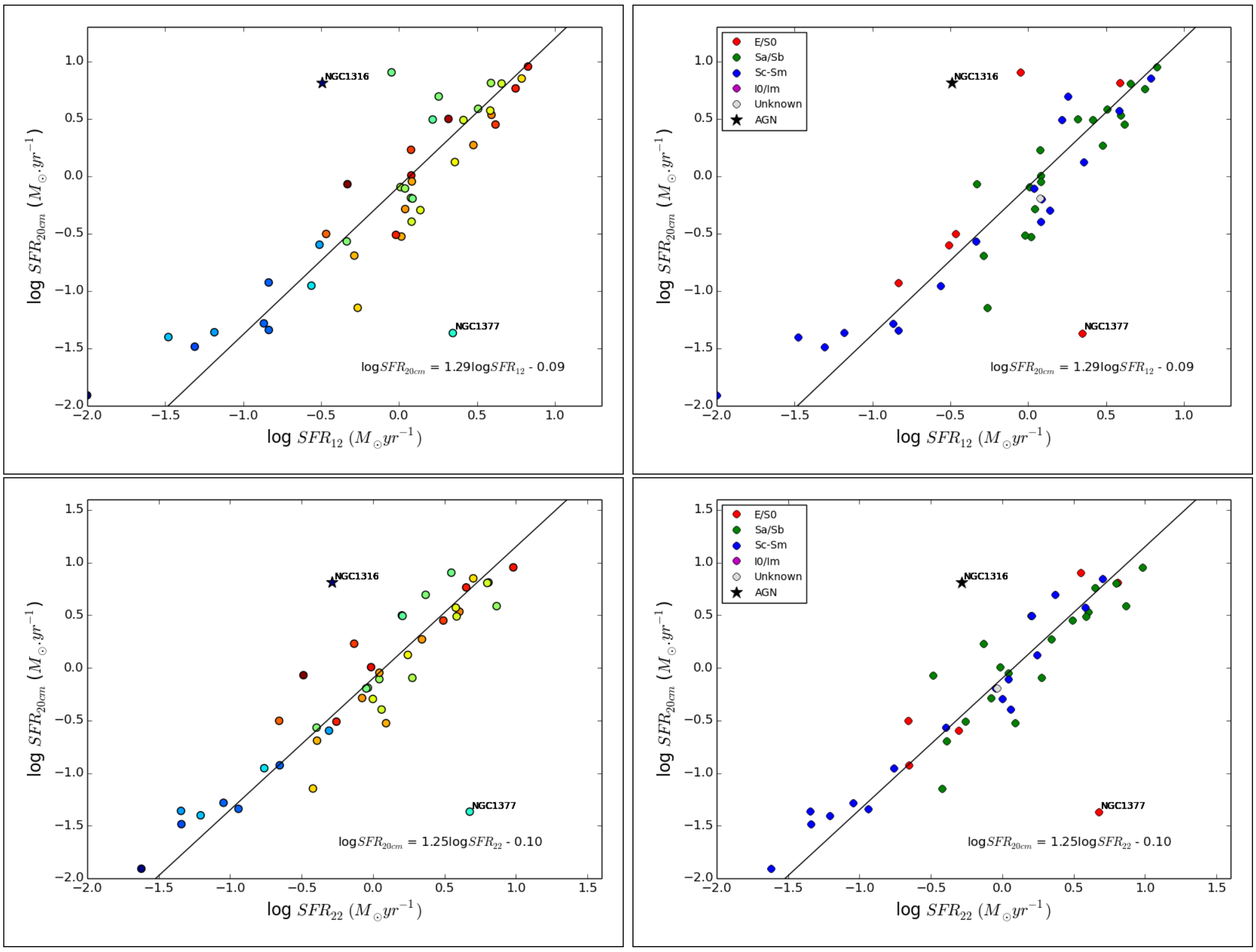

Figure 4.12: *Comparison of our star formation rates with those from radio continuum* (B.1)*. Top: 20cm vs 12μm (PAHs possibly combined with other sources) SFR* (4.9)*. Bottom: 20cm vs 22μm warm dust SFR* (4.10)*. Colour-coded by stellar mass (left) and morphology (right). Error bars are generally smaller than points. Highlighted sources: Table 4.7.*

Figure 4.12 is a comparison between our two relations and SFRs obtained from SINGS[17] 20cm radio continuum fluxes. The radio SFR traces the supernova remnants of massive stars, that, although they have "died", that is, undergone a supernova explosion, are still considered young enough (in the case of massive stars, this occurs after ∼ 10 million years) to be considered star formation. The correlation between radio and infrared fluxes is well-known (Condon 1992) and thus this comparison is useful.

The comparison for the most part is quite favourable and suggests that our relations are consistent with the radio results. There is, however, a systematic difference - the *WISE* SFR is consistently larger than the radio SFR by ∼ 20%. Also noteworthy is that the reasonable comparison holds true across our entire mass (10^6 - 10^{11} $M_{\odot}$) and morphology ranges.
The two outliers are NGC1316, the brightest radio galaxy in the Fornax galaxy cluster, which hosts a powerful AGN; and NGC1377, a lenticular galaxy, which likely has a significant dust lane but a negligible amount of massive star formation happening within the galaxy.

---

[17] Either from VLA or WSRT (Kennicutt et al. 2003).

4.7 Summary

In this chapter, the majority of our results and analysis has been presented. We've discovered that the *WISE* and *Spitzer* bands containing PAH emission, namely W_3 and IRAC4, behave similarly. Since the IRAC4 broadband flux is correlated with its PAH emission at $7.7\mu m$, this suggests that the $11.3\mu m$ PAH contribution is correlated with and may dominate the W_3 broadband flux.

We've calibrated the luminosity from the 12 and $22\mu m$ *WISE* bands with respect to the TIR luminosity, and formulated new relations based on this calibration. We've compared these new relations with other measures of SFR, and found that they behave similarly and are thus reliable relations.

Chapter 5

Conclusions

The main objectives of this thesis are twofold: to ascertain the reliability of the *WISE* star formation indicators; as well as investigate the link between PAH molecules and star formation.

The first objective was achieved by calibrating our two *WISE* indicators, W_3 and W_4, in terms of the total infrared luminosity (L_{TIR}); and the second was achieved by comparing the *Spitzer* and *WISE* luminosities: in particular IRAC4 and W_3, since they contain the $7.7\mu m$ and $11.3\mu m$ PAH emission respectively.

These required a sample of galaxies that had both *WISE* and *Spitzer* photometry for the PAH investigation, as well as far infrared data from *Herschel* to make the L_{TIR} calibration possible. Thus, we chose 74 galaxies from the *Spitzer* surveys SINGS and KINGFISH, with the additions of M82 and M87, that fulfilled our requirements.

The two bands that are of interest in our study of PAH molecules, namely the IRAC4 band with the $7.7\mu m$ PAH contribution and the W_3 band with the $11.3\mu m$ PAH contribution (among other possible sources[1]), have been found to be correlated, but not have a one-to-one relation (4.4). This is the kind of behaviour we would expect from the PAH luminosities *alone*, since they are two different molecules, but are presumably the by-product of the same processes. Since the IRAC4 broadband flux is correlated with its PAH emission at $7.7\mu m$(see 1.5), this suggests that the $11.3\mu m$ PAH contribution is correlated with and may dominate the W_3 broadband flux. This also implies that possible contaminates (see section 1.7) do not seem to have an effect on our results.
On the other hand, the correlation could be due to the overlap between the two bands. The warm dust contribution was not subtracted from the two bands and could be contributing towards the strong correlation.

Star formation relations in terms of the two *Spitzer* indicators, i.e. the continuum-subtracted IRAC4 luminosity and the MIPS24 luminosity (see figures 4.5, 4.6 respectively), suggest that both are also possible star formation tracers since there is a definite trend between the two parameters in the plots, quantified by the relations:

$$logSFR_{TIR} = 0.81(\pm 0.03) log\nu L_{IRAC4} - 7.34(\pm 0.29)$$
$$logSFR_{TIR} = 0.92(\pm 0.04) log\nu L_{MIPS24} - 8.18(\pm 0.32)$$

The vertical scatter for both the IRAC4 and the MIPS24 relation is 18%. A comparison of the two SFR-IRAC4 plots shows that the highest-mass galaxies in our sample are early-type spirals.

We have seen that both *WISE* star formation indicators behave similarly to the TIR luminosity, and are thus reliable star formation tracers.
Accordingly, we have determined two SFR relations, one for W_3 and another for W_4 (see figures 4.9, 4.10 respectively):

$$\boxed{\begin{array}{l} log_{10}SFR_{TIR}(M_{\odot}yr^{-1}) = 0.87(\pm 0.03) log_{10}\nu L_{W3}(L_{\odot}) - 7.72(\pm 0.22) \\ log_{10}SFR_{TIR}(M_{\odot}yr^{-1}) = 0.93(\pm 0.04) log_{10}\nu L_{W4}(L_{\odot}) - 8.25(\pm 0.32) \end{array}}$$

The vertical scatter in the IRAC4 relation is 18%, and the error in the intercept is 29%, which are both larger than in the W_3 relation (15%, 22% respectively). This suggests that W_3 is measuring the star formation more robustly than IRAC4.
When comparing the MIPS24 statistics with that of W_4 , the vertical scatter for the MIPS24 relation is 18% which is

---

[1] see section 1.3

slightly lower than the W_4 scatter at 19%, and the error in the intercept in both cases is 32%. This suggests that W_4 is as good an indicator as MIPS24.
The vertical scatter is greater in the W_4 case (20%) than in the W_3 case (15%). The error in the intercept in the W_4 relation is also greater (32%) than in the W_3 case (22%). In other words, W_3 is a more precise tracer than W_4, at least for our sample. This is opposite to what we expect, and is most likely due to the poor sensitivity of the W_4 band.

Our new relations ((4.9) and (4.10)) are comparable with previous works, but also improve upon them in mass- (10^6 - 10^{11} $M_\odot$), metallicity- ($8.0 - 9.2$), and luminosity ($\sim 10^6$ - 10^{11} $L_\odot$ for both W_3 and W_4) range. Excluding the lowest-metallicity galaxies has a negligible effect on the fit.

We have tested these new relations and found that the two relations converge at higher SFRs (see figure 4.11), around the value of 3 $M_\odot . yr^{-1}$. The new relations also largely agree (with some scatter) with SFRs determined from radio continuum fluxes (see figure 4.12), which suggests that our relations are reliable.

Chapter 6

References

- Allamandola, L.J., Tielens, A.G.G.M., Barker, J.R., 1989, ApJS, 71:733
- Brown, M.J.I., et al. 2014, ApJS, 22:18
- Boselli, A., et al., 2002, A&A, 385:454
- Calzetti, D., et al. 2007, ApJ, 666:870
- Calzetti, D., 2012, `http://arxiv.org/abs/1208.2997v1`
- Carroll, B.W. & Ostlie, D.A., 2006, An Introduction to Modern Astrophysics (2nd Edition), Pearson.
- Cluver, M. et al., 2014, ApJ, 782:90
- Condon, J. J., 1992, ARA&A, 30:575.
- Cordiner, M.A., et al., 2008, A&A, 492:L5
- Cox, N.L.J., et al., 2007, A&A, 470:941
- Dale, D.A., et al., 2009, ApJ. 703:517
- Dale, D.A., et al., 2014, ApJ, 784:83
- Dole, H., et al., 2006, A&A 451:417
- Draine, B.T. & Li, A., 2007, ApJ, 657:810
- Helou, G., et al., 2004, ApJ, 154:253
- Hemachandra, D., et al., 2015, MNRAS, 454:818
- Herwig, F., 2005, ARA&A, 43:435
- Ho, L.C. & Keto, E., 2007, ApJ, 658:314
- Jarrett, T.H., et al. 2012, AJ, 144:68
- Jarrett, T.H., et al., 2013, AJ, 145:6
- Jarrett, T.H., et al. 2017, ApJ, 836:182
- Joblin, C., et al., 2008, A&A, 490:189
- Justtanont, K., et al., 1996, A&A, 309:612
- Kennicutt, R.C., Jr., et al., 2003, PASP, 115:928
- Kennicutt, R.C., Jr., et al., 2011, PASP, 123:1347
- Kennicutt, R.C., Jr. & Evans, N.J., 2012, ARA&A, 50:531
- Kobulnicky, H.A. & Kewley, L.J., 2004, ApJ, 617:240
- Kroupa, P., 2001, MNRAS, 322:231
- Kwok, S. & Zhang, Y., 2013, ApJ, 771:5
- Li, A., & Draine, B.T. 2001, ApJ, 554:778

- Masci, F. 2013, ascl soft, 2010
- Madau, P., & Dickinson, M., 2014, A&A, 52:415
- Narayanan, D., 2016, NatPh, 12:636
- Pilyugin, L.S. & Thuan, T. X., 2005, ApJ, 631:231
- Polletta, M., et al. 2006, ApJ, 642:673
- Polletta, M., et al. 2007, ApJ, 663:81
- Popescu, C.C., et al., 2011, A&A, 527:A109
- Ressler, M.E., et al., 2010, AJ, 410:1882
- Rhee, Y.M., et al., 2007, PNAS, 104:5274
- Robotham, A.S.G., & Obreschkow, D., 2015, PASA, 32:33
- Sellgren, K., 1984, ApJ, 277:623
- Silva, L., et al., 1998, ApJ, 509:103
- Smith, J.D., et al., 2007, ApJ, 656:770
- Werner, M.W., et al., 2004, ApJS, 154:1
- Wickramashinghe, T. & Ukwatta, T.N., 2010, MNRAS, 406:548
- Witt, A.N., et al. 2008, ApJ, 679:497
- Wright, E.L., et al. 2010, AJ, 140:1868
- Van Dyk, S., Werner, M., & Silbermann, N., 2013, *Spitzer* Space Telescope Handbook (version 2.1).
- Yun, M.S., Reddy, N.A. & Condon, J.J., 2001, ApJ, 554:803
- http://ned.ipac.caltech.edu/cgi-bin/objsearch?objname=NGC+300&extend=no&hconst=73&omegam=0.27&omegav=0.73&corr_z=1&out_csys=Equatorial&out_equinox=J2000.0&obj_sort=RA+or+Longitude&of=pre_text&zv_breaker=30000.0&list_limit=5&img_stamp=YES
- http://wise2.ipac.caltech.edu/docs/release/allsky/expsup/sec4_4c.html
- http://www.nasa.gov/mission_pages/spitzer/multimedia/pia14402.html
- https://www.spacetelescope.org/images/heic0819d/
- https://www.spacetelescope.org/images/potw1134a/
- http://www.spitzer.caltech.edu/images/2095-sig07-025-Lifestyles-of-the-Galaxies-Next-Door
- http://www.spitzer.caltech.edu/images/5163-sig12-005-A-Pinwheel-Galaxy-Rainbow
- http://www.spitzer.caltech.edu/news/436-ssc2009-12-NASA-s-Spitzer-Begins-Warm-Mission.
- http://wise2.ipac.caltech.edu/docs/release/allsky/expsup/figures/sec4_4hf5b.gif

Appendix A

Sample images

This appendix contains classifications of our galaxies, as well as the *WISE* and *Spitzer* photometric images of the galaxies in our sample.

The classifications, in the order they appear in the sub-headings, are: morphology from NED; distance from either SINGS or KINGFISH (denoted by D_{KF}) or NED (indicated by footnote 2); luminosity class (if available) from NED; activity type (if available) from NED. The exception is M87, in that instance all details are from NED.

The *WISE* photometric images show, from left to right, a three-colour image (W1+2+3) as well as each of the four *WISE* bands for each galaxy, with the initial images in the top row and the processed images in the bottom row. The *Spitzer* images, from top left to bottom right, show IRAC1 to IRAC4, MIPS24, and a three-colour image (IRAC1+2+4).

In the SEDs, green squares are broadband values from *Spitzer* , blue circles from *WISE* , magenta triangles from SDSS, green circles from 2MASS.

In some cases, the SED curve may not seem to fit the data points. This doesn't affect our main results, however, since the total flux from W_1, W_3 and W_4 were used in the important calculations (such as SFR).

A.1 DDO053: Im; D = 3.5 Mpc; LC V-VI

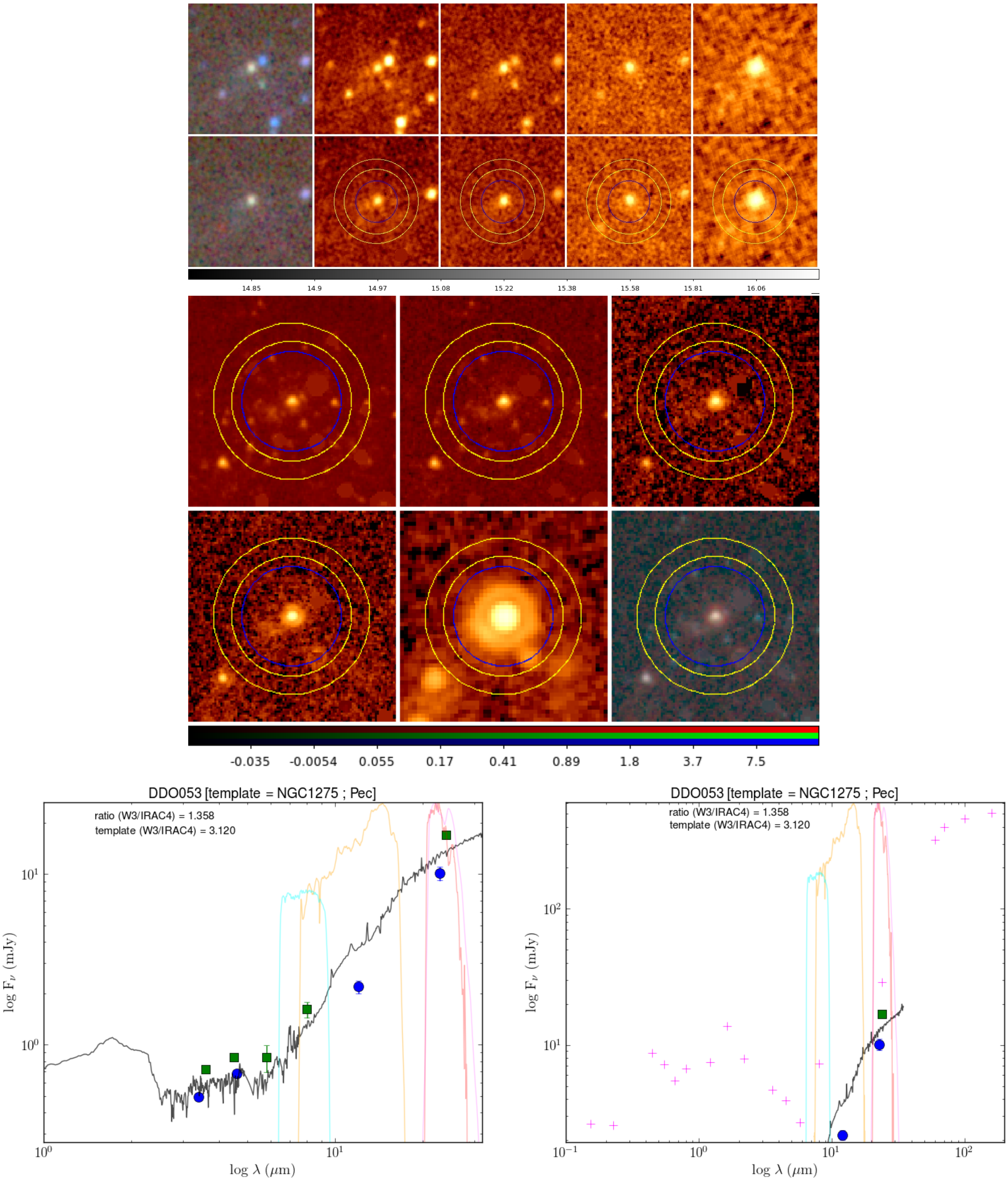

Figure A.1: *Top: WISE imaging of DDO053, unprocessed and processed. Yellow ellipses are sky annulus borders; blue ellipse is 1σ isophotal ellipse. Left to right: Three-colour (W1+2+3); W$_1$; W$_2$; W$_3$; W$_4$. Middle: Spitzer imaging of DDO053. Top left to bottom right: IRAC1, IRAC2, IRAC3, IRAC4, MIPS24, three-colour (IRAC1+2+4). Bottom left: SED of DDO053. Bottom right: SED of DDO053 with all its SINGS data.*

A.2 DDO154: IBm; D = 5.4 Mpc; LC V-VI

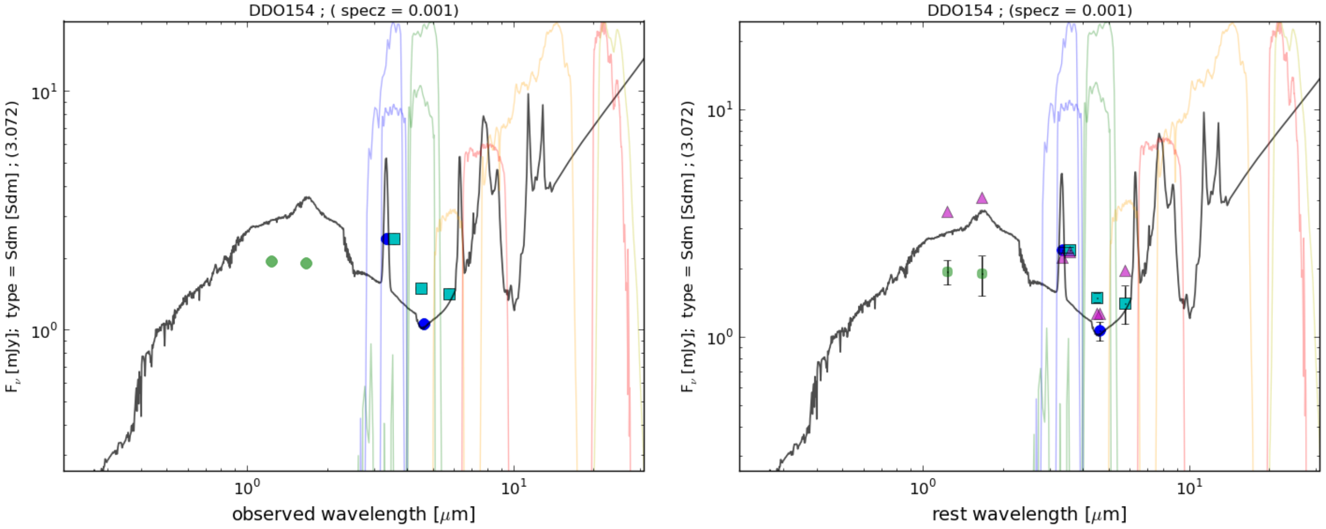

Figure A.2: *Left: SED of DDO154. Right: Rest-wavelength SED of DDO154.*

A.3 DDO165: Im; D = 3.5 Mpc; LC V-VI

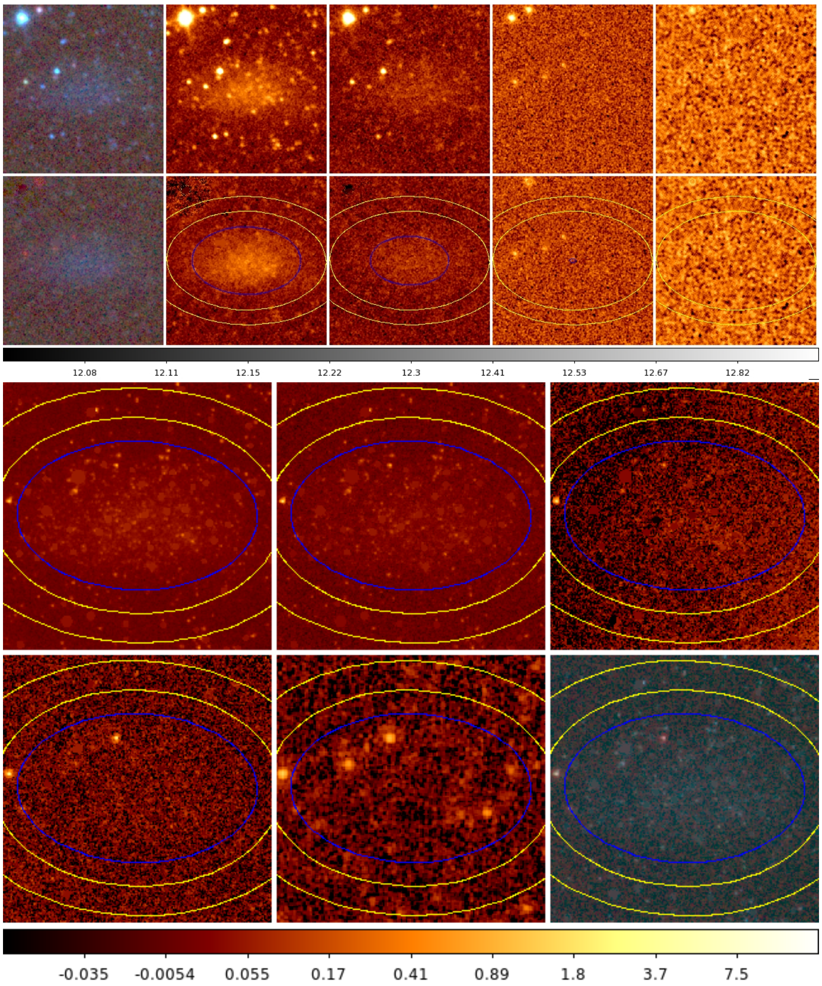

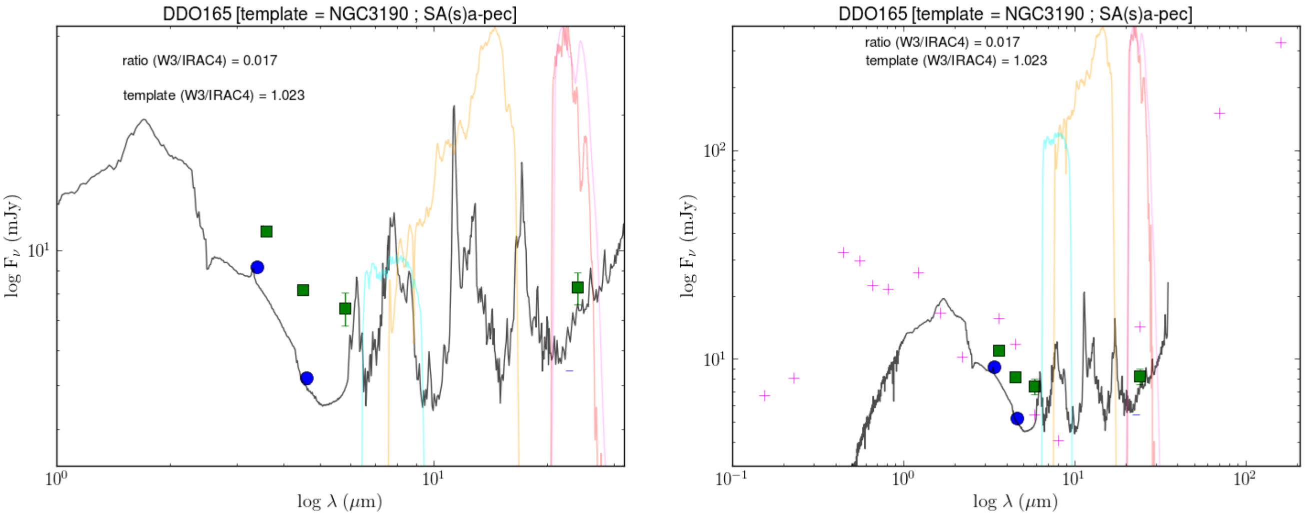

Figure A.3: *Top: WISE imaging of DDO165, unprocessed and processed. Yellow ellipses are sky annulus borders; blue ellipse is 1σ isophotal ellipse. Left to right: Three-colour (W1+2+3); W_1; W_2; W_3; W_4. Middle: Spitzer imaging of DDO165. Top left to bottom right: IRAC1, IRAC2, IRAC3, IRAC4, MIPS24, three-colour (IRAC1+2+4). Bottom left: SED of DDO165. Bottom right: SED of DDO165 with all its SINGS data.*

A.4 IC0342: SABcd; D_{KF} = 3.28 Mpc; LC III-IV; Activity: HII/Sbst

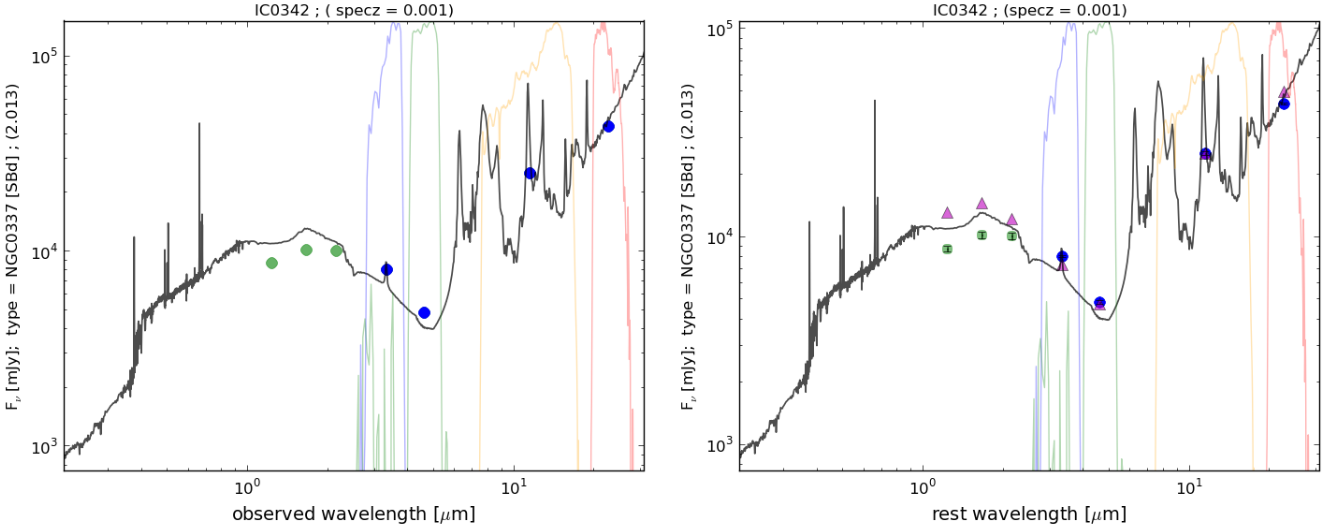

Figure A.4: *Left: SED of IC342. Right: Rest-wavelength SED of IC342.*

A.5 IC2574: SAB(s)m; D = 3.5 Mpc; LC V; Activity: HII

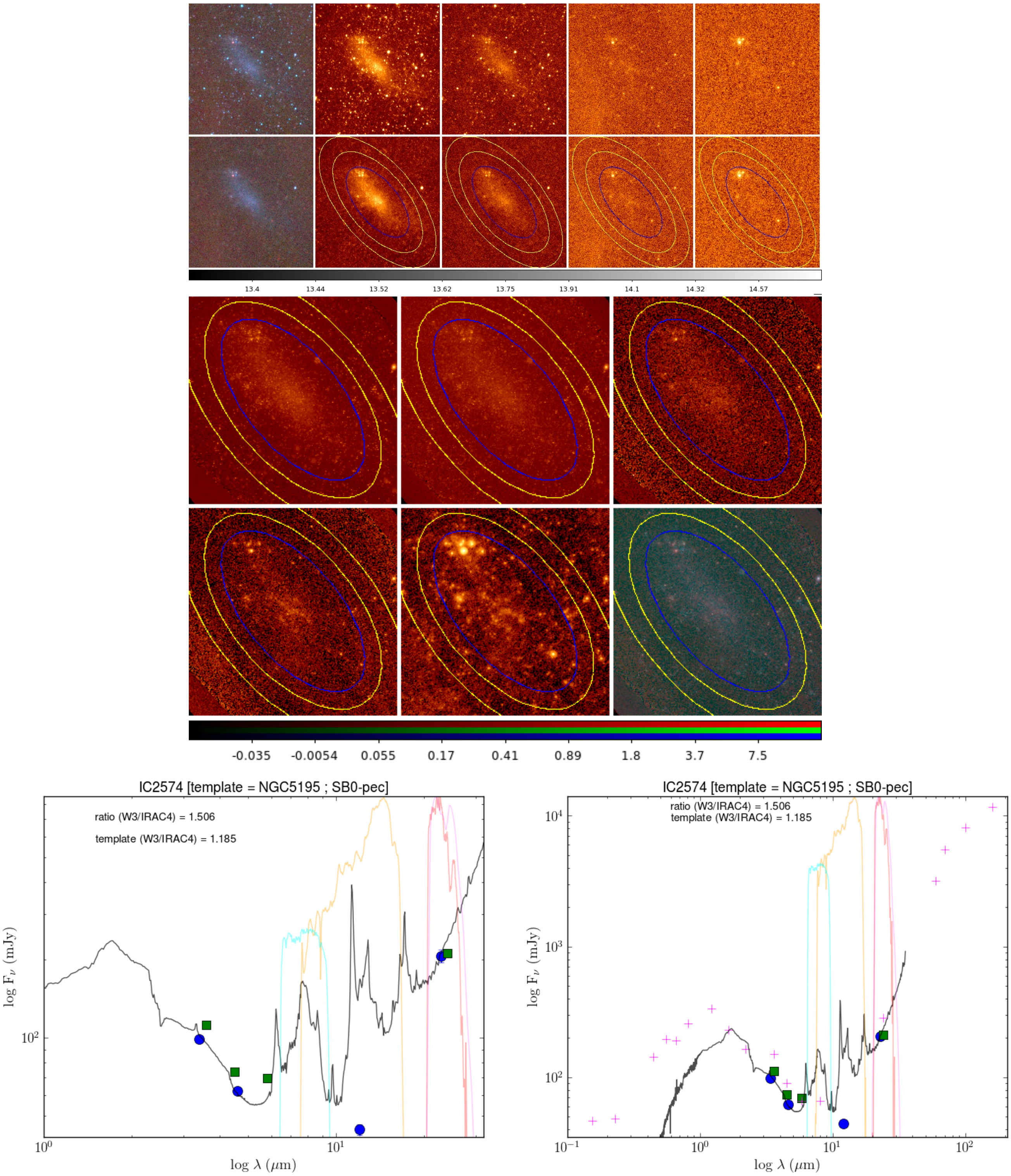

Figure A.5: *Top: WISE imaging of IC2574, unprocessed and processed. Yellow ellipses are sky annulus borders; blue ellipse is 1σ isophotal ellipse. Left to right: Three-colour (W1+2+3); W_1; W_2; W_3; W_4. Middle: Spitzer imaging of IC2574. Top left to bottom right: IRAC1, IRAC2, IRAC3, IRAC4, MIPS24, three-colour (IRAC1+2+4). Bottom left: SED of IC2574. Bottom right: SED of IC2574 with all its SINGS data.*

A.6 IC4710: SB(s)m; D = 8.5 Mpc; LC V; Activity: HII

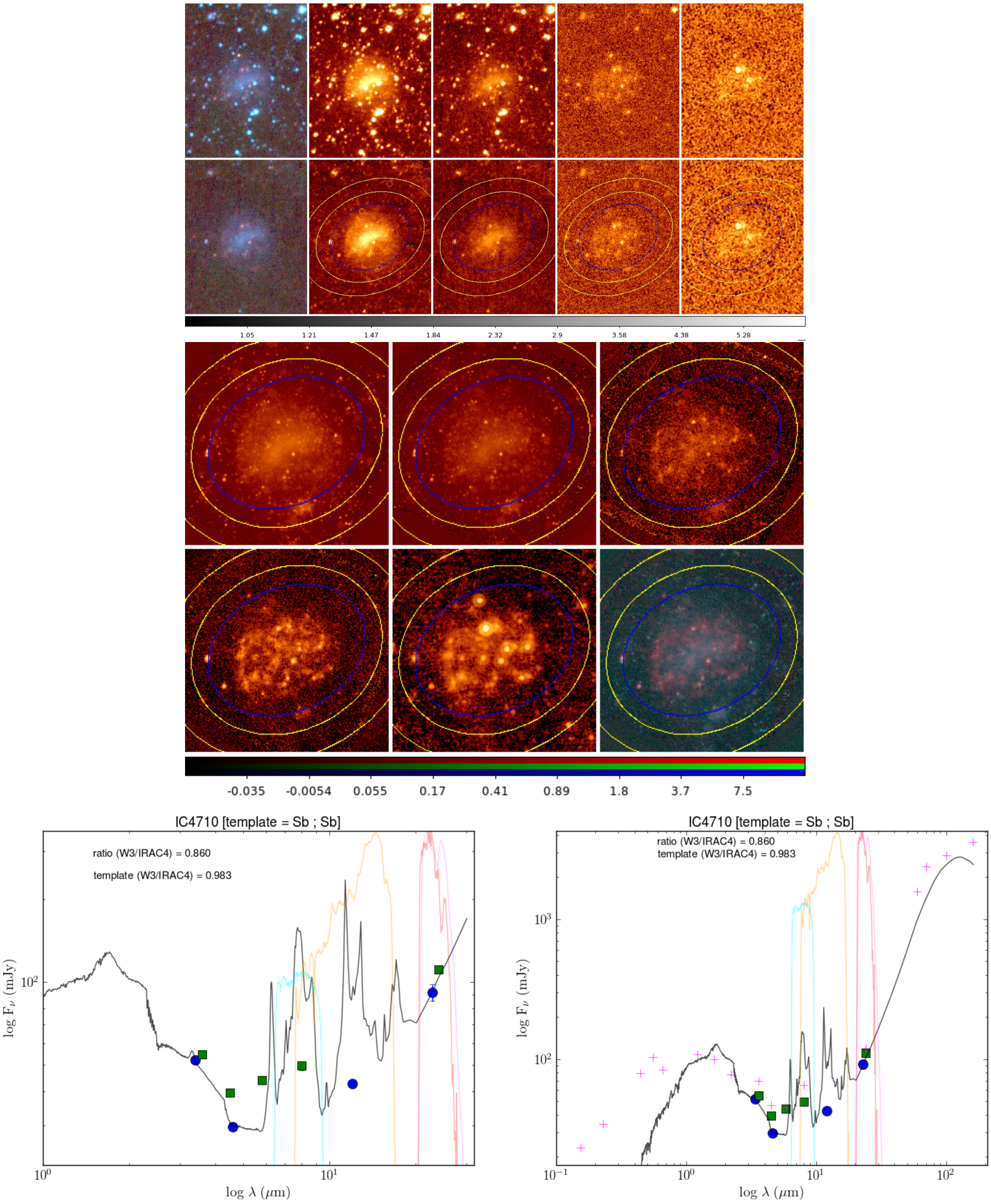

Figure A.6: *Top: WISE imaging of IC4710, unprocessed and processed. Yellow ellipses are sky annulus borders; blue ellipse is 1σ isophotal ellipse. Left to right: Three-colour (W1+2+3); W$_1$; W$_2$; W$_3$; W$_4$. Middle: Spitzer imaging of IC4710. Top left to bottom right: IRAC1, IRAC2, IRAC3, IRAC4, MIPS24, three-colour (IRAC1+2+4). Bottom left: SED of IC4710. Bottom right: SED of IC4710 with all its SINGS data.*

A.7 M81DwB: Im; D = 3.5 Mpc

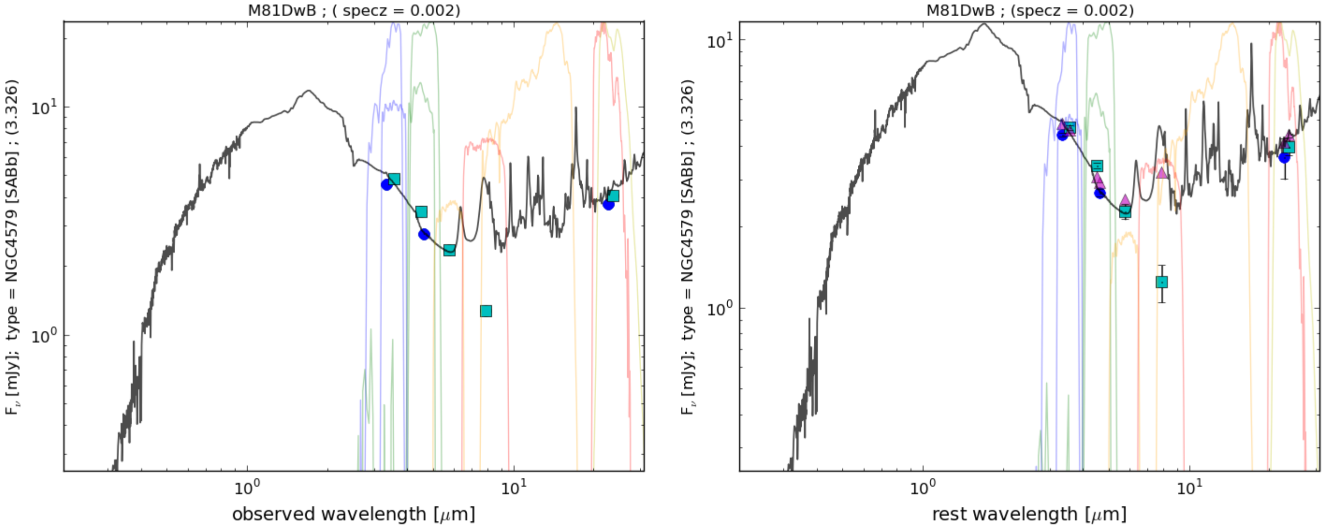

Figure A.7: *Left: SED of M81DwB. Right: Rest-wavelength SED of M81DwB.*

A.8 M87/Virgo A: cD; D = 16.4 Mpc; Activity: NRLG, Sy

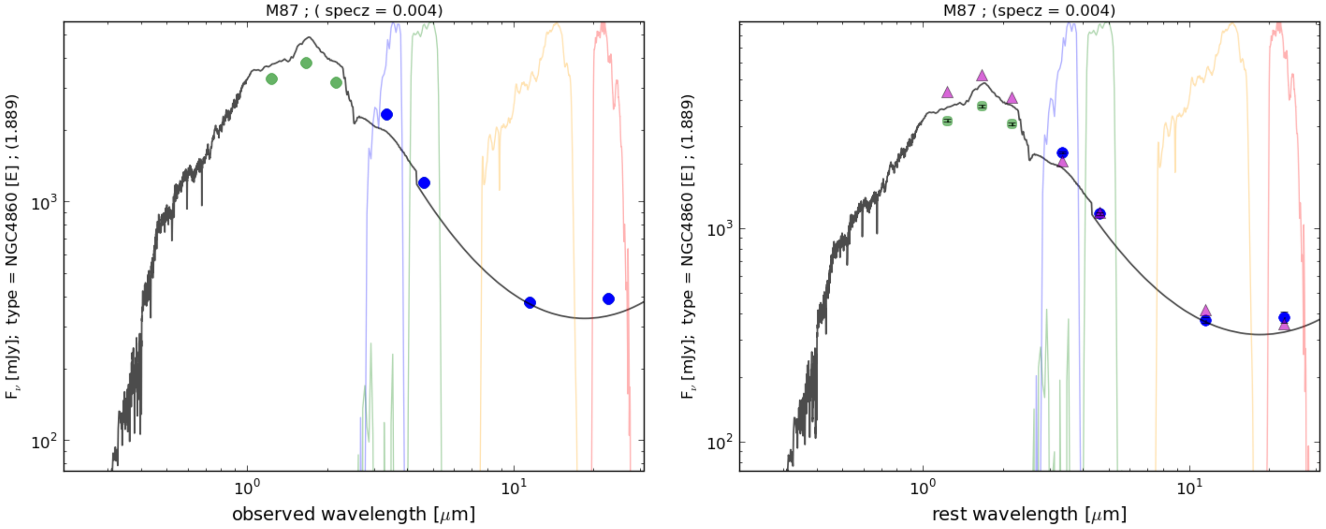

Figure A.8: *Left: SED of M87. Right: Rest-wavelength SED of M87.*

A.9 M101: SABcd; D_{KF} = 6.7 Mpc; LC III-IV; Activity: HII

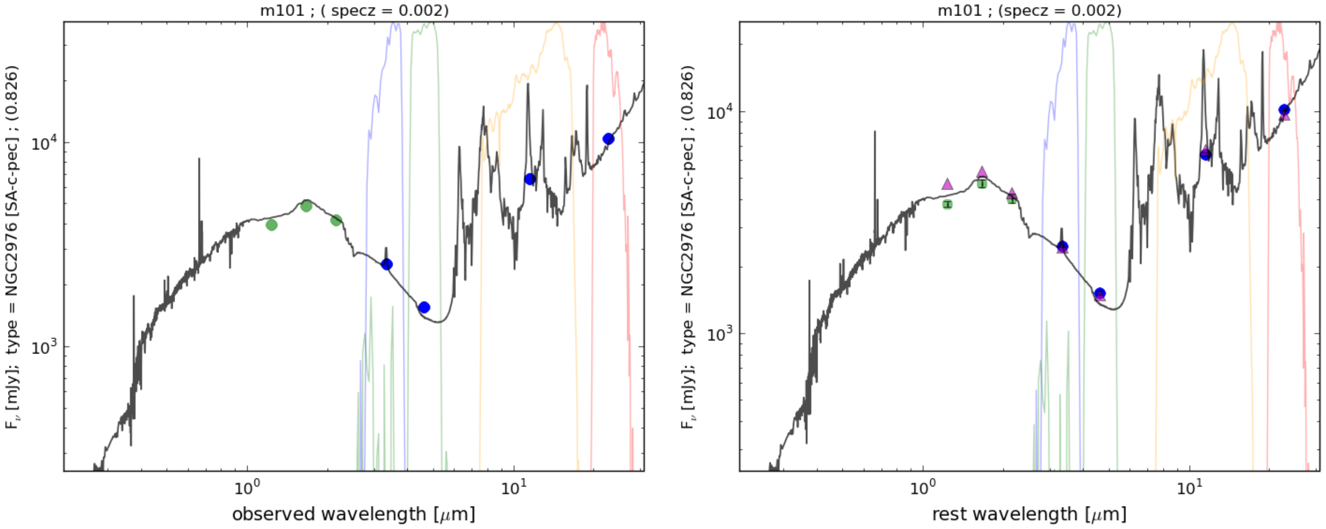

Figure A.9: *Left: SED of M101. Right: Rest-wavelength SED of M101.*

A.10 Mark33: Imp; D = 21.3 Mpc; LC V-VI; Activity: HII/WR

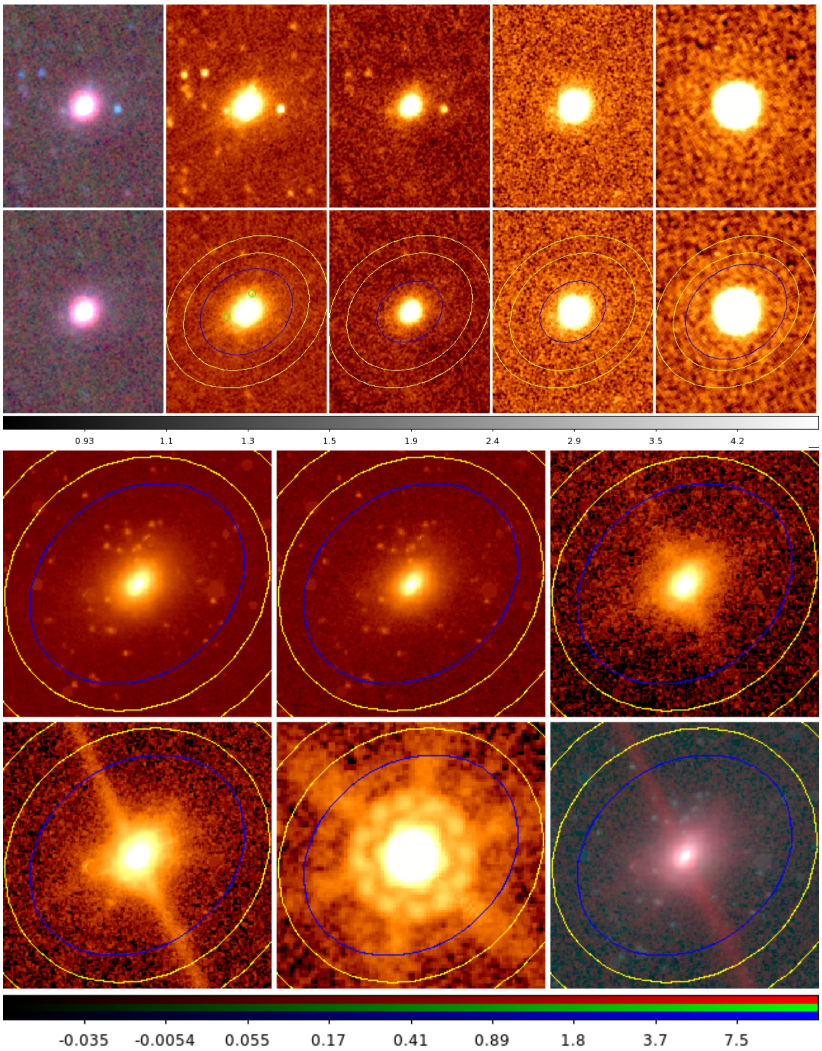

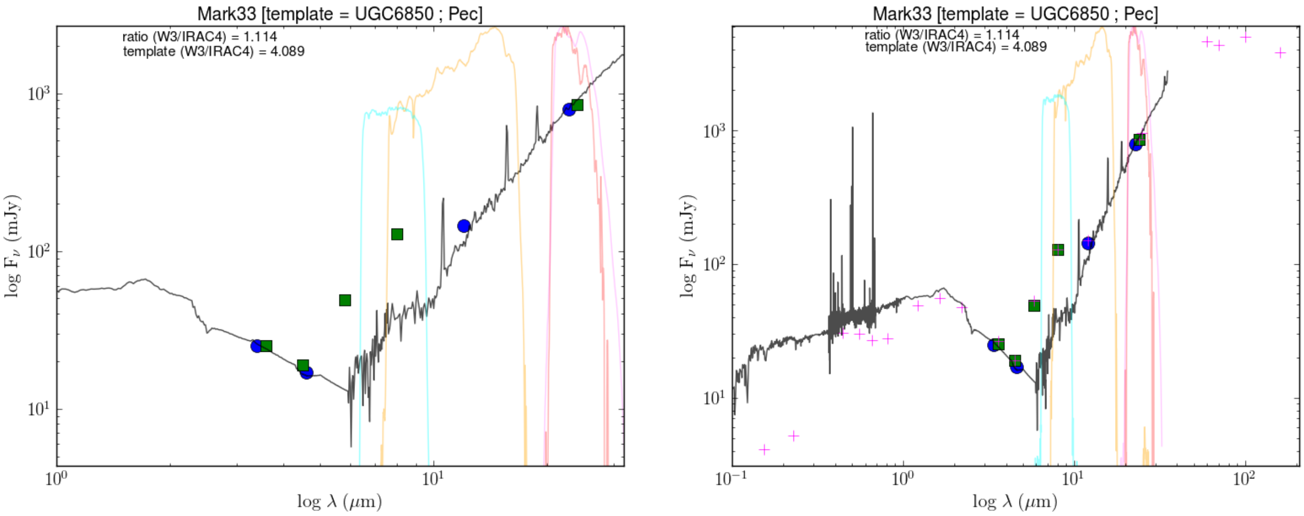

Figure A.10: *Top: WISE imaging of Mark33, unprocessed and processed. Yellow ellipses are sky annulus borders; blue ellipse is 1σ isophotal ellipse. Left to right: Three-colour (W1+2+3); W_1; W_2; W_3; W_4. Middle: Spitzer imaging of Mark33. Top left to bottom right: IRAC1, IRAC2, IRAC3, IRAC4, MIPS24, three-colour (IRAC1+2+4). Bottom left: SED of Mark33. Bottom right: SED of Mark33 with all its SINGS data.*

A.11 NGC0024: SA(s)c; D = 8.2 Mpc; LC III; Activity: HII

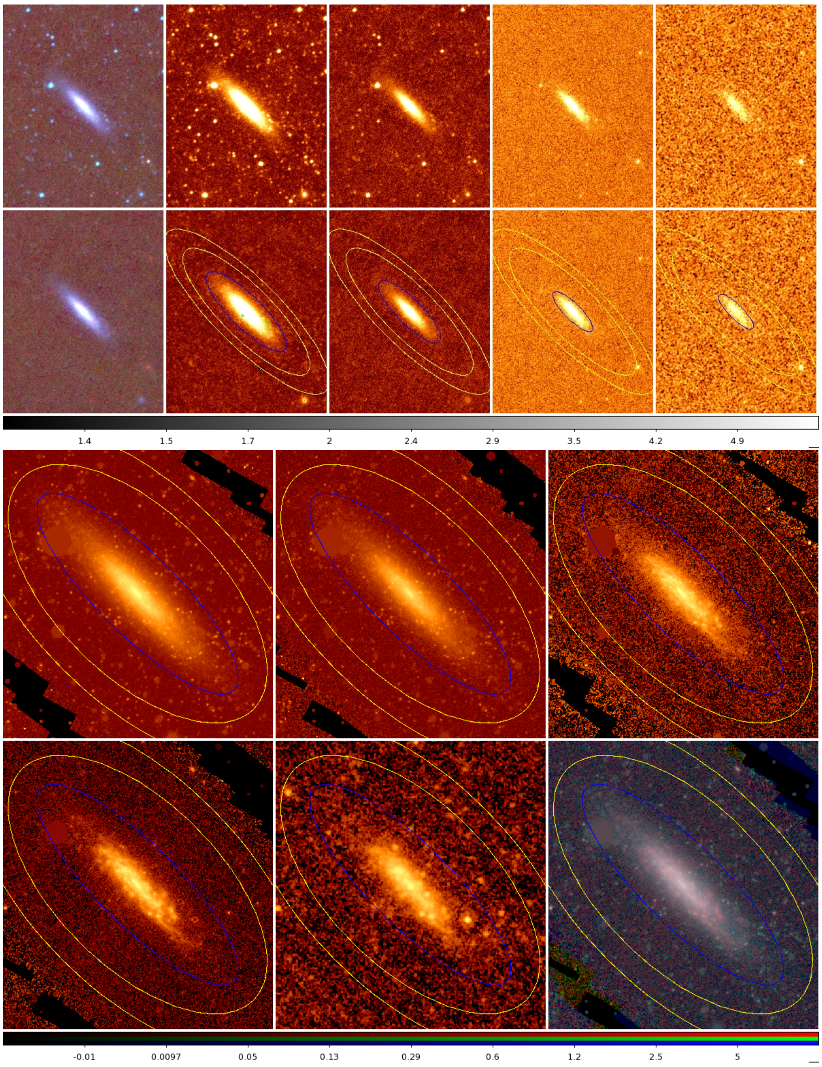

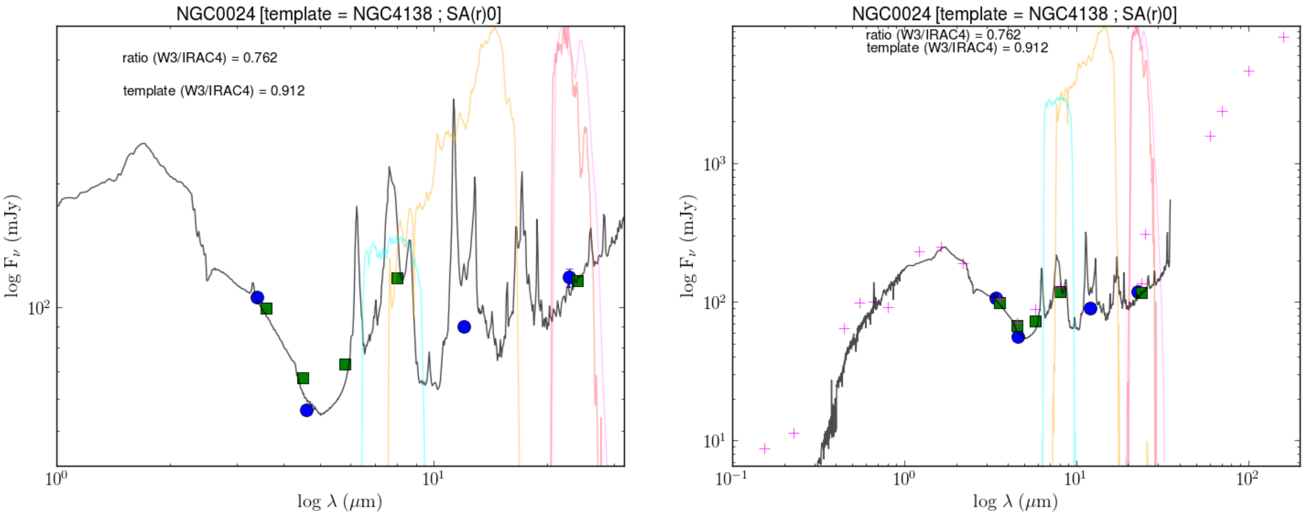

Figure A.11: *Top: WISE imaging of NGC0024, unprocessed and processed. Yellow ellipses are sky annulus borders; blue ellipse is 1σ isophotal ellipse. Left to right: Three-colour (W1+2+3); W$_1$; W$_2$; W$_3$; W$_4$. Middle: Spitzer imaging of NGC0024. Top left to bottom right: IRAC1, IRAC2, IRAC3, IRAC4, MIPS24, three-colour (IRAC1+2+4). Bottom left: SED of NGC0024. Bottom right: SED of NGC0024 with all its SINGS data.*

A.12 NGC0337: SB(s)d; D = 24.7 Mpc; LC IV; Activity: HII

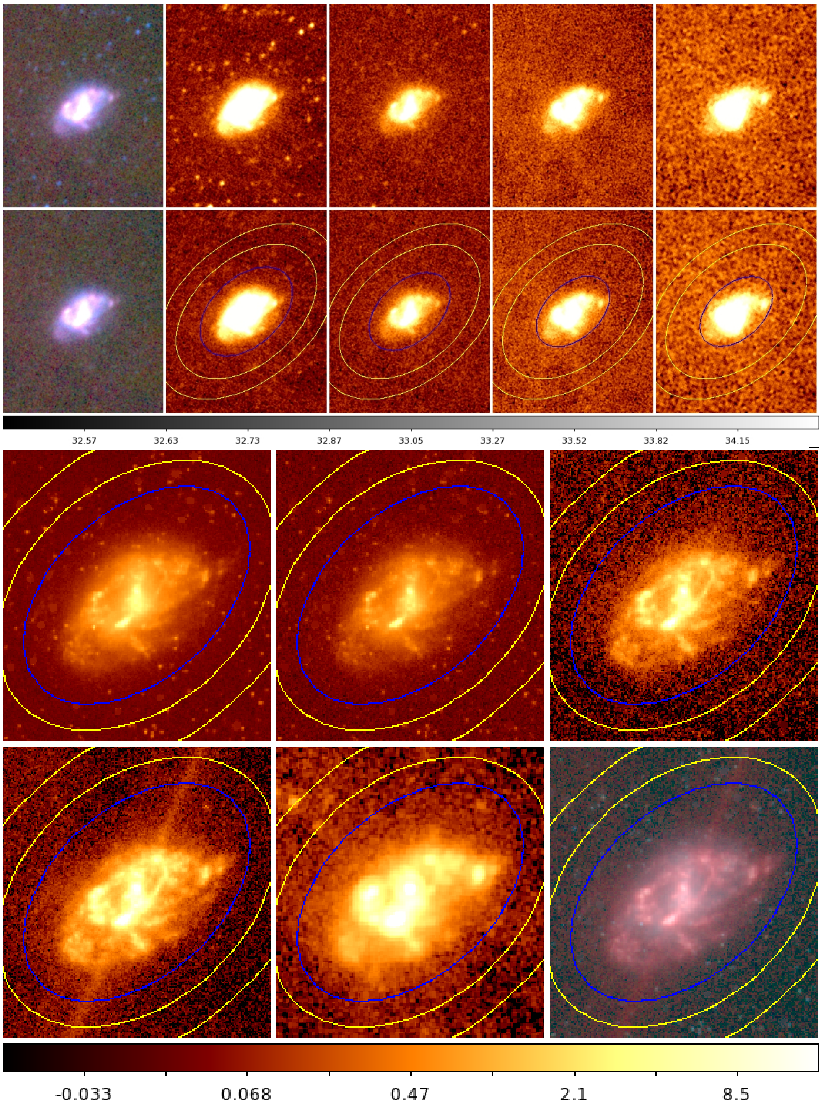

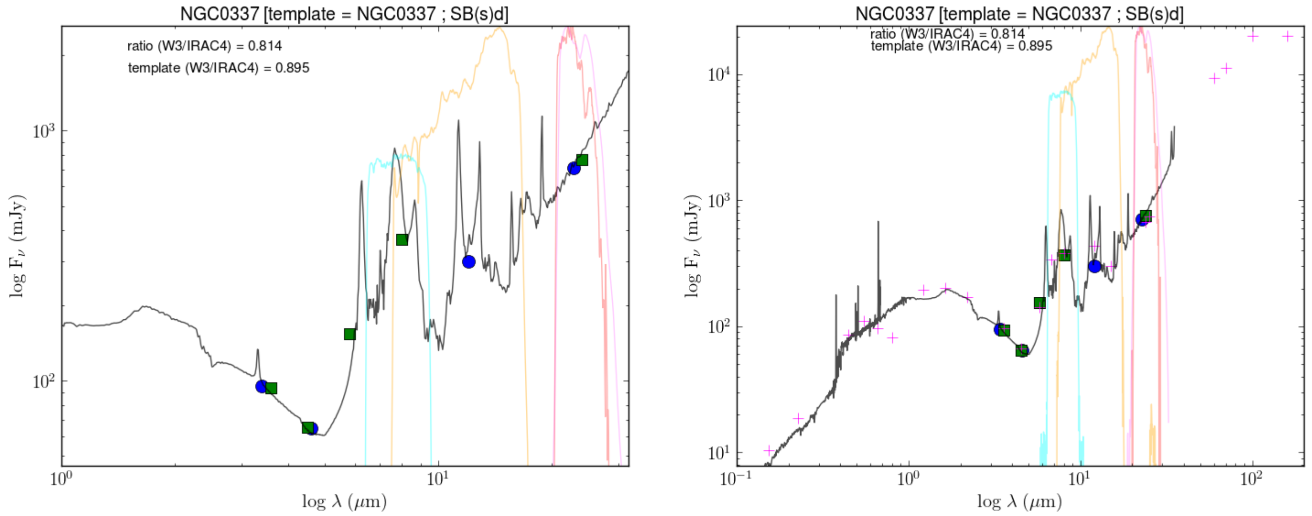

Figure A.12: *Top: WISE imaging of NGC0337, unprocessed and processed. Yellow ellipses are sky annulus borders; blue ellipse is 1σ isophotal ellipse. Left to right: Three-colour (W1+2+3); W$_1$; W$_2$; W$_3$; W$_4$. Middle: Spitzer imaging of NGC0337. Top left to bottom right: IRAC1, IRAC2, IRAC3, IRAC4, MIPS24, three-colour (IRAC1+2+4). Bottom left: SED of NGC0337. Bottom right: SED of NGC0337 with all its SINGS data.*

A.13 NGC0584: E4; D = 27.6 Mpc

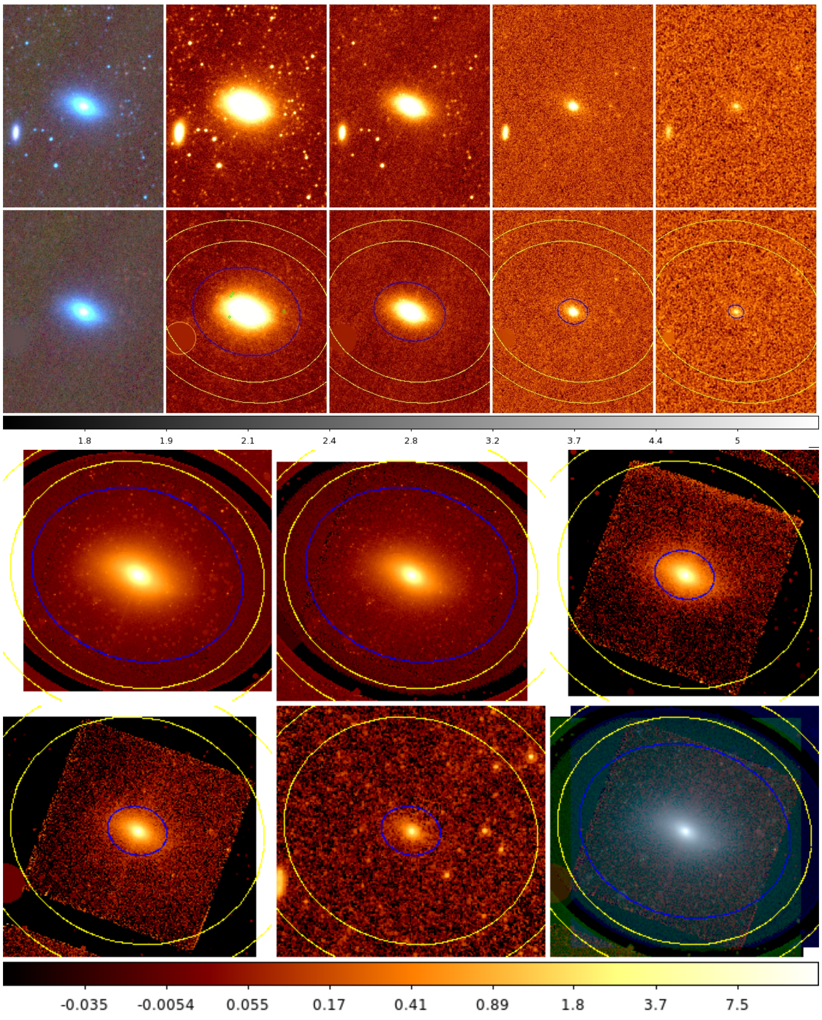

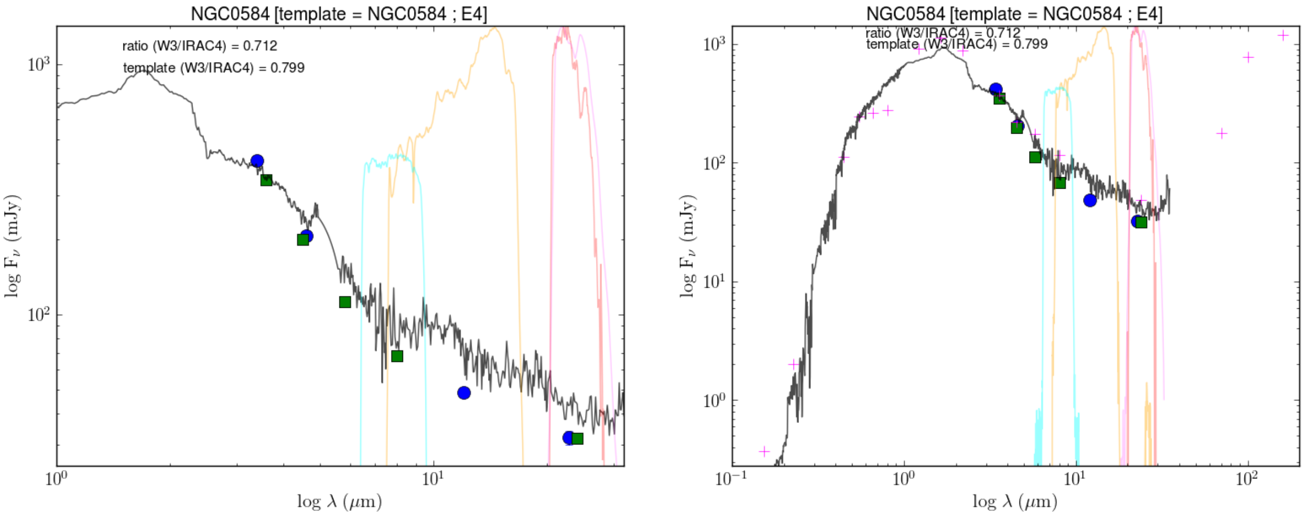

Figure A.13: *Top: WISE imaging of NGC0584, unprocessed and processed. Yellow ellipses are sky annulus borders; blue ellipse is 1σ isophotal ellipse. Left to right: Three-colour (W1+2+3); W$_1$; W$_2$; W$_3$; W$_4$. Middle: Spitzer imaging of NGC0584. Top left to bottom right: IRAC1, IRAC2, IRAC3, IRAC4, MIPS24, three-colour (IRAC1+2+4). Bottom left: SED of NGC0584. Bottom right: SED of NGC0584 with all its SINGS data.*

A.14 NGC0628/M74: SAc; D = 11.4 Mpc; LC III; Activity: HII

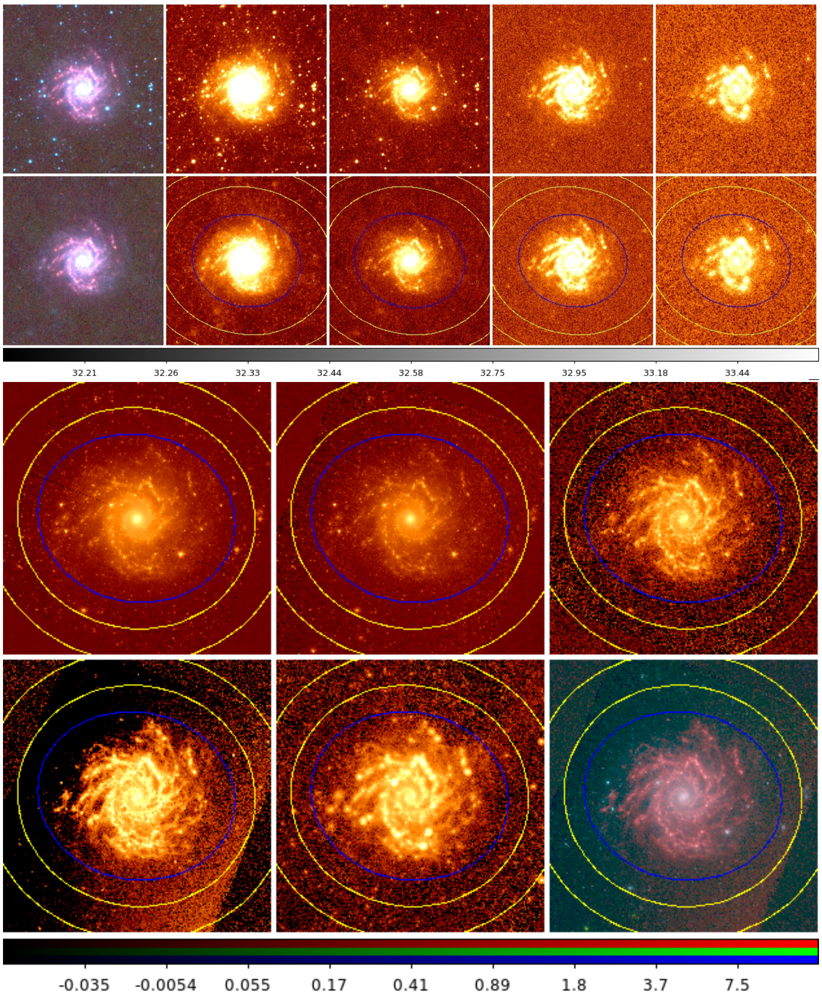

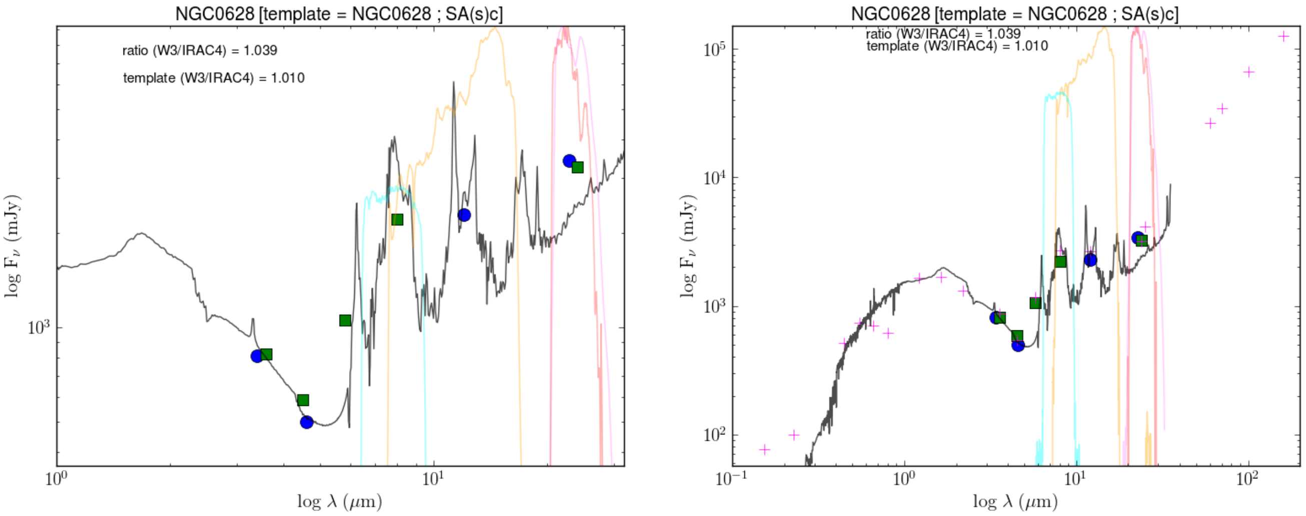

Figure A.14: *Top: WISE imaging of NGC0628, unprocessed and processed. Yellow ellipses are sky annulus borders; blue ellipse is 1σ isophotal ellipse. Left to right: Three-colour (W1+2+3); W_1; W_2; W_3; W_4. Middle: Spitzer imaging of NGC0628. Top left to bottom right: IRAC1, IRAC2, IRAC3, IRAC4, MIPS24, three-colour (IRAC1+2+4). Bottom left: SED of NGC0628. Bottom right: SED of NGC0628 with all its SINGS data.*

A.15 NGC0855: SA(s)c; D = 9.6 Mpc; Activity: HII

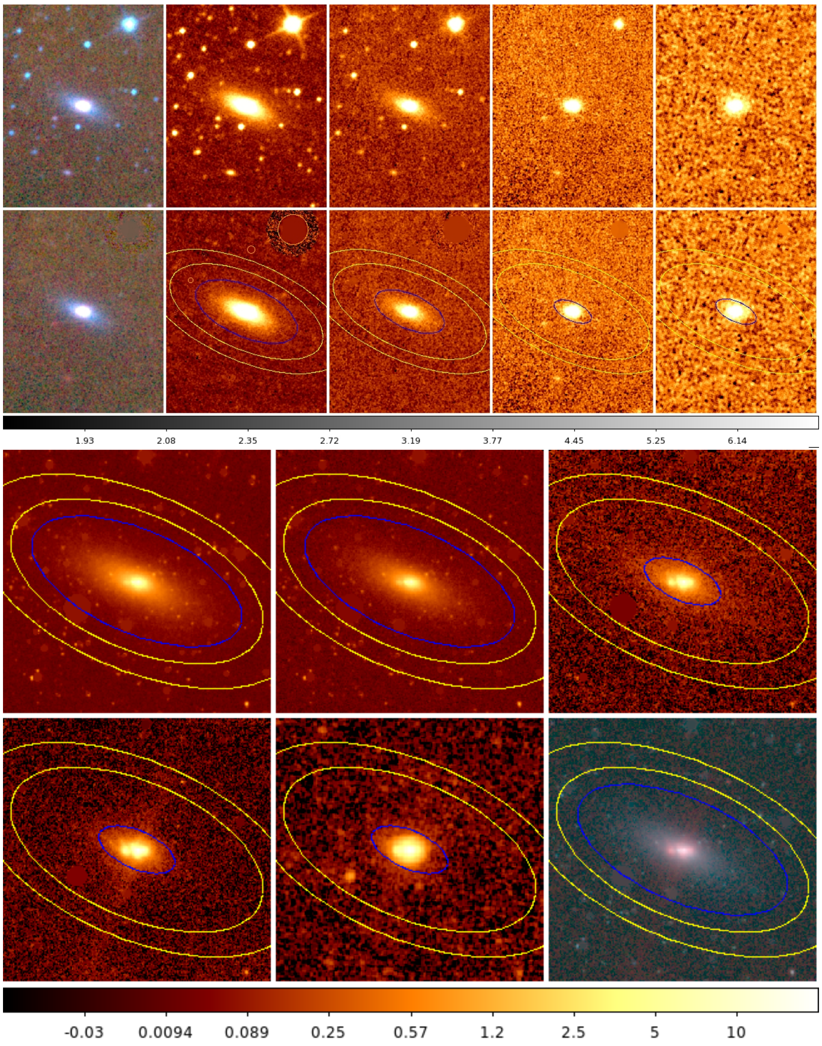

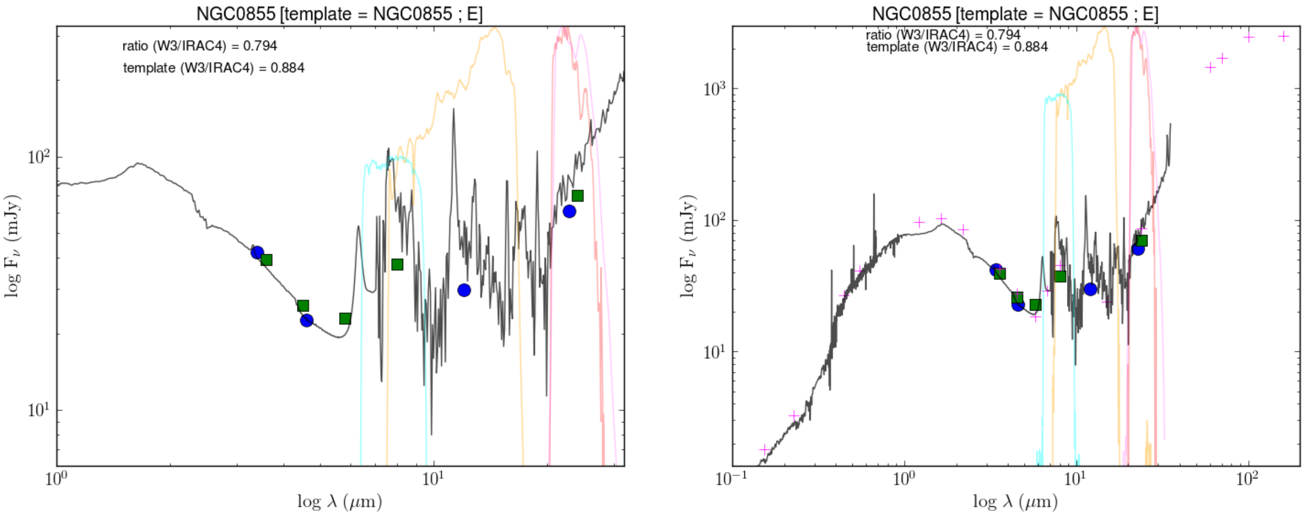

Figure A.15: *Top: WISE imaging of NGC0855, unprocessed and processed. Yellow ellipses are sky annulus borders; blue ellipse is 1σ isophotal ellipse. Left to right: Three-colour (W1+2+3); W_1; W_2; W_3; W_4. Middle: Spitzer imaging of NGC0855. Top left to bottom right: IRAC1, IRAC2, IRAC3, IRAC4, MIPS24, three-colour (IRAC1+2+4). Bottom left: SED of NGC0855. Bottom right: SED of NGC0855 with all its SINGS data.*

A.16 NGC0925: SAB(s)d; D = 10.1 Mpc; LC IV; Activity: HII

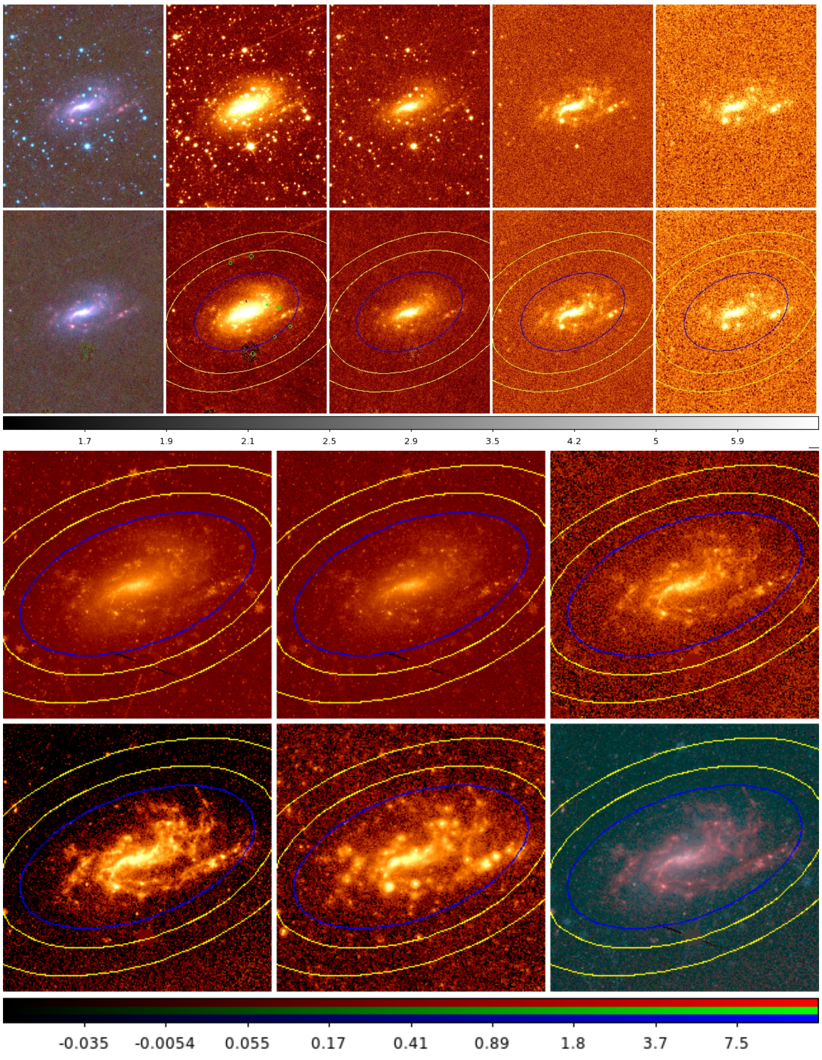

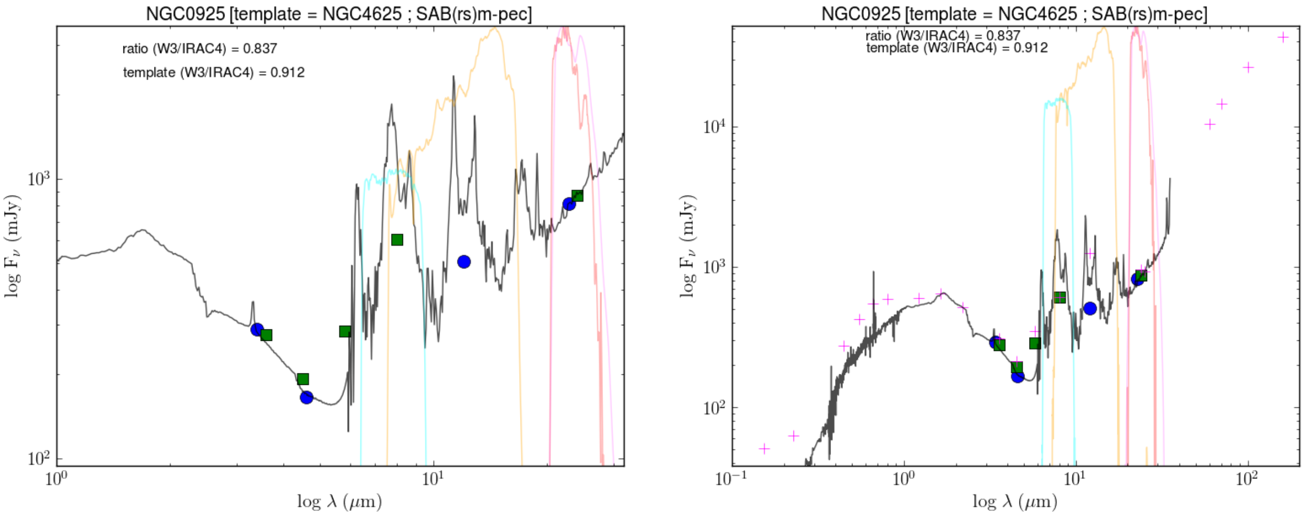

Figure A.16: *Top: WISE imaging of NGC0925, unprocessed and processed. Yellow ellipses are sky annulus borders; blue ellipse is 1σ isophotal ellipse. Left to right: Three-colour (W1+2+3); W_1; W_2; W_3; W_4. Middle: Spitzer imaging of NGC0925. Top left to bottom right: IRAC1, IRAC2, IRAC3, IRAC4, MIPS24, three-colour (IRAC1+2+4). Bottom left: SED of NGC0925. Bottom right: SED of NGC0925 with all its SINGS data.*

A.17 NGC1097: SBb; D = 16.9 Mpc; LC II; Activity: Sy1

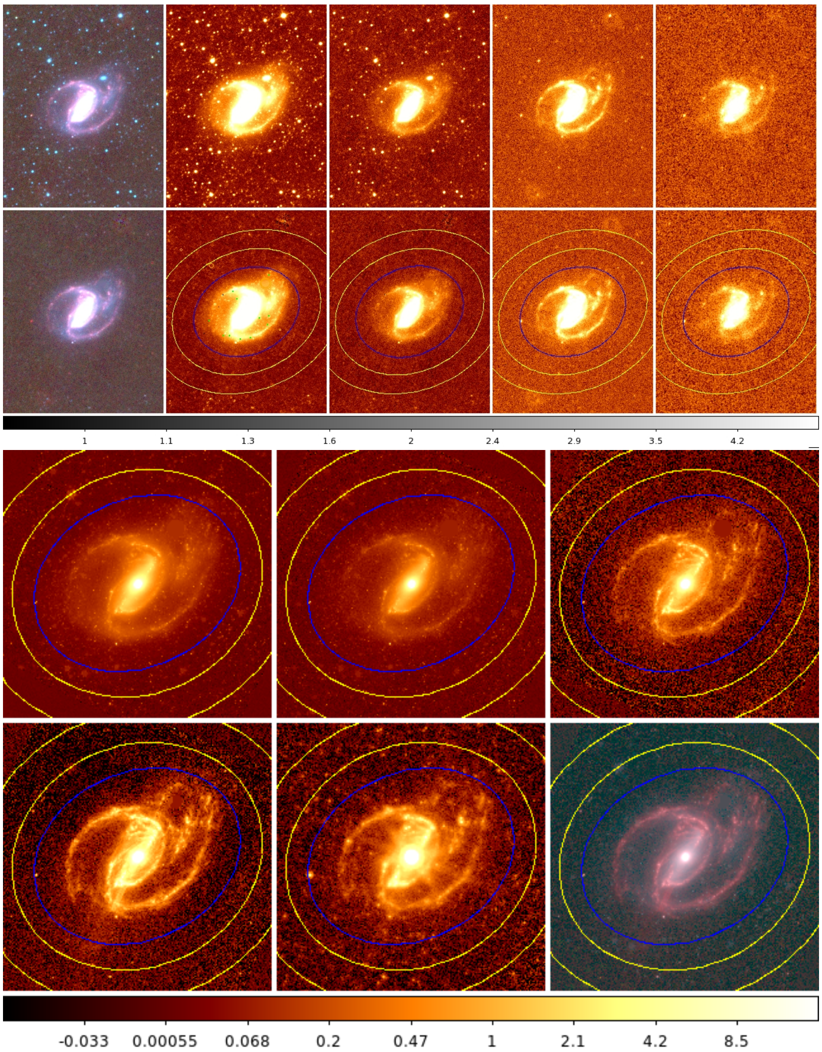

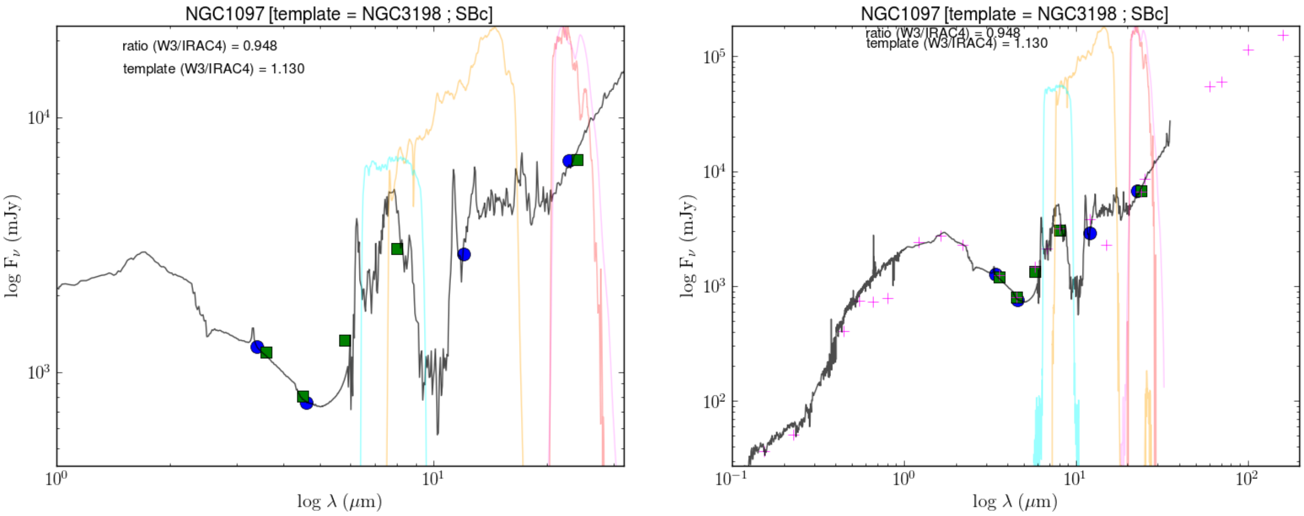

Figure A.17: *Top: WISE imaging of NGC1097, unprocessed and processed. Yellow ellipses are sky annulus borders; blue ellipse is 1σ isophotal ellipse. Left to right: Three-colour (W1+2+3); W$_1$; W$_2$; W$_3$; W$_4$. Middle: Spitzer imaging of NGC1097. Top left to bottom right: IRAC1, IRAC2, IRAC3, IRAC4, MIPS24, three-colour (IRAC1+2+4). Bottom left: SED of NGC1097. Bottom right: SED of NGC1097 with all its SINGS data.*

A.18 NGC1266: SB(rs)0p; D = 31.3 Mpc; Activity: LINER

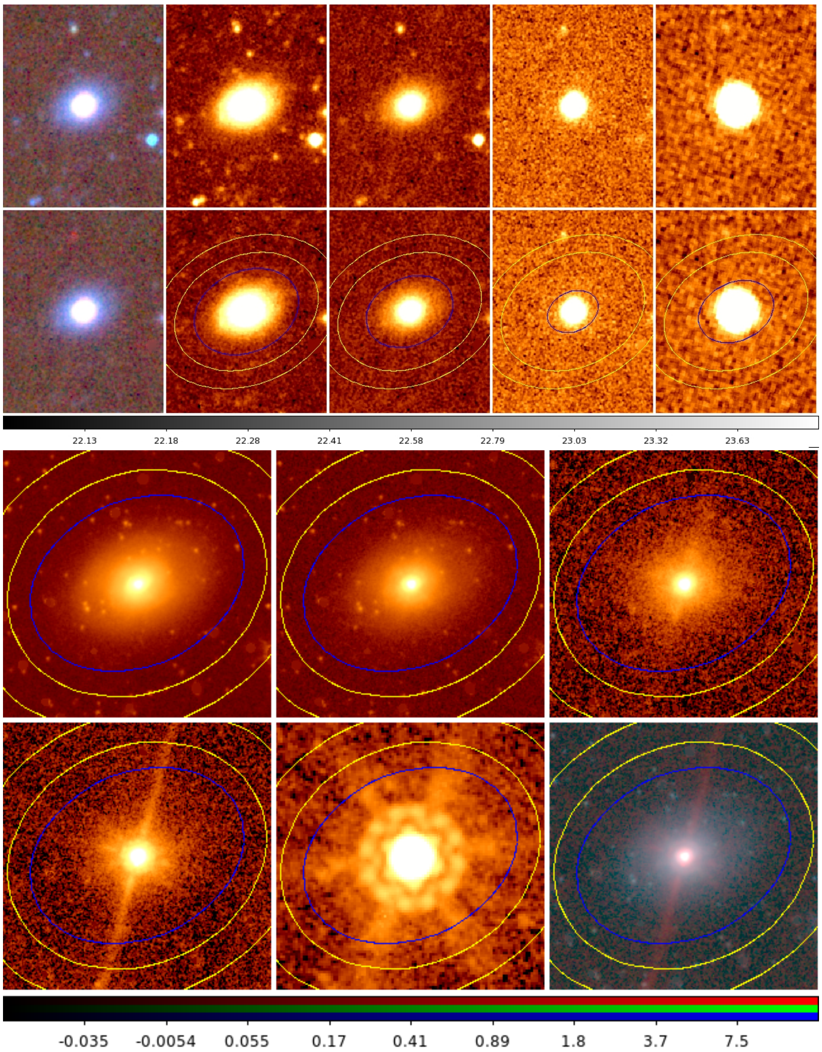

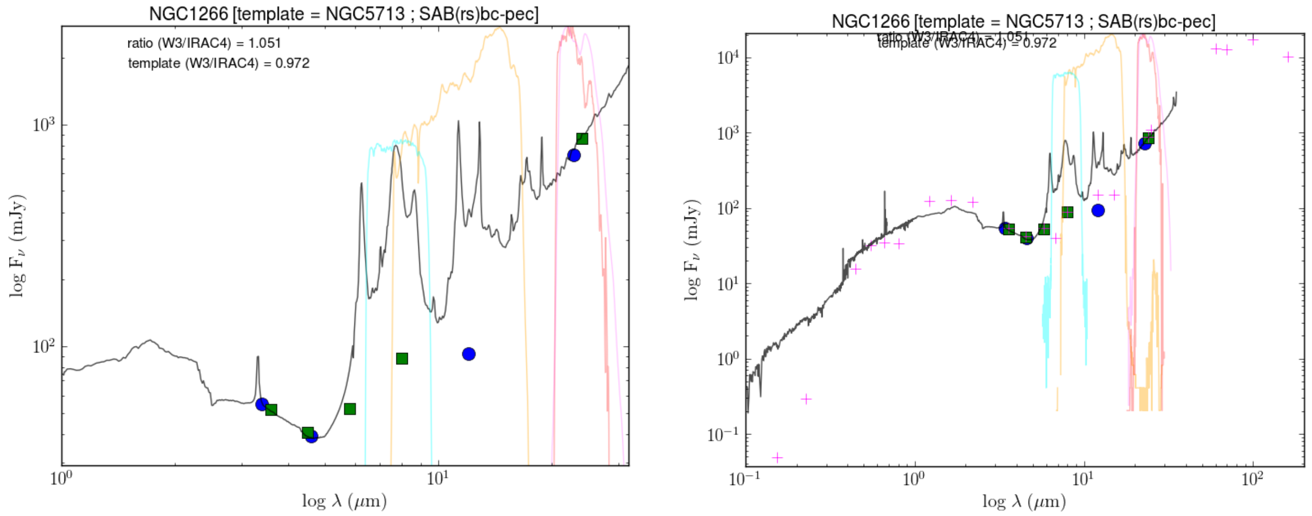

Figure A.18: *Top: WISE imaging of NGC1266, unprocessed and processed. Yellow ellipses are sky annulus borders; blue ellipse is 1σ isophotal ellipse. Left to right: Three-colour (W1+2+3); W_1; W_2; W_3; W_4. Middle: Spitzer imaging of NGC1266. Top left to bottom right: IRAC1, IRAC2, IRAC3, IRAC4, MIPS24, three-colour (IRAC1+2+4). Bottom left: SED of NGC1266. Bottom right: SED of NGC1266 with all its SINGS data.*

A.19 NGC1291: SBa; D = 9.7 Mpc; Activity: HII

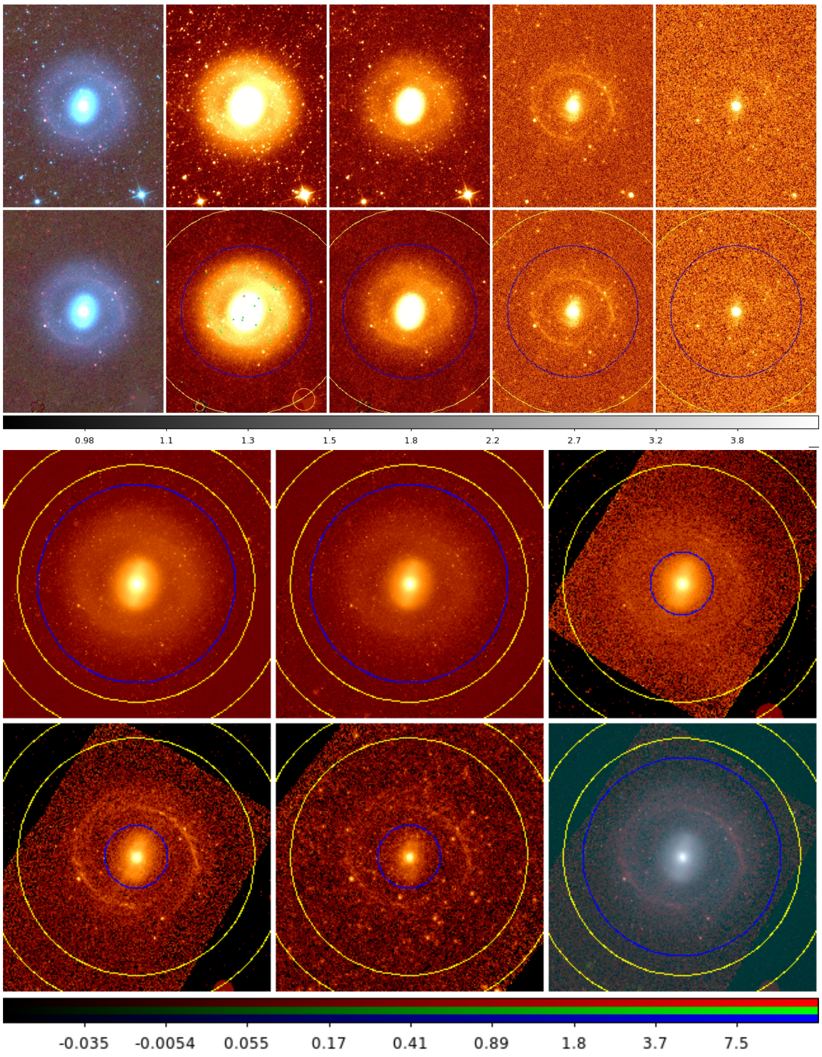

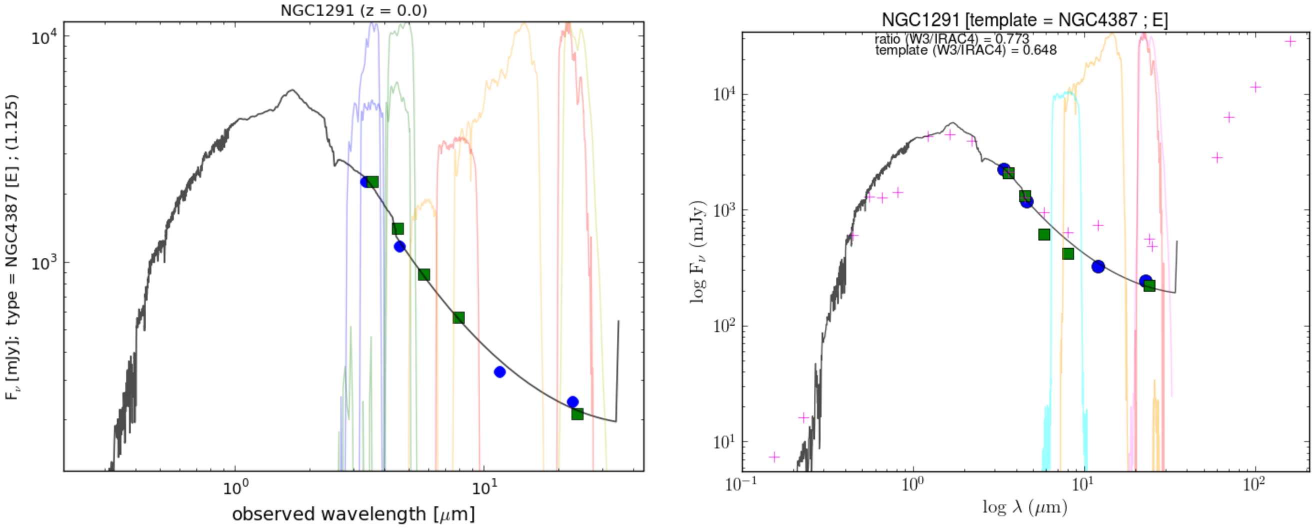

Figure A.19: *Top: WISE imaging of NGC1291, unprocessed and processed. Yellow ellipses are sky annulus borders; blue ellipse is 1σ isophotal ellipse. Left to right: Three-colour (W1+2+3);* W_1; W_2; W_3; W_4. *Middle: Spitzer imaging of NGC1291. Top left to bottom right: IRAC1, IRAC2, IRAC3, IRAC4, MIPS24, three-colour (IRAC1+2+4). Bottom left: SED of NGC1291. Bottom right: SED of NGC1291 with all its SINGS data.*

A.20 NGC1316: SAB(s)0; D = 26.3 Mpc; Activity: LINER

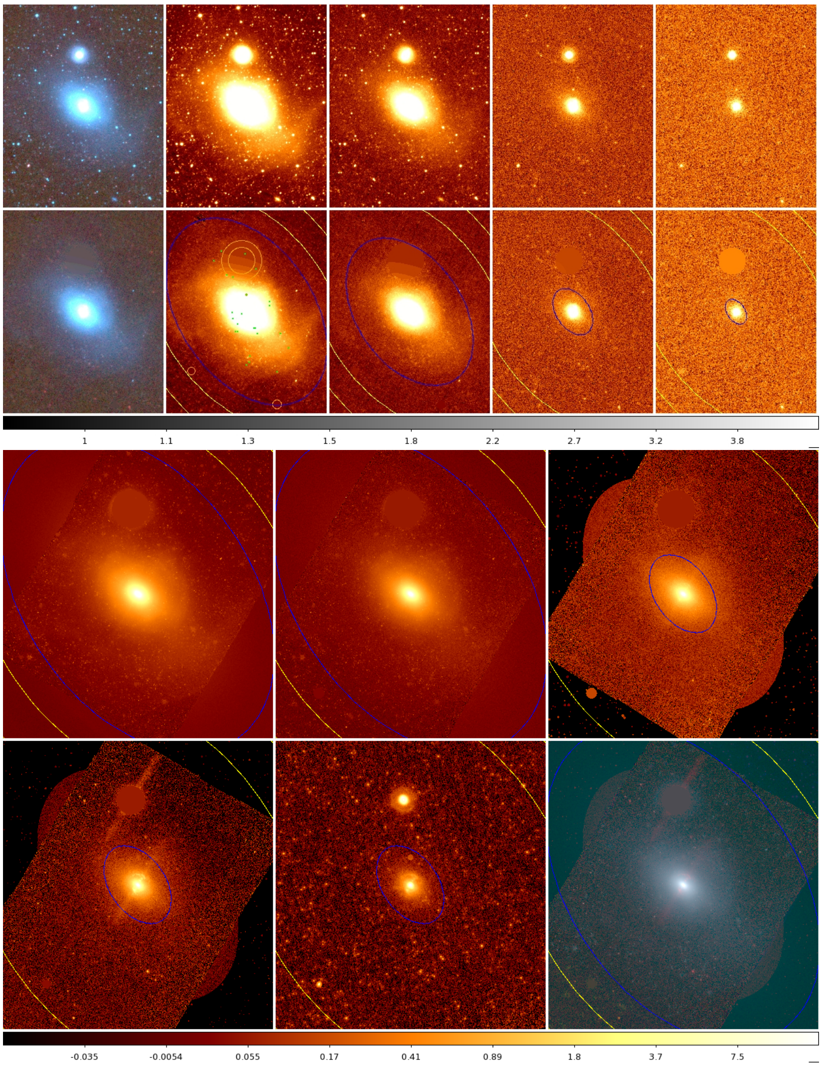

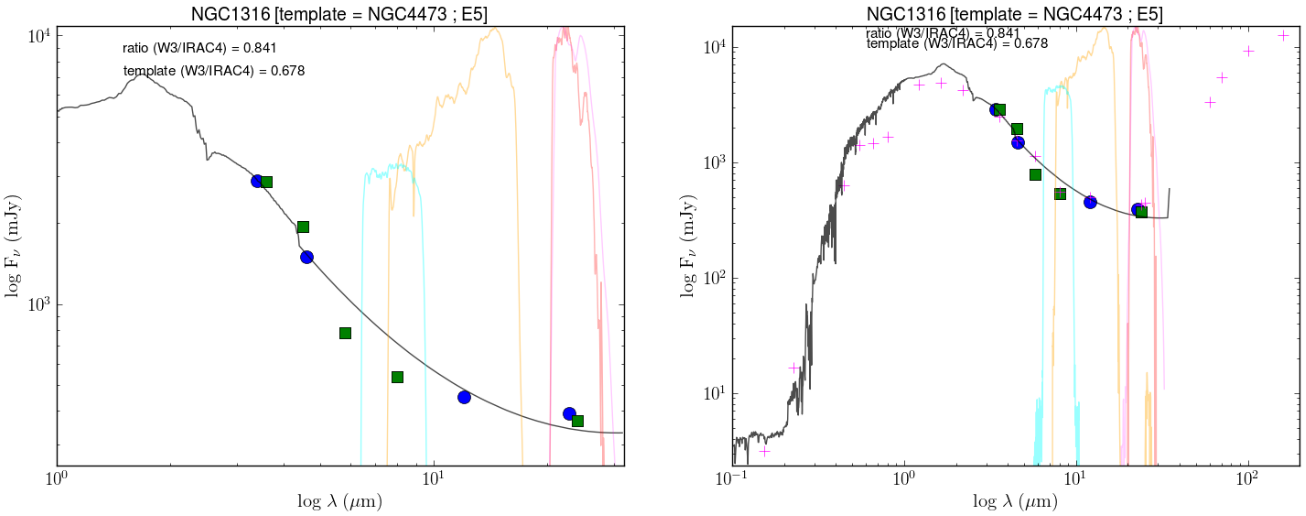

Figure A.20: *Top: WISE imaging of NGC1316, unprocessed and processed. Yellow ellipses are sky annulus borders; blue ellipse is 1σ isophotal ellipse. Left to right: Three-colour (W1+2+3); W_1; W_2; W_3; W_4. Middle: Spitzer imaging of NGC1316. Top left to bottom right: IRAC1, IRAC2, IRAC3, IRAC4, MIPS24, three-colour (IRAC1+2+4). Bottom left: SED of NGC1316. Bottom right: SED of NGC1316 with all its SINGS data.*

A.21 NGC1377: S0; D = 24.4 Mpc; Activity: HII

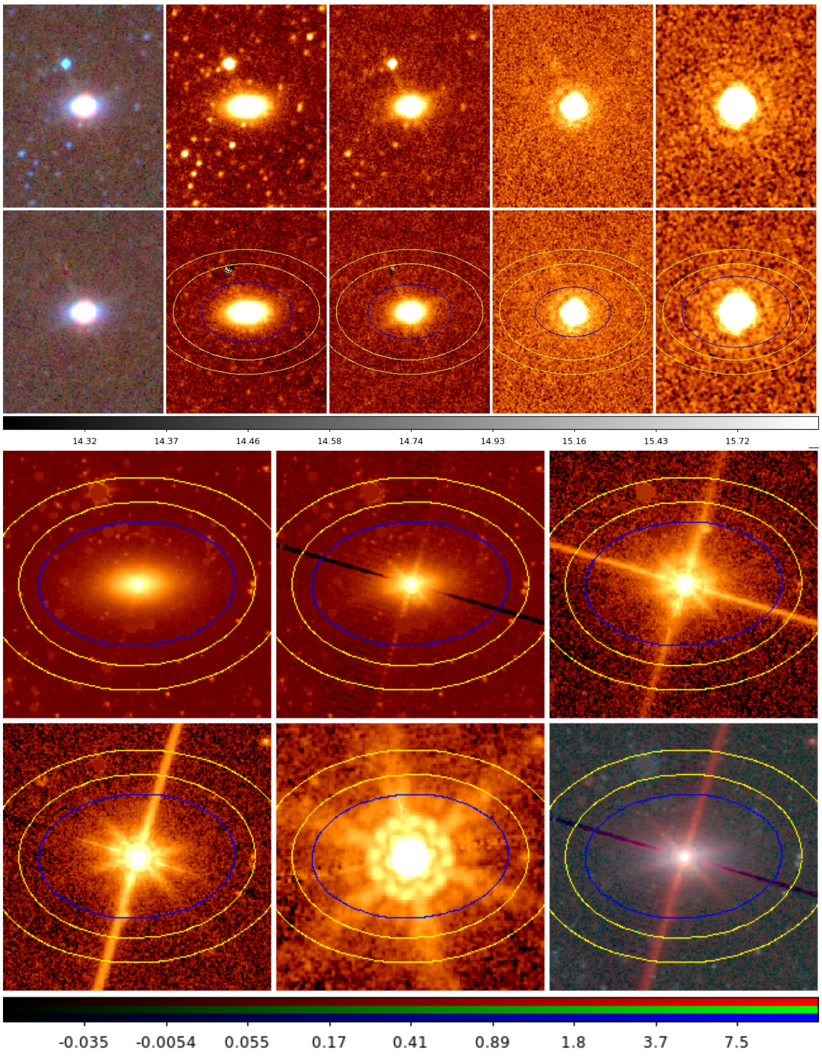

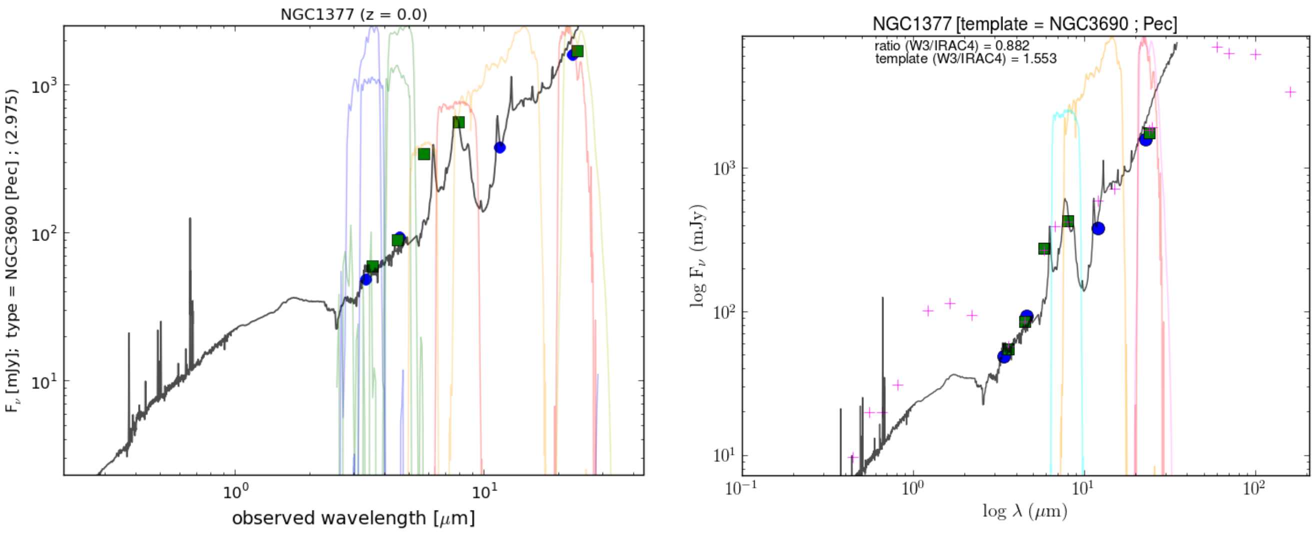

Figure A.21: *Top: WISE imaging of NGC1377, unprocessed and processed. Yellow ellipses are sky annulus borders; blue ellipse is 1σ isophotal ellipse. Left to right: Three-colour (W1+2+3); W$_1$; W$_2$; W$_3$; W$_4$. Middle: Spitzer imaging of NGC1377. Top left to bottom right: IRAC1, IRAC2, IRAC3, IRAC4, MIPS24, three-colour (IRAC1+2+4). Bottom left: SED of NGC1377. Bottom right: SED of NGC1377 with all its SINGS data.*

A.22 NGC1404: E1; D = 25.1 Mpc

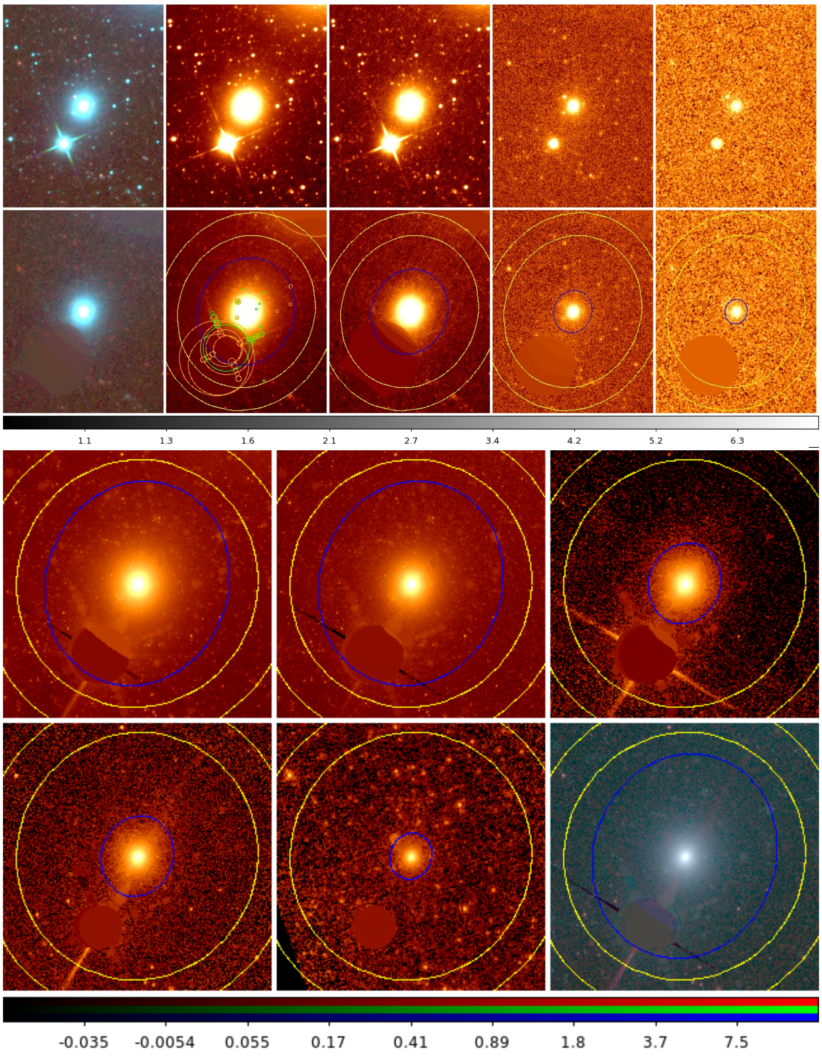

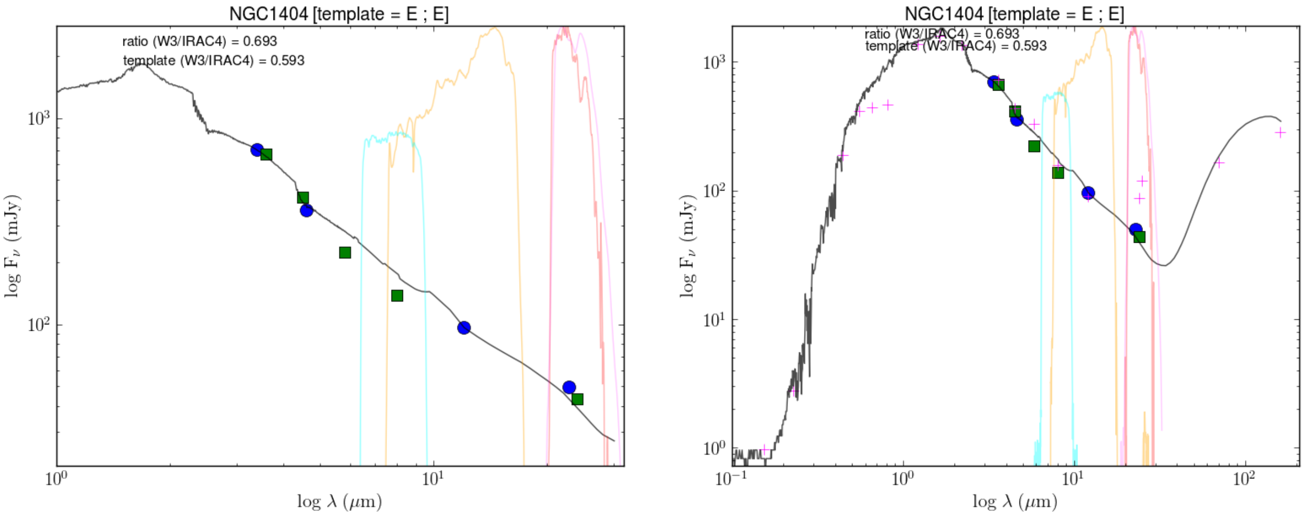

Figure A.22: *Top: WISE imaging of NGC1404, unprocessed and processed. Yellow ellipses are sky annulus borders; blue ellipse is 1σ isophotal ellipse. Left to right: Three-colour (W1+2+3); W_1; W_2; W_3; W_4. Middle: Spitzer imaging of NGC1404. Top left to bottom right: IRAC1, IRAC2, IRAC3, IRAC4, MIPS24, three-colour (IRAC1+2+4). Bottom left: SED of NGC1404. Bottom right: SED of NGC1404 with all its SINGS data.*

A.23 NGC1482: SA0p; D = 22.0 Mpc; Activity: HII

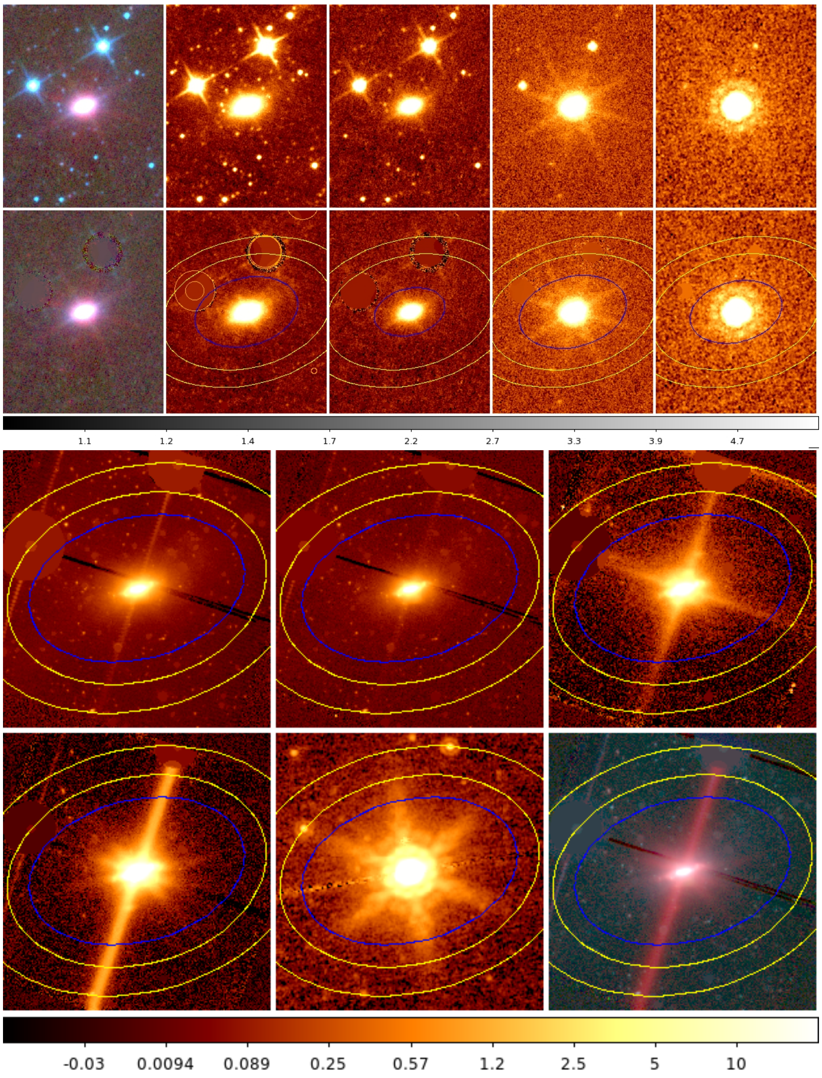

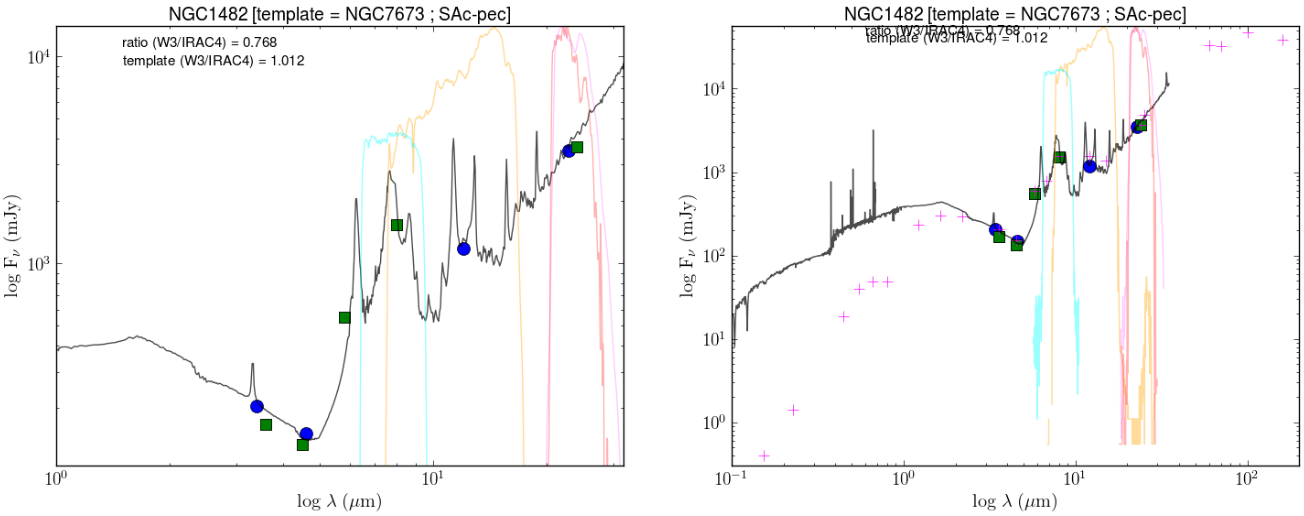

Figure A.23: *Top: WISE imaging of NGC1482, unprocessed and processed. Yellow ellipses are sky annulus borders; blue ellipse is 1σ isophotal ellipse. Left to right: Three-colour (W1+2+3); W$_1$; W$_2$; W$_3$; W$_4$. Middle: Spitzer imaging of NGC1482. Top left to bottom right: IRAC1, IRAC2, IRAC3, IRAC4, MIPS24, three-colour (IRAC1+2+4). Bottom left: SED of NGC1482. Bottom right: SED of NGC1482 with all its SINGS data.*

A.24 NGC1512: SB(r)ab; D = 10.4 Mpc; LC I; Activity: AGN

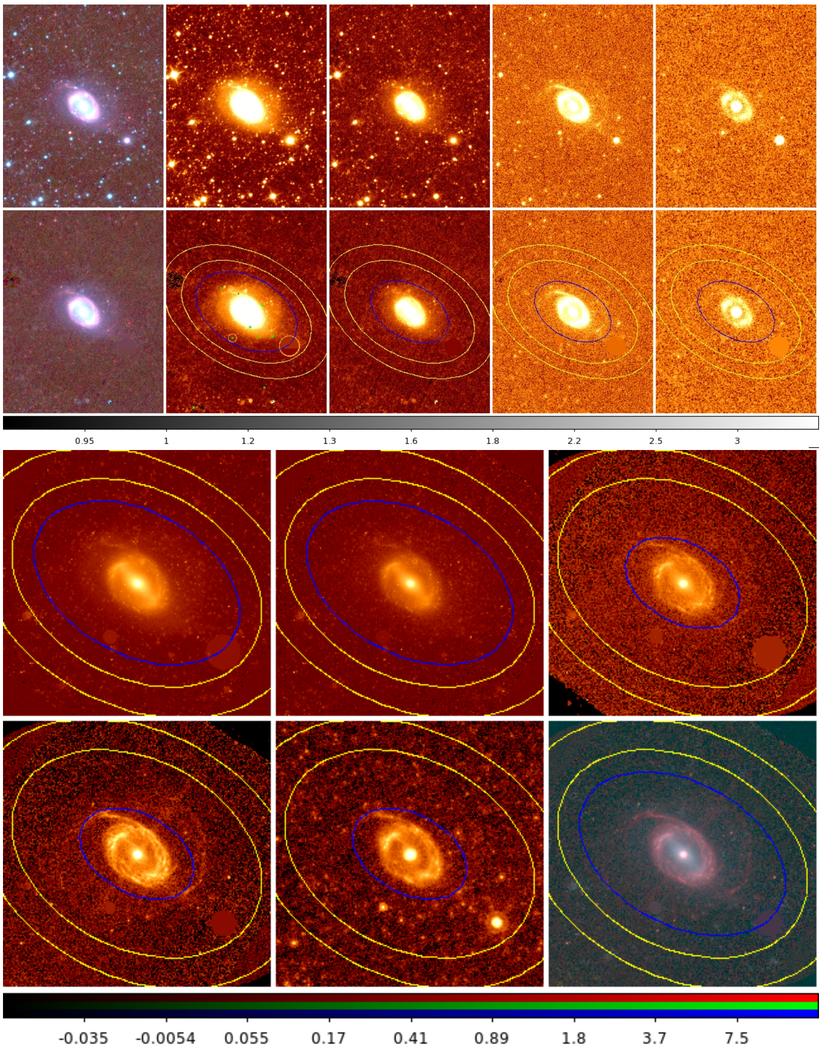

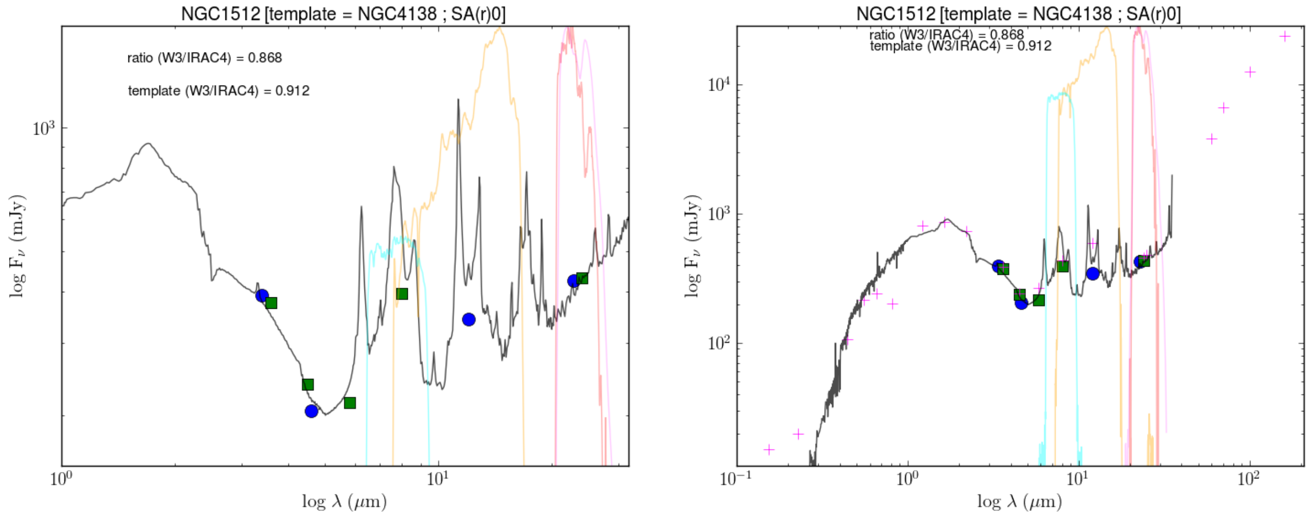

Figure A.24: *Top: WISE imaging of NGC1512, unprocessed and processed. Yellow ellipses are sky annulus borders; blue ellipse is 1σ isophotal ellipse. Left to right: Three-colour (W1+2+3); W_1; W_2; W_3; W_4. Middle: Spitzer imaging of NGC1512. Top left to bottom right: IRAC1, IRAC2, IRAC3, IRAC4, MIPS24, three-colour (IRAC1+2+4). Bottom left: SED of NGC1512. Bottom right: SED of NGC1512 with all its SINGS data.*

A.25 NGC1566: SAB(rs)bc; D = 18.0 Mpc; LC II-III; Activity: Sy1

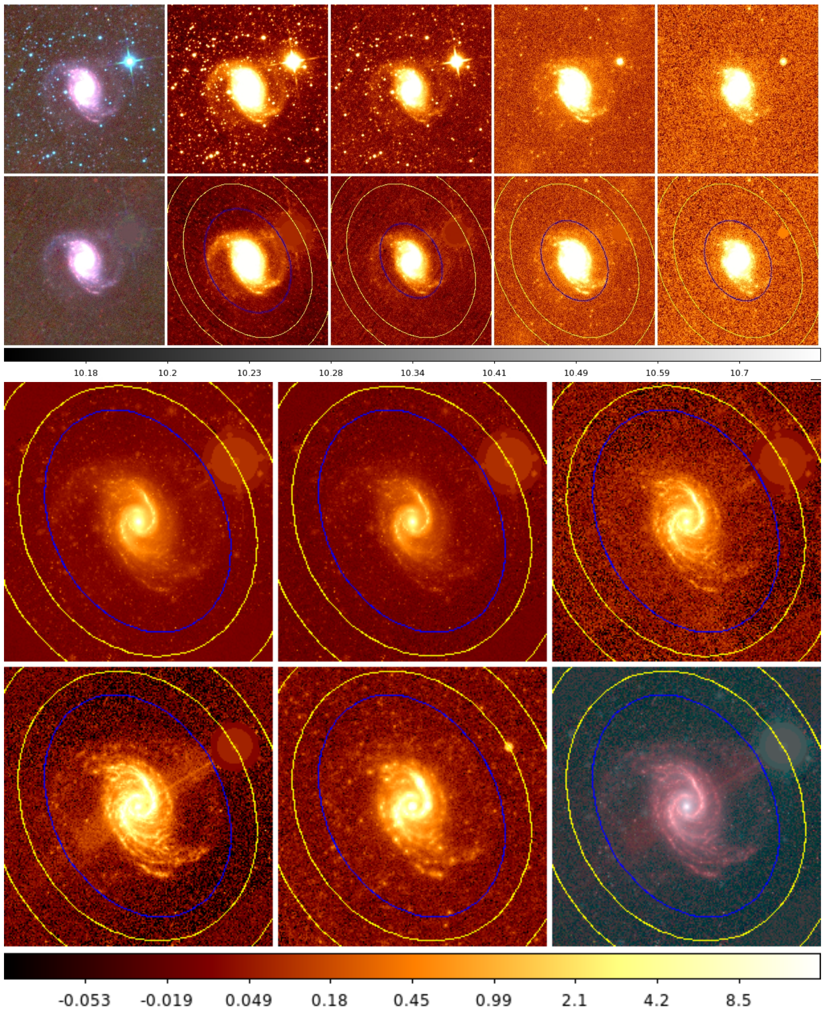

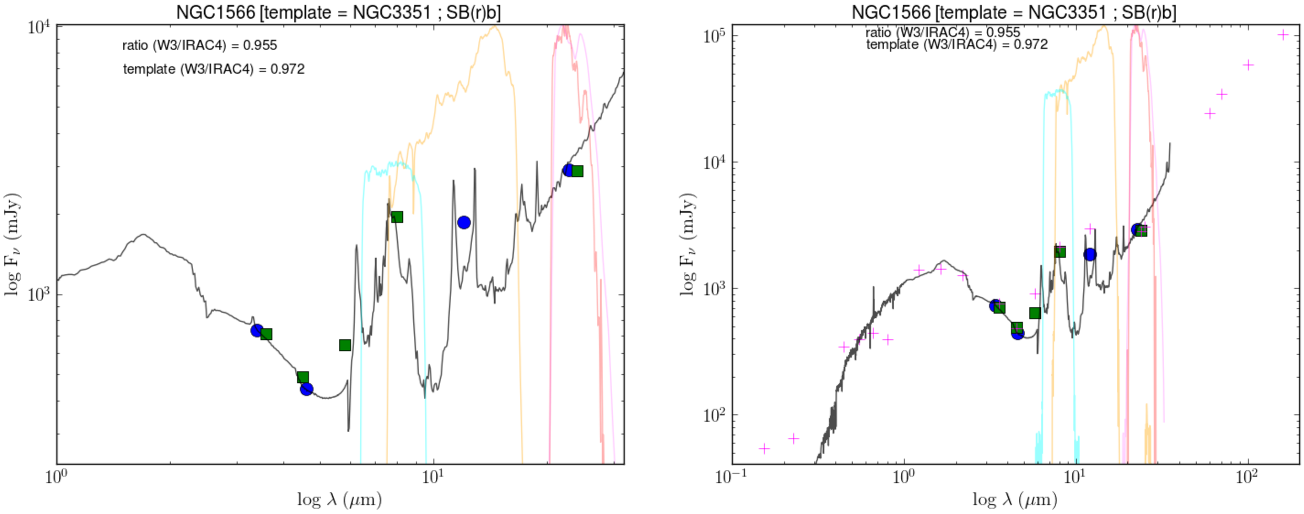

Figure A.25: *Top: WISE imaging of NGC1566, unprocessed and processed. Yellow ellipses are sky annulus borders; blue ellipse is 1σ isophotal ellipse. Left to right: Three-colour (W1+2+3); W$_1$; W$_2$; W$_3$; W$_4$. Middle: Spitzer imaging of NGC1566. Top left to bottom right: IRAC1, IRAC2, IRAC3, IRAC4, MIPS24, three-colour (IRAC1+2+4). Bottom left: SED of NGC1566. Bottom right: SED of NGC1566 with all its SINGS data.*

A.26 NGC1705: SA0p; D = 5.8 Mpc; Activity: HII

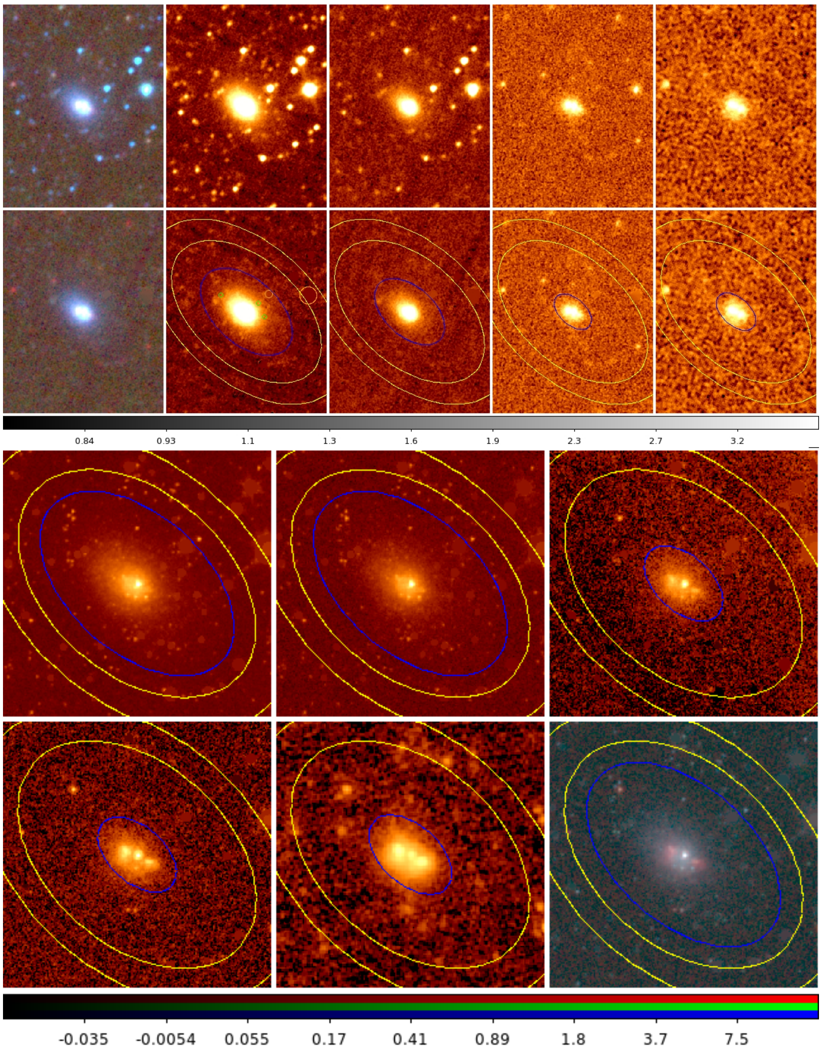

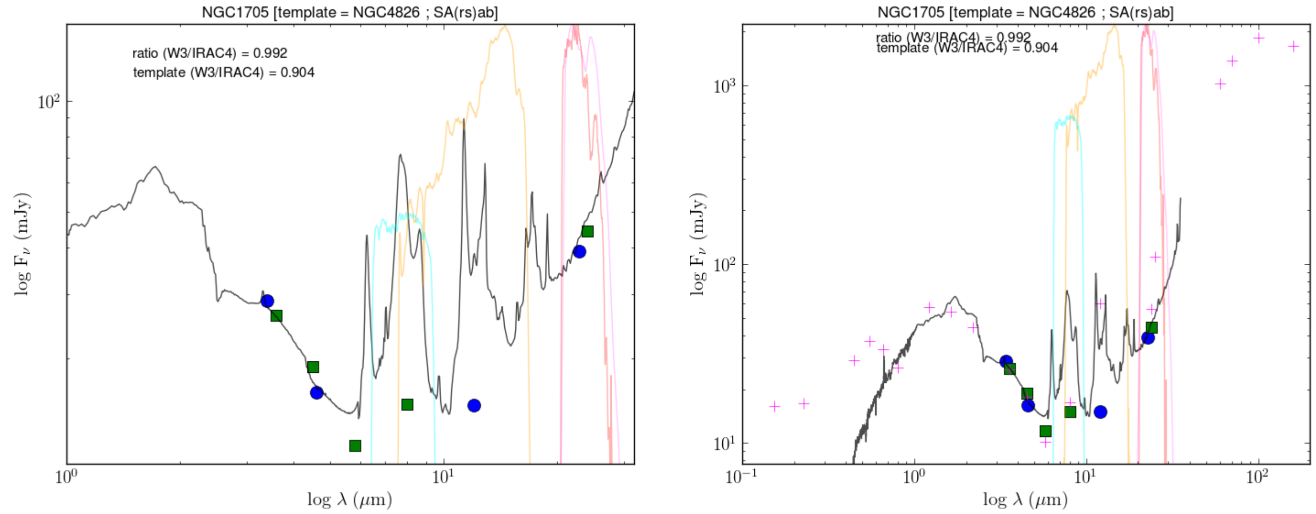

Figure A.26: *Top: WISE imaging of NGC1705, unprocessed and processed. Yellow ellipses are sky annulus borders; blue ellipse is 1σ isophotal ellipse. Left to right: Three-colour (W1+2+3); W_1; W_2; W_3; W_4. Middle: Spitzer imaging of NGC1705. Top left to bottom right: IRAC1, IRAC2, IRAC3, IRAC4, MIPS24, three-colour (IRAC1+2+4). Bottom left: SED of NGC1705. Bottom right: SED of NGC1705 with all its SINGS data.*

A.27 NGC2146: SBab; D_{KF} = 17.2 Mpc; LIRG; Activity: HII

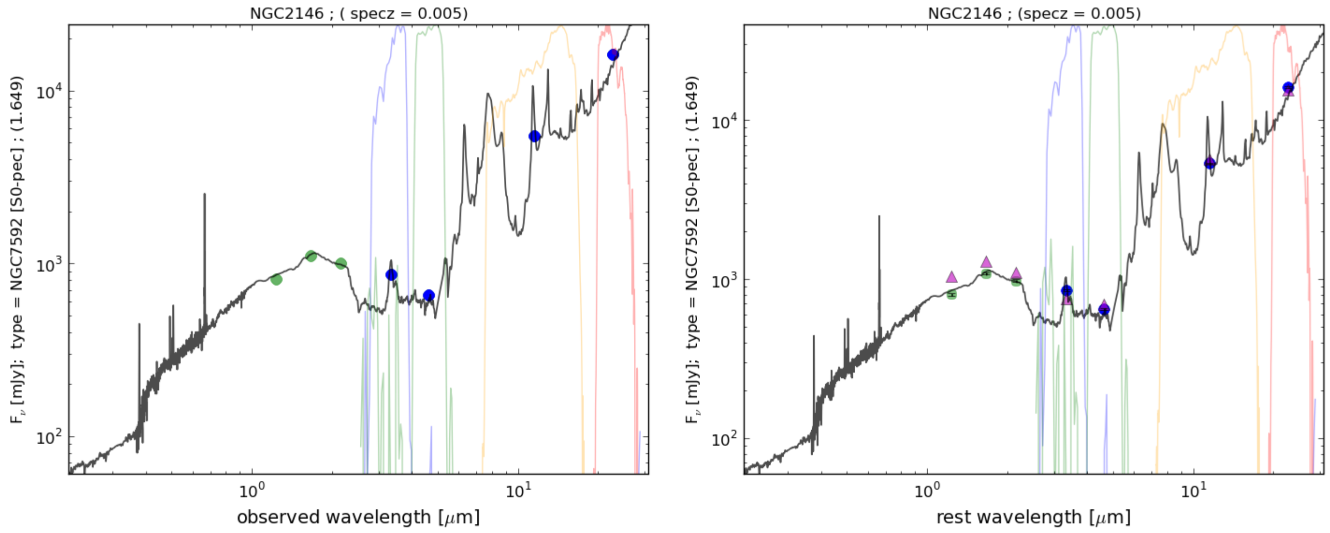

Figure A.27: *Left: SED of NGC2146. Right: Rest-wavelength SED of NGC2146.*

A.28 NGC2403: SABcd; D = 3.5 Mpc; LC III-IV; Activity: HII

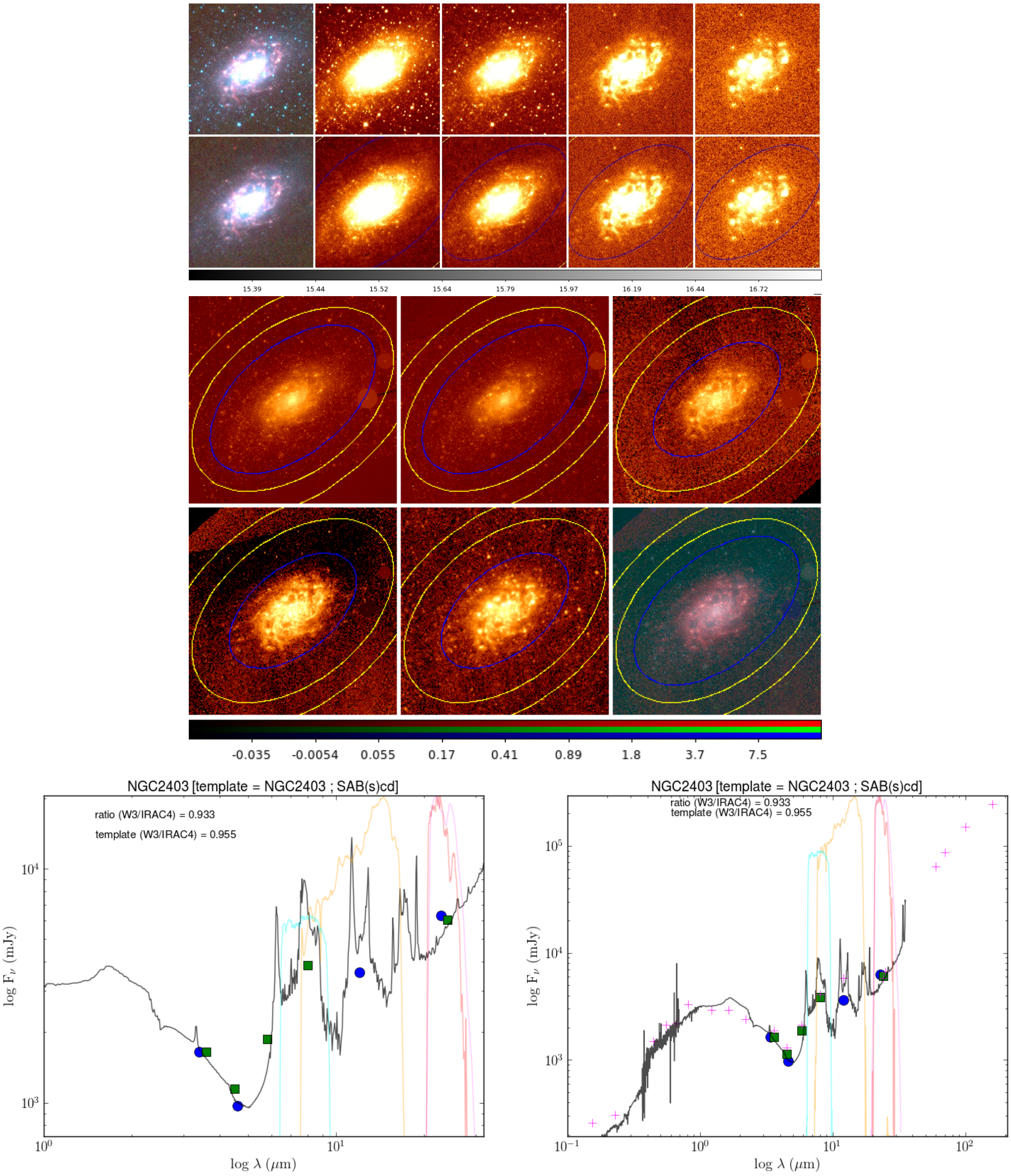

Figure A.28: *Top: WISE imaging of NGC2403, unprocessed and processed. Yellow ellipses are sky annulus borders; blue ellipse is 1σ isophotal ellipse. Left to right: Three-colour (W1+2+3); W_1; W_2; W_3; W_4. Middle: Spitzer imaging of NGC2403. Top left to bottom right: IRAC1, IRAC2, IRAC3, IRAC4, MIPS24, three-colour (IRAC1+2+4). Bottom left: SED of NGC2403. Bottom right: SED of NGC2403 with all its SINGS data.*

A.29 NGC2798: SB(s)ap; D = 24.7 Mpc; LC I; Activity: HII

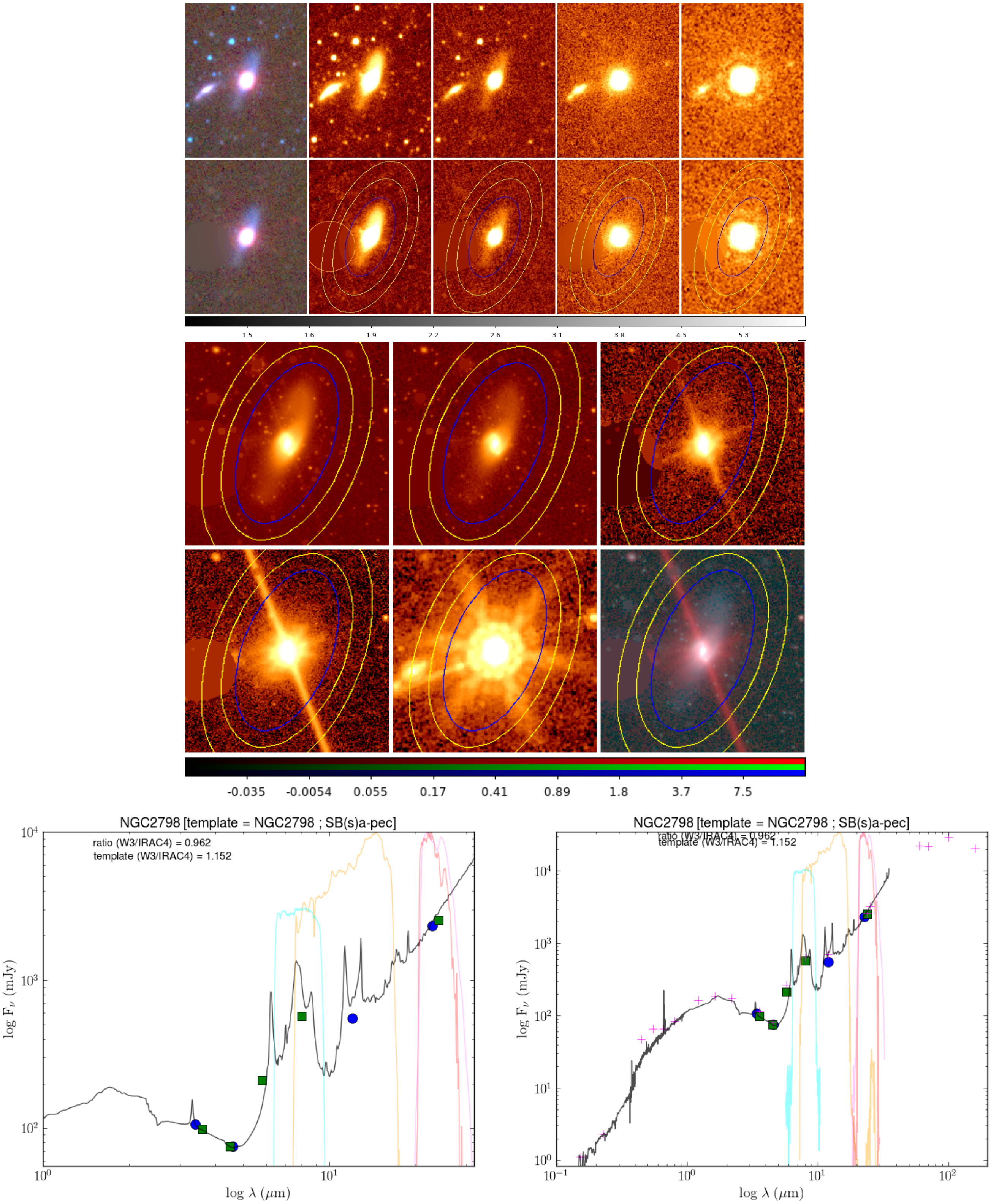

Figure A.29: *Top: WISE imaging of NGC2798, unprocessed and processed. Yellow ellipses are sky annulus borders; blue ellipse is 1σ isophotal ellipse. Left to right: Three-colour (W1+2+3);* W_1*;* W_2*;* W_3*;* W_4*. Middle: Spitzer imaging of NGC2798. Top left to bottom right: IRAC1, IRAC2, IRAC3, IRAC4, MIPS24, three-colour (IRAC1+2+4). Bottom left: SED of NGC2798. Bottom right: SED of NGC2798 with all its SINGS data.*

A.30 NGC2841: SA(r)b; D = 9.8 Mpc; LC II; Activity: LINER/Sy1

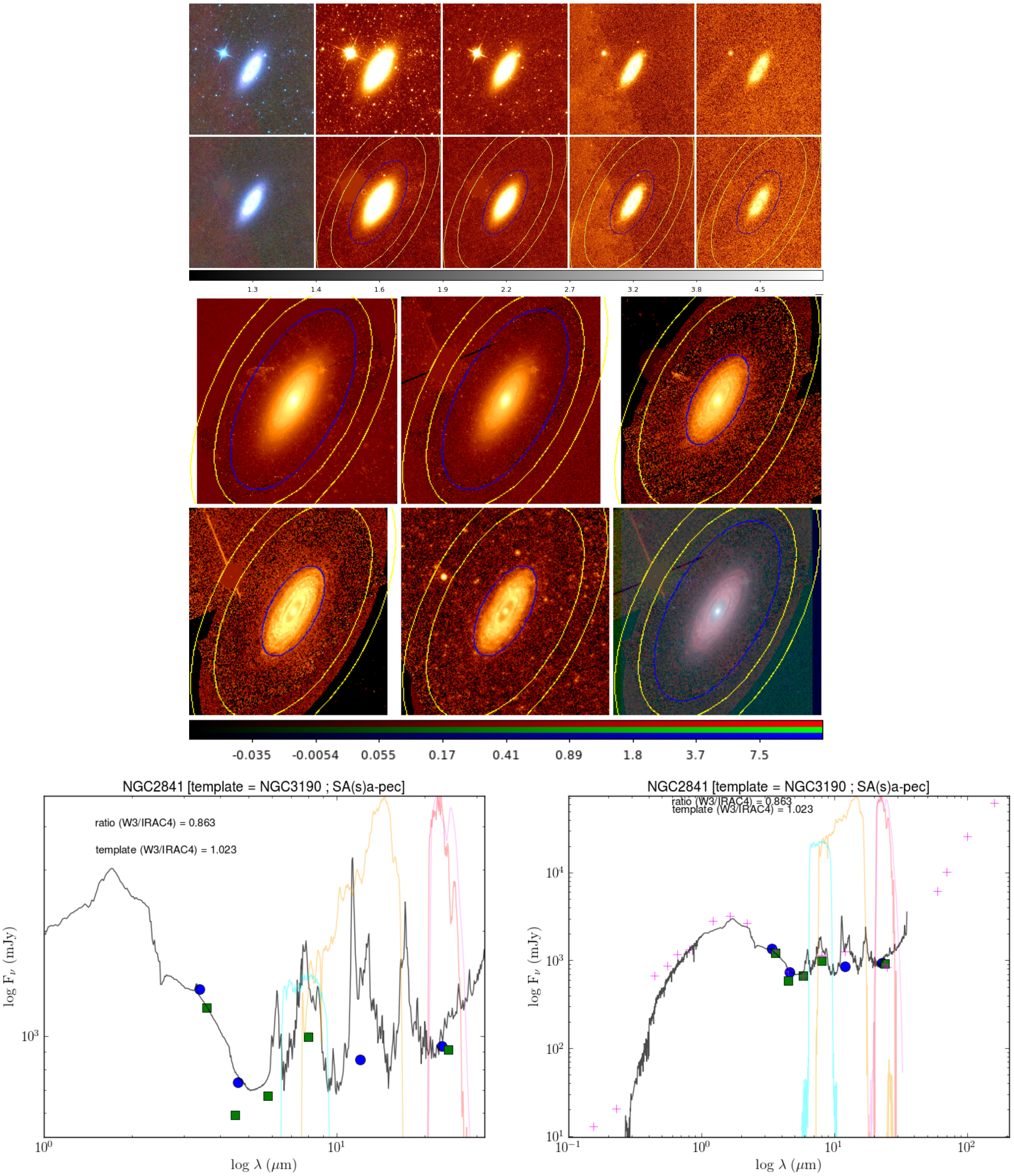

Figure A.30: *Top: WISE imaging of NGC2841, unprocessed and processed. Yellow ellipses are sky annulus borders; blue ellipse is 1σ isophotal ellipse. Left to right: Three-colour (W1+2+3);* W_1; W_2; W_3; W_4. *Middle: Spitzer imaging of NGC2841. Top left to bottom right: IRAC1, IRAC2, IRAC3, IRAC4, MIPS24, three-colour (IRAC1+2+4). Bottom left: SED of NGC2841. Bottom right: SED of NGC2841 with all its SINGS data.*

A.31 NGC2915: I0; D = 2.7 Mpc; Activity: HII

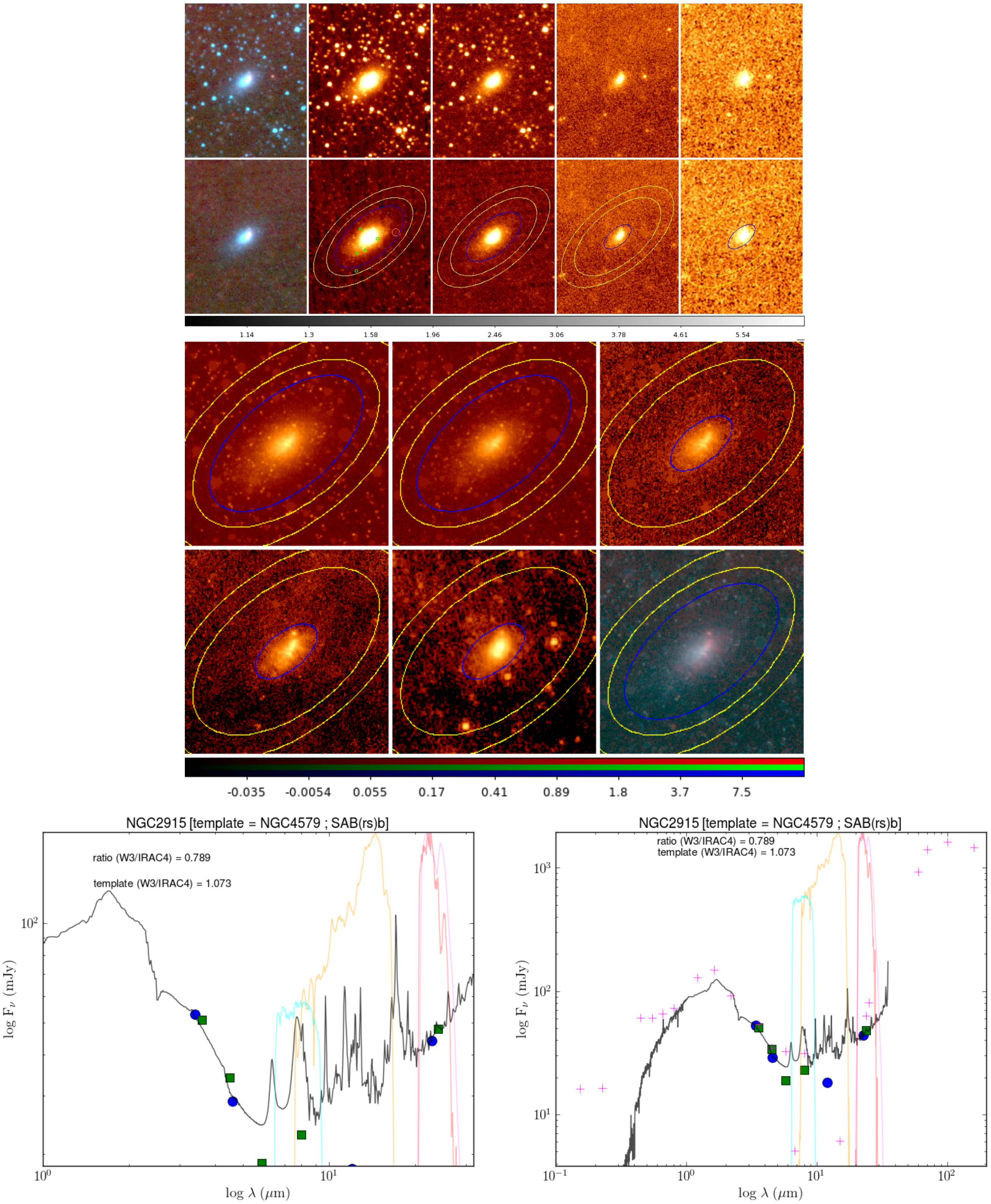

Figure A.31: *Top: WISE imaging of NGC2915, unprocessed and processed. Yellow ellipses are sky annulus borders; blue ellipse is 1σ isophotal ellipse. Left to right: Three-colour (W1+2+3); W_1; W_2; W_3; W_4. Middle: Spitzer imaging of NGC2915. Top left to bottom right: IRAC1, IRAC2, IRAC3, IRAC4, MIPS24, three-colour (IRAC1+2+4). Bottom left: SED of NGC2915. Bottom right: SED of NGC2915 with all its SINGS data.*

A.32 NGC2976: SAcp; D = 3.5 Mpc; LC III; Activity: HII

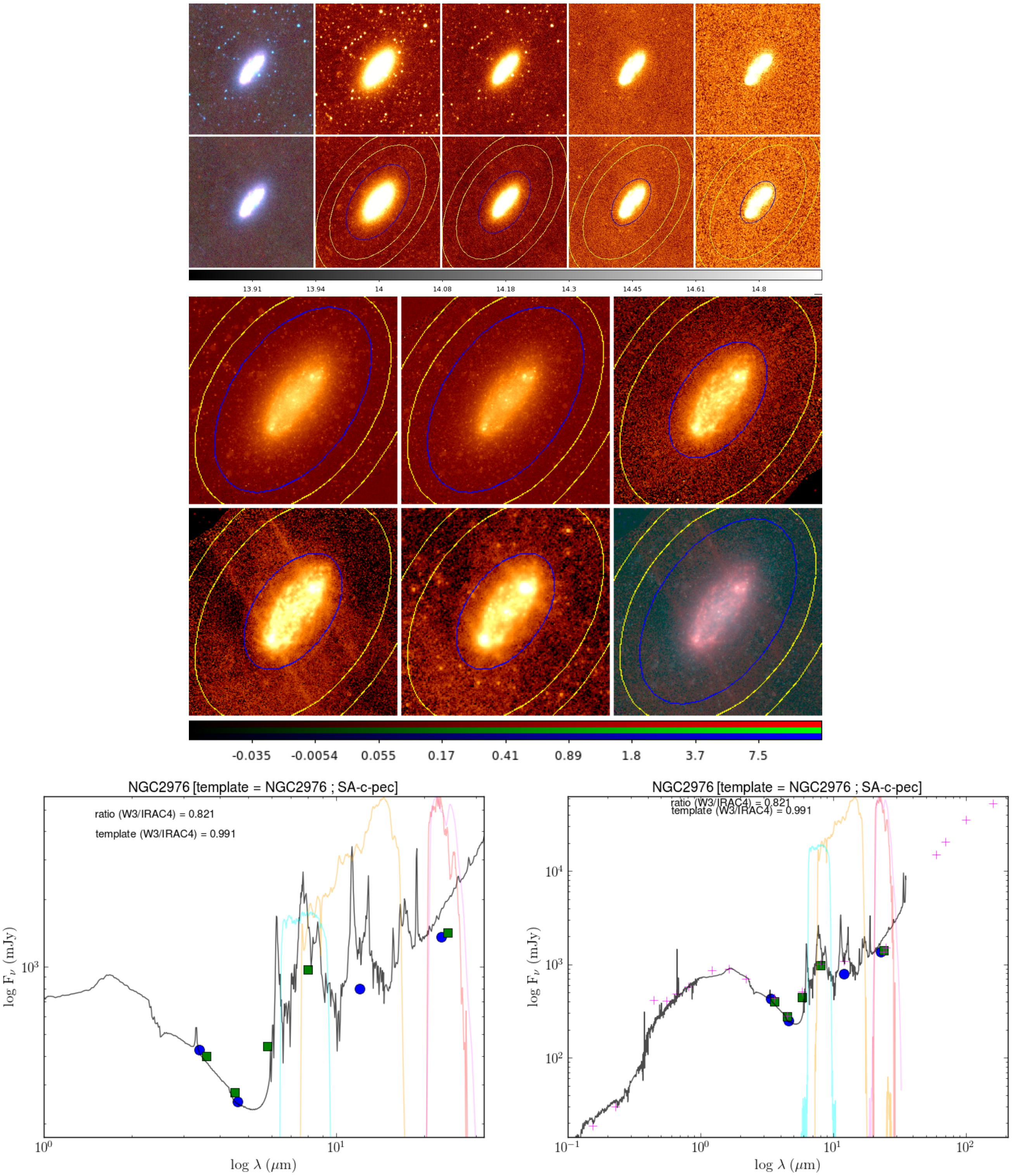

Figure A.32: *Top: WISE imaging of NGC2976, unprocessed and processed. Yellow ellipses are sky annulus borders; blue ellipse is 1σ isophotal ellipse. Left to right: Three-colour (W1+2+3); W_1; W_2; W_3; W_4. Middle: Spitzer imaging of NGC2976. Top left to bottom right: IRAC1, IRAC2, IRAC3, IRAC4, MIPS24, three-colour (IRAC1+2+4). Bottom left: SED of NGC2976. Bottom right: SED of NGC2976 with all its SINGS data.*

A.33 NGC3031/M81: SA(s)ab; D = 3.5 Mpc; LC I-II; Activity: LINER/Sy

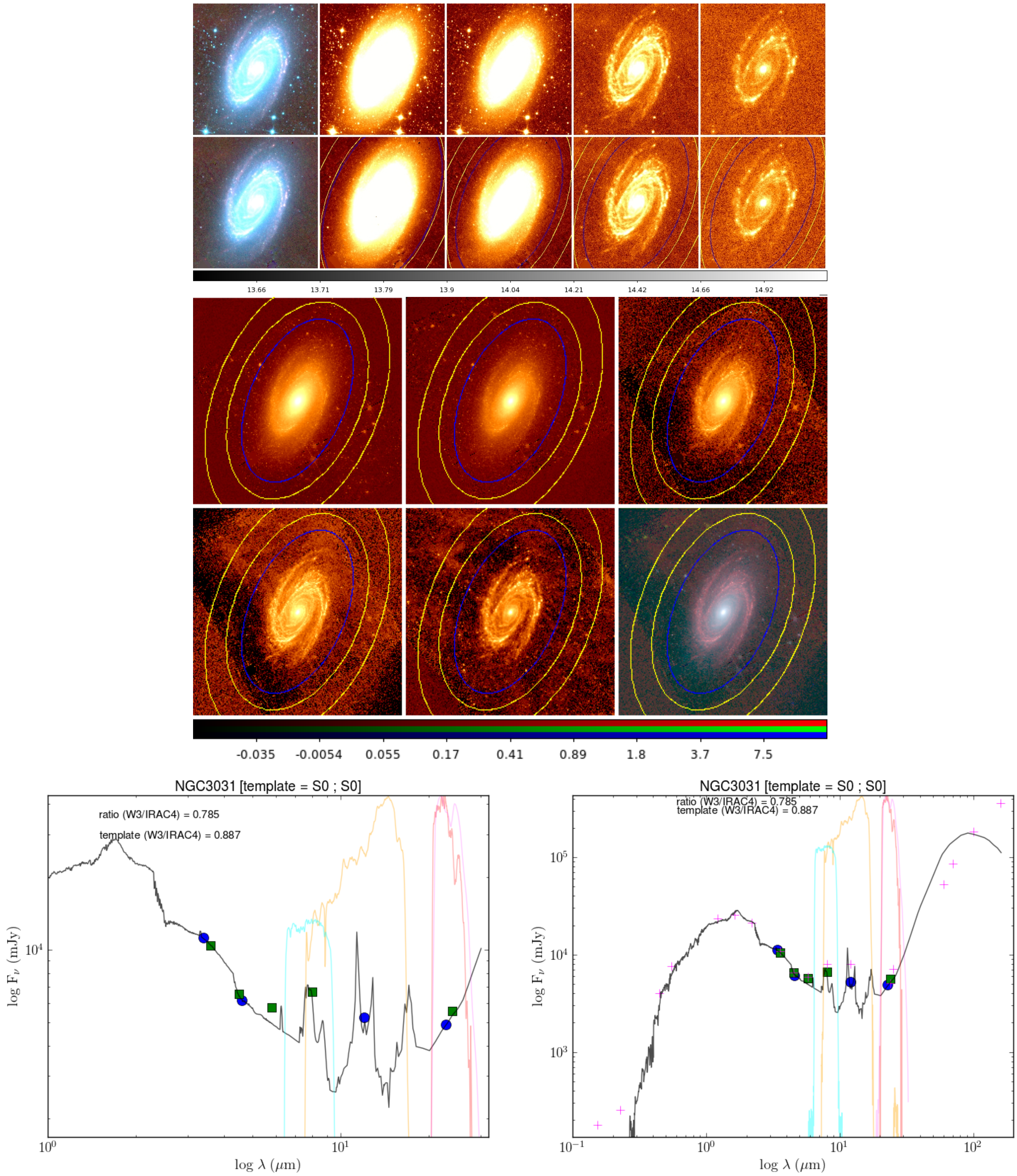

Figure A.33: *Top: WISE imaging of NGC3031/M81, unprocessed and processed. Yellow ellipses are sky annulus borders; blue ellipse is 1σ isophotal ellipse. Left to right: Three-colour (W1+2+3); W_1; W_2; W_3; W_4. Middle: Spitzer imaging of NGC3031/M81. Top left to bottom right: IRAC1, IRAC2, IRAC3, IRAC4, MIPS24, three-colour (IRAC1+2+4). Bottom left: SED of NGC3031/M81. Bottom right: SED of NGC3031/M81 with all its SINGS data.*

A.34 NGC3034/M82: I0; D = 3.5 Mpc; Activity: HII/Sbst

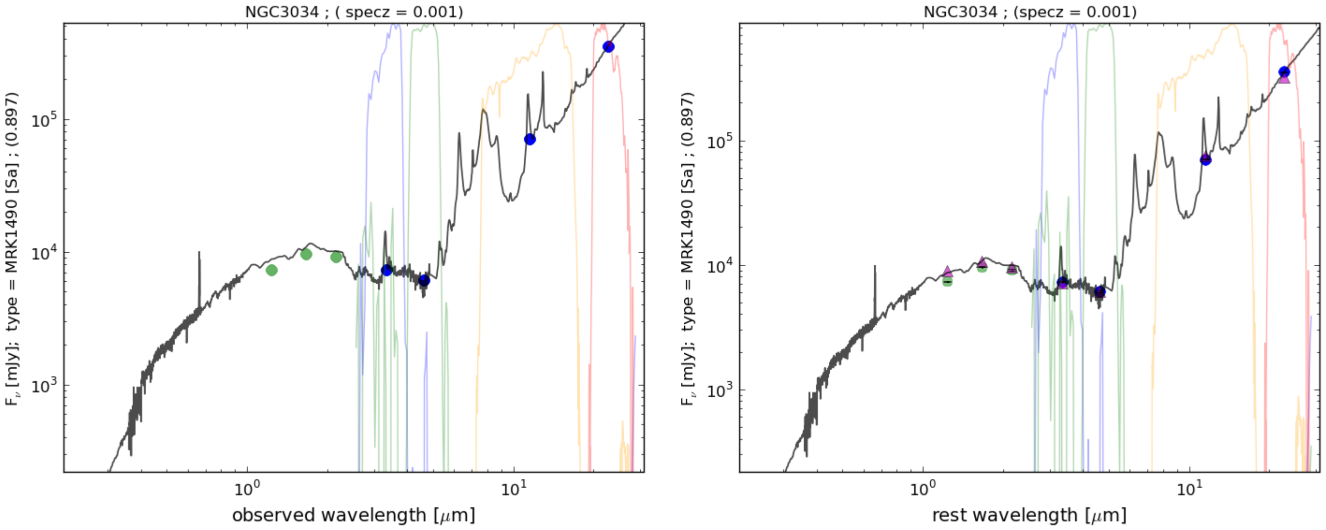

Figure A.34: *Left: SED of M82. Right: Rest-wavelength SED of M82.*

A.35 NGC3049: SB(rs)ab; D = 19.6 Mpc; LC I-II; Activity: HII/Sbst

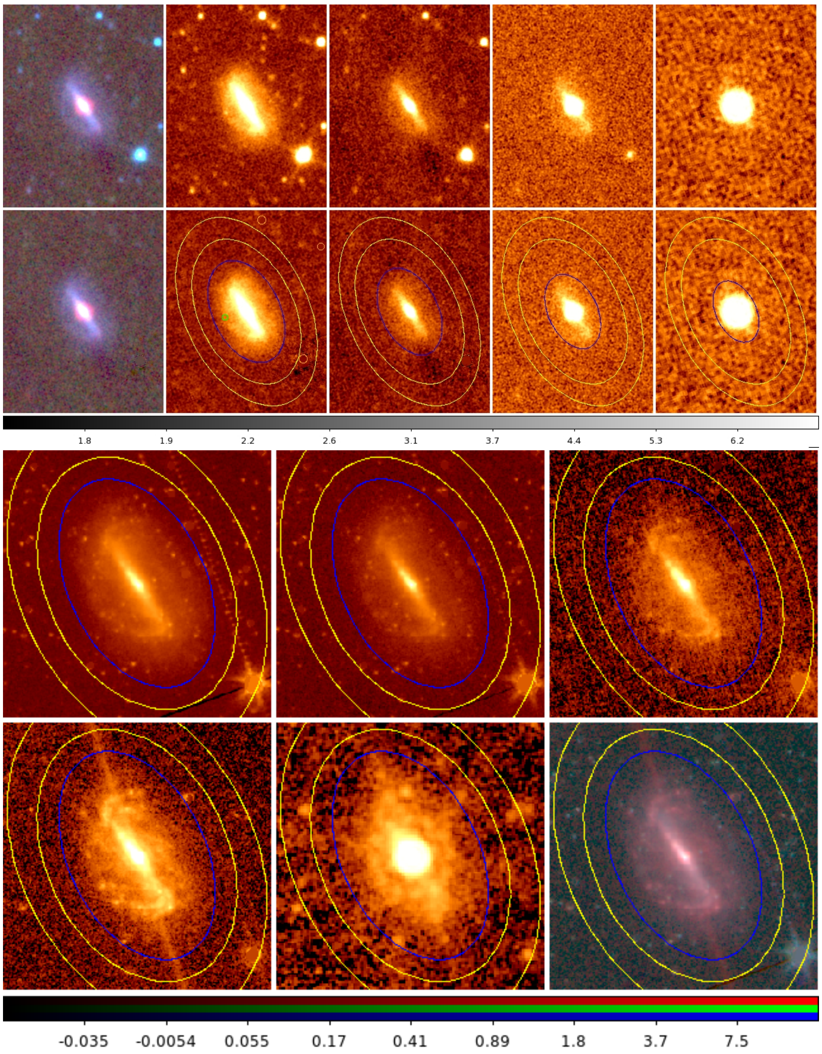

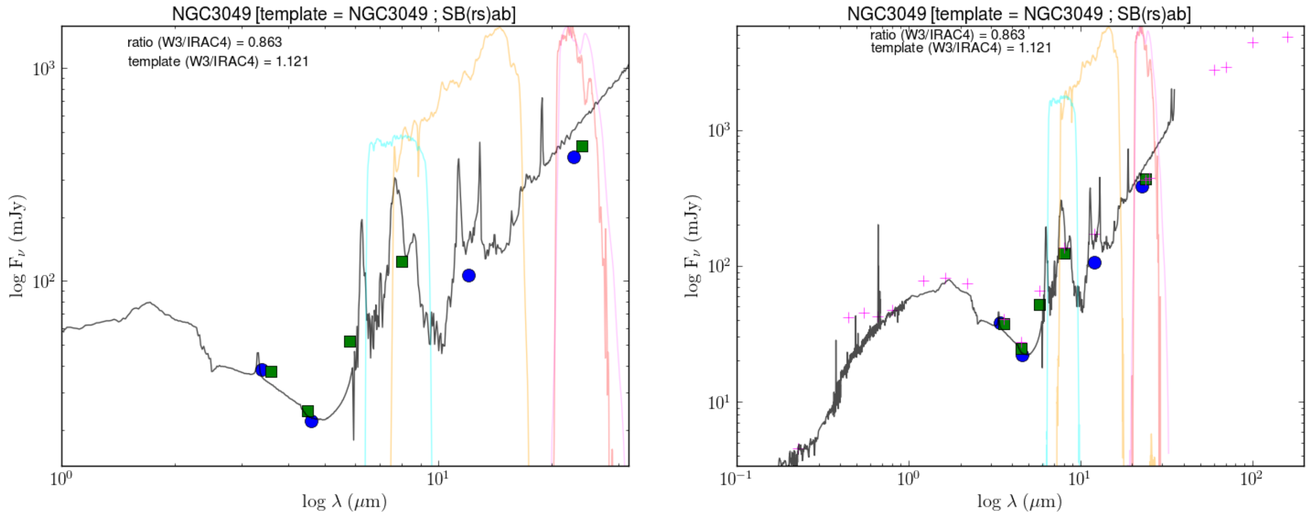

Figure A.35: *Top: WISE imaging of NGC3049, unprocessed and processed. Yellow ellipses are sky annulus borders; blue ellipse is 1σ isophotal ellipse. Left to right: Three-colour (W1+2+3); W_1; W_2; W_3; W_4. Middle: Spitzer imaging of NGC3049. Top left to bottom right: IRAC1, IRAC2, IRAC3, IRAC4, MIPS24, three-colour (IRAC1+2+4). Bottom left: SED of NGC3049. Bottom right: SED of NGC3049 with all its SINGS data.*

A.36 NGC3077: I0 pec; D_{KF} = 3.83 Mpc; Activity: HII

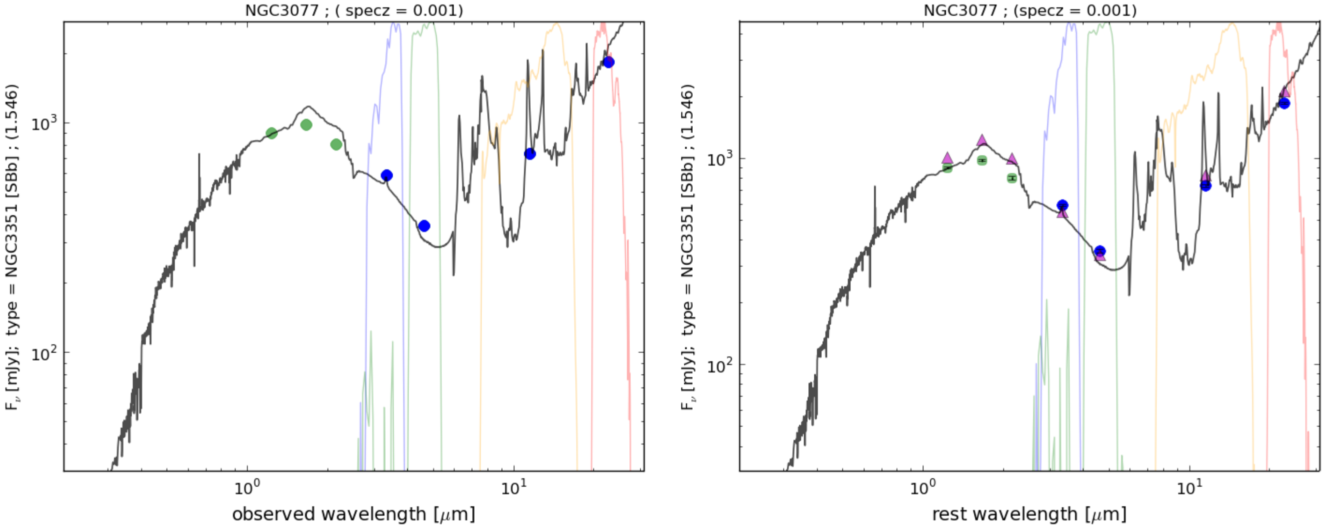

Figure A.36: *Left: SED of NGC3077. Right: Rest-wavelength SED of NGC3077.*

A.37 NGC3184: SAB(rs)cd; D = 8.6 Mpc; LC III-IV; Activity: HII

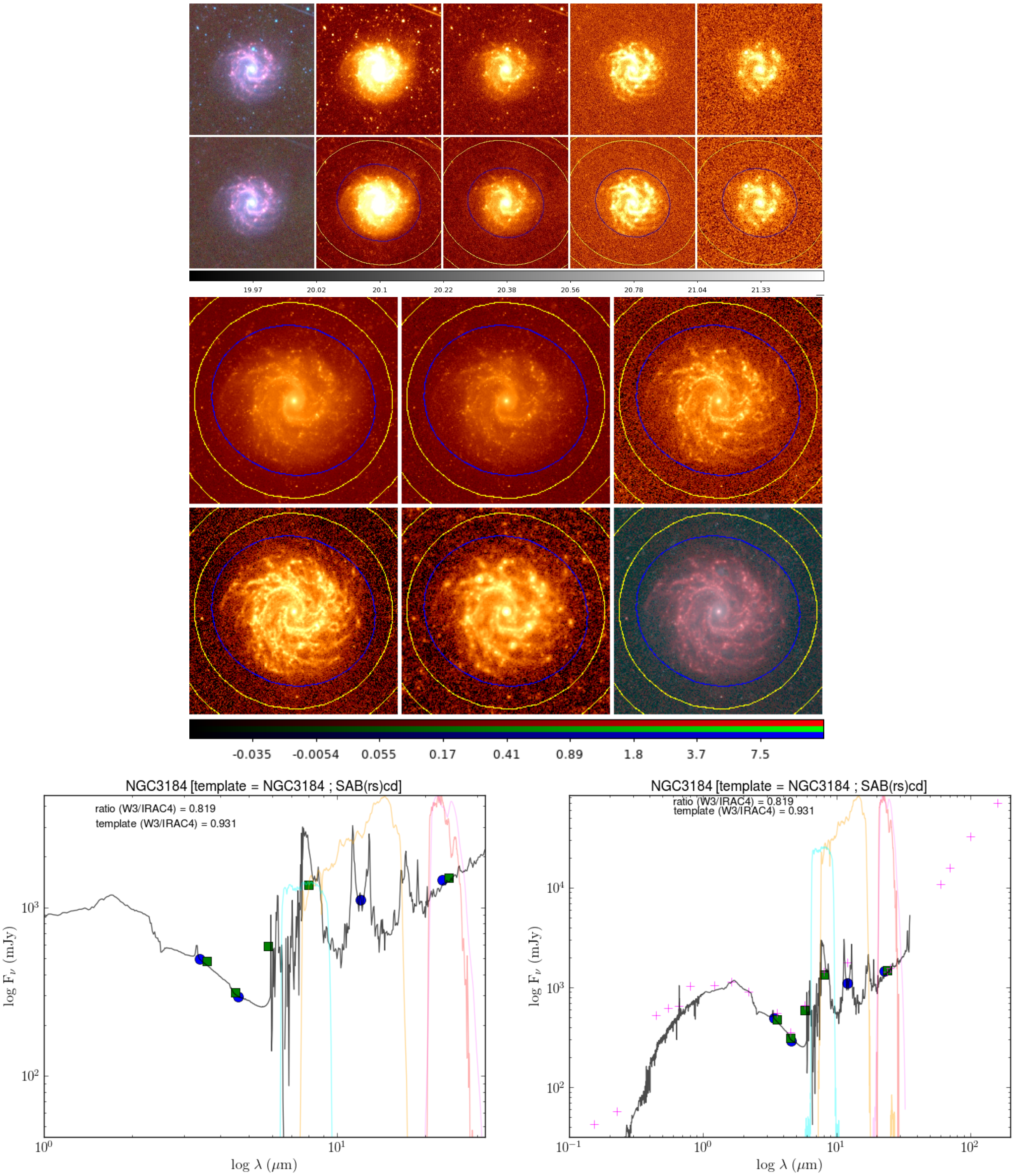

Figure A.37: *Top: WISE imaging of NGC3184, unprocessed and processed. Yellow ellipses are sky annulus borders; blue ellipse is 1σ isophotal ellipse. Left to right: Three-colour (W1+2+3);* W_1; W_2; W_3; W_4. *Middle: Spitzer imaging of NGC3184. Top left to bottom right: IRAC1, IRAC2, IRAC3, IRAC4, MIPS24, three-colour (IRAC1+2+4). Bottom left: SED of NGC3184. Bottom right: SED of NGC3184 with all its SINGS data.*

A.38 NGC3190: SA(s)ap; D = 17.4 Mpc; LC I; Activity: LINER

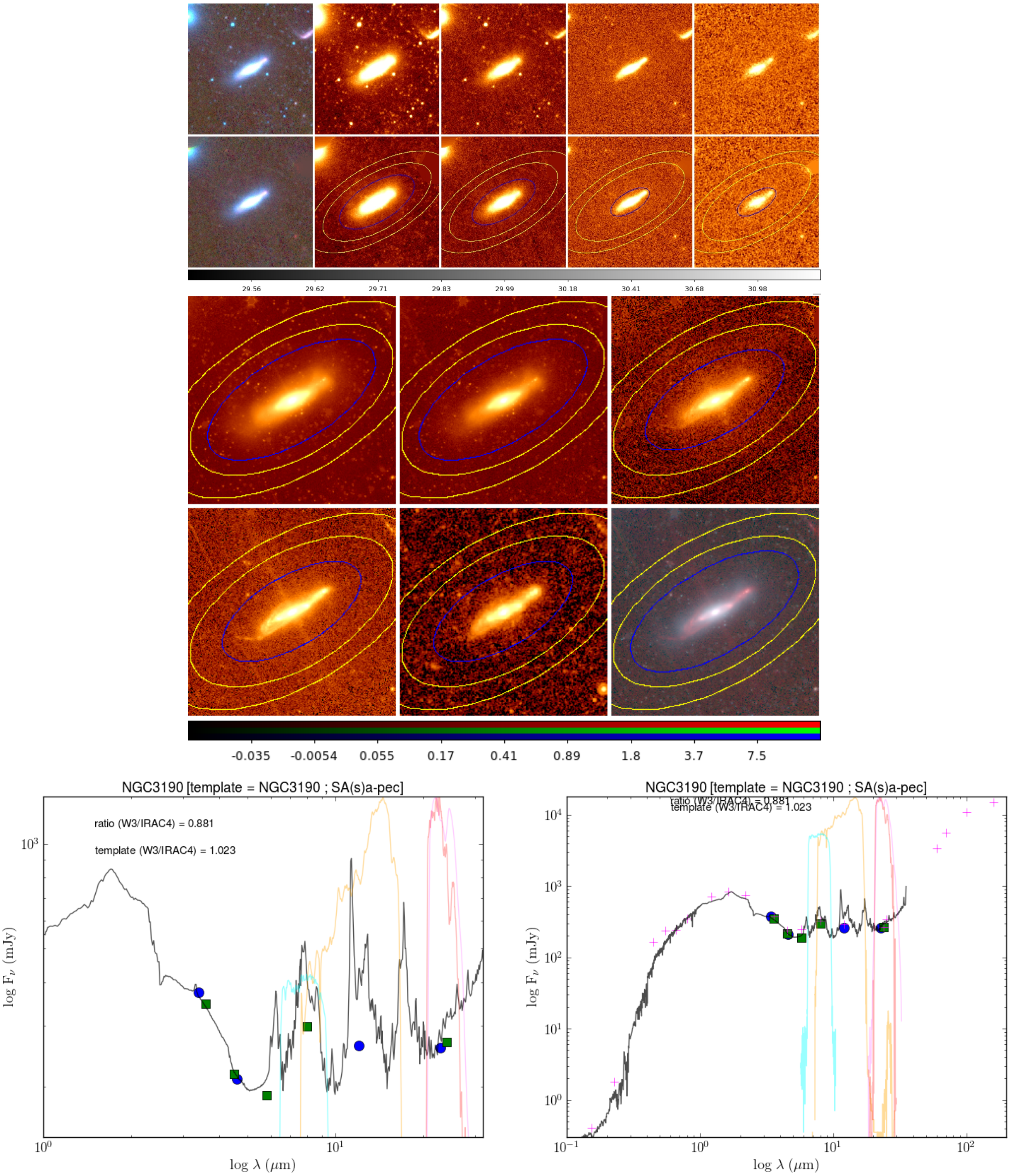

Figure A.38: *Top: WISE imaging of NGC3190, unprocessed and processed. Yellow ellipses are sky annulus borders; blue ellipse is 1σ isophotal ellipse. Left to right: Three-colour (W1+2+3); W_1; W_2; W_3; W_4. Middle: Spitzer imaging of NGC3190. Top left to bottom right: IRAC1, IRAC2, IRAC3, IRAC4, MIPS24, three-colour (IRAC1+2+4). Bottom left: SED of NGC3190. Bottom right: SED of NGC3190 with all its SINGS data.*

A.39 NGC3198: SB(rs)c; D = 9.8 Mpc; LC III; Activity: HII

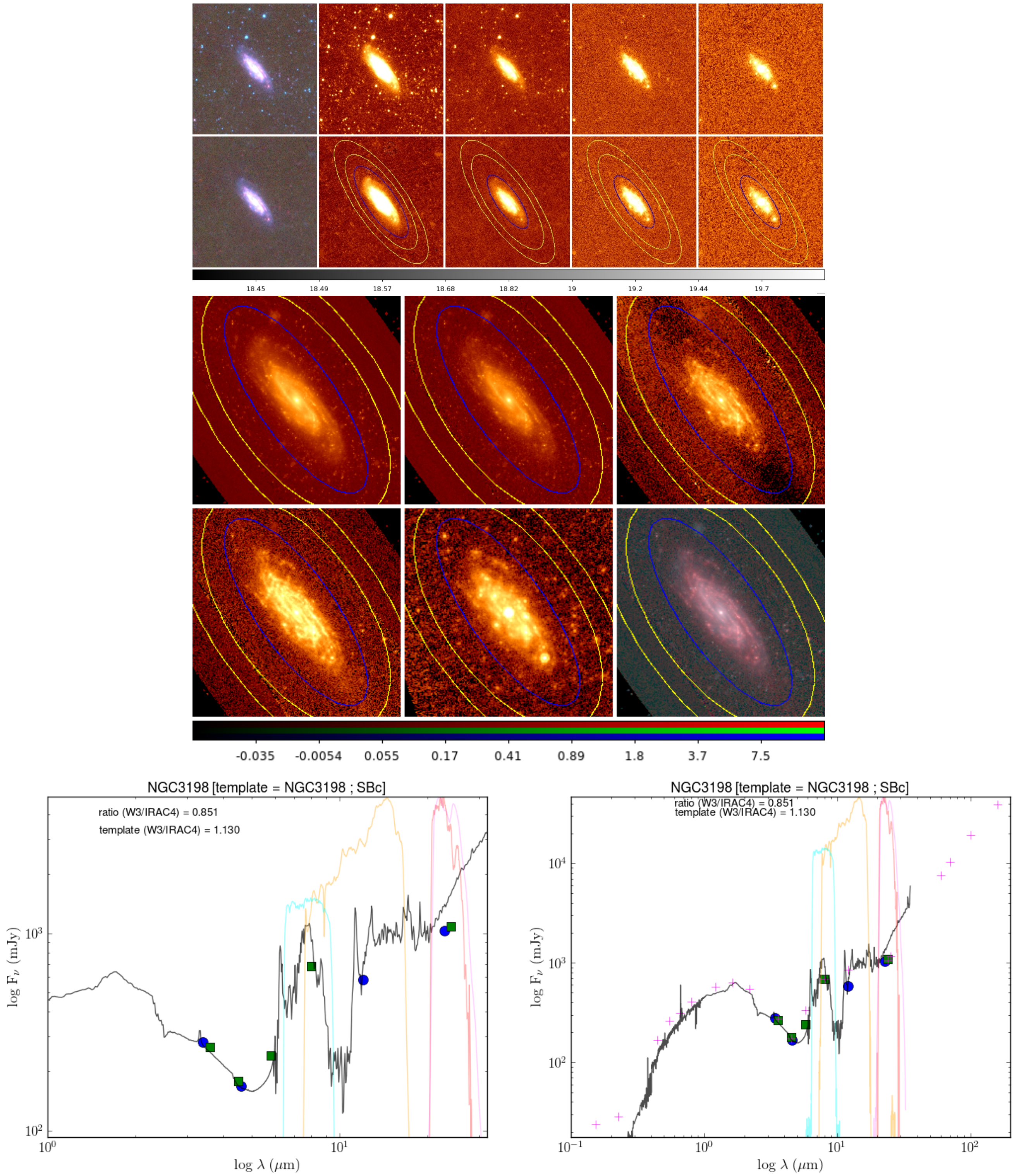

Figure A.39: *Top: WISE imaging of NGC3198, unprocessed and processed. Yellow ellipses are sky annulus borders; blue ellipse is 1σ isophotal ellipse. Left to right: Three-colour (W1+2+3); W$_1$; W$_2$; W$_3$; W$_4$. Middle: Spitzer imaging of NGC3198. Top left to bottom right: IRAC1, IRAC2, IRAC3, IRAC4, MIPS24, three-colour (IRAC1+2+4). Bottom left: SED of NGC3198. Bottom right: SED of NGC3198 with all its SINGS data.*

A.40 NGC3265: E; D = 20.0 Mpc; Activity: HII/WR

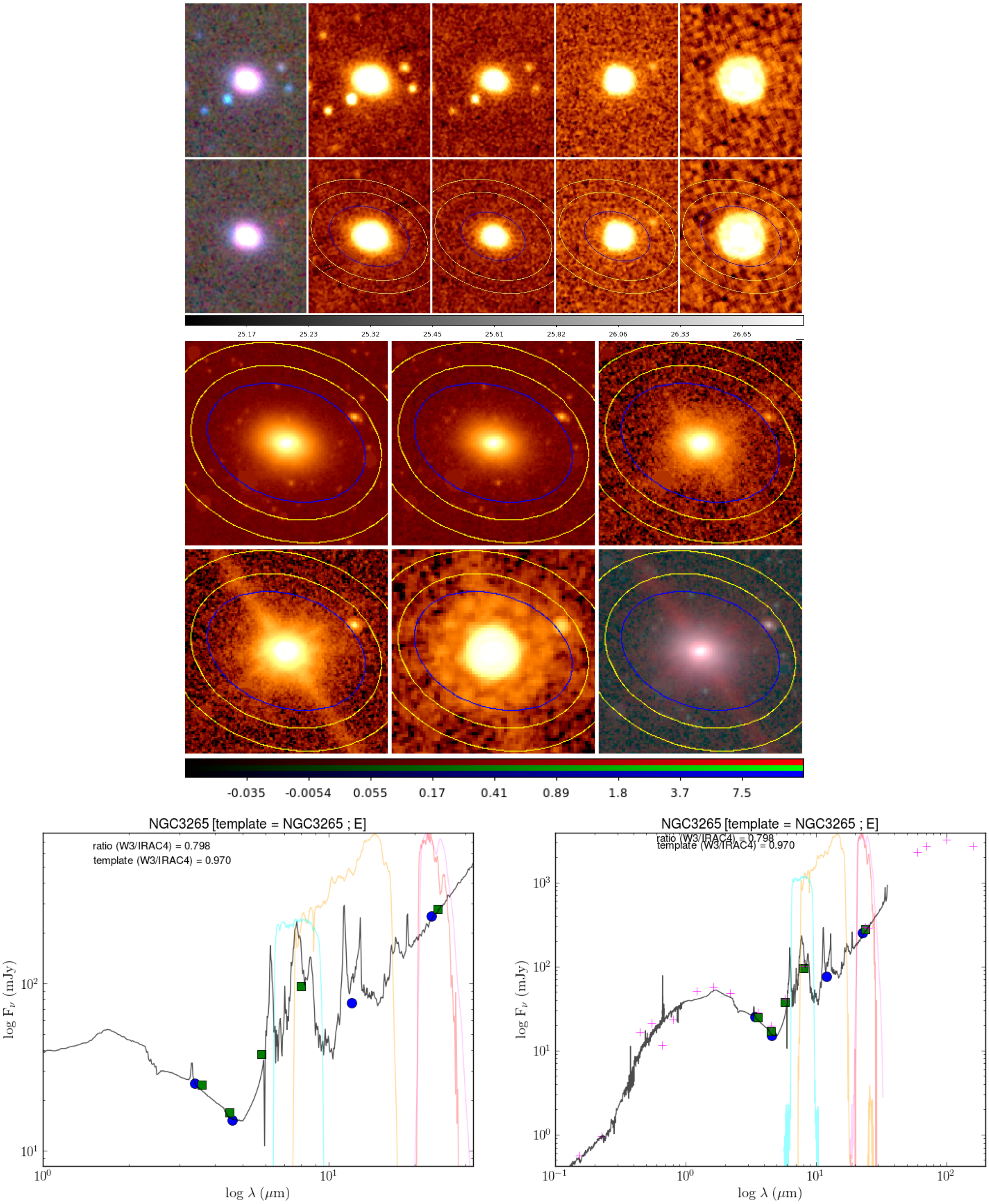

Figure A.40: *Top: WISE imaging of NGC3265, unprocessed and processed. Yellow ellipses are sky annulus borders; blue ellipse is 1σ isophotal ellipse. Left to right: Three-colour (W1+2+3); W$_1$; W$_2$; W$_3$; W$_4$. Middle: Spitzer imaging of NGC3265. Top left to bottom right: IRAC1, IRAC2, IRAC3, IRAC4, MIPS24, three-colour (IRAC1+2+4). Bottom left: SED of NGC3265. Bottom right: SED of NGC3265 with all its SINGS data.*

A.41 NGC3351: SB(r)b; D = 9.3 Mpc; LC II; Activity: HII/Sbst

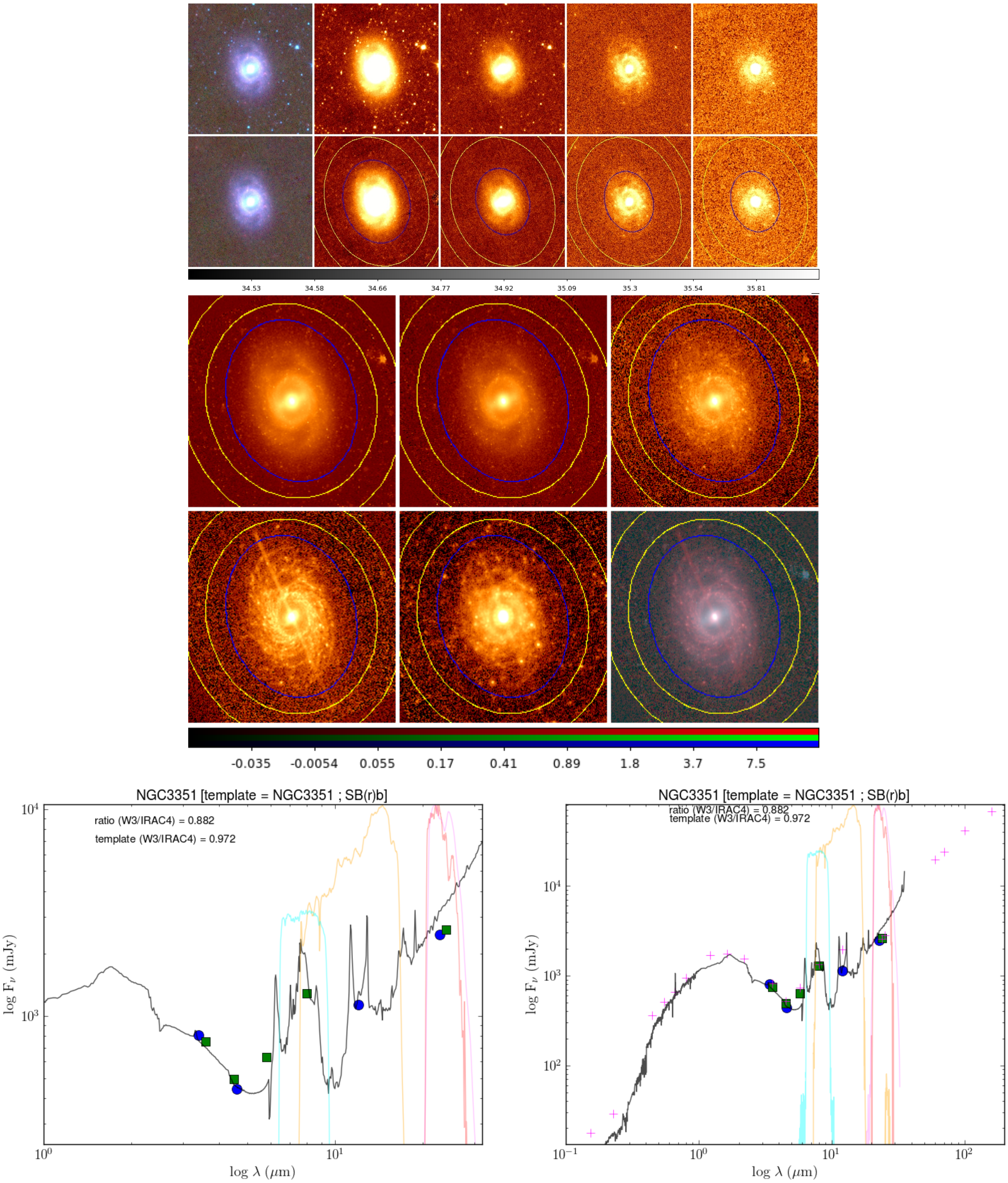

Figure A.41: *Top: WISE imaging of NGC3351, unprocessed and processed. Yellow ellipses are sky annulus borders; blue ellipse is 1σ isophotal ellipse. Left to right: Three-colour (W1+2+3); W_1; W_2; W_3; W_4. Middle: Spitzer imaging of NGC3351. Top left to bottom right: IRAC1, IRAC2, IRAC3, IRAC4, MIPS24, three-colour (IRAC1+2+4). Bottom left: SED of NGC3351. Bottom right: SED of NGC3351 with all its SINGS data.*

A.42 NGC3521: SAB(rs)bc; D = 9.0 Mpc; LC II-III; Activity: HII/LINER

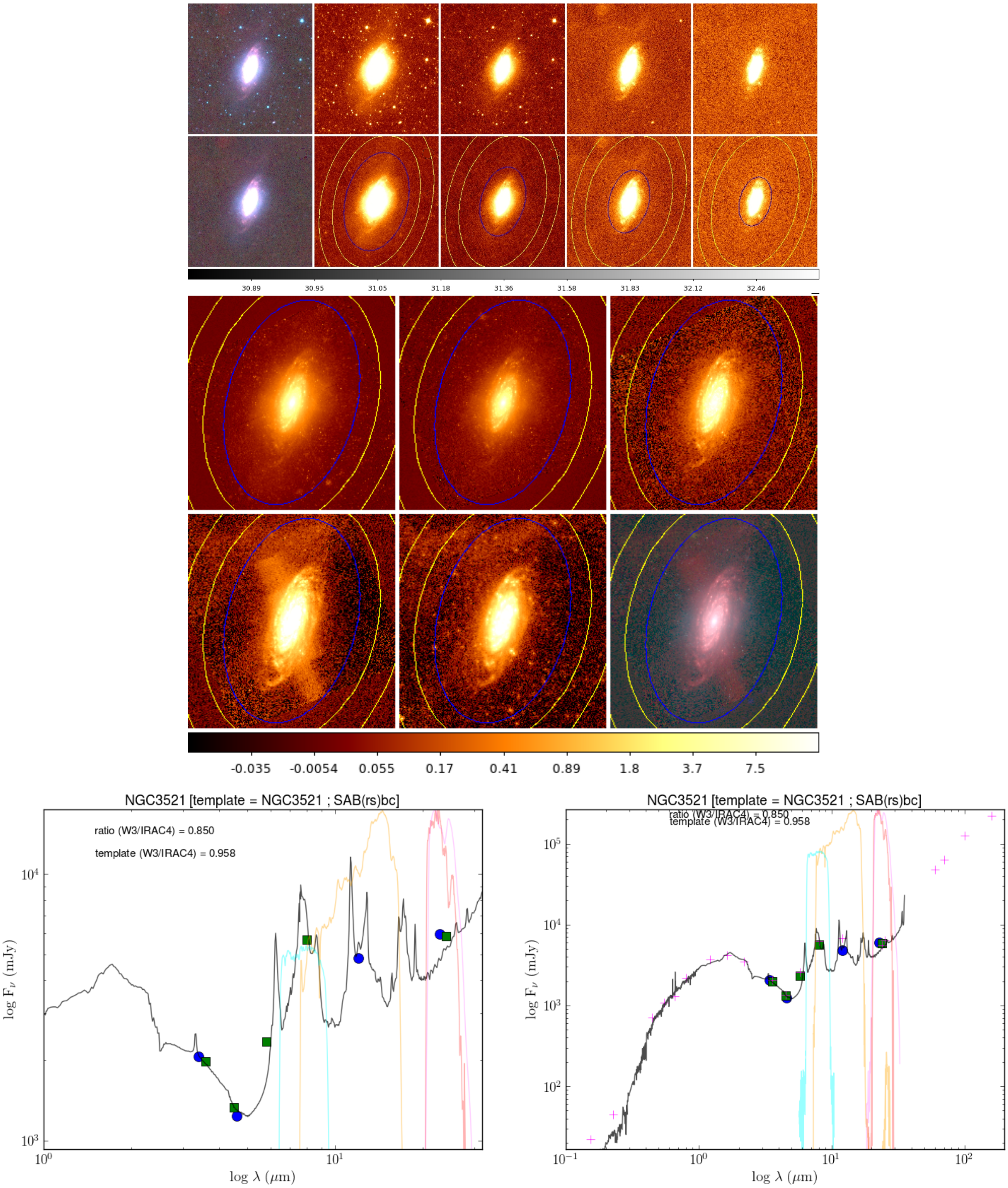

Figure A.42: *Top: WISE imaging of NGC3521, unprocessed and processed. Yellow ellipses are sky annulus borders; blue ellipse is 1σ isophotal ellipse. Left to right: Three-colour (W1+2+3); W_1; W_2; W_3; W_4. Middle: Spitzer imaging of NGC3521. Top left to bottom right: IRAC1, IRAC2, IRAC3, IRAC4, MIPS24, three-colour (IRAC1+2+4). Bottom left: SED of NGC3521. Bottom right: SED of NGC3521 with all its SINGS data.*

A.43 NGC3621: SA(s)d; D = 6.2 Mpc; LC IV; Activity: HII

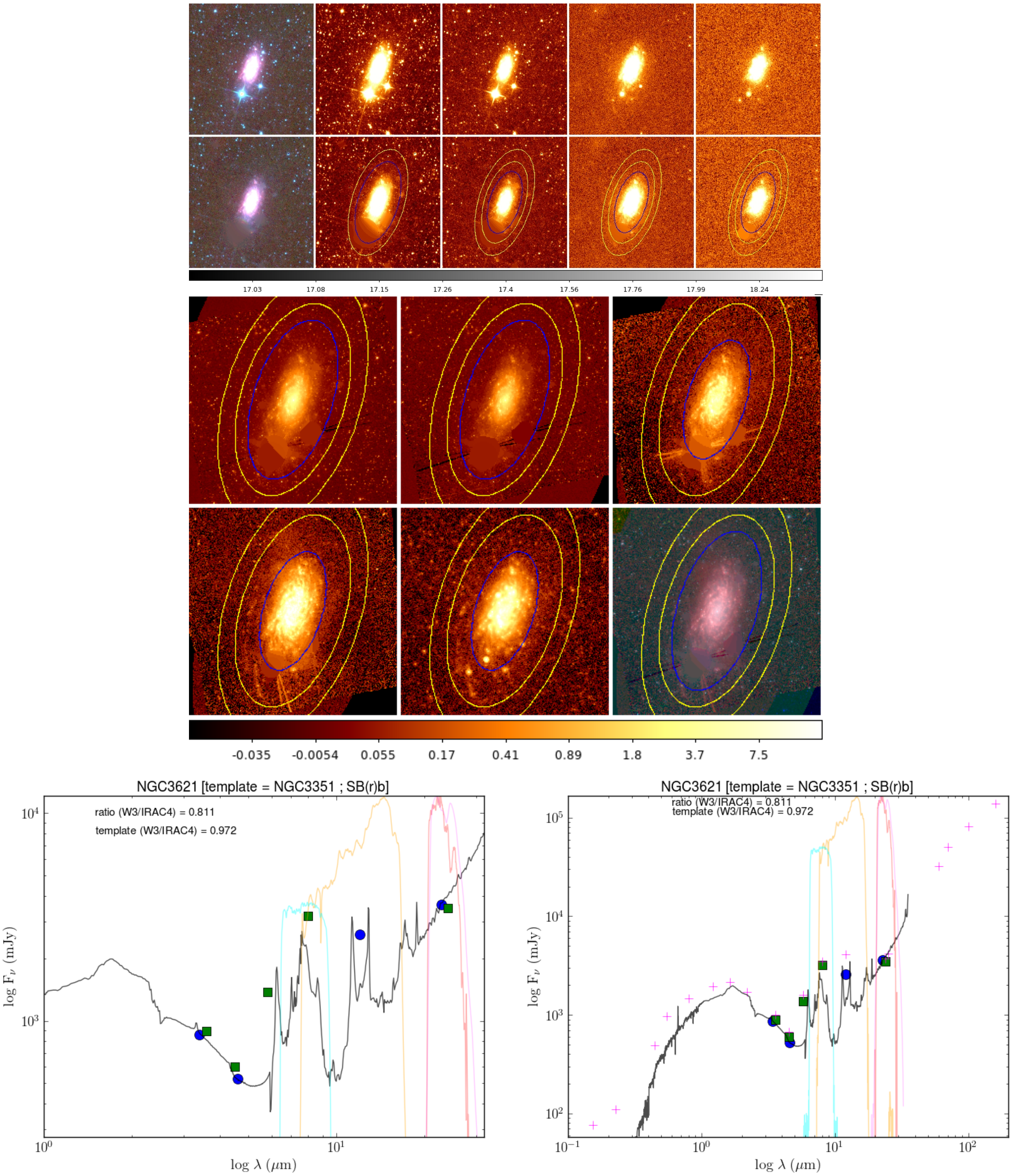

Figure A.43: *Top: WISE imaging of NGC3621, unprocessed and processed. Yellow ellipses are sky annulus borders; blue ellipse is 1σ isophotal ellipse. Left to right: Three-colour (W1+2+3);* W_1; W_2; W_3; W_4. *Middle: Spitzer imaging of NGC3621. Top left to bottom right: IRAC1, IRAC2, IRAC3, IRAC4, MIPS24, three-colour (IRAC1+2+4). Bottom left: SED of NGC3621. Bottom right: SED of NGC3621 with all its SINGS data.*

A.44 NGC3627/M66: SAB(s)b; D = 8.9 Mpc; LC II; Activity: LINER/Sy2

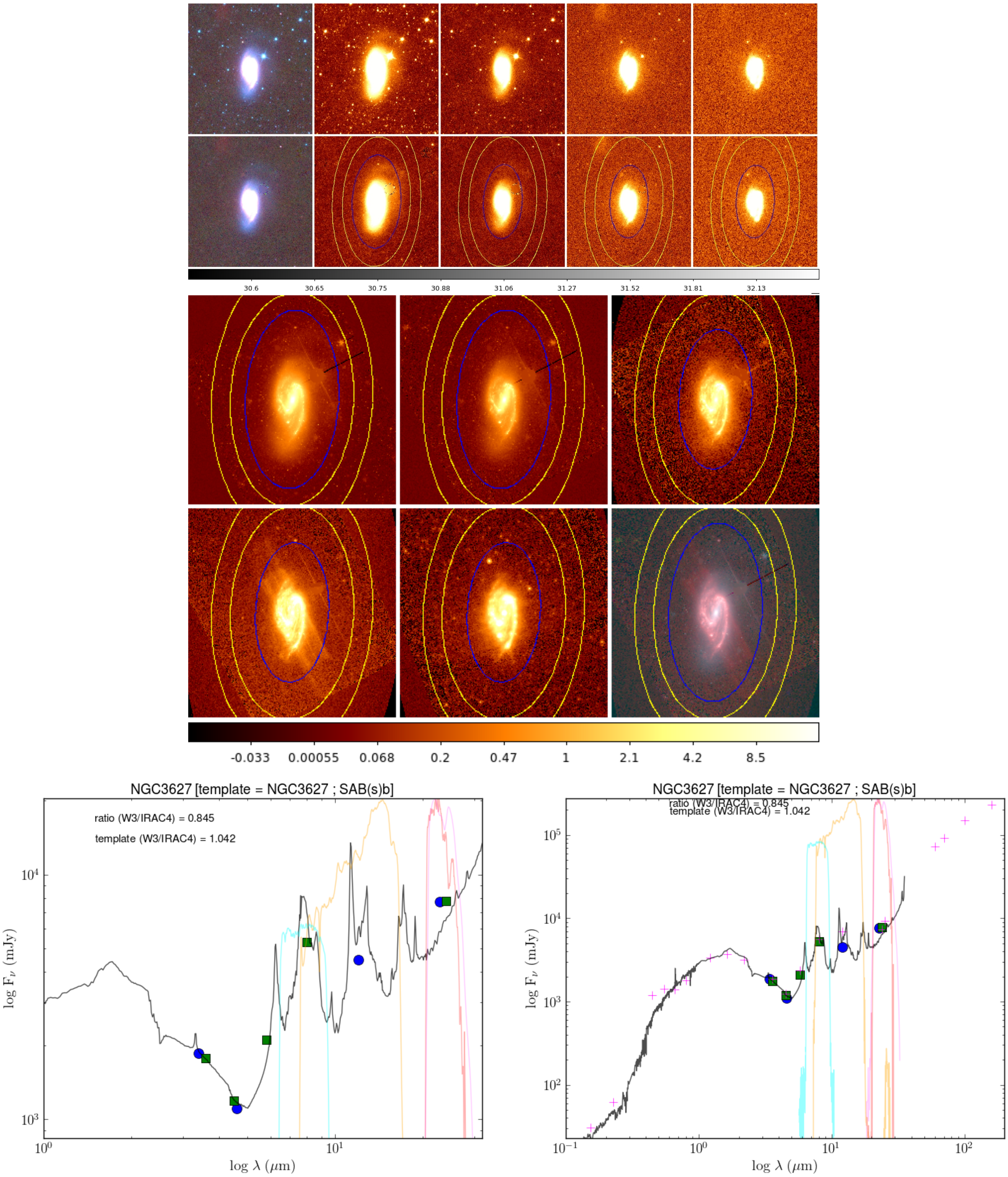

Figure A.44: *Top: WISE imaging of NGC3627, unprocessed and processed. Yellow ellipses are sky annulus borders; blue ellipse is 1σ isophotal ellipse. Left to right: Three-colour (W1+2+3); W_1; W_2; W_3; W_4. Middle: Spitzer imaging of NGC3627. Top left to bottom right: IRAC1, IRAC2, IRAC3, IRAC4, MIPS24, three-colour (IRAC1+2+4). Bottom left: SED of NGC3627. Bottom right: SED of NGC3627 with all its SINGS data.*

A.45 NGC3773: SA0; D = 12.9 Mpc; Activity: HII

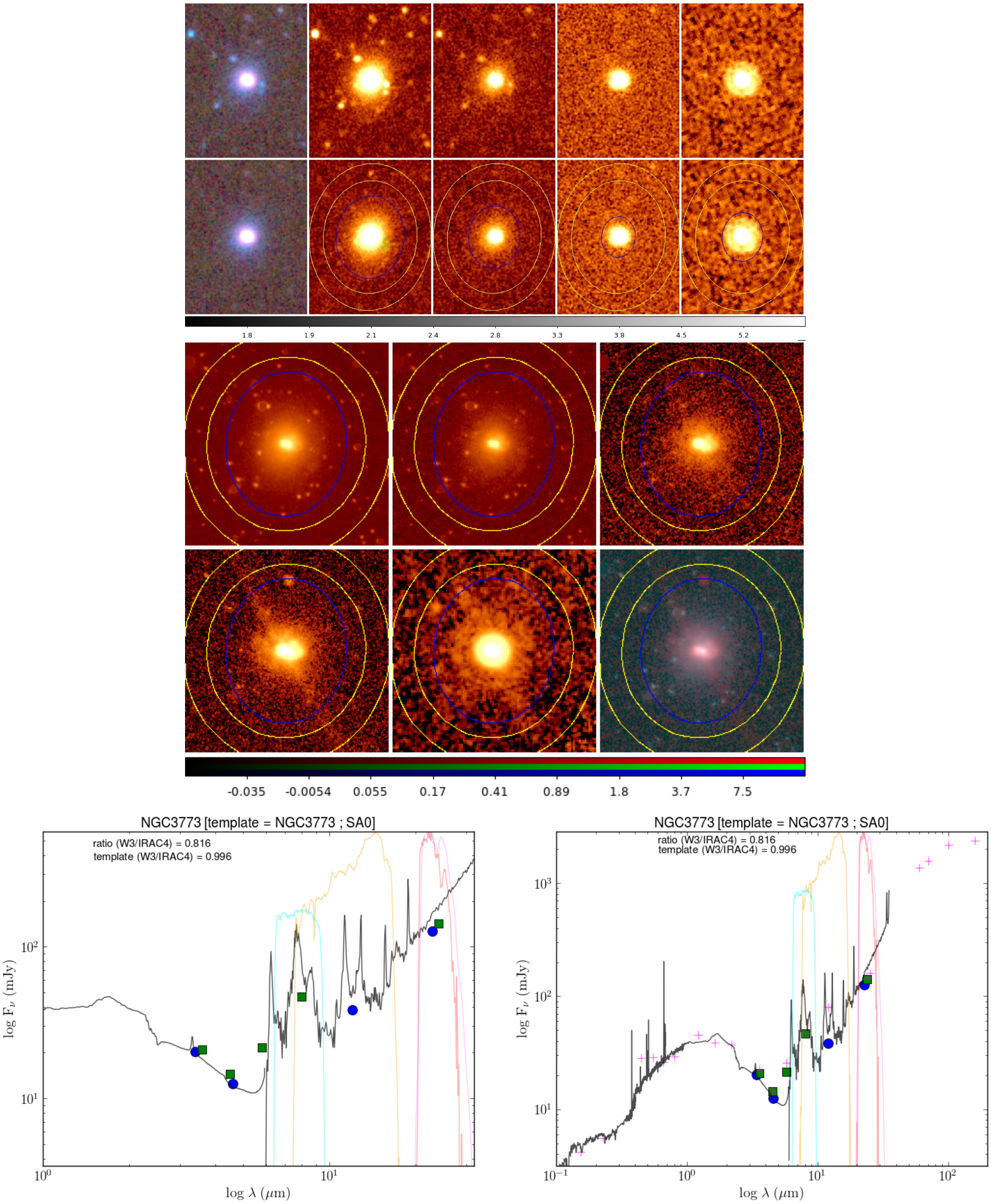

Figure A.45: *Top: WISE imaging of NGC3773, unprocessed and processed. Yellow ellipses are sky annulus borders; blue ellipse is 1σ isophotal ellipse. Left to right: Three-colour (W1+2+3); W_1; W_2; W_3; W_4. Middle: Spitzer imaging of NGC3773. Top left to bottom right: IRAC1, IRAC2, IRAC3, IRAC4, MIPS24, three-colour (IRAC1+2+4). Bottom left: SED of NGC3773. Bottom right: SED of NGC3773 with all its SINGS data.*

A.46 NGC3938: SA(s)c; D = 20.0 Mpc; LC III; Activity: HII

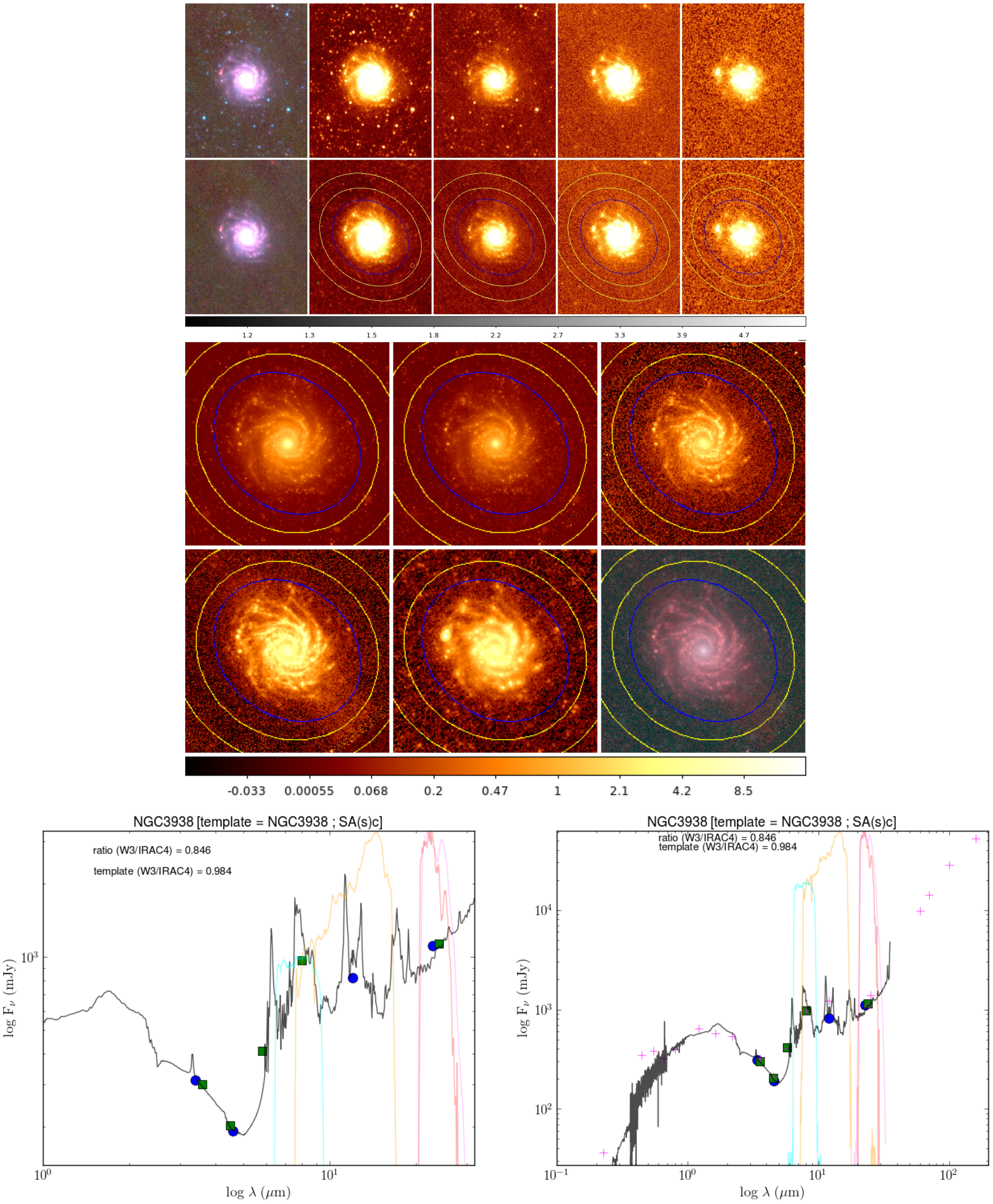

Figure A.46: *Top: WISE imaging of NGC3938, unprocessed and processed. Yellow ellipses are sky annulus borders; blue ellipse is 1σ isophotal ellipse. Left to right: Three-colour (W1+2+3); W_1; W_2; W_3; W_4. Middle: Spitzer imaging of NGC3938. Top left to bottom right: IRAC1, IRAC2, IRAC3, IRAC4, MIPS24, three-colour (IRAC1+2+4). Bottom left: SED of NGC3938. Bottom right: SED of NGC3938 with all its SINGS data.*

A.47 NGC4125: E6p; D = 21.4 Mpc; Activity: LINER

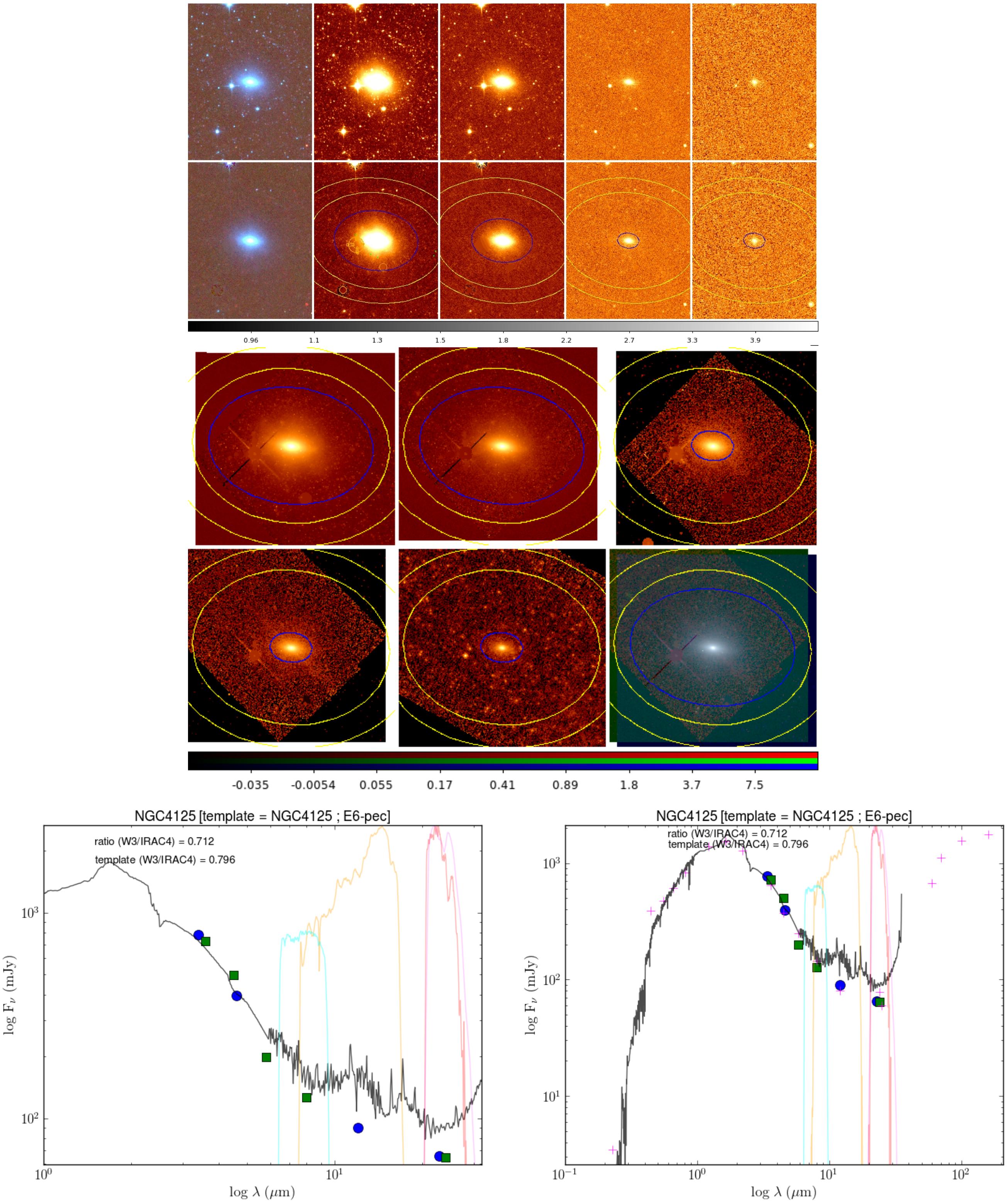

Figure A.47: *Top: WISE imaging of NGC4125, unprocessed and processed. Yellow ellipses are sky annulus borders; blue ellipse is 1σ isophotal ellipse. Left to right: Three-colour (W1+2+3); W$_1$; W$_2$; W$_3$; W$_4$. Middle: Spitzer imaging of NGC4125. Top left to bottom right: IRAC1, IRAC2, IRAC3, IRAC4, MIPS24, three-colour (IRAC1+2+4). Bottom left: SED of NGC4125. Bottom right: SED of NGC4125 with all its SINGS data.*

A.48 NGC4236: SB(s)dm; D = 3.5 Mpc; LC IV-V

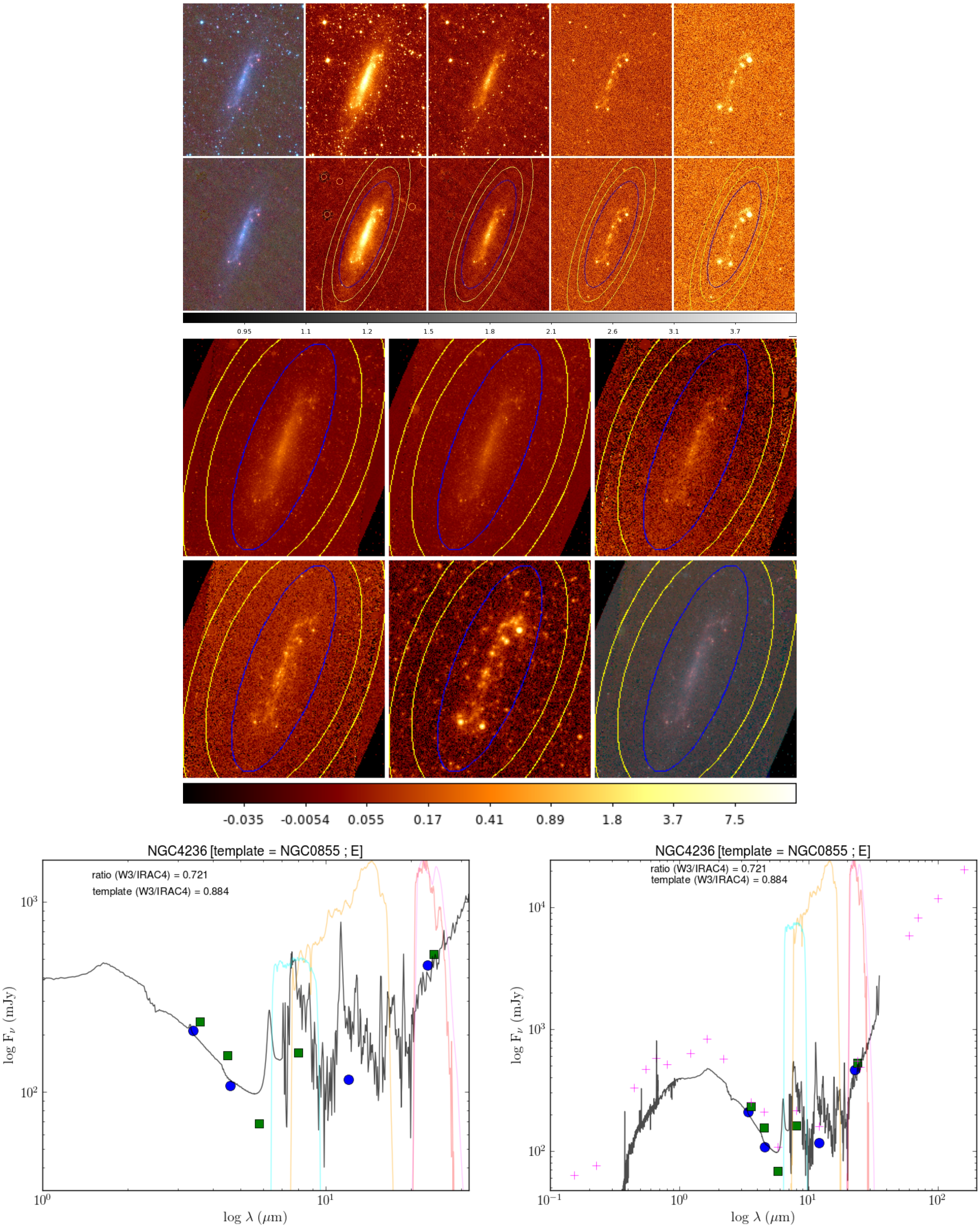

Figure A.48: *Top: WISE imaging of NGC4236, unprocessed and processed. Yellow ellipses are sky annulus borders; blue ellipse is 1σ isophotal ellipse. Left to right: Three-colour (W1+2+3); W_1; W_2; W_3; W_4. Middle: Spitzer imaging of NGC4236. Top left to bottom right: IRAC1, IRAC2, IRAC3, IRAC4, MIPS24, three-colour (IRAC1+2+4). Bottom left: SED of NGC4236. Bottom right: SED of NGC4236 with all its SINGS data.*

A.49 NGC4254/M99: SA(s)c; D = 20.0 Mpc; LC III; Activity: HII/LINER

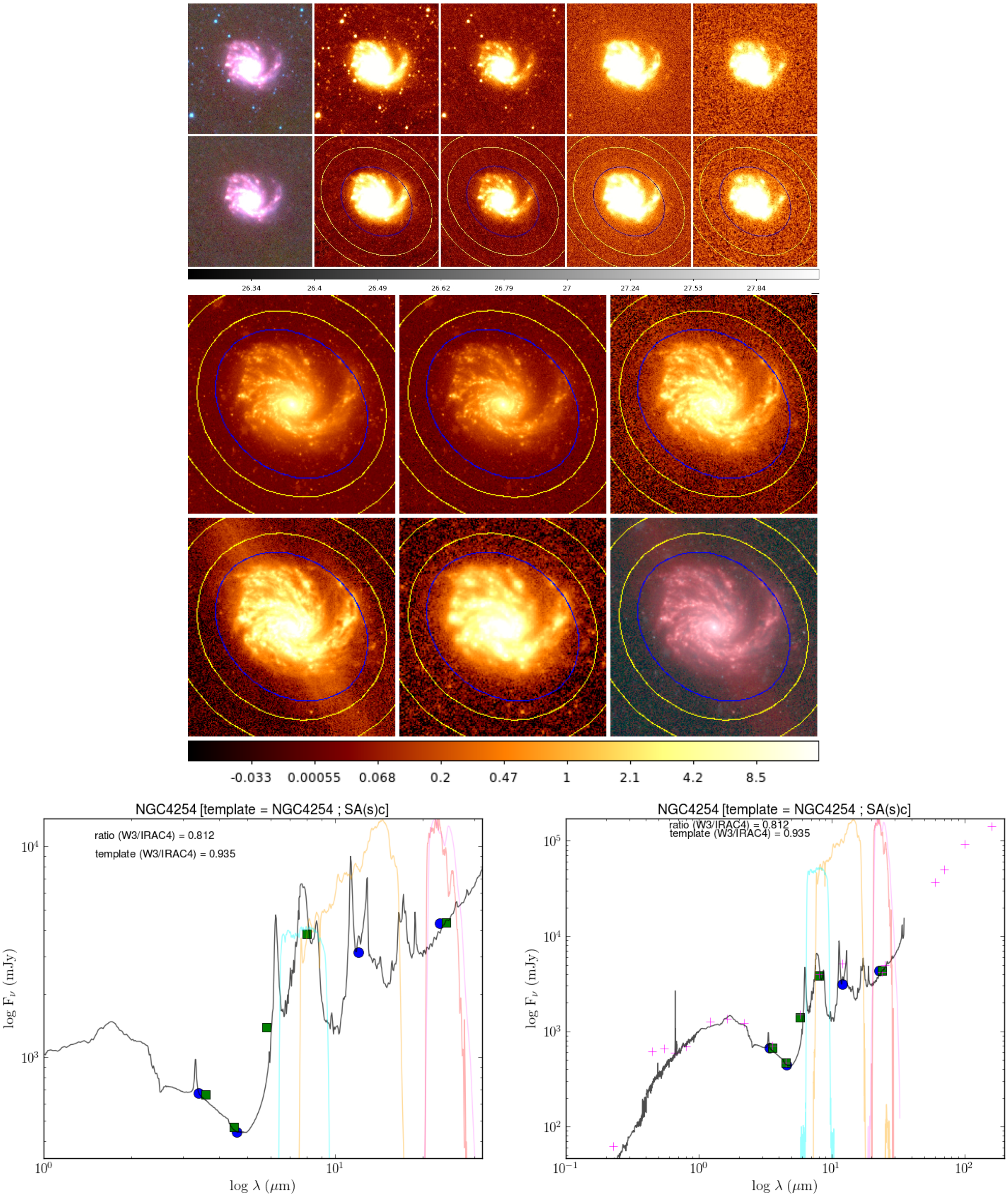

Figure A.49: *Top: WISE imaging of NGC4254, unprocessed and processed. Yellow ellipses are sky annulus borders; blue ellipse is 1σ isophotal ellipse. Left to right: Three-colour (W1+2+3); W_1; W_2; W_3; W_4. Middle: Spitzer imaging of NGC4254. Top left to bottom right: IRAC1, IRAC2, IRAC3, IRAC4, MIPS24, three-colour (IRAC1+2+4). Bottom left: SED of NGC4254. Bottom right: SED of NGC4254 with all its SINGS data.*

A.50 NGC4450: SA(s)ab; D = 20.0 Mpc; LC I-II; Activity: LINER/Sy3

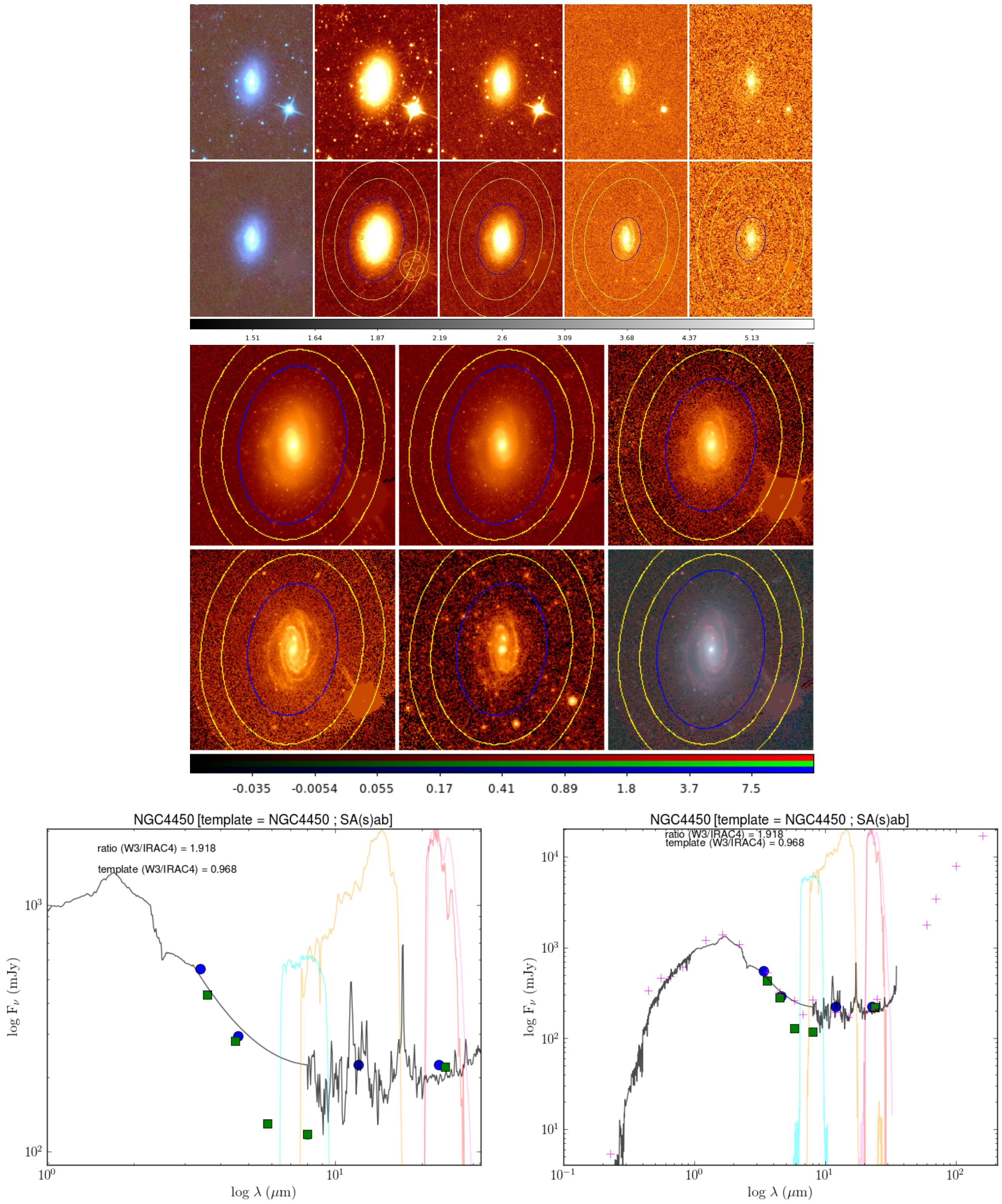

Figure A.50: *Top: WISE imaging of NGC4450, unprocessed and processed. Yellow ellipses are sky annulus borders; blue ellipse is 1σ isophotal ellipse. Left to right: Three-colour (W1+2+3); W_1; W_2; W_3; W_4. Middle: Spitzer imaging of NGC4450. Top left to bottom right: IRAC1, IRAC2, IRAC3, IRAC4, MIPS24, three-colour (IRAC1+2+4). Bottom left: SED of NGC4450. Bottom right: SED of NGC4450 with all its SINGS data.*

A.51 NGC4536: SAB(rs)bc; D = 25.0 Mpc; LC II-III; Activity: HII/Sbst

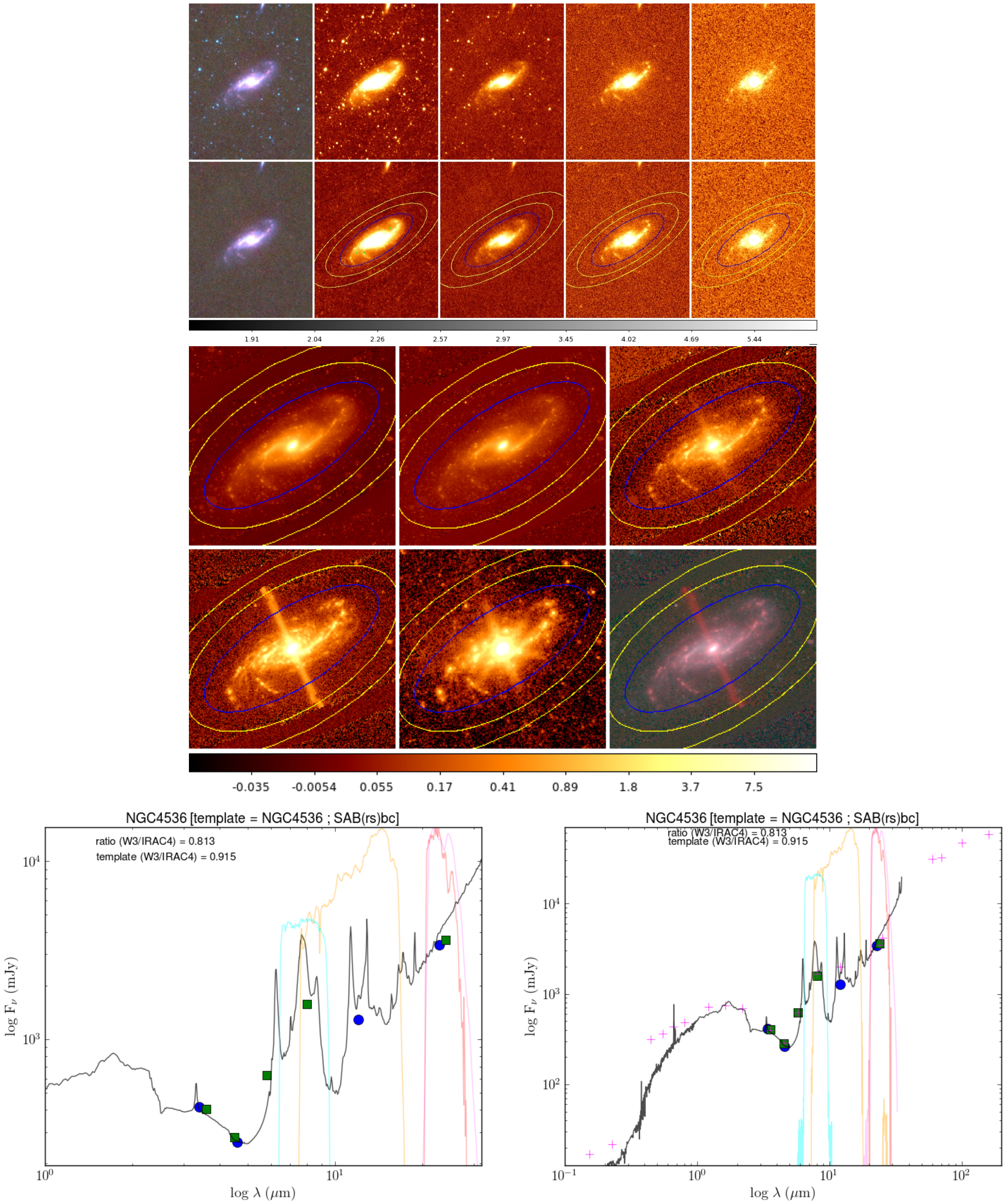

Figure A.51: *Top: WISE imaging of NGC4536, unprocessed and processed. Yellow ellipses are sky annulus borders; blue ellipse is 1σ isophotal ellipse. Left to right: Three-colour (W1+2+3);* W_1; W_2; W_3; W_4. *Middle: Spitzer imaging of NGC4536. Top left to bottom right: IRAC1, IRAC2, IRAC3, IRAC4, MIPS24, three-colour (IRAC1+2+4). Bottom left: SED of NGC4536. Bottom right: SED of NGC4536 with all its SINGS data.*

A.52 NGC4552: E; D = 4.5 Mpc; Activity: HII/LINER/Sy2

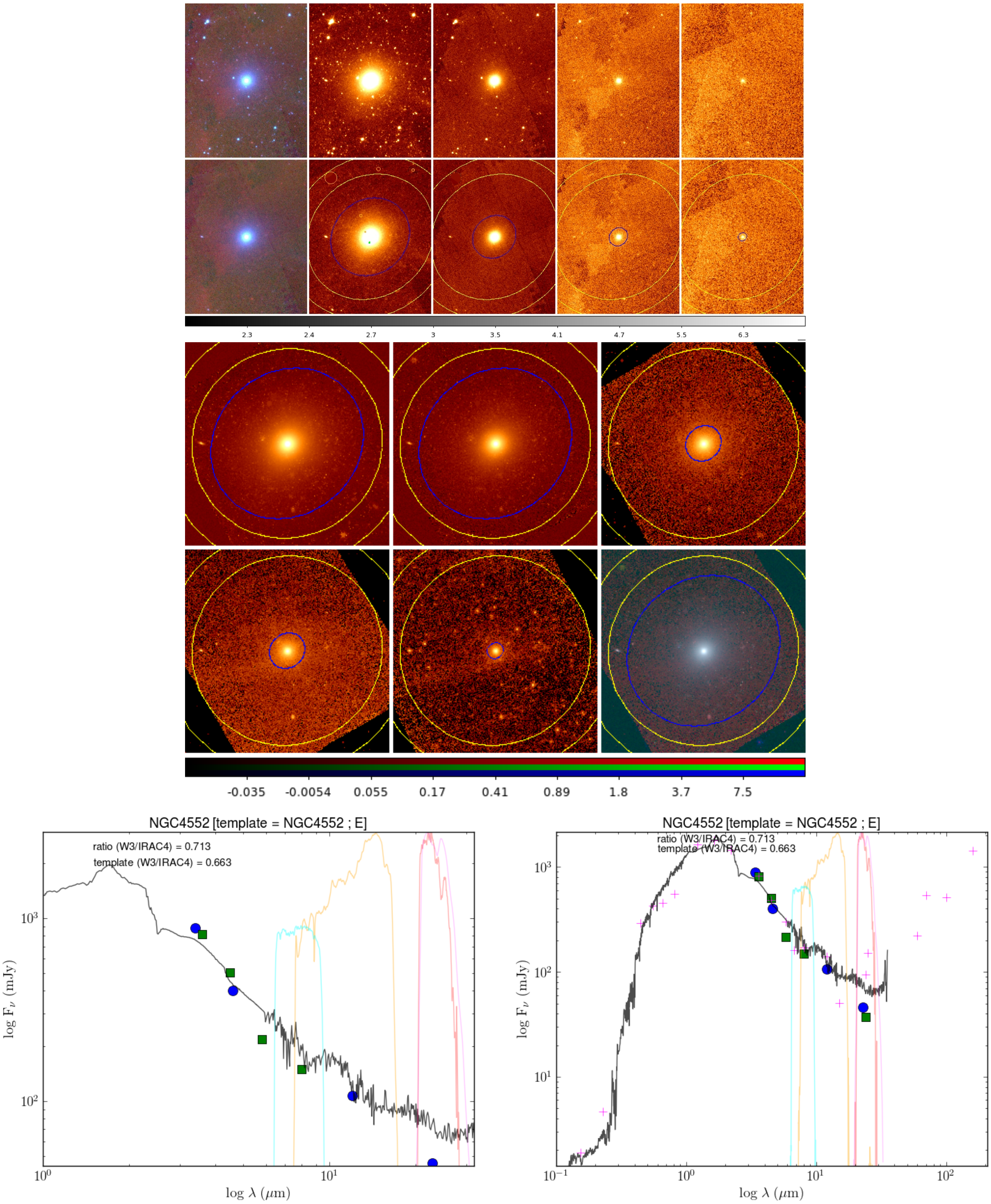

Figure A.52: *Top: WISE imaging of NGC4552, unprocessed and processed. Yellow ellipses are sky annulus borders; blue ellipse is 1σ isophotal ellipse. Left to right: Three-colour (W1+2+3); W_1; W_2; W_3; W_4. Middle: Spitzer imaging of NGC4552. Top left to bottom right: IRAC1, IRAC2, IRAC3, IRAC4, MIPS24, three-colour (IRAC1+2+4). Bottom left: SED of NGC4552. Bottom right: SED of NGC4552 with all its SINGS data.*

A.53 NGC4559: SAB(rs)cd; D = 11.6 Mpc; LC III-IV; Activity: HII

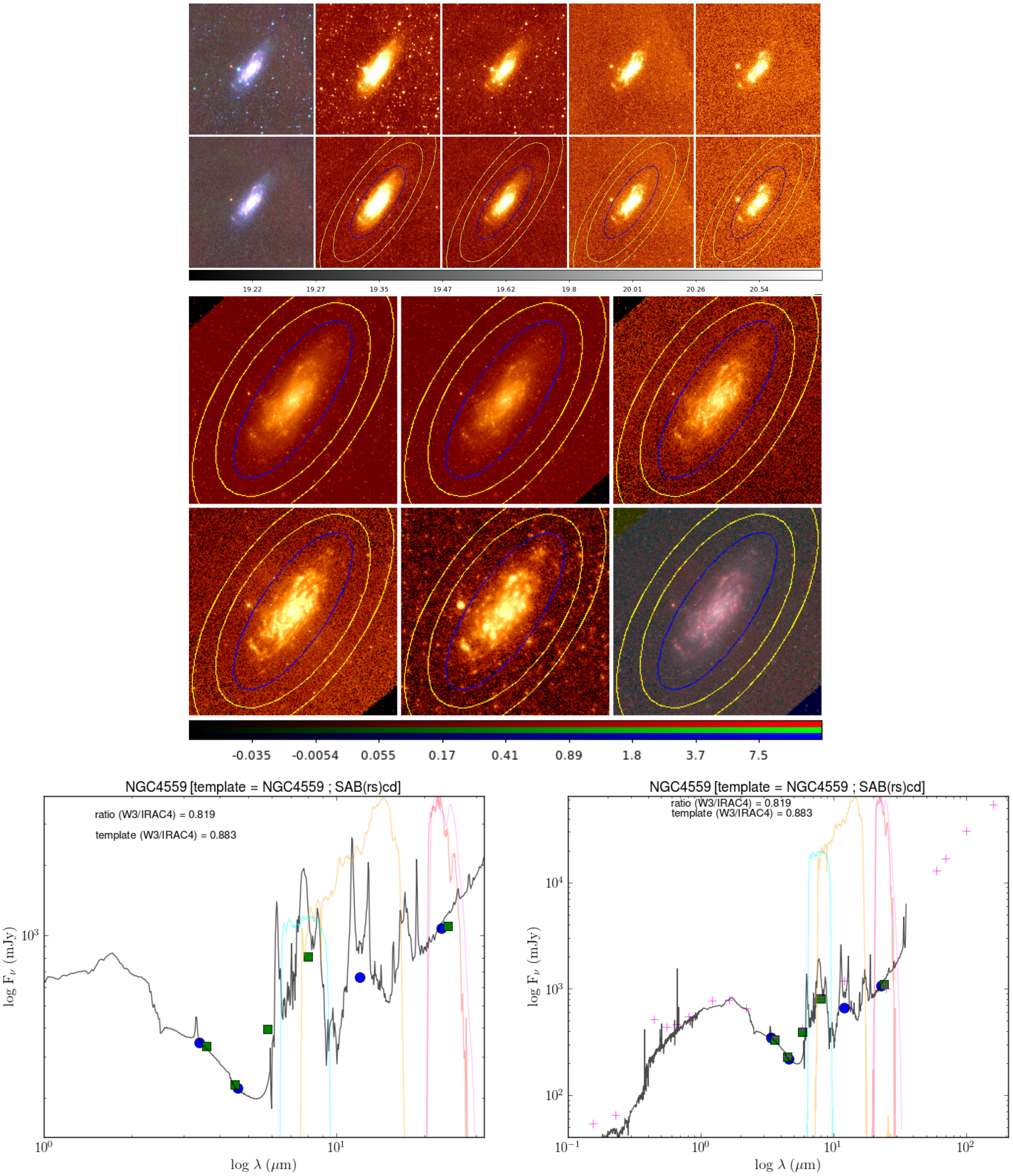

Figure A.53: *Top: WISE imaging of NGC4559, unprocessed and processed. Yellow ellipses are sky annulus borders; blue ellipse is 1σ isophotal ellipse. Left to right: Three-colour (W1+2+3); W_1; W_2; W_3; W_4. Middle: Spitzer imaging of NGC4559. Top left to bottom right: IRAC1, IRAC2, IRAC3, IRAC4, MIPS24, three-colour (IRAC1+2+4). Bottom left: SED of NGC4559. Bottom right: SED of NGC4559 with all its SINGS data.*

A.54 NGC4569: SAB(rs)ab; D = 20.0 Mpc; LC I-II; Activity: LINER/Sy

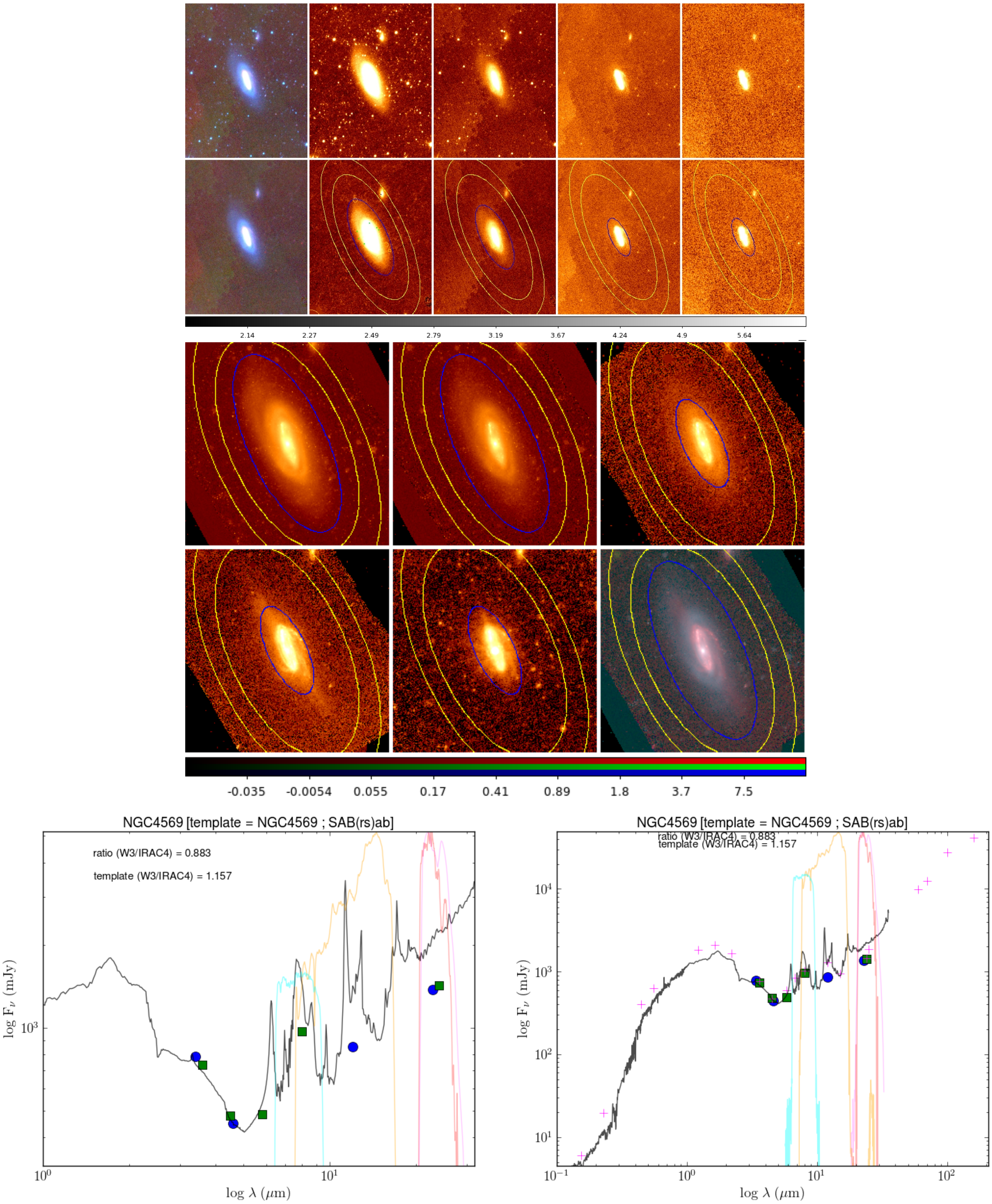

Figure A.54: *Top: WISE imaging of NGC4569, unprocessed and processed. Yellow ellipses are sky annulus borders; blue ellipse is 1σ isophotal ellipse. Left to right: Three-colour (W1+2+3); W$_1$; W$_2$; W$_3$; W$_4$. Middle: Spitzer imaging of NGC4569. Top left to bottom right: IRAC1, IRAC2, IRAC3, IRAC4, MIPS24, three-colour (IRAC1+2+4). Bottom left: SED of NGC4569. Bottom right: SED of NGC4569 with all its SINGS data.*

A.55 NGC4579: SAB(rs)b; D = 20.0 Mpc; LC II-III; Activity: LINER/Sy

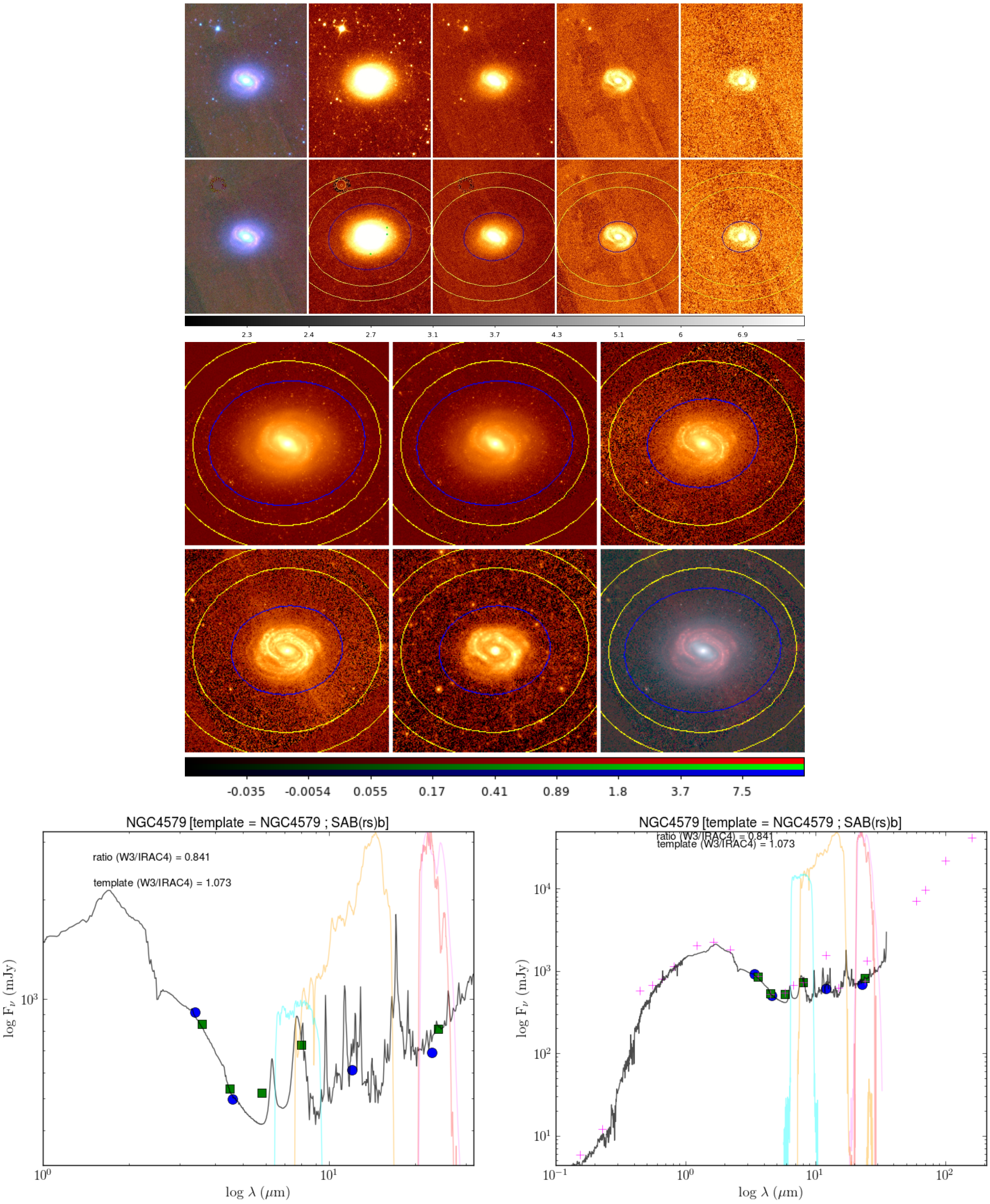

Figure A.55: *Top: WISE imaging of NGC4579, unprocessed and processed. Yellow ellipses are sky annulus borders; blue ellipse is 1σ isophotal ellipse. Left to right: Three-colour (W1+2+3); W_1; W_2; W_3; W_4. Middle: Spitzer imaging of NGC4579. Top left to bottom right: IRAC1, IRAC2, IRAC3, IRAC4, MIPS24, three-colour (IRAC1+2+4). Bottom left: SED of NGC4579. Bottom right: SED of NGC4579 with all its SINGS data.*

A.56 NGC4594: SA(s)a; D = 13.7 Mpc; LC I; Activity: LINER/Sy

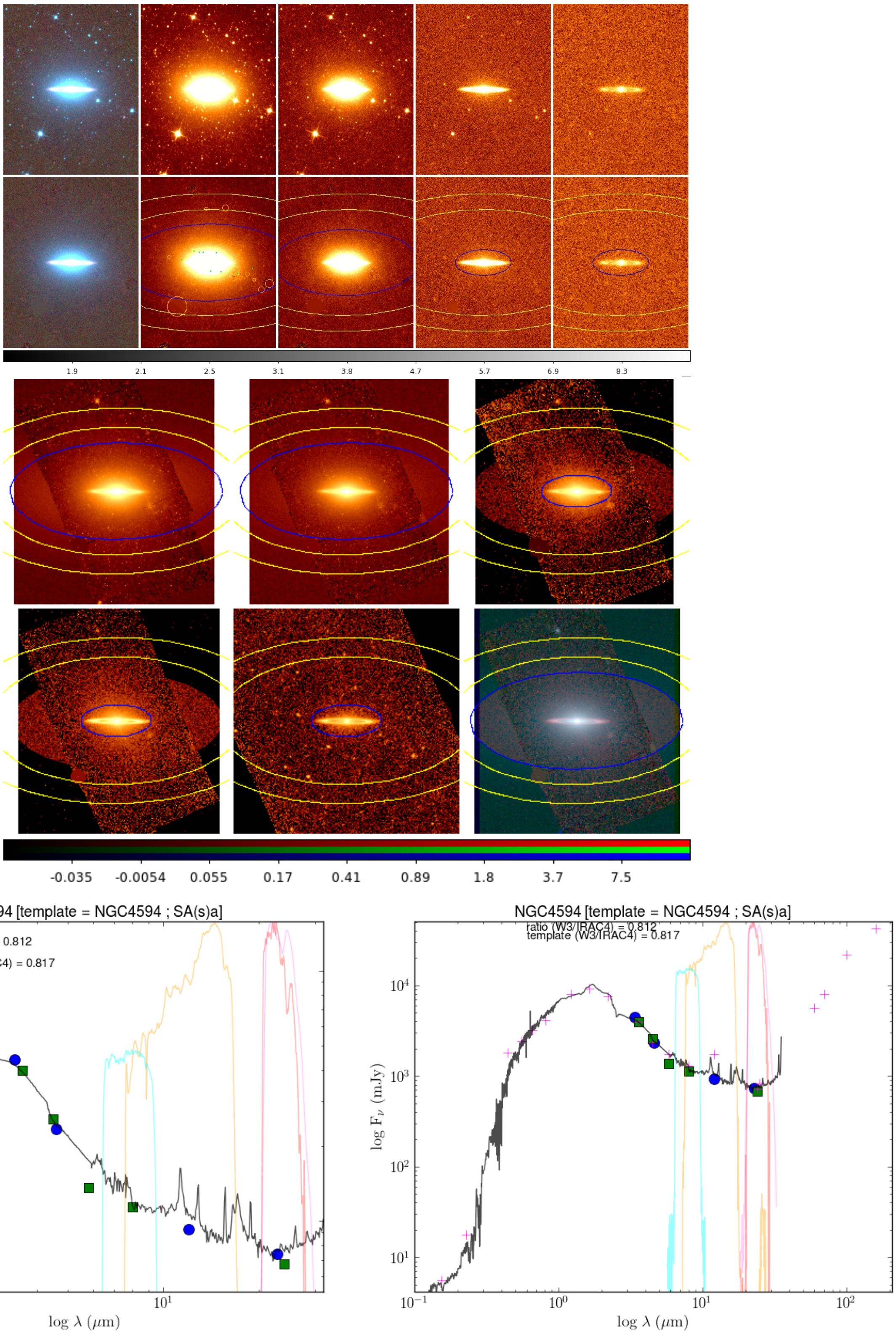

Figure A.56: *Top: WISE imaging of NGC4594, unprocessed and processed. Yellow ellipses are sky annulus borders; blue ellipse is 1σ isophotal ellipse. Left to right: Three-colour (W1+2+3); W*$_1$*; W*$_2$*; W*$_3$*; W*$_4$*. Middle: Spitzer imaging of NGC4594. Top left to bottom right: IRAC1, IRAC2, IRAC3, IRAC4, MIPS24, three-colour (IRAC1+2+4). Bottom left: SED of NGC4594. Bottom right: SED of NGC4594 with all its SINGS data.*

A.57 NGC4625: SAB(rs)mp; D = 9.5 Mpc; LC V

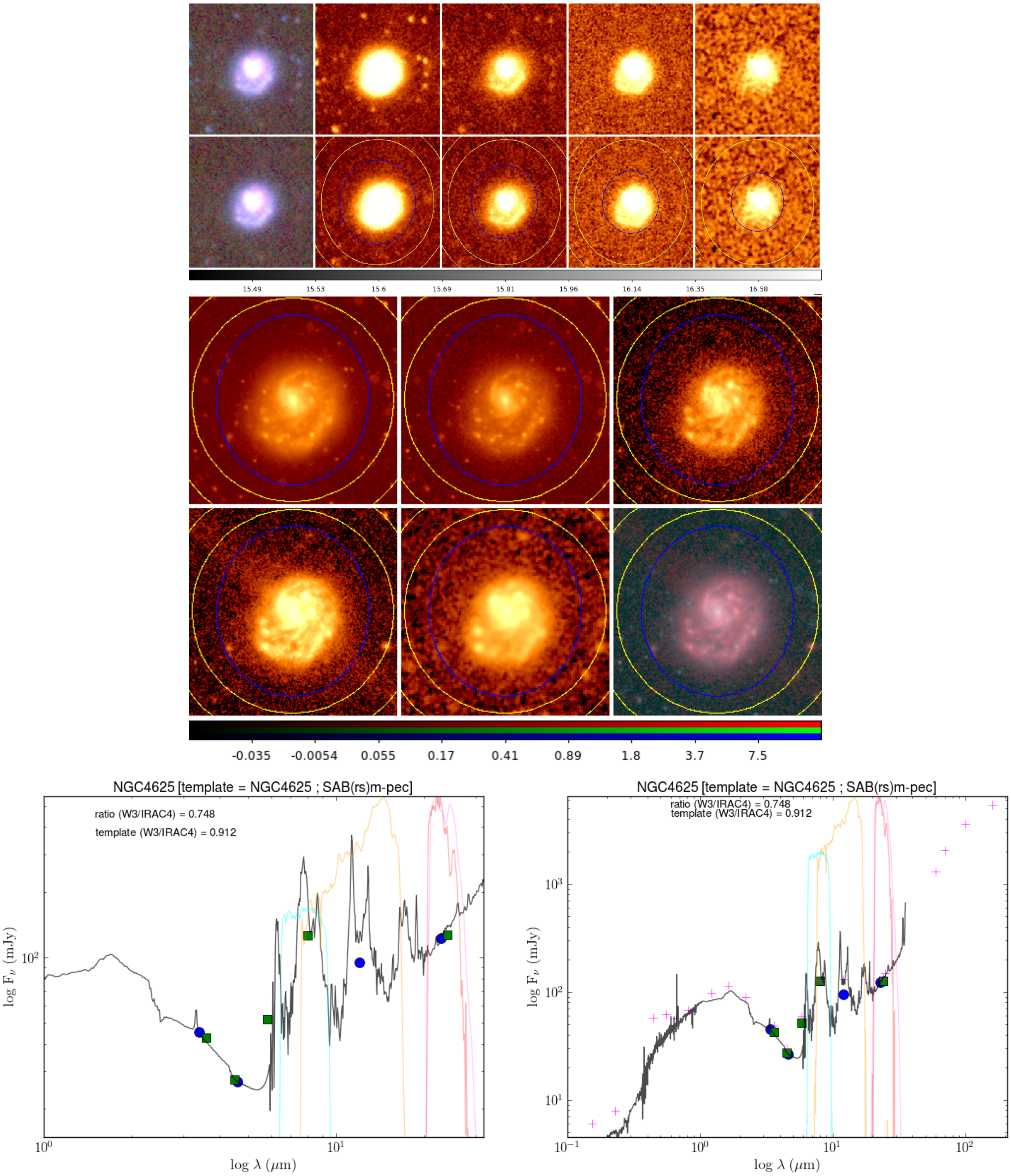

Figure A.57: *Top: WISE imaging of NGC4625, unprocessed and processed. Yellow ellipses are sky annulus borders; blue ellipse is 1σ isophotal ellipse. Left to right: Three-colour (W1+2+3); W$_1$; W$_2$; W$_3$; W$_4$. Middle: Spitzer imaging of NGC4625. Top left to bottom right: IRAC1, IRAC2, IRAC3, IRAC4, MIPS24, three-colour (IRAC1+2+4). Bottom left: SED of NGC4625. Bottom right: SED of NGC4625 with all its SINGS data.*

A.58 NGC4631: SB(s)d; D = 9.0 Mpc; LC IV; Activity: HII

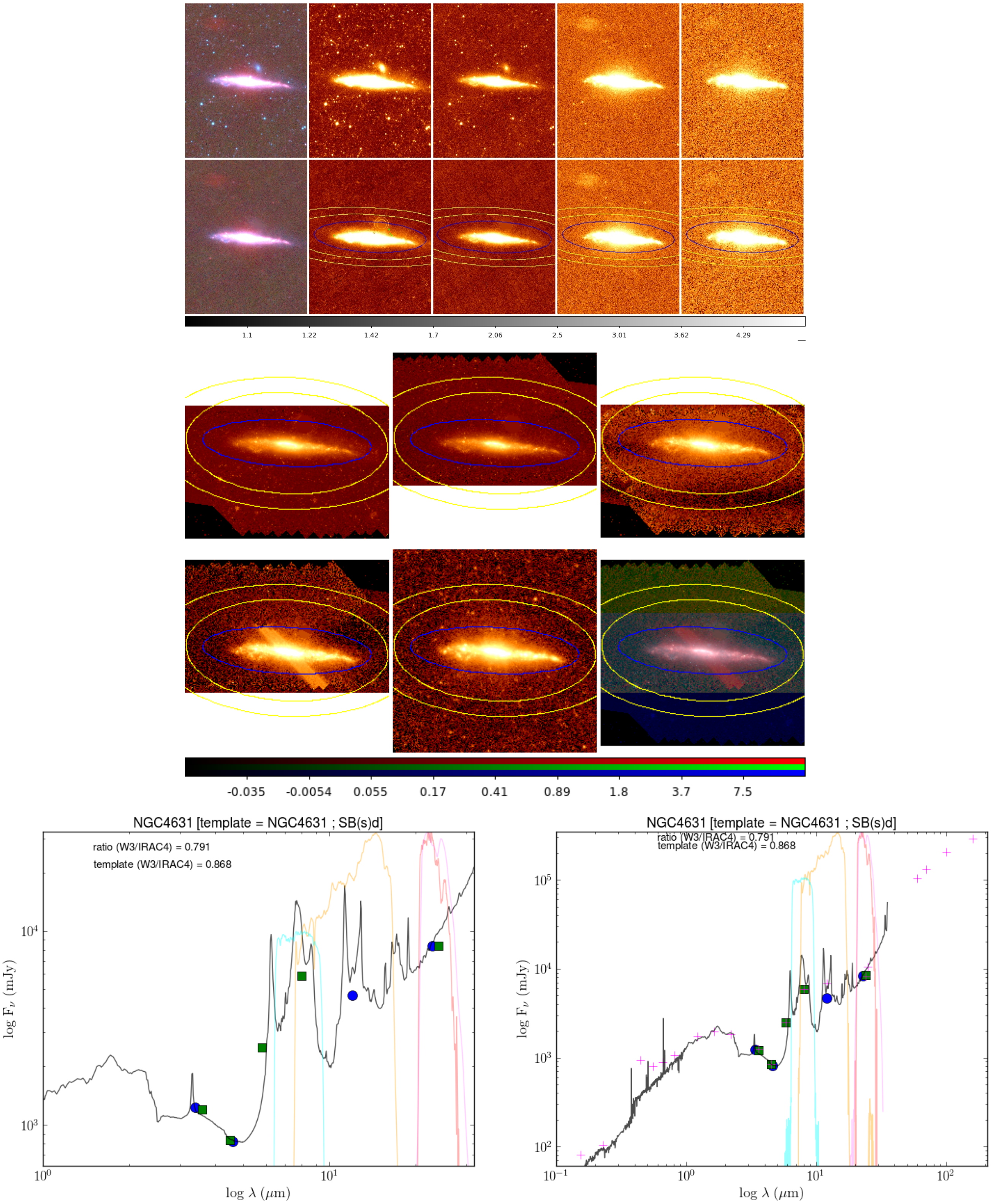

Figure A.58: *Top: WISE imaging of NGC4631, unprocessed and processed. Yellow ellipses are sky annulus borders; blue ellipse is 1σ isophotal ellipse. Left to right: Three-colour (W1+2+3); W_1; W_2; W_3; W_4. Middle: Spitzer imaging of NGC4631. Top left to bottom right: IRAC1, IRAC2, IRAC3, IRAC4, MIPS24, three-colour (IRAC1+2+4). Bottom left: SED of NGC4631. Bottom right: SED of NGC4631 with all its SINGS data.*

A.59 NGC4725: SAB(r)abp; D = 17.1 Mpc; LC I-II; Activity: Sy2

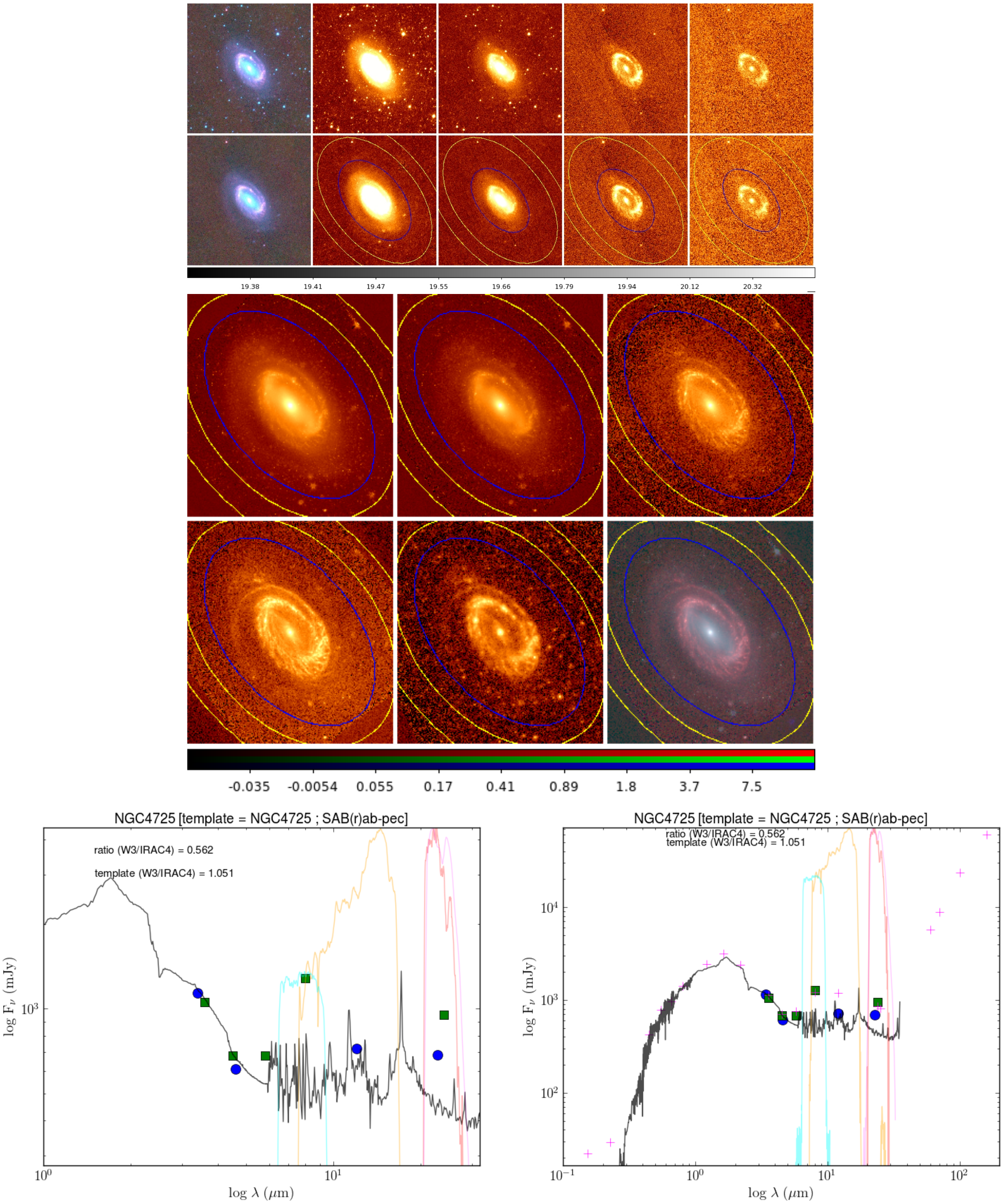

Figure A.59: *Top: WISE imaging of NGC4725, unprocessed and processed. Yellow ellipses are sky annulus borders; blue ellipse is 1σ isophotal ellipse. Left to right: Three-colour (W1+2+3); W_1; W_2; W_3; W_4. Middle: Spitzer imaging of NGC4725. Top left to bottom right: IRAC1, IRAC2, IRAC3, IRAC4, MIPS24, three-colour (IRAC1+2+4). Bottom left: SED of NGC4725. Bottom right: SED of NGC4725 with all its SINGS data.*

A.60 NGC4736: SA(r)ab; D = 5.3 Mpc; LC I-II; Activity: LINER/Sy2

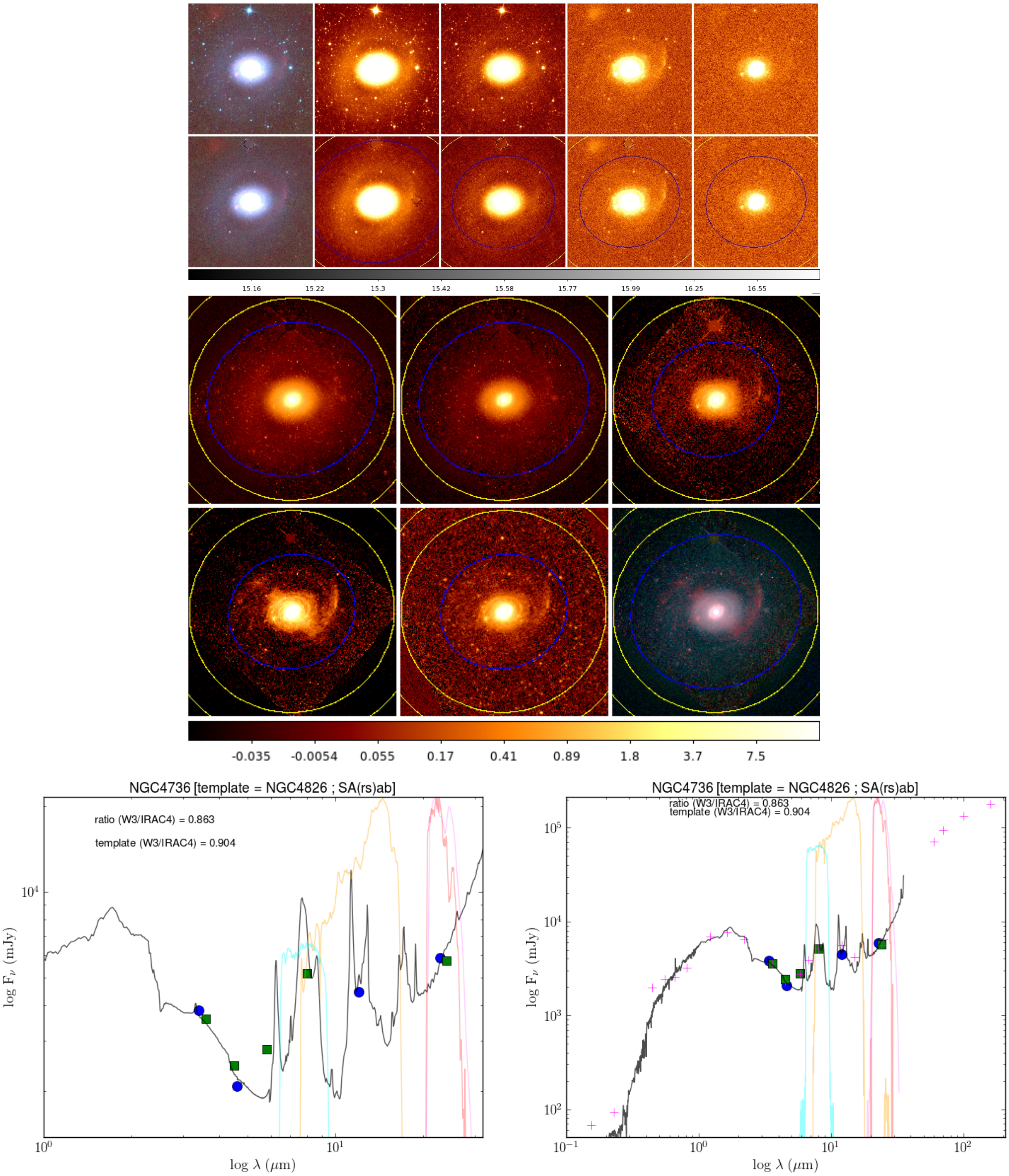

Figure A.60: *Top: WISE imaging of NGC4736, unprocessed and processed. Yellow ellipses are sky annulus borders; blue ellipse is 1σ isophotal ellipse. Left to right: Three-colour (W1+2+3); W*$_1$*; W*$_2$*; W*$_3$*; W*$_4$*. Middle: Spitzer imaging of NGC4736. Top left to bottom right: IRAC1, IRAC2, IRAC3, IRAC4, MIPS24, three-colour (IRAC1+2+4). Bottom left: SED of NGC4736. Bottom right: SED of NGC4736 with all its SINGS data.*

A.61 NGC4826: SA(rs)ab; D = 5.6 Mpc; LC I-II; Activity: HII/Sy2

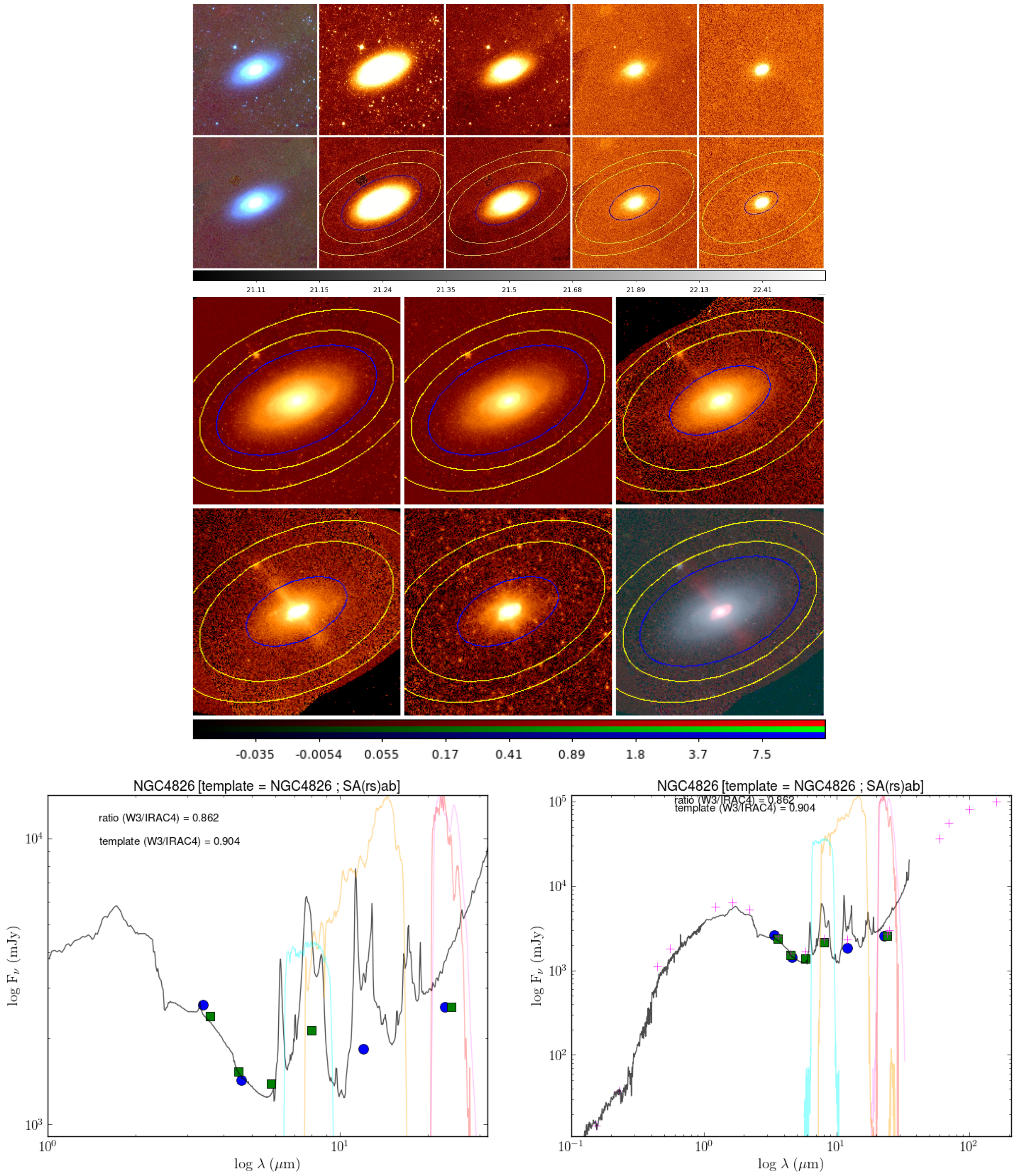

Figure A.61: *Top: WISE imaging of NGC4826, unprocessed and processed. Yellow ellipses are sky annulus borders; blue ellipse is 1σ isophotal ellipse. Left to right: Three-colour (W1+2+3); W_1; W_2; W_3; W_4. Middle: Spitzer imaging of NGC4826. Top left to bottom right: IRAC1, IRAC2, IRAC3, IRAC4, MIPS24, three-colour (IRAC1+2+4). Bottom left: SED of NGC4826. Bottom right: SED of NGC4826 with all its SINGS data.*

A.62 NGC5033: SA(s)c; D = 13.3 Mpc; LC III; Activity: HII/Sy1

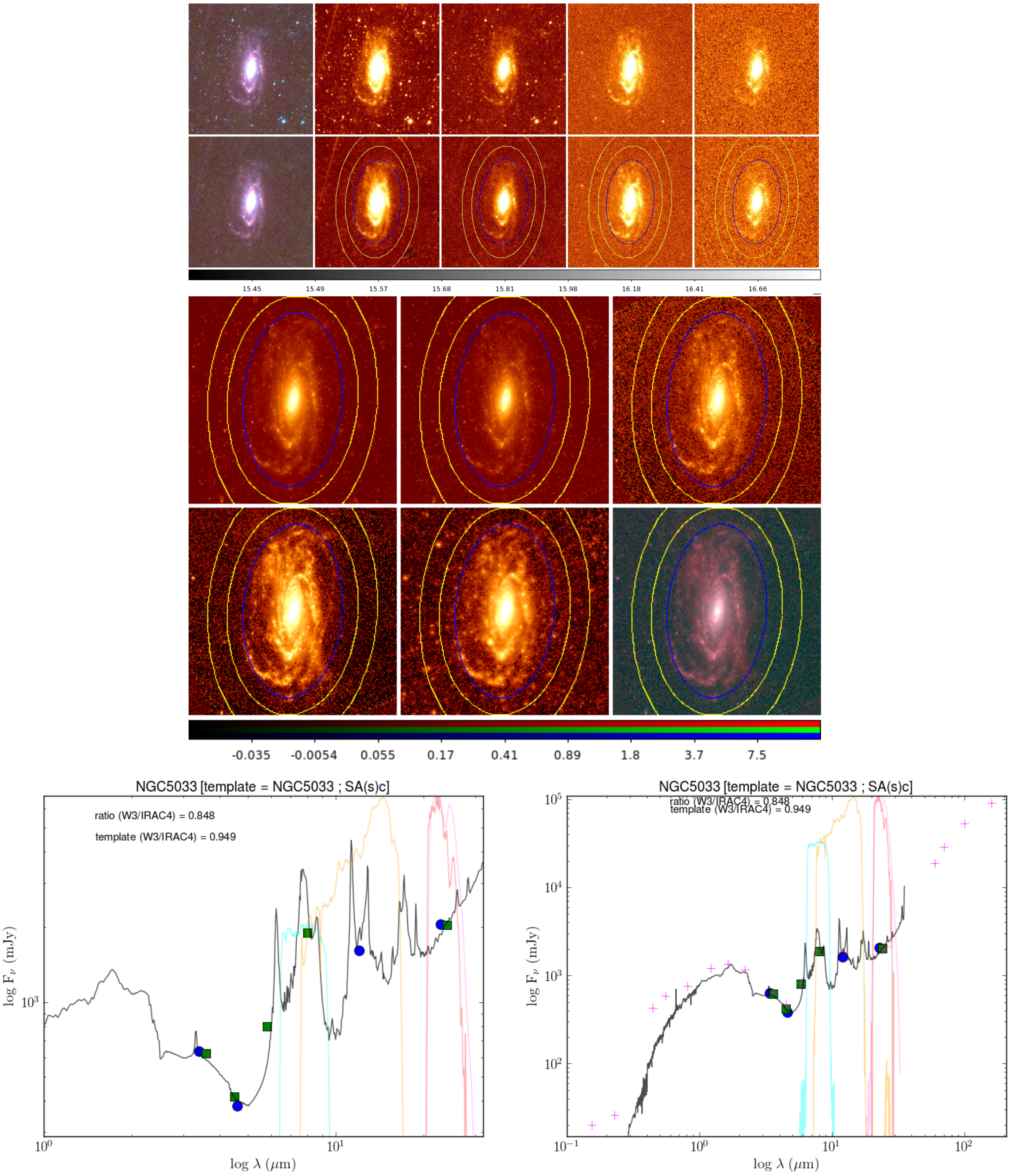

Figure A.62: *Top: WISE imaging of NGC5033, unprocessed and processed. Yellow ellipses are sky annulus borders; blue ellipse is 1σ isophotal ellipse. Left to right: Three-colour (W1+2+3); W_1; W_2; W_3; W_4. Middle: Spitzer imaging of NGC5033. Top left to bottom right: IRAC1, IRAC2, IRAC3, IRAC4, MIPS24, three-colour (IRAC1+2+4). Bottom left: SED of NGC5033. Bottom right: SED of NGC5033 with all its SINGS data.*

A.63 NGC5055: SA(rs)bc; D = 8.2 Mpc; LC II-III; Activity: HII/LINER

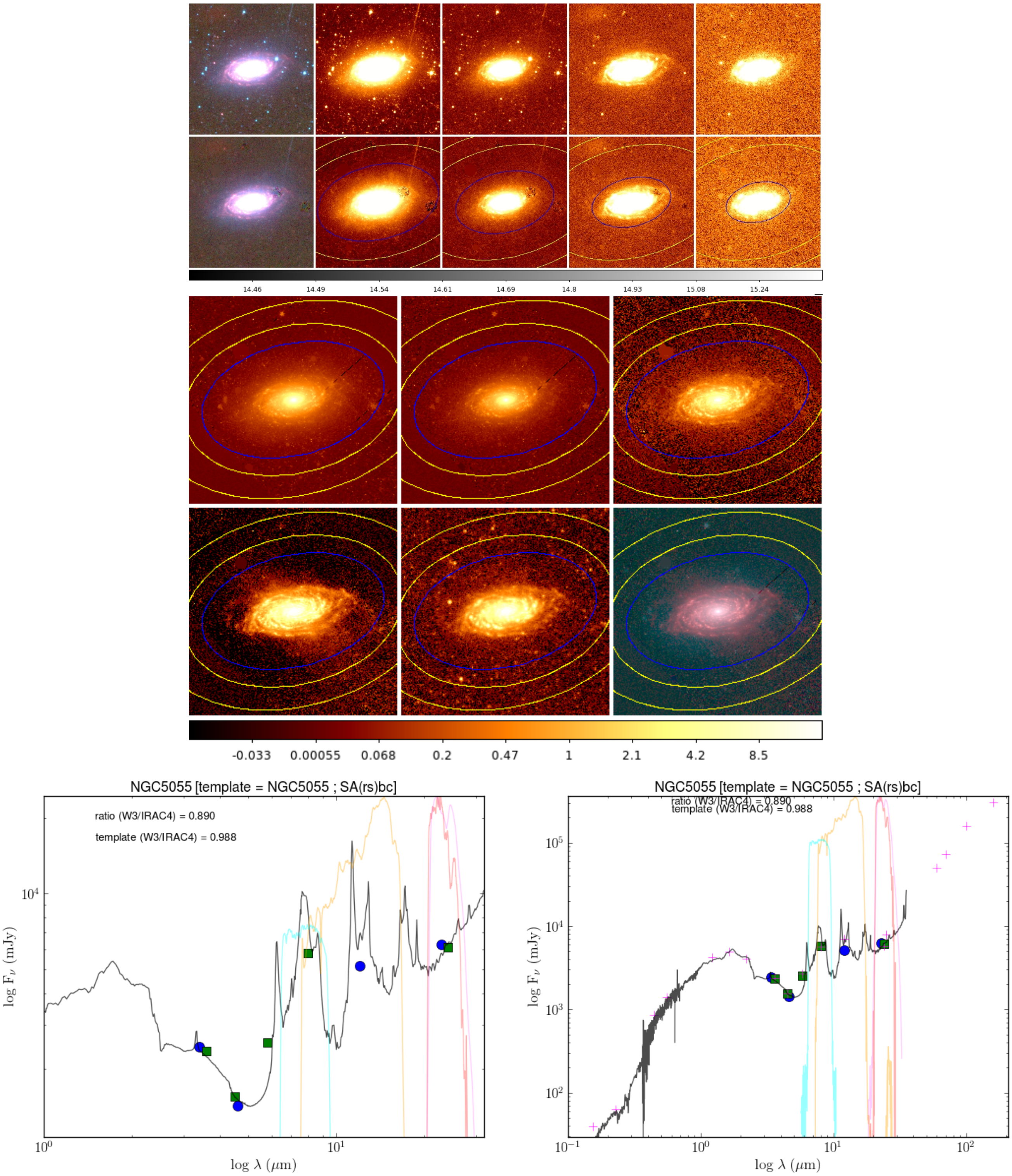

Figure A.63: *Top: WISE imaging of NGC5055, unprocessed and processed. Yellow ellipses are sky annulus borders; blue ellipse is 1σ isophotal ellipse. Left to right: Three-colour (W1+2+3);* W_1*;* W_2*;* W_3*;* W_4*. Middle: Spitzer imaging of NGC5055. Top left to bottom right: IRAC1, IRAC2, IRAC3, IRAC4, MIPS24, three-colour (IRAC1+2+4). Bottom left: SED of NGC5055. Bottom right: SED of NGC5055 with all its SINGS data.*

A.64 NGC5194/M51a: SA(s)bc; D = 8.2 Mpc; LC II-III; Activity: HII/Sy2

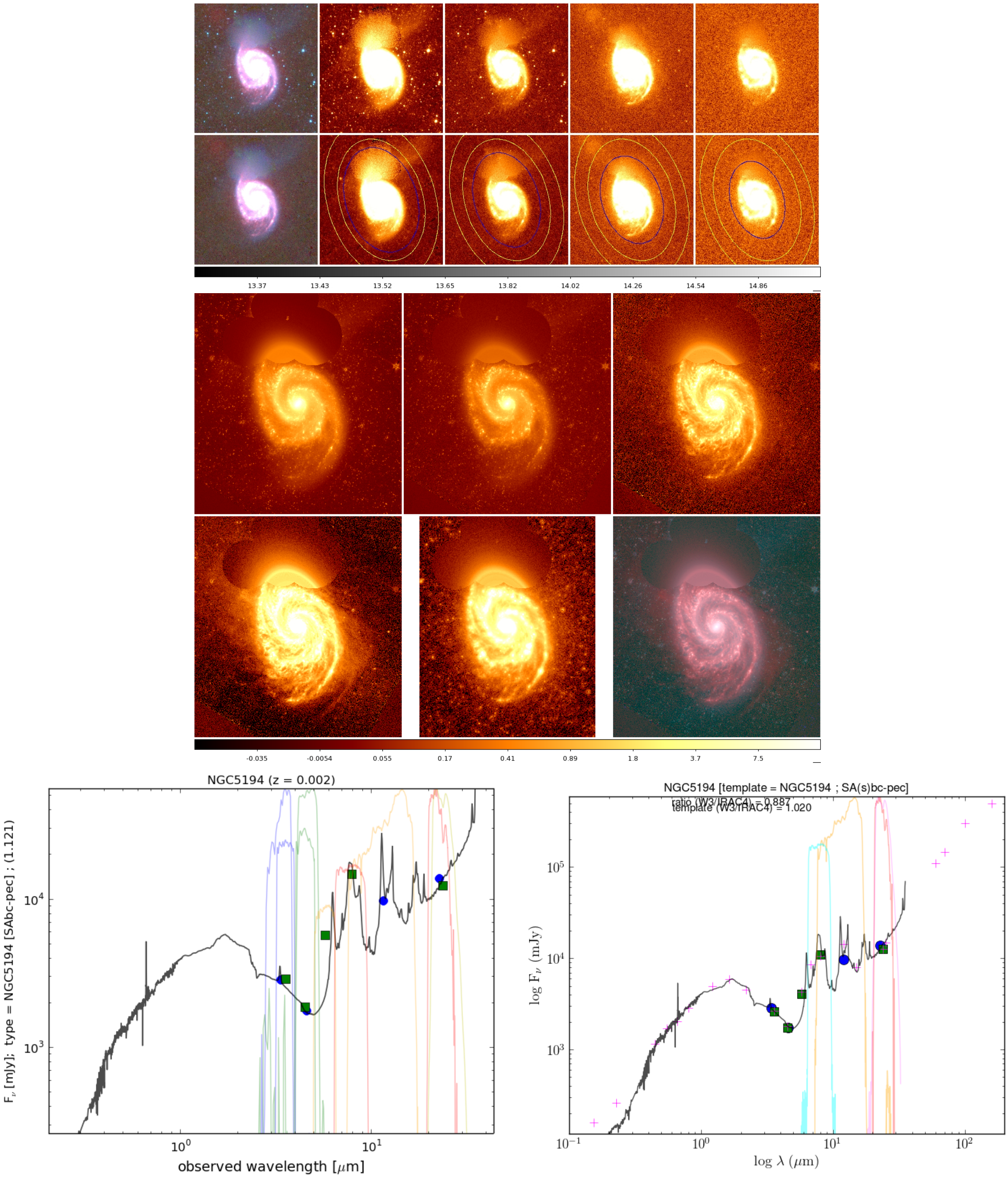

Figure A.64: *Top: WISE imaging of NGC5194, unprocessed and processed. Yellow ellipses are sky annulus borders; blue ellipse is 1σ isophotal ellipse. Left to right: Three-colour (W1+2+3);* W_1; W_2; W_3; W_4. *Middle: Spitzer imaging of NGC5194. Top left to bottom right: IRAC1, IRAC2, IRAC3, IRAC4, MIPS24, three-colour (IRAC1+2+4). Bottom left: SED of NGC5194. Bottom right: SED of NGC5194 with all its SINGS data.*

A.65 NGC5195/M51b: SB0p; D = 8.2 Mpc; Activity: LINER

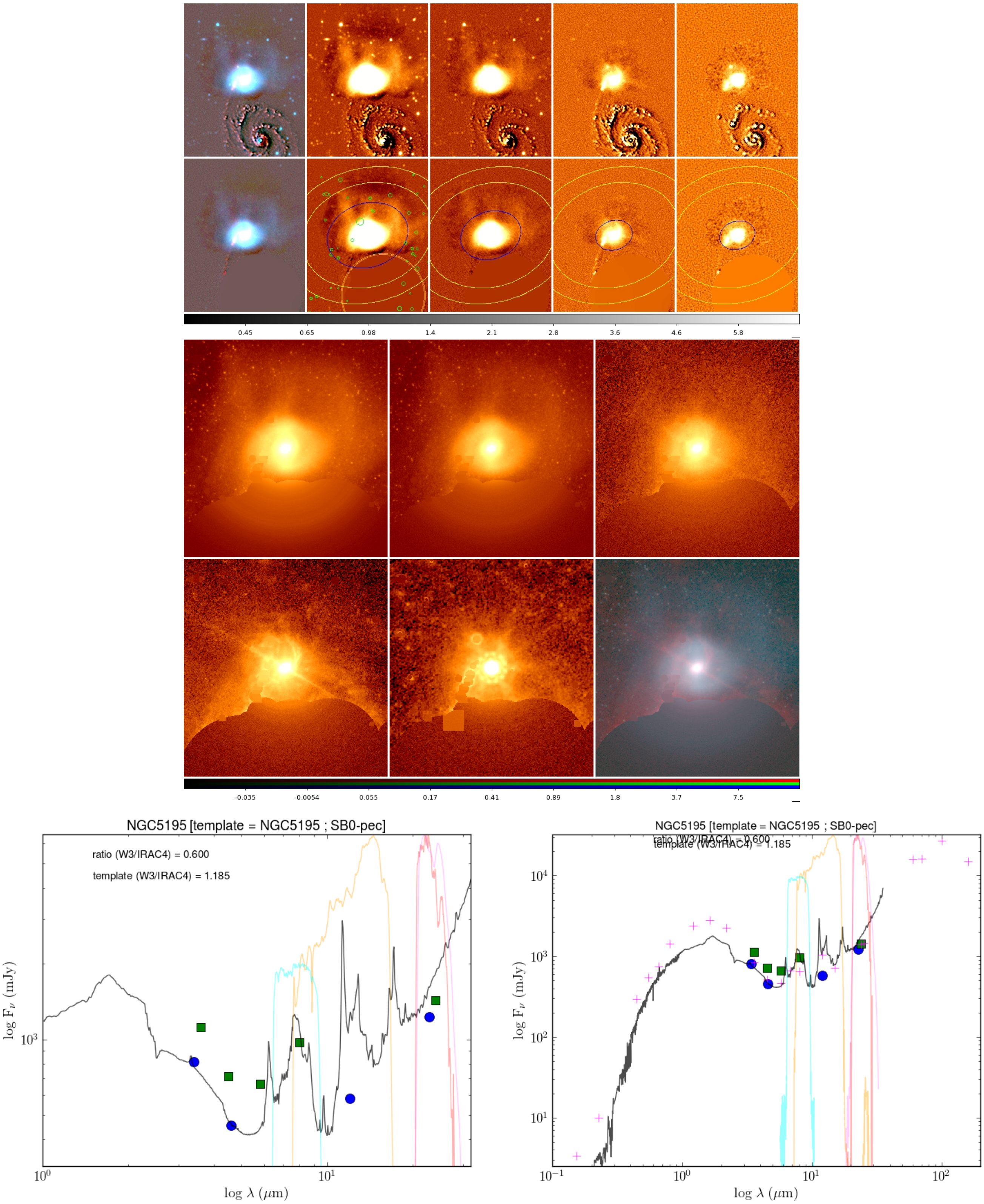

Figure A.65: *Top: WISE imaging of NGC5195, unprocessed and processed. Yellow ellipses are sky annulus borders; blue ellipse is 1σ isophotal ellipse. Left to right: Three-colour (W1+2+3); W_1; W_2; W_3; W_4. Middle: Spitzer imaging of NGC5195. Top left to bottom right: IRAC1, IRAC2, IRAC3, IRAC4, MIPS24, three-colour (IRAC1+2+4). Bottom left: SED of NGC5195. Bottom right: SED of NGC5195 with all its SINGS data.*

A.66 NGC5398: SBdm; D_{KF} = 7.66 Mpc; LC IV-V

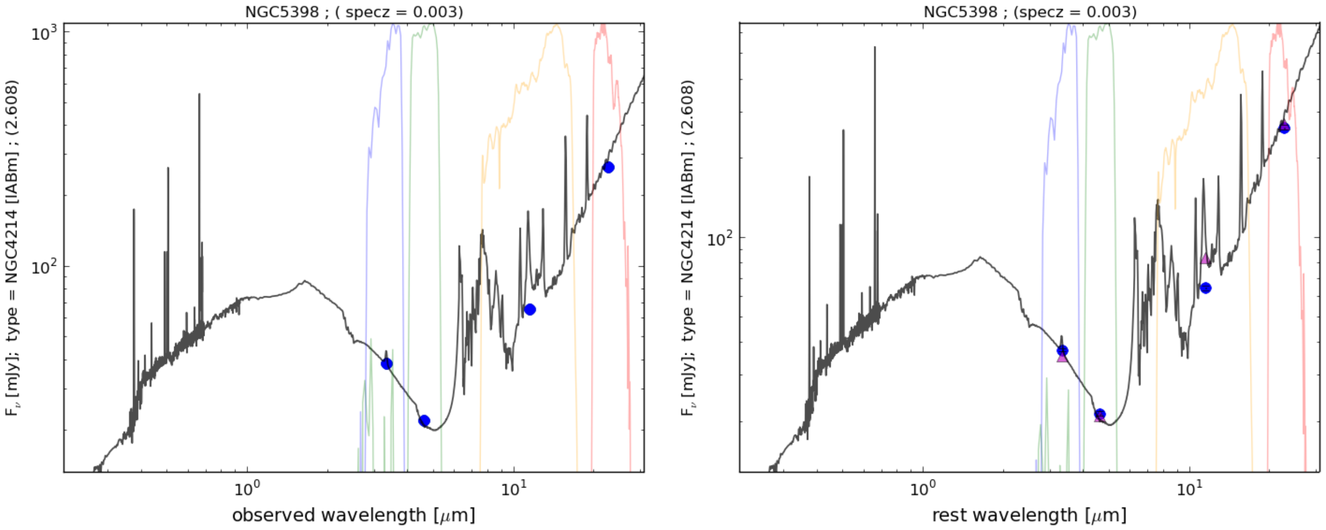

Figure A.66: *Left: SED of NGC5398. Right: Rest-wavelength SED of NGC5398.*

A.67 NGC5408: IB(s)m; D = 4.5 Mpc; LC V-VI; Activity: HII

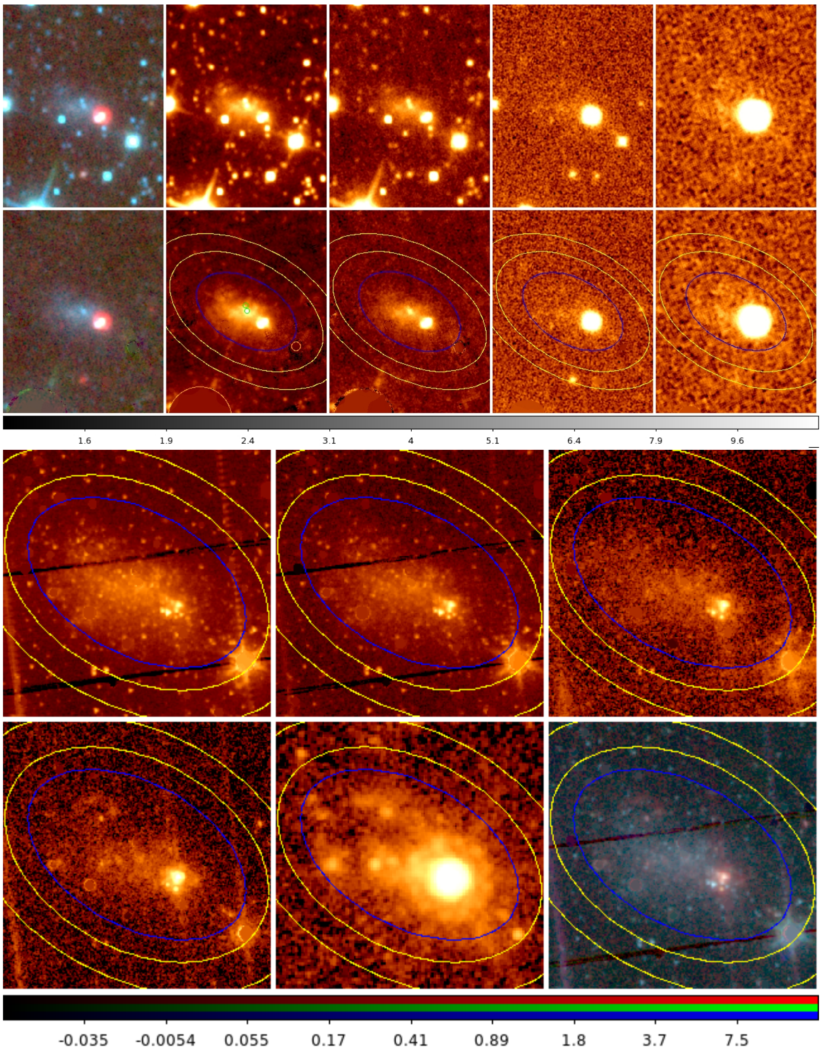

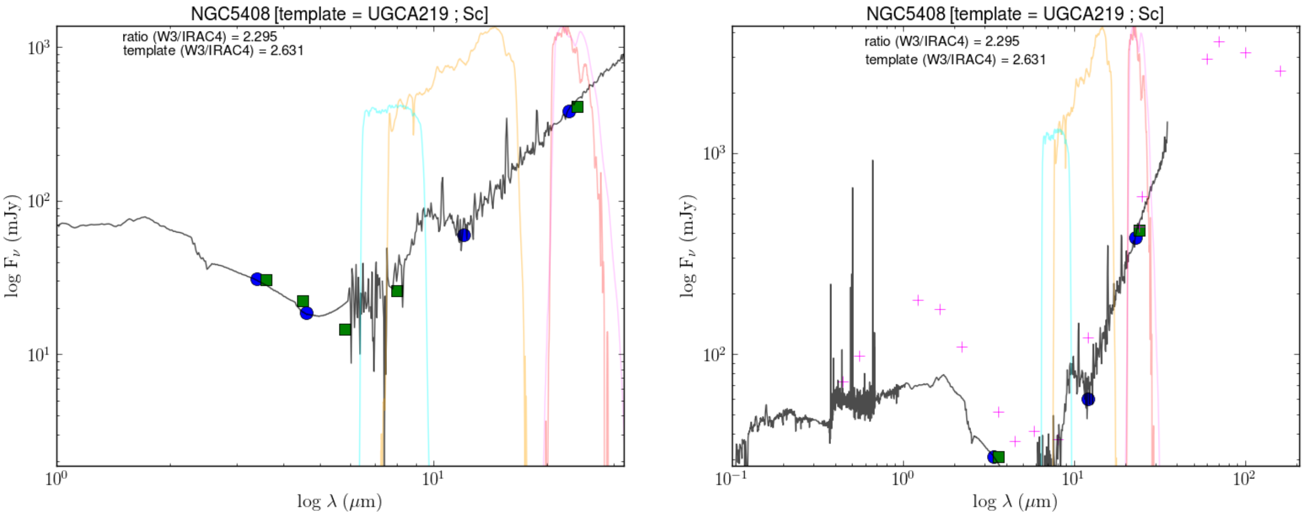

Figure A.67: *Top: WISE imaging of NGC5408, unprocessed and processed. Yellow ellipses are sky annulus borders; blue ellipse is 1σ isophotal ellipse. Left to right: Three-colour (W1+2+3); W_1; W_2; W_3; W_4. Middle: Spitzer imaging of NGC5408. Top left to bottom right: IRAC1, IRAC2, IRAC3, IRAC4, MIPS24, three-colour (IRAC1+2+4). Bottom left: SED of NGC5408. Bottom right: SED of NGC5408 with all its SINGS data.*

A.68 NGC5474: SA(s)cdp; D = 6.9 Mpc; LC III-IV; Activity: HII

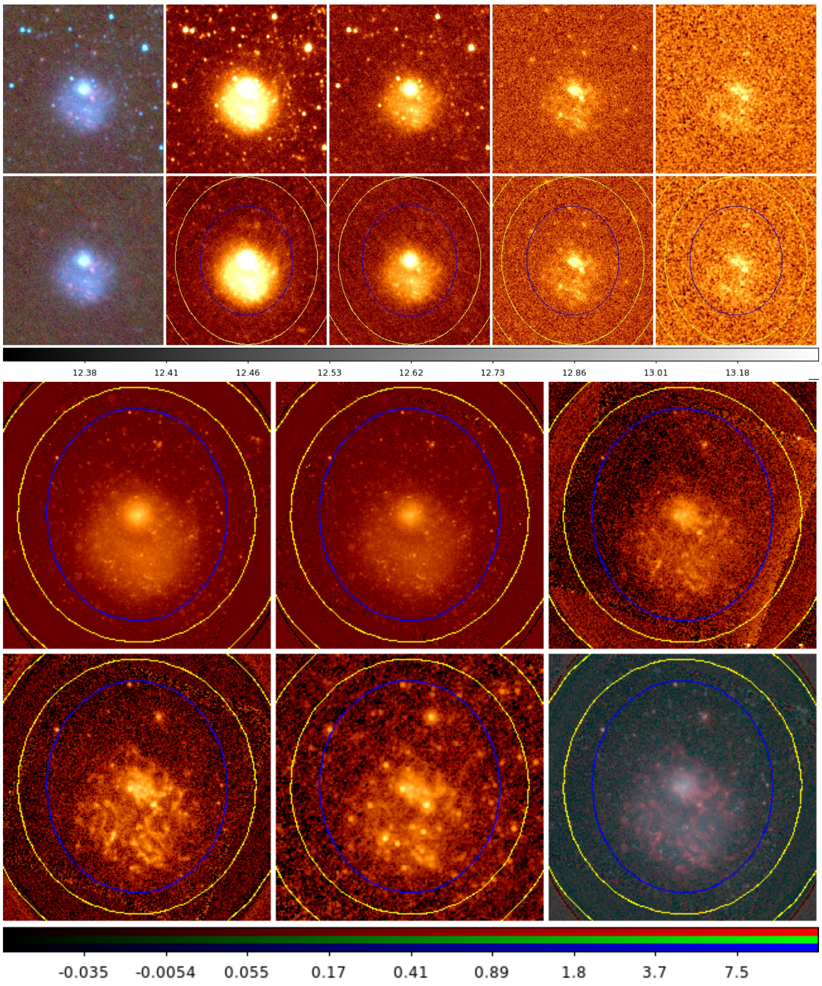

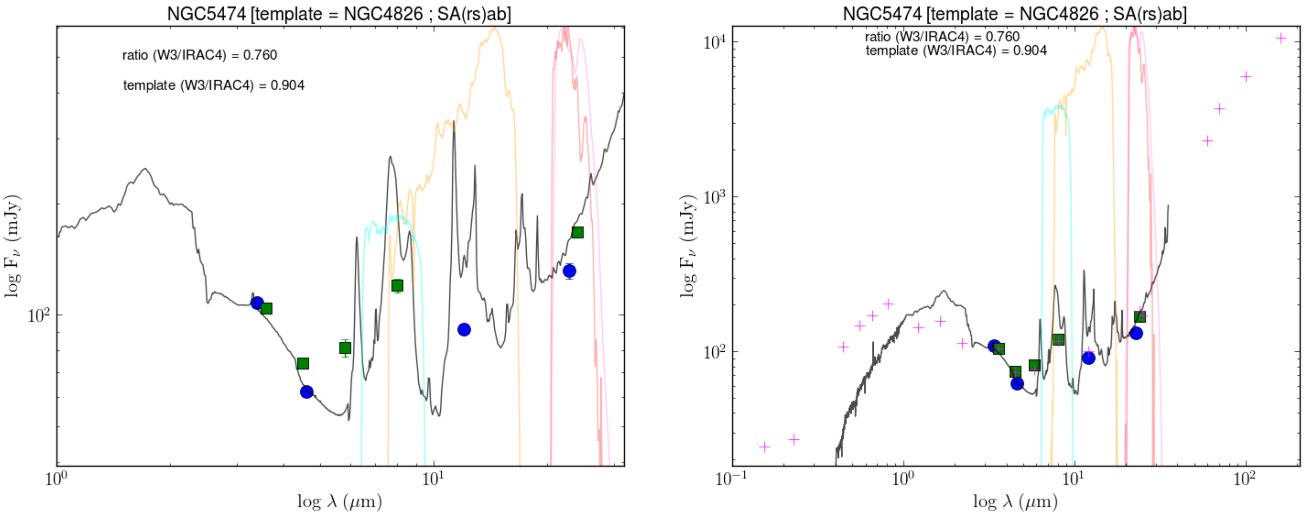

Figure A.68: *Top: WISE imaging of NGC5474, unprocessed and processed. Yellow ellipses are sky annulus borders; blue ellipse is 1σ isophotal ellipse. Left to right: Three-colour (W1+2+3); W$_1$; W$_2$; W$_3$; W$_4$. Middle: Spitzer imaging of NGC5474. Top left to bottom right: IRAC1, IRAC2, IRAC3, IRAC4, MIPS24, three-colour (IRAC1+2+4). Bottom left: SED of NGC5474. Bottom right: SED of NGC5474 with all its SINGS data.*

A.69 NGC5713: SAB(rs)bcp; D = 26.6 Mpc; LC II-III; Activity: HII

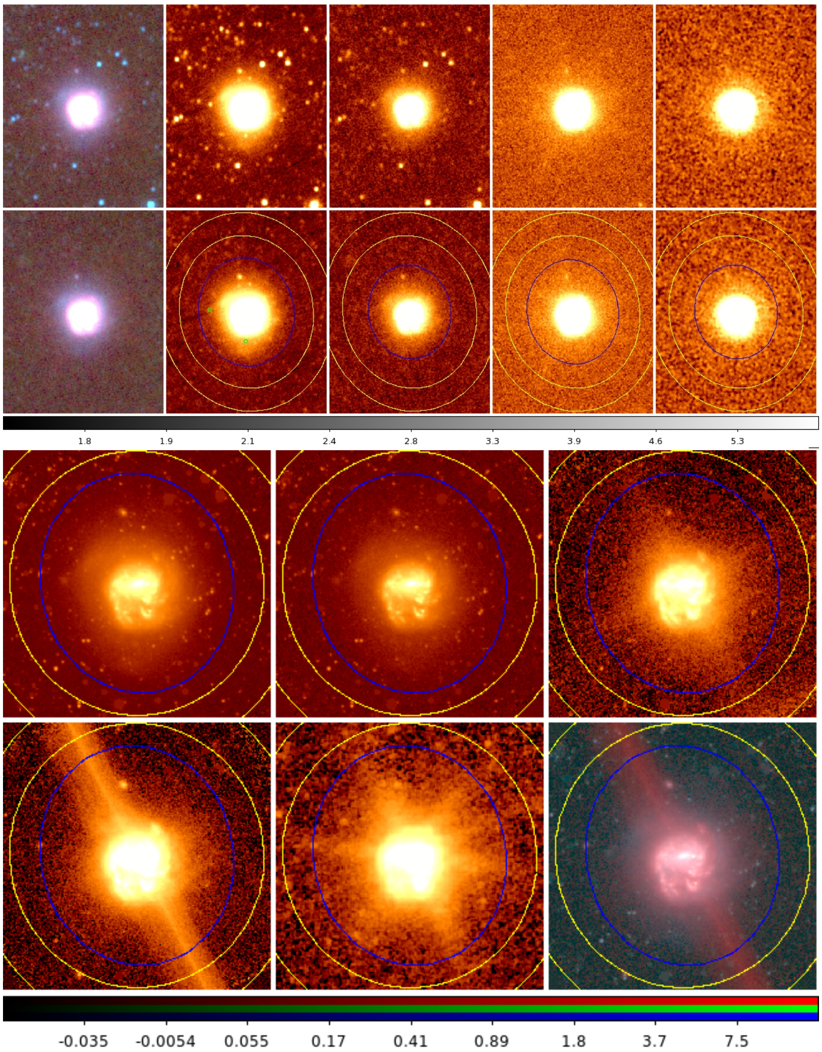

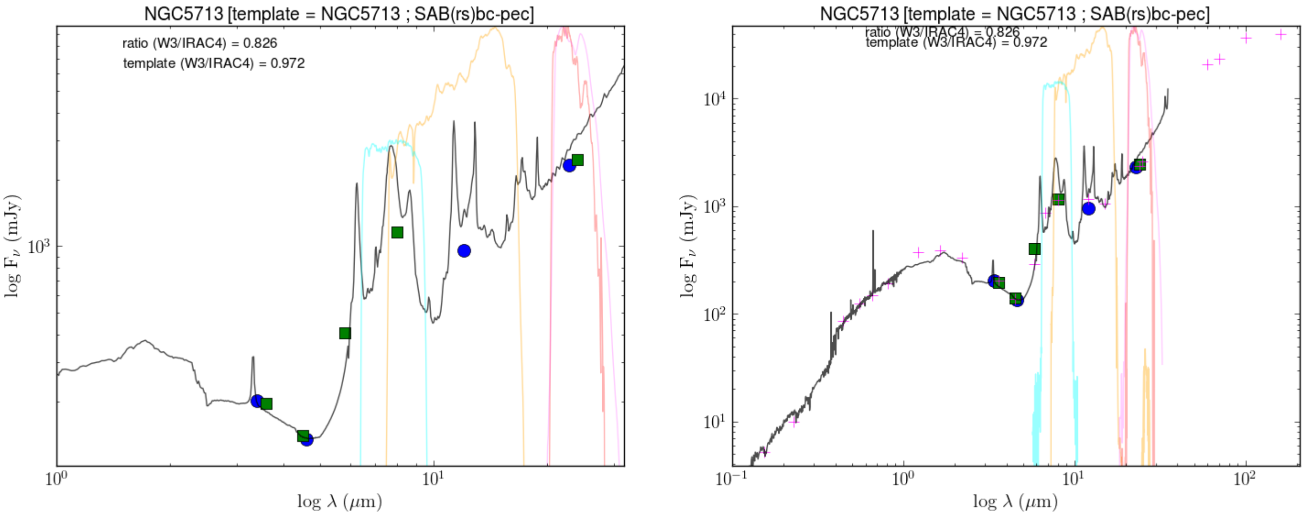

Figure A.69: *Top: WISE imaging of NGC5713, unprocessed and processed. Yellow ellipses are sky annulus borders; blue ellipse is 1σ isophotal ellipse. Left to right: Three-colour (W1+2+3); W_1; W_2; W_3; W_4. Middle: Spitzer imaging of NGC5713. Top left to bottom right: IRAC1, IRAC2, IRAC3, IRAC4, MIPS24, three-colour (IRAC1+2+4). Bottom left: SED of NGC5713. Bottom right: SED of NGC5713 with all its SINGS data.*

A.70 NGC5866: S0; D = 12.5 Mpc; Activity: HII/LINER

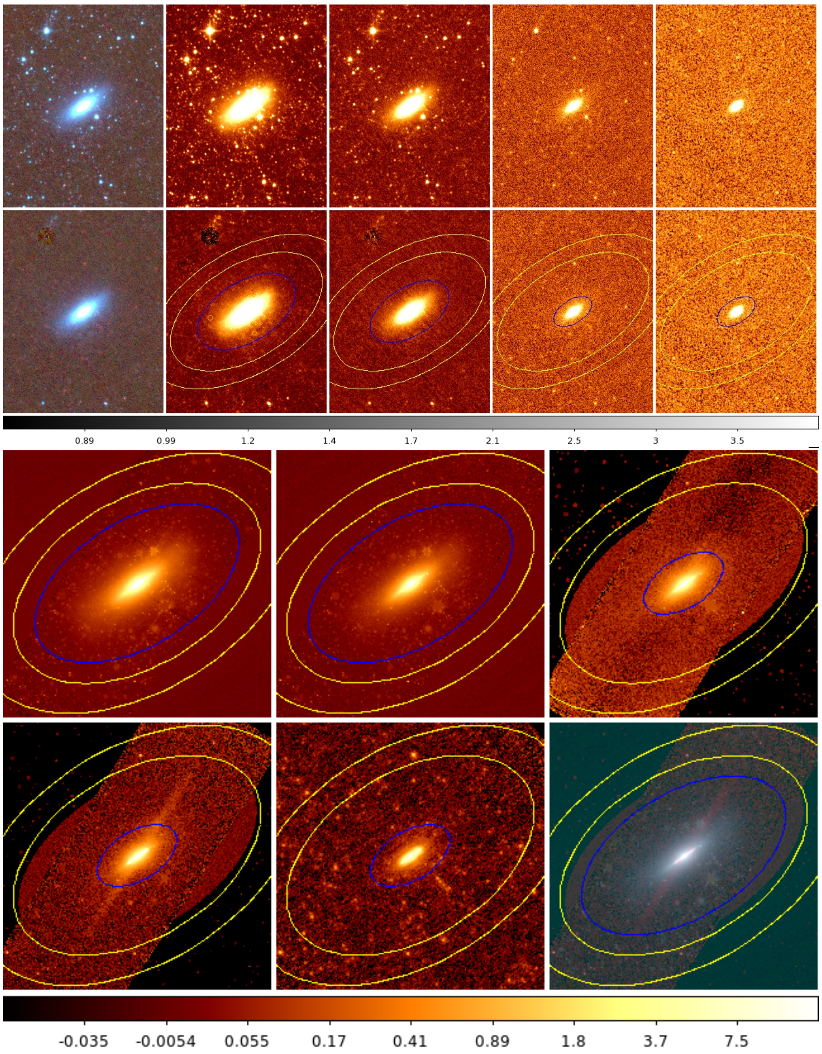

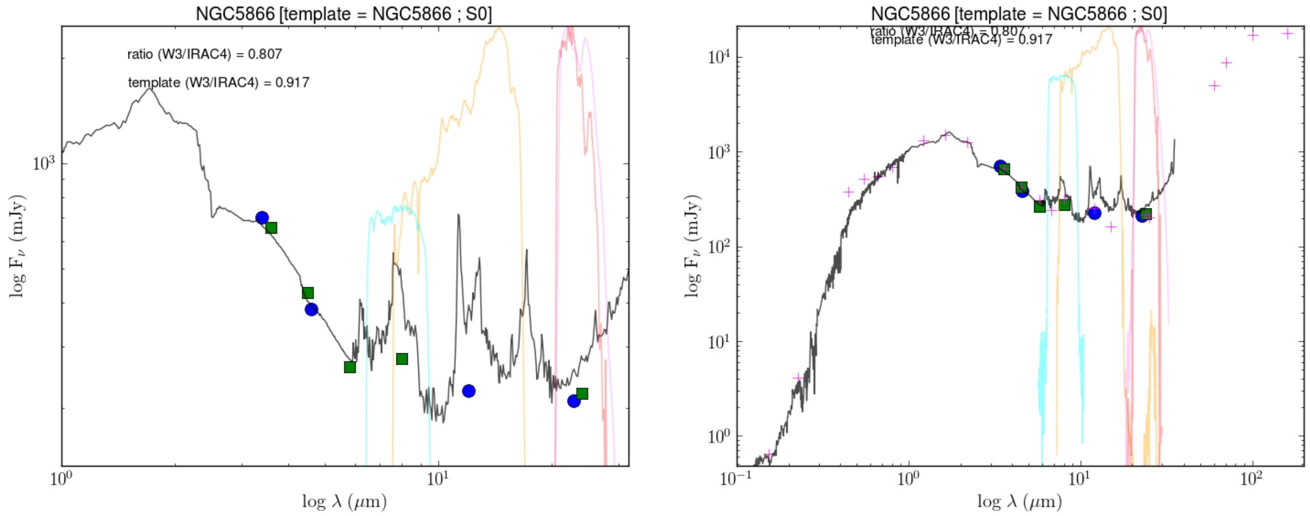

Figure A.70: *Top: WISE imaging of NGC5866, unprocessed and processed. Yellow ellipses are sky annulus borders; blue ellipse is 1σ isophotal ellipse. Left to right: Three-colour (W1+2+3);* W_1; W_2; W_3; W_4. *Middle: Spitzer imaging of NGC5866. Top left to bottom right: IRAC1, IRAC2, IRAC3, IRAC4, MIPS24, three-colour (IRAC1+2+4). Bottom left: SED of NGC5866. Bottom right: SED of NGC5866 with all its SINGS data.*

A.71 NGC6822: IB(s)m; D = 0.6 Mpc; LC V-VI

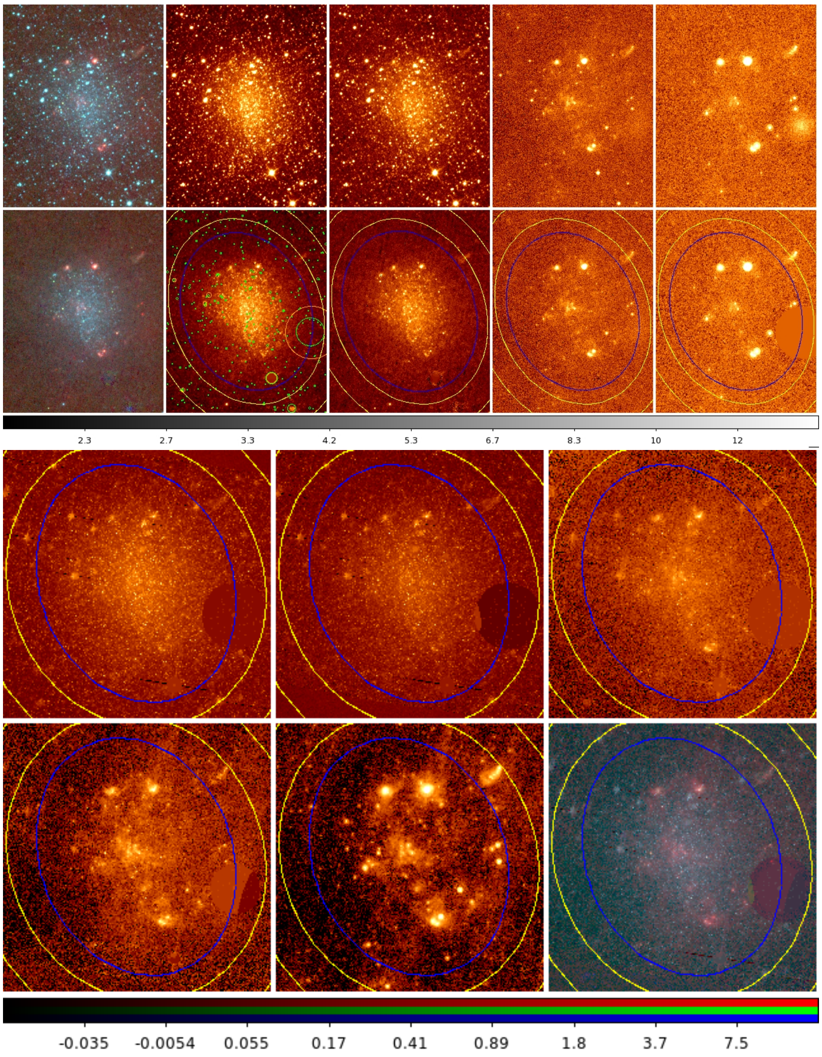

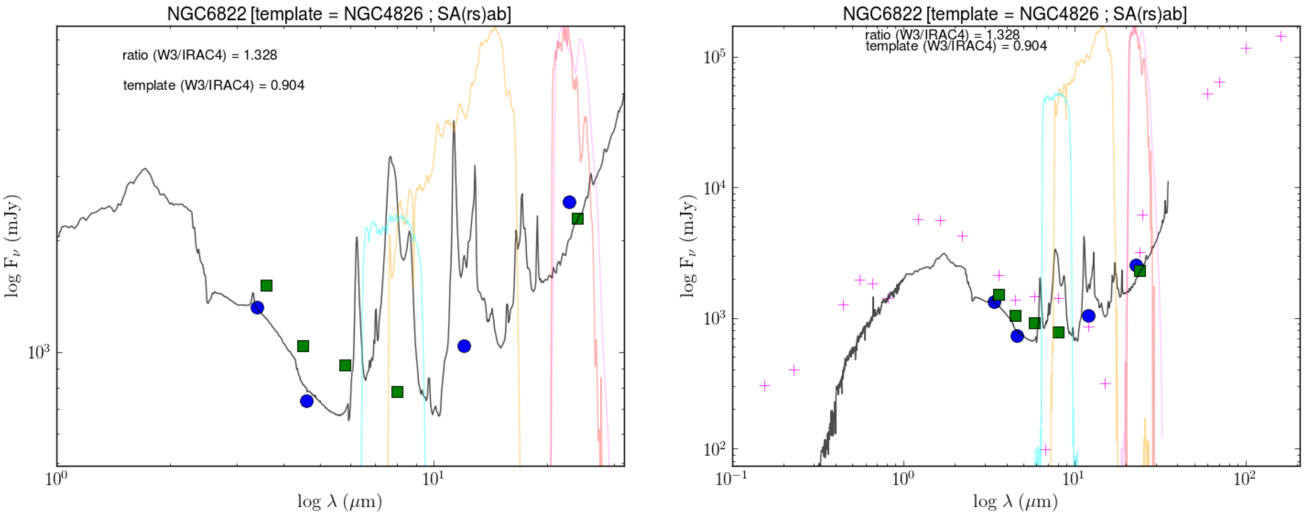

Figure A.71: *Top: WISE imaging of NGC6822, unprocessed and processed. Yellow ellipses are sky annulus borders; blue ellipse is 1σ isophotal ellipse. Left to right: Three-colour (W1+2+3);* W_1; W_2; W_3; W_4. *Middle: Spitzer imaging of NGC6822. Top left to bottom right: IRAC1, IRAC2, IRAC3, IRAC4, MIPS24, three-colour (IRAC1+2+4). Bottom left: SED of NGC6822. Bottom right: SED of NGC6822 with all its SINGS data.*

A.72 NGC6946: SAB(rs)cd; D = 5.5 Mpc; LC III-IV; Activity: HII/Sy2

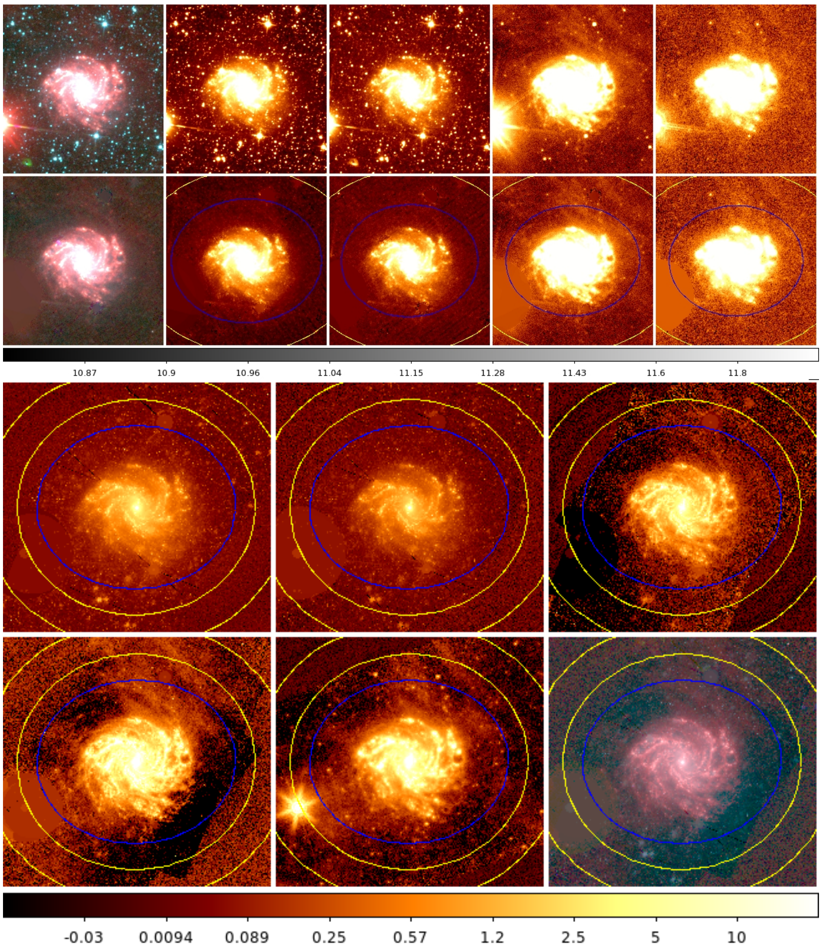

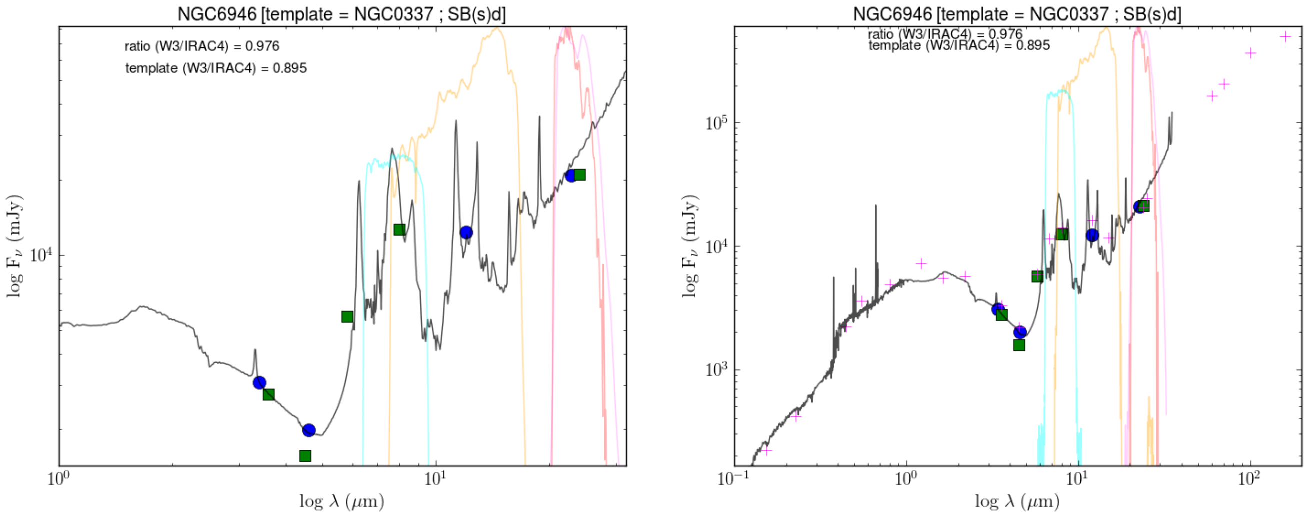

Figure A.72: *Top: WISE imaging of NGC6946, unprocessed and processed. Yellow ellipses are sky annulus borders; blue ellipse is 1σ isophotal ellipse. Left to right: Three-colour (W1+2+3); W*$_1$*; W*$_2$*; W*$_3$*; W*$_4$*. Middle: Spitzer imaging of NGC6946. Top left to bottom right: IRAC1, IRAC2, IRAC3, IRAC4, MIPS24, three-colour (IRAC1+2+4). Bottom left: SED of NGC6946. Bottom right: SED of NGC6946 with all its SINGS data.*

A.73 NGC7331: SA(s)b; D = 15.7 Mpc; LC II; Activity: HII/LINER

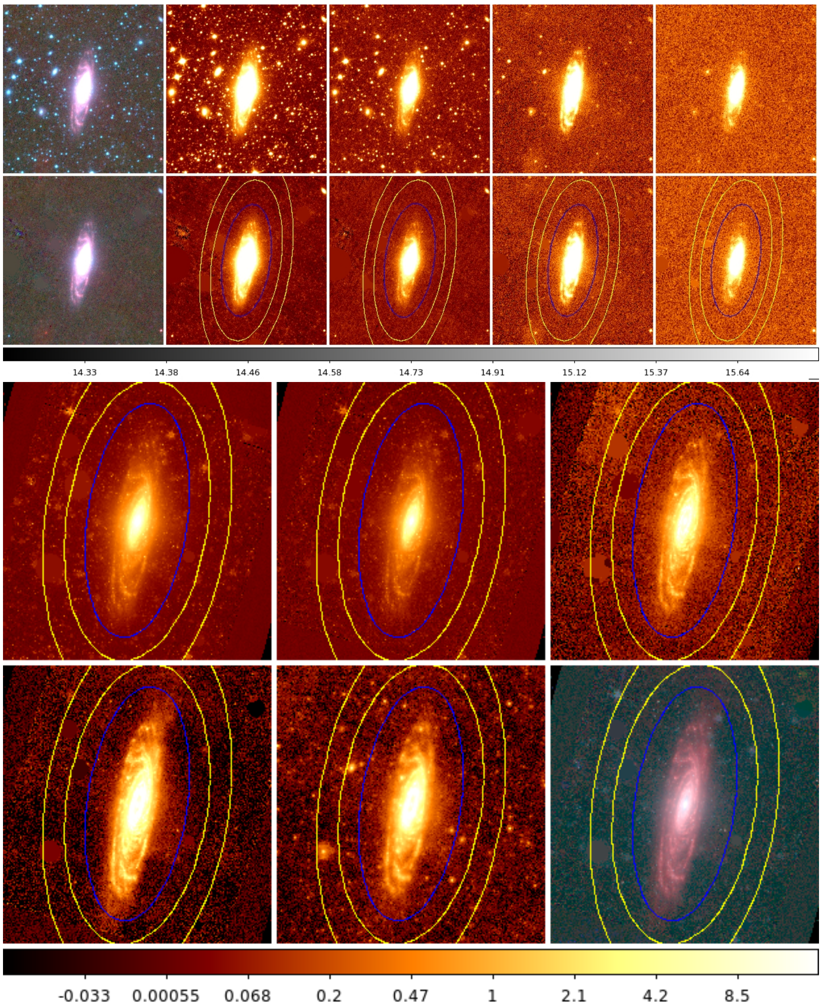

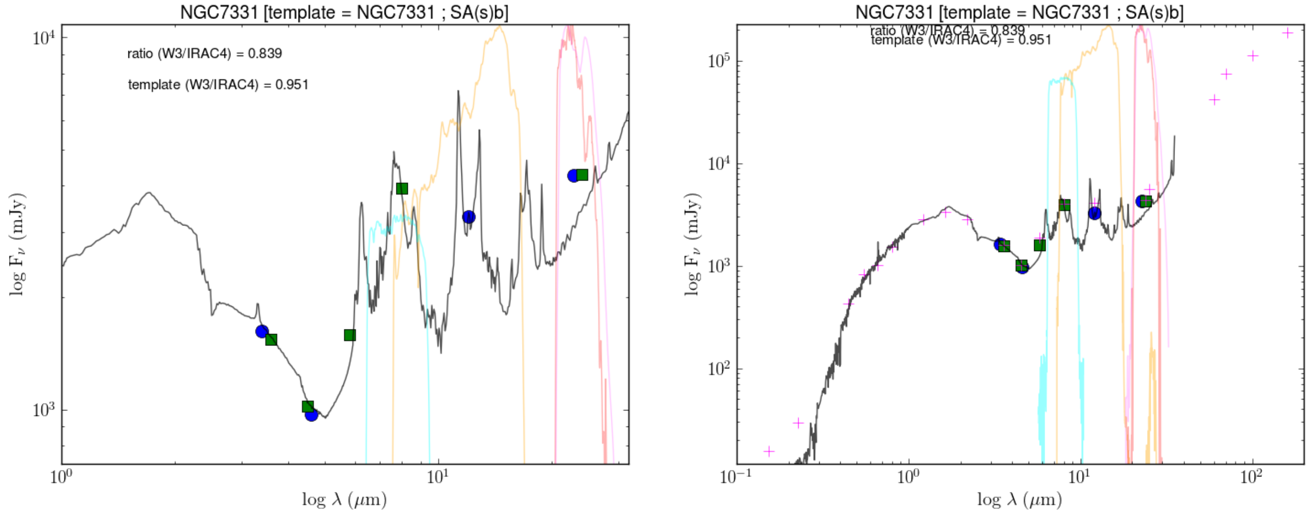

Figure A.73: *Top: WISE imaging of NGC7331, unprocessed and processed. Yellow ellipses are sky annulus borders; blue ellipse is 1σ isophotal ellipse. Left to right: Three-colour (W1+2+3); W_1; W_2; W_3; W_4. Middle: Spitzer imaging of NGC7331. Top left to bottom right: IRAC1, IRAC2, IRAC3, IRAC4, MIPS24, three-colour (IRAC1+2+4). Bottom left: SED of NGC7331. Bottom right: SED of NGC7331 with all its SINGS data.*

A.74 NGC7552: SB(s)ab; D = 22.3 Mpc; LC LIRG; Activity: HII/LINER

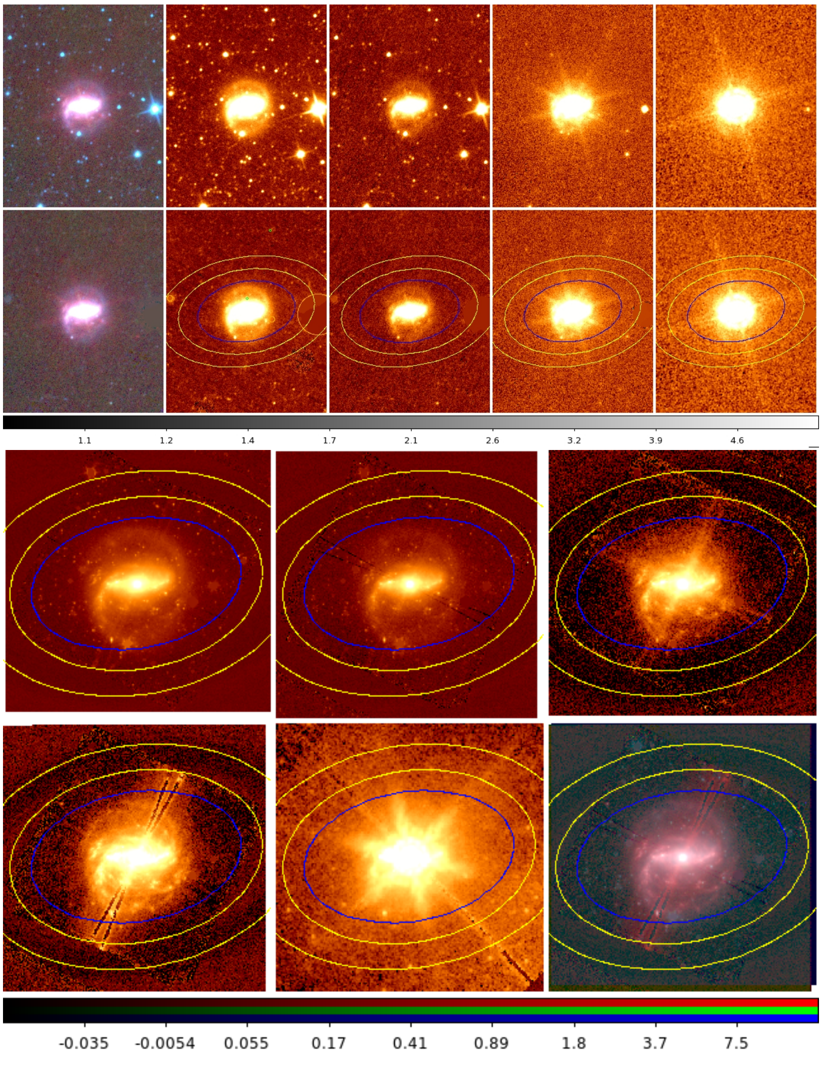

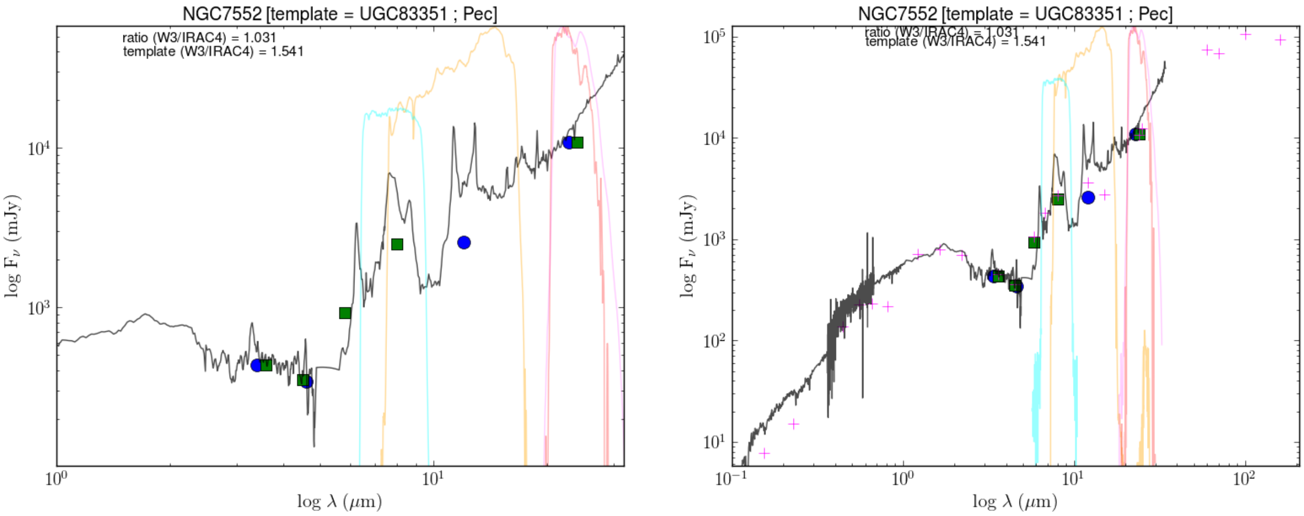

Figure A.74: *Top: WISE imaging of NGC7552, unprocessed and processed. Yellow ellipses are sky annulus borders; blue ellipse is 1σ isophotal ellipse. Left to right: Three-colour (W1+2+3); W$_1$; W$_2$; W$_3$; W$_4$. Middle: Spitzer imaging of NGC7552. Top left to bottom right: IRAC1, IRAC2, IRAC3, IRAC4, MIPS24, three-colour (IRAC1+2+4). Bottom left: SED of NGC7552. Bottom right: SED of NGC7552 with all its SINGS data.*

A.75 NGC7793: SA(s)d; D = 3.2 Mpc; LC IV; Activity: HII

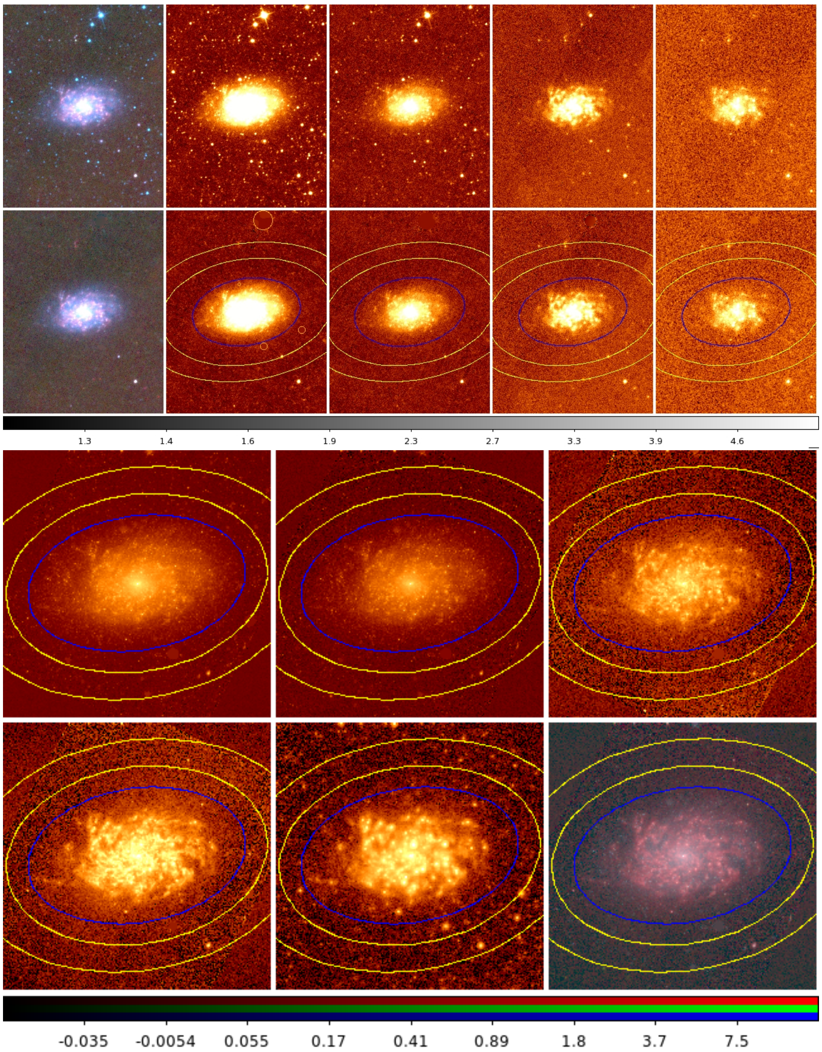

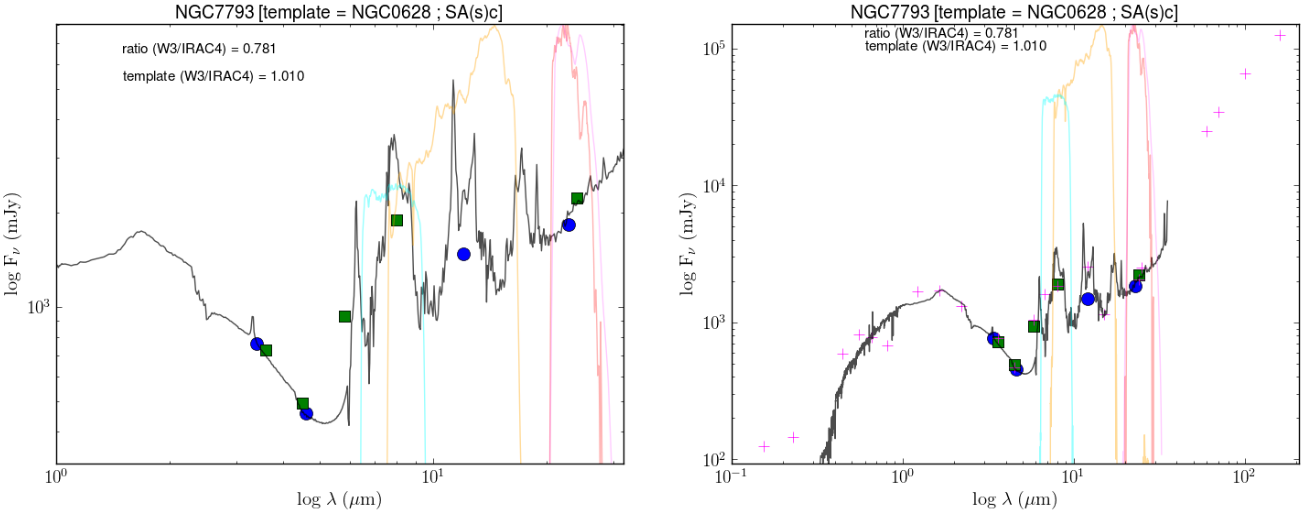

Figure A.75: *Top: WISE imaging of NGC7793, unprocessed and processed. Yellow ellipses are sky annulus borders; blue ellipse is 1σ isophotal ellipse. Left to right: Three-colour (W1+2+3); W_1; W_2; W_3; W_4. Middle: Spitzer imaging of NGC7793. Top left to bottom right: IRAC1, IRAC2, IRAC3, IRAC4, MIPS24, three-colour (IRAC1+2+4). Bottom left: SED of NGC7793. Bottom right: SED of NGC7793 with all its SINGS data.*

Appendix B

Extra plots

Table B.1: Various TIR measurements

Name	log $L(TIR_{DL07})$	log $L(TIR_{Spitzer})$	log $L(TIR_{KF})$	log $L(TIR)$
DDO053	null	null	null	6.9189
DDO165	null	null	null	6.8396
IC0342	10.1711028664374	null	null	null
IC2574	8.38230629686141	8.44008821322979	8.39461814041193	8.1201
IC4710	null	null	null	8.4517
M81DwB	null	null	null	6.8942
Mark33	null	null	null	10.2636
NGC0024	null	null	null	8.3222
NGC0337	10.3366774299295	10.3050876768435	10.3246682707411	10.2194
NGC0584	null	null	null	8.5194
NGC0628	9.91591161150507	9.91907226815406	9.90119749450474	9.7727
NGC0855	8.62657607209869	8.60666846917956	8.63876583777625	8.3866
NGC0925	9.66943302850200	9.66406786090621	9.58567099893709	9.4055
NGC1097	10.8627072259027	10.8414553632568	10.8448215256346	10.8417
NGC1266	10.4346212829012	10.4142403718323	10.4553491970243	10.4574
NGC1291	9.37614027019028	9.38750899968003	9.27105098698929	9.1419
NGC1316	9.91448596302022	9.81755806554917	9.80483082307763	9.6611
NGC1377	10.1547819543271	10.0952285869823	10.1066350611049	10.5567
NGC1404	null	null	null	8.7661
NGC1482	10.5863984321560	10.5240848244029	10.5754963546370	10.6731
NGC1512	9.60862933917192	9.61722269442064	9.57442789338478	9.3423
NGC1566	null	null	null	10.6193
NGC1705	null	null	null	7.6439
NGC2146	11.3490587212398	null	null	null
NGC2798	10.5973945670854	10.5581152325500	10.5769301649488	10.7482
NGC2841	10.0664591615115	10.0552465217953	9.97583407381638	9.7363
NGC2915	7.68132724728763	7.63062490245421	7.56837061579596	7.4297
NGC2976	8.94927936673943	8.96066532227608	8.92118328396487	8.8221
NGC3031	null	null	null	9.4066
NGC3034	null	null	null	null
NGC3049	9.98508057343922	9.95422835661961	9.96534491277232	10.1475
NGC3077	8.95543778115771	null	null	null
NGC3184	10.0412363440947	10.0204424544075	9.94602975052489	9.822
NGC3190	10.0769705600118	10.0373341262882	10.0582249132193	9.7186
NGC3198	10.0176777603421	10.0088630011144	9.93164084967907	9.898
NGC3265	9.39345580155039	9.33743182491014	9.31781414839287	9.4994
NGC3351	9.9321813627779	9.96109077726502	9.91835973440375	9.9351
NGC3521	10.3323399161863	10.3126810849834	10.3212655012269	10.1643

Continued on next page

Table B.1 – continued from previous page

Name	log $L(TIR_{DL07})$[1] ($L_\odot$)	log $L(TIR_{Spitzer})$[2] ($L_\odot$)	log $L(TIR_{KF})$[3] ($L_\odot$)	log $L(TIR)$[4] ($L_\odot$)
NGC3621	9.97235049184163	9.92842939721226	9.90529775079127	9.7402
NGC3627	10.5600296824159	10.5367964587488	10.5213780442089	10.4399
NGC3773	9.13375220154729	9.10656518808792	9.03449884316997	9.1673
NGC3938	10.3032342297415	10.2842540738043	10.2218004534098	10.0749
NGC4125	null	null	null	9.049
NGC4236	8.69915867188935	8.75173853823977	8.71355402187591	8.5004
NGC4254	10.7098120198674	10.6604546180308	10.6506607448693	10.5416
NGC4450	null	null	null	9.4699
NGC4536	10.3979666196060	10.3540196344889	10.3745442615037	10.4373
NGC4552	null	null	null	8.9972
NGC4559	10.0687302138425	10.0591758775560	9.97726953909113	9.8068
NGC4569	9.95447721016058	9.92164488776981	9.93349913329454	9.8773
NGC4579	10.3455949854240	10.3334800716562	10.2938666138599	10.1019
NGC4594	9.67654939800029	9.61290921328326	9.58647079223507	9.4428
NGC4625	8.89804379836359	8.88016735444344	8.78250278964571	8.6808
NGC4631	10.2147887646187	10.1842368566090	10.1535656087690	10.0223
NGC4725	10.0067719461577	9.99019015482796	9.90045576162492	9.6048
NGC4736	9.92434991286882	9.86874201513725	9.84067292417820	9.7299
NGC4826	9.65199730907508	9.63675724236245	9.62436771805784	9.4088
NGC5033	null	null	null	10.3314
NGC5055	10.5549451714078	10.5578637837423	10.5013196218102	10.3219
NGC5194	null	null	null	10.4266
NGC5195	null	null	null	9.5102
NGC5398	9.16099569642910	null	null	null
NGC5408	8.30043337240787	8.28582969463521	8.26279653370511	8.542
NGC5474	8.79379214501345	8.84052268933765	8.71915360099318	8.5005
NGC5713	10.6486972932643	10.6015045128100	10.6310674157846	10.6664
NGC5866	9.71697828313296	9.68030722720615	9.67935839605139	9.1852
NGC6822	null	null	null	7.3085
NGC6946	10.4943936962654	10.4481656664880	10.4878205487329	10.424
NGC7331	10.7872961260426	10.7517908431988	10.7152282804950	10.5001
NGC7552	null	null	null	11.0213
NGC7793	9.32649709191566	9.35875476910355	9.25884200310362	9.0938

---

[1] Sourced from Draine & Li 2007.

[2] TIR flux determined through equation (1.2) with photometry from SINGS. Converted to luminosity using luminosity distance.

[3] TIR flux determined through equation (1.2) with photometry from SINGS ($24 \mu m$) and KINGFISH (70, 160 μm). Converted to luminosity using luminosity distance.

[4] Determined using our $24 \mu m$ photometry.

B.1 Star formation relations used

Yun, Reddy & Condon 2001 radio SFR relation:

$$SFR_{20cm}(M_{\odot}.yr^{-1}) = 5.9(\pm1.8) \times 10^{-22} L_{20}(W.Hz^{-1}) \tag{B.1}$$

Calzetti 2012 relation from TIR:

$$SFR_{TIR}(M_{\odot}.yr^{-1}) = 2.8 \times 10^{-44} L(TIR)(erg.s^{-1}) \tag{B.2}$$

Cluver et al. 2014 relations:

$$log_{10}SFR_{H\alpha}(M_{\odot}.yr^{-1}) = 1.13 log_{10}\nu L_{12}(L_{\odot}) - 10.24 \tag{B.3}$$

$$log_{10}SFR_{H\alpha}(M_{\odot}.yr^{-1}) = 0.82 log_{10}\nu L_{22}(L_{\odot}) - 7.3 \tag{B.4}$$

Jarrett et al. 2013 relations:

$$SFR_{IR}(\pm0.28)(M_{\odot}.yr^{-1}) = 4.91(\pm0.39) \times 10^{-10} \nu L_{12}(L_{\odot}) \tag{B.5}$$

$$SFR_{IR}(\pm0.04)(M_{\odot}.yr^{-1}) = 7.50(\pm0.07) \times 10^{-10} \nu L_{12}(L_{\odot}) \tag{B.6}$$

B.2 Additional figures

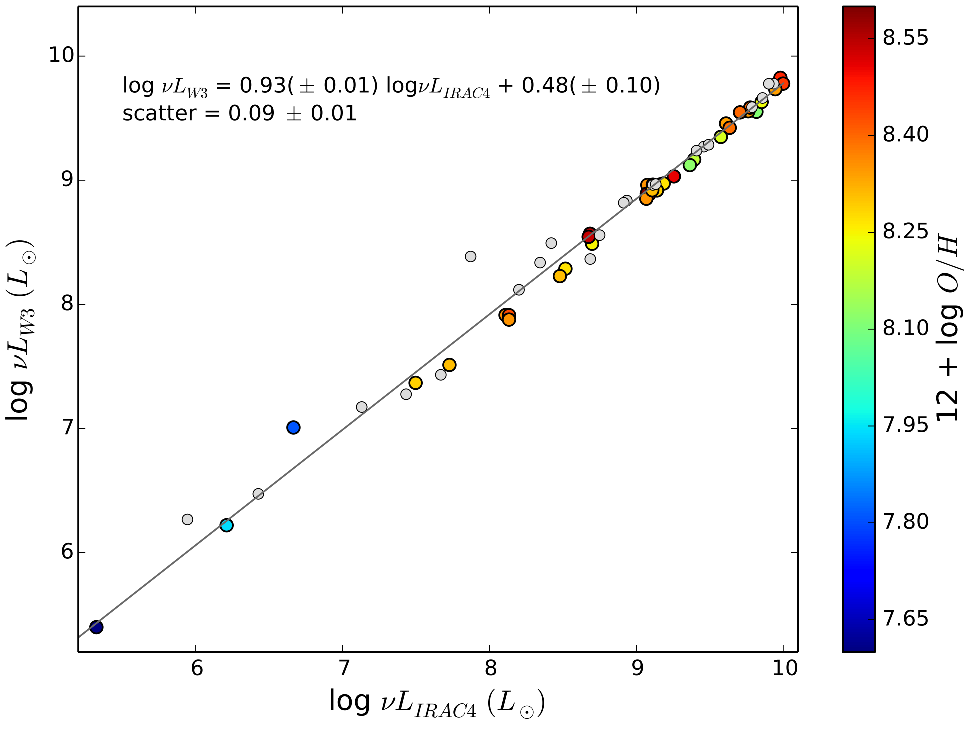

Figure B.1: *Luminosity comparison between the stellar continuum-subtracted W3 and IRAC4, colour-coded by metallicity (oxygen abundances from Pilyugin & Thuan 2005).*

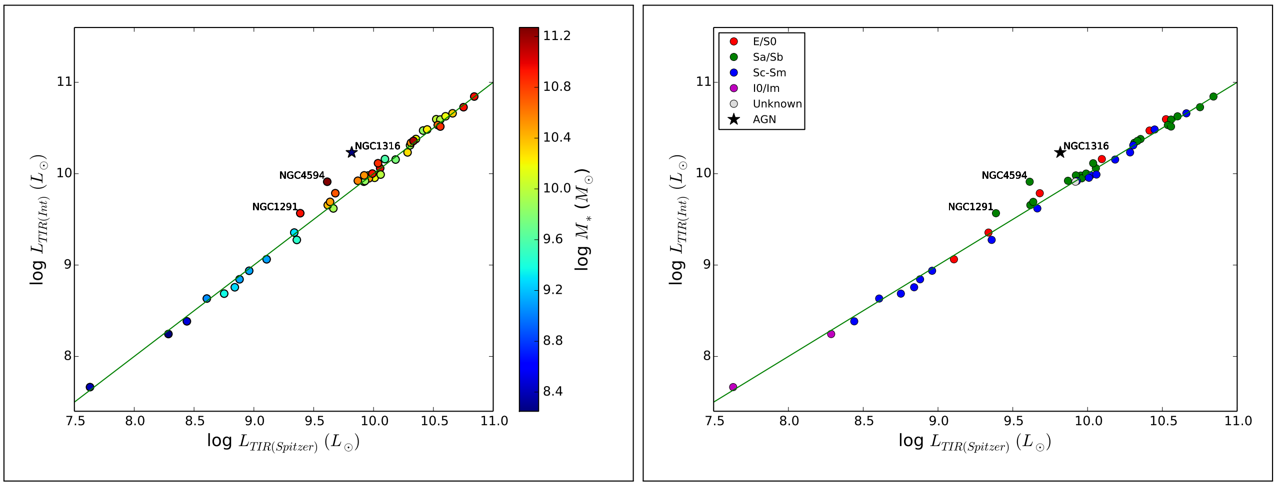

Figure B.2: *Comparison of TIR luminosities, from integrating under SED fits (Draine & Li 2007) and* Spitzer *photometry, colour-coded by stellar mass (left) and morphology (right). Highlighted sources: Table 4.7.*

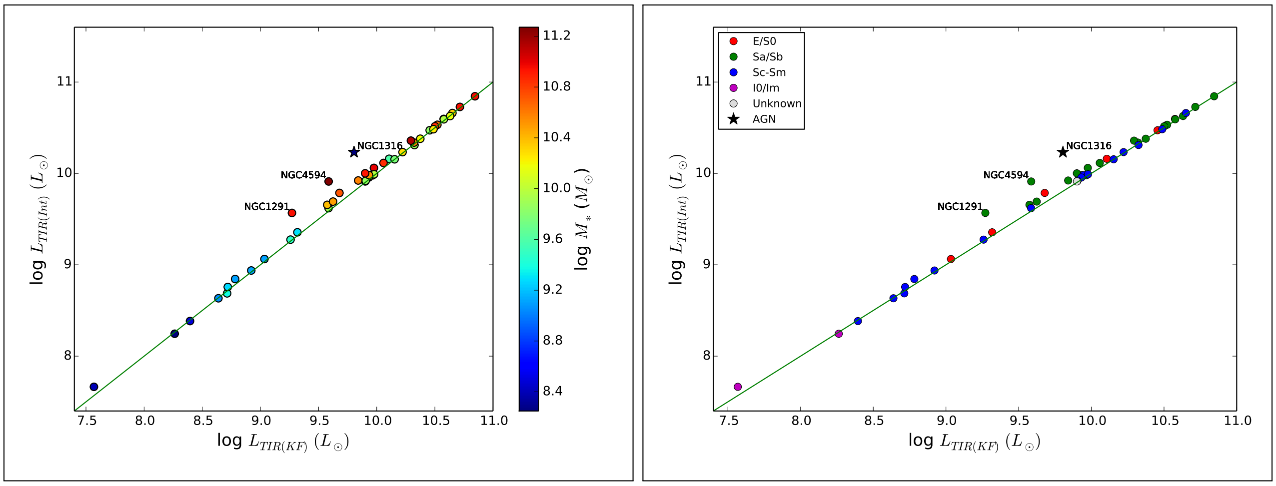

Figure B.3: *Comparison of TIR luminosities, from integrating under SED fits (Draine & Li 2007) and* Spitzer *and* Herschel *photometry, colour-coded by stellar mass (left) and morphology (right). Highlighted sources: Table 4.7.*

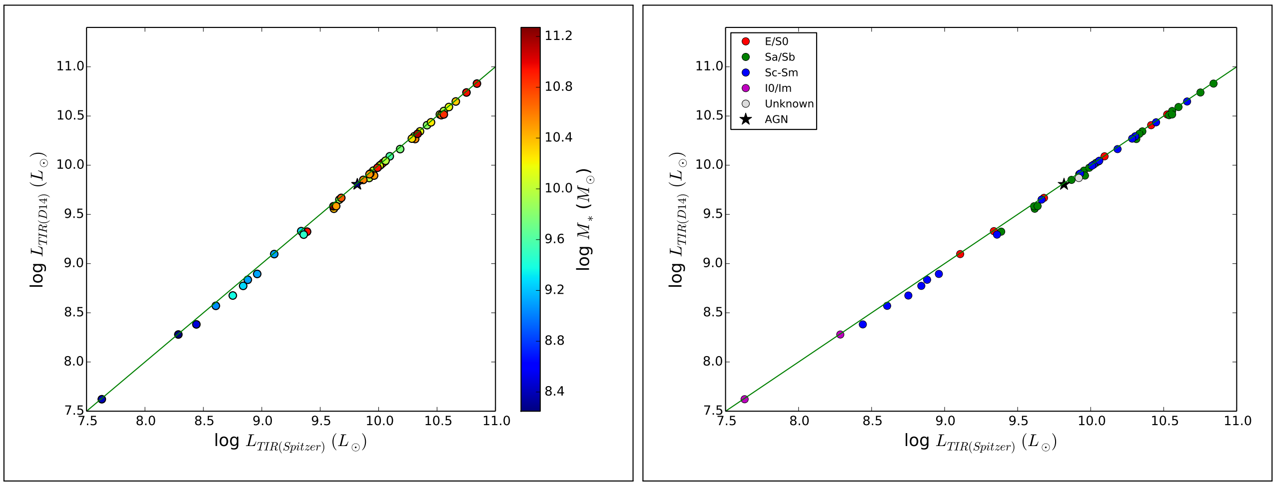

Figure B.4: *Comparison of TIR luminosities, from Dale et al. 2014 and* Spitzer *photometry, colour-coded by stellar mass (left) and morphology (right). Highlighted sources: Table 4.7.*

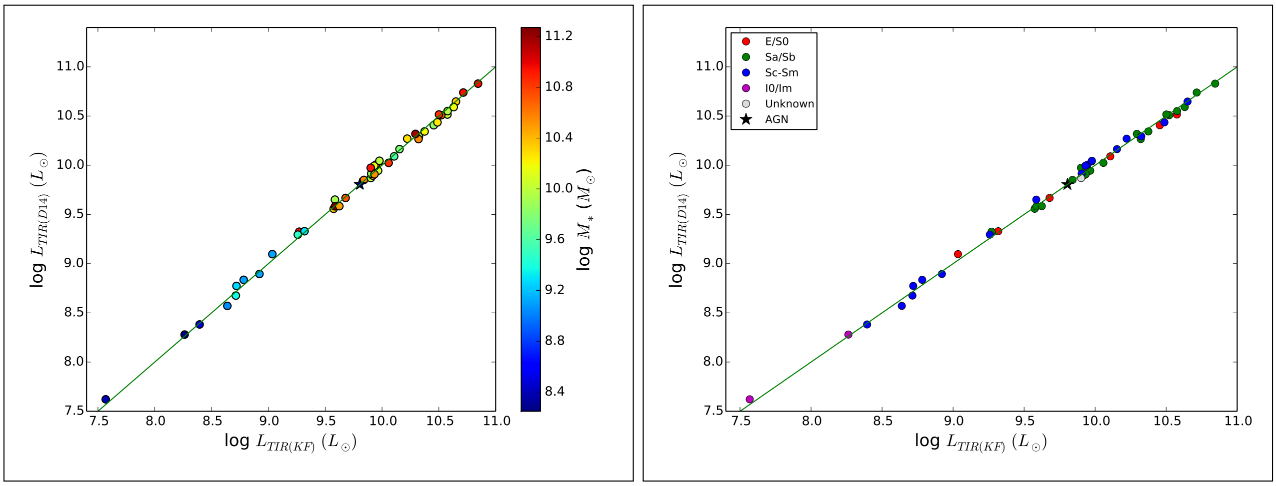

Figure B.5: *Comparison of TIR luminosities, from Dale et al. 2014 and* Spitzer *and* Herschel *photometry, colour-coded by stellar mass (left) and morphology (right). Highlighted sources: Table 4.7.*

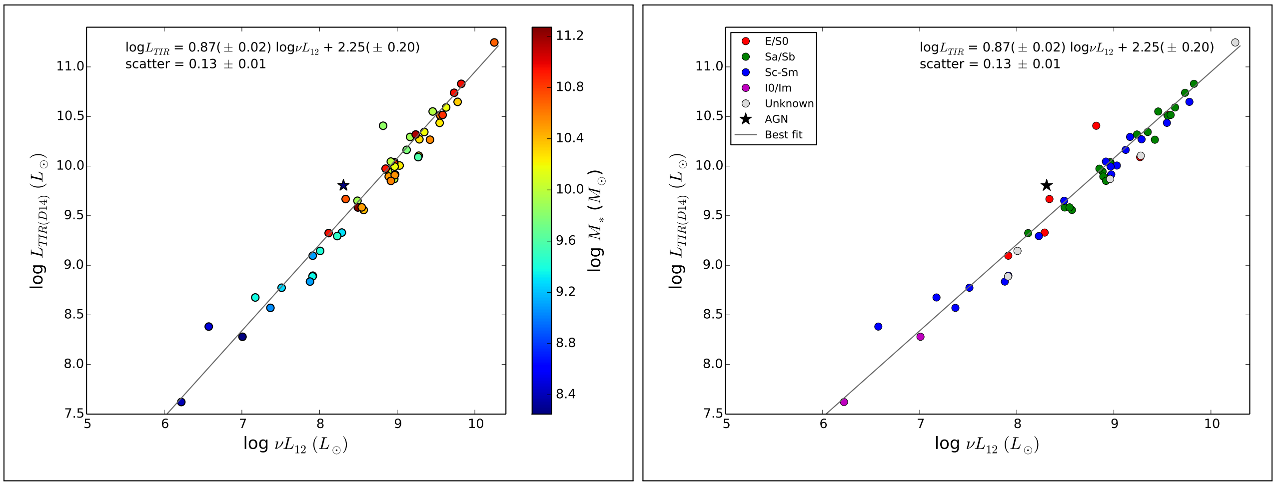

Figure B.6: *Variation of the 11.3 μm PAH and TIR luminosities. TIR is determined from* Spitzer *photometry (Dale et al. 2014), colour-coded by stellar mass (left) and morphology (right).*

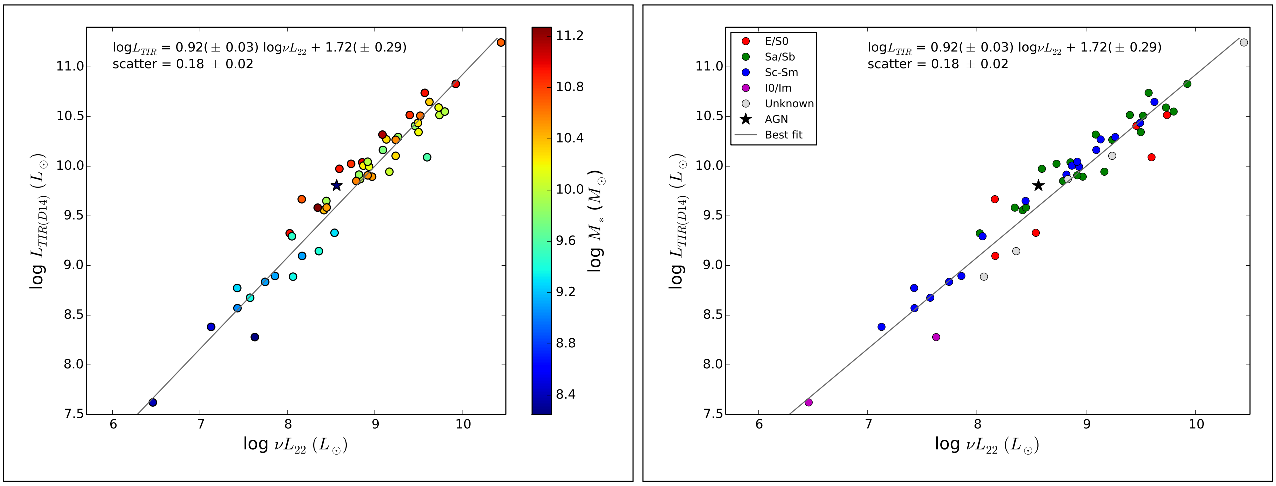

Figure B.7: *Variation of the 22 μm dust and TIR luminosities. TIR is determined from* Spitzer *photometry (Dale et al. 2014), colour-coded by stellar mass (left) and morphology (right).*

The next two sets of plots have two different TIR metrics: the datapoint-determined measurement from Dale et al. 2014, denoted by TIR_{D14}; and the integrated TIR flux from Draine & Li 2007, denoted by TIR_{Int}. This is due to the difference between the two metrics being negligible.

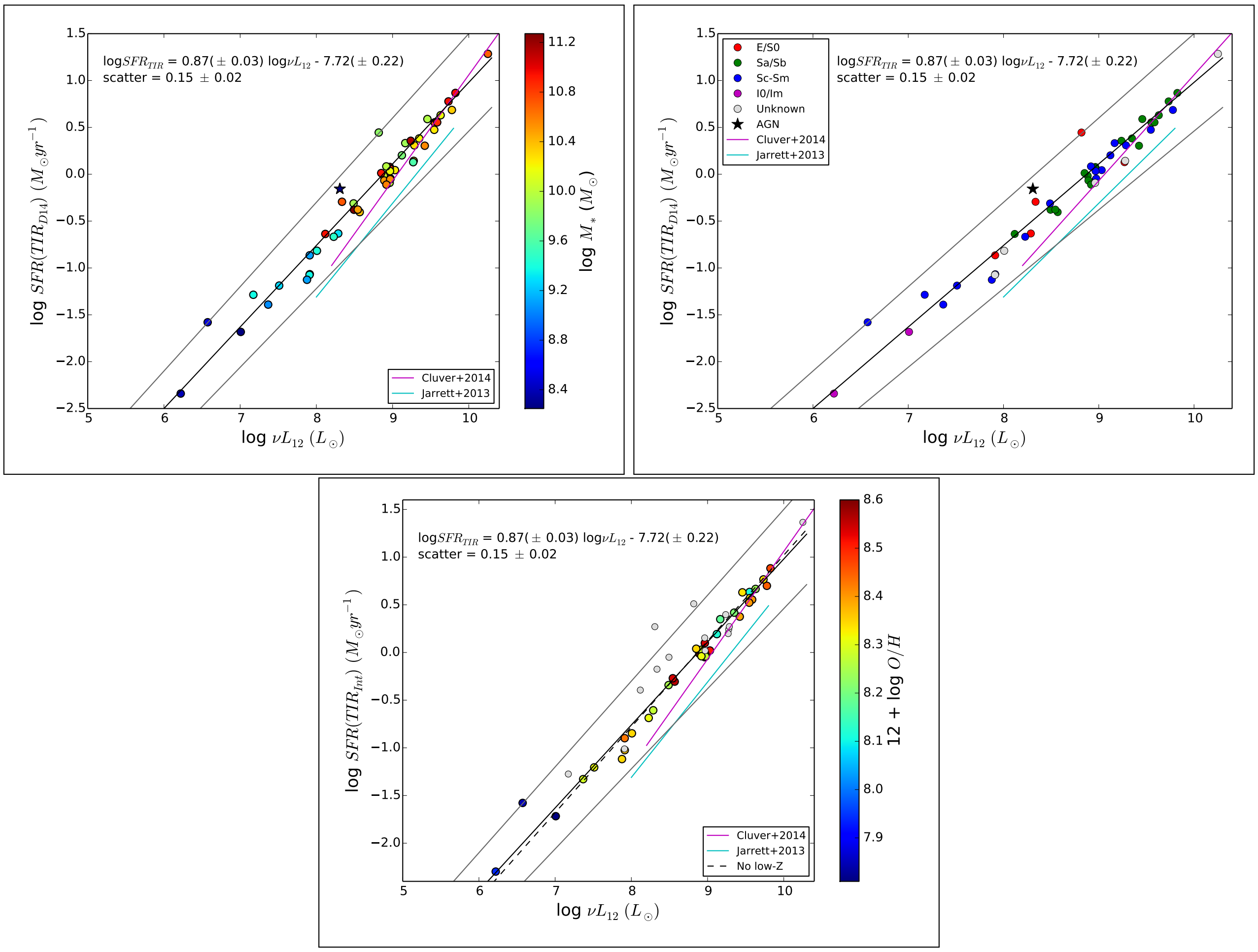

Figure B.8: *SFR comparison with W3 luminosity. Top left: colour-coded by stellar mass; Top right: colour-coded by morphology; Bottom: colour-coded by metallicity (oxygen abundances from Pilyugin & Thuan 2005). The dotted line is the best-fit relation for all the points excluding the three lowest-metallicity galaxies (IC2574, NGC2915, NGC5408).*

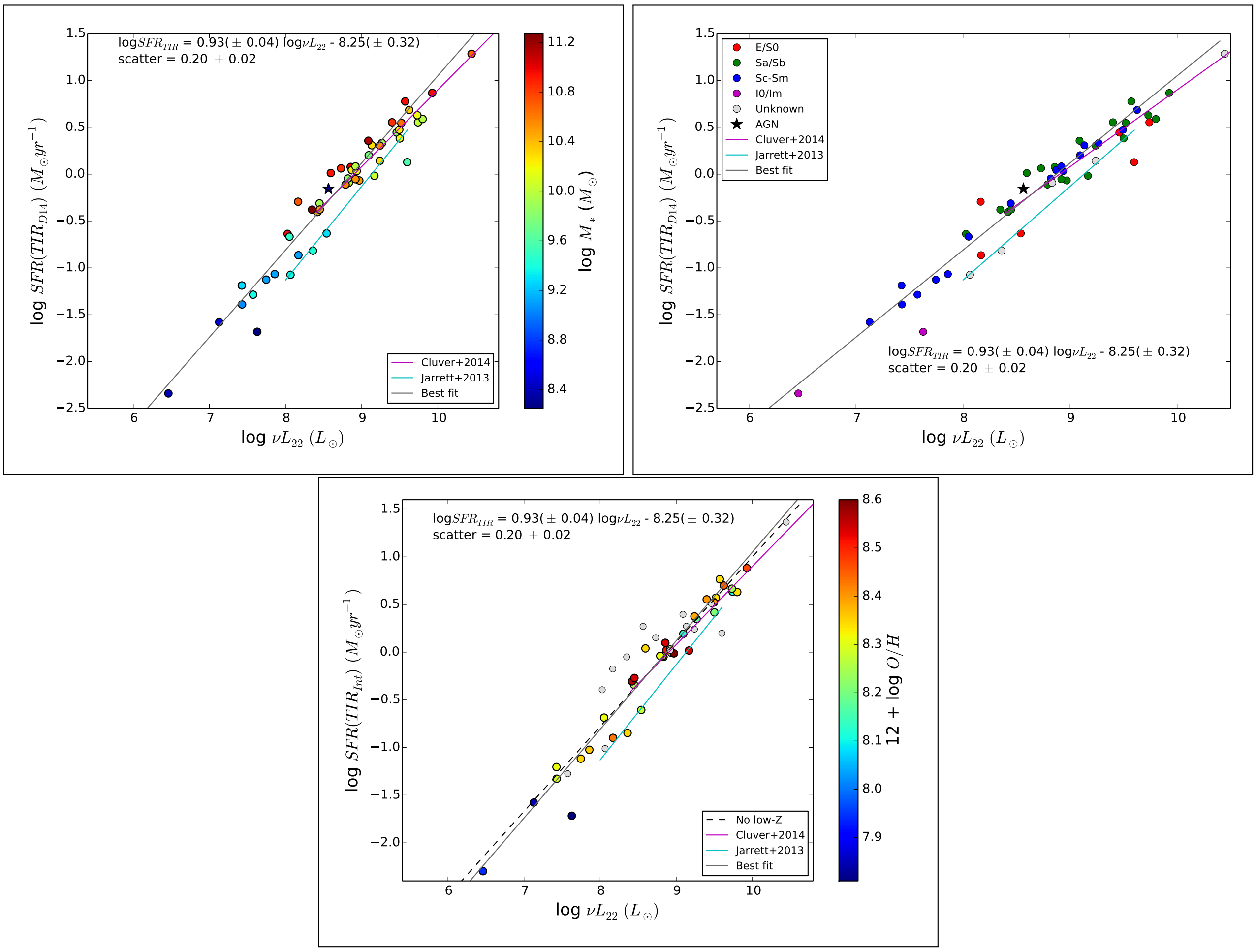

Figure B.9: *SFR comparison with W4 luminosity. Top left: colour-coded by stellar mass; Top right: colour-coded by morphology; Bottom: colour-coded by metallicity (oxygen abundances from Pilyugin & Thuan 2005). The dotted line is the best-fit relation for all the points excluding the three lowest-metallicity galaxies (IC2574, NGC2915, NGC5408).*